



# Durham E-Theses

---

## *Impacts of road construction on landsliding in Nepal*

PRADHAN, SAMPRADA

### How to cite:

---

PRADHAN, SAMPRADA (2021) *Impacts of road construction on landsliding in Nepal*, Durham theses, Durham University. Available at Durham E-Theses Online: <http://etheses.dur.ac.uk/14069/>

### Use policy

---

The full-text may be used and/or reproduced, and given to third parties in any format or medium, without prior permission or charge, for personal research or study, educational, or not-for-profit purposes provided that:

- a full bibliographic reference is made to the original source
- a [link](#) is made to the metadata record in Durham E-Theses
- the full-text is not changed in any way

The full-text must not be sold in any format or medium without the formal permission of the copyright holders.

Please consult the [full Durham E-Theses policy](#) for further details.

# Impacts of road construction on landsliding in Nepal

Samprada Pradhan

Thesis submitted towards the degree of Doctor of Philosophy

Department of Engineering

Durham University

United Kingdom



2021

# Impacts of road construction on landsliding in Nepal

## Abstract

---

Rainfall-induced landslides occur extensively across the mountainous terrain of Nepal during the monsoon. Anthropogenic factors such as slope cutting for local road construction has been reported to have further aggravated the risk of rainfall-induced landsliding in Nepal. Although roads are vital infrastructure for development, the increased rate of landsliding due to road construction has reversed the anticipated benefits from improved road access. For the prevention and mitigation of such landslides, it is imperative to assess how the two key factors- road and rainfall interact to cause landslides. This study aims to better understand this interaction by conducting research that integrates reconnaissance surveys, in-situ tests, laboratory testing, field monitoring and numerical modelling using concepts of unsaturated soil mechanics.

In this study, reconnaissance surveys were conducted along a newly widened local road (Daklang-Listi) in Sindhupalchok, Nepal to identify the issues related to local road construction that are conducive to landsliding. The field observations revealed that the non-engineered road widening involving slope cutting at steep angles without suitable slope protection, drainage and control over spoil disposal increased the susceptibility to rainfall-induced landsliding. For the investigation of the physical process of landsliding caused by the road-rainfall interaction using numerical modelling, the scope of this study was narrowed down to a case study of Kanglang landslide which occurred during the monsoon in July 2018 after road widening. In-situ testing and trial pit excavations were undertaken for the evaluation of subsoil conditions and for soil sampling at the selected location. Laboratory testing was performed to determine the physical, mechanical and hydraulic properties of the soil samples. To understand the hydrologic response of the soil during atmospheric drying and wetting, a field-monitoring station was installed near the Kanglang landslide, which consisted of a rain gauge, 10HS water content sensors and a data logger. The temporal variation of volumetric water content due to soil-atmospheric interaction was evaluated and the factors influencing the volumetric water content response were identified. The monitored data showed that the progressive wetting of soil during wet periods could lead to soil approaching saturation at shallow depths, which can reduce the soil suction and ultimately cause shallow slope failures. A back-analysis of the Kanglang landslide was performed using fully coupled flow-deformation analysis and safety analysis in PLAXIS 2D to evaluate the effect of the road cut and rainfall on the failure mechanism. Before the back-analysis, the numerical model was calibrated against the field-measured volumetric water contents. The calibration results confirmed that the model was capable of capturing the in-situ changes in soil water content due to infiltration and drying. The back-analysis results demonstrated that the ingress of rainwater caused a reduction of soil suction at shallow depths and the presence of the road cut promoted the failure leading to accelerated displacements at the road cut. To reinforce this observation, the back-analysis was replicated in a model without a road cut. The results of this analysis showed that the presence of the road cut decreases the initial factor of safety, thereby, increasing the susceptibility to failure. In addition, it was also demonstrated that the rainfall event that triggered the Kanglang landslide would not have triggered a failure in the absence of the road cut, hence, confirming that the presence of road cut in the hillslopes can be detrimental to slope stability during rainfall.

# Declaration

---

I hereby declare that the work in this thesis has not been submitted for any other degree or qualification. This is all my work based on research conducted at Durham University, unless referenced otherwise in the text. A part of this study has been published in the following paper:

Pradhan, S., Toll, D. G., Rosser, N. J., and Brain, M. J. (2020) 'Field monitoring of soil-moisture to understand the hydrological response of a road-cut slope', *E3S Web of Conferences*. Edited by R. Cardoso, C. Jommi, and E. Romero, 195, p. 01029. doi: 10.1051/e3sconf/202019501029. (Appendix A-3)

Copyright © 2021 Samprada Pradhan

*"The copyright of this thesis rests with the author. No quotation from it should be published without the author's prior written consent and information derived from it should be acknowledged."*



*Dedicated to my parents Mrs Sakuntala Pradhan and Mr Mani Raj Pradhan*

*and to my husband Swastik Shrestha*

# Acknowledgements

---

Before getting into the research I would like to take a moment to thank everyone who have supported me during this study.

My utmost gratitude goes to my incredible supervisors Prof David Toll, Prof Nick Rosser and Dr Matthew Brain for the unwavering support and encouragement. Thank you for giving me this lifetime opportunity to learn from you. This research would not have been possible without your constructive feedback and guidance.

I am thankful to Dr Ashutosh Kumar and Dr Arash Azizi for being the most encouraging mentors/friends. Ashutosh and Arash, thank you. Your insightful advice throughout this study, from setting up experiments to writing this thesis helped me immensely in overcoming several challenges.

I am thankful to the Institute of Hazard, Risk, and Resilience (IHRR) for generously funding this study. My sincere thanks to Prof Louise Bracken, Prof Julian Williams and Mrs Julie Dobson for creating a friendly and supportive environment at the institute.

I would also like to express my appreciation for Dr Amod Mani Dixit and Prof Tara Nidhi Bhattarai for sharing valuable experiences and helping me during my fieldwork in Nepal. I also wish to thank my field assistant Sushma, everyone at the Last resort and the communities in Listi, Baldung and Kanglang for all the help with the fieldwork.

I am indebted to my parents for their love and support since 1991. If it was not for my parents and my sister Samridhi, I would have never believed that I was capable of doing this. Thank you for inspiring me to never stop dreaming. I hope I can make you proud someday. I would also like to thank my little nephews Paris, Priam and Prayan for bringing joy and happiness during the difficult times. I am grateful to my in-laws Mr Krishna Shankar Shrestha and Mrs Shanti Shrestha for their love. I would also like to thank my friends in Durham. I shall cherish all the happy memories we created together.

Last but not the least, special thanks to my husband Swastik for being there for me and for picking me up every time when I almost gave up. I could not have asked for a better husband, friend, mentor, chef, field assistant and proof-reader. Thank you for all the sacrifices you have made to be here with me. Thank you for everything.

# Table of Contents

---

<b>Abstract</b> .....	<b>i</b>
<b>Declaration</b> .....	<b>ii</b>
<b>Acknowledgements</b> .....	<b>iv</b>
<b>List of figures</b> .....	<b>ix</b>
<b>List of tables</b> .....	<b>xvii</b>
<b>List of symbols</b> .....	<b>xix</b>
<b>1 Introduction</b> .....	<b>1</b>
1.1 Background and motivation for study.....	1
1.2 Overall aim and objectives .....	3
1.3 Methodology .....	3
1.4 Thesis structure.....	6
<b>2 Rainfall, roads, and landslides in Nepal</b> .....	<b>8</b>
2.1 Chapter outline.....	8
2.2 Background.....	8
2.3 Local road construction in Nepal.....	11
2.4 Effects of slope cutting for road construction on slope stability.....	13
2.5 Case study.....	16
2.5.1 Geological condition.....	17
2.5.2 Climate and rainfall .....	19
2.6 Reconnaissance surveys.....	21
2.6.1 Reconnaissance survey before monsoon .....	21
2.6.2 Reconnaissance survey during monsoon.....	27
2.7 Site selection for further investigation.....	38
2.8 Chapter summary.....	39
<b>3 Geotechnical field investigation</b> .....	<b>42</b>

3.1 Chapter outline.....	42
3.2 General information about Kanglang landslide.....	42
3.3 Objectives of geotechnical field investigation.....	44
3.4 Selection of methods for investigation.....	45
3.5 Geotechnical field investigation in Kanglang landslide.....	46
3.5.1 Borehole drilling.....	46
3.5.2 Standard penetration test in BH-1.....	49
3.5.3 Standard penetration test with 60° cone in BH-2.....	51
3.5.4 Trial pit excavation.....	52
3.6 Sampling, storage, and transportation of the samples.....	54
3.7 Chapter summary.....	56
<b>4 Determination of soil properties .....</b>	<b>58</b>
4.1 Chapter outline.....	58
4.2 Theoretical concepts.....	59
4.2.1 Mechanical behaviour of saturated soils.....	59
4.2.2 Hydraulic behaviour of saturated soils.....	62
4.2.3 Mechanical behaviour of unsaturated soils.....	62
4.2.4 Hydraulic behaviour of unsaturated soils.....	65
4.3 Determination of physical soil properties.....	74
4.3.1 Laboratory techniques.....	74
4.3.2 Summary of index properties.....	77
4.4 Determination of mechanical soil properties.....	83
4.4.1 Laboratory technique.....	83
4.4.2 Sample preparation.....	83
4.4.3 Triaxial test stages.....	86
4.4.4 Summary of the triaxial compression test results.....	87
4.5 Determination of soil-water retention curve.....	90
4.5.1 Sample preparation.....	91
4.5.2 Laboratory technique.....	92
4.5.3 Summary of soil-water retention curve measurements.....	93
4.6 Determination of saturated coefficient of permeability.....	99
4.6.1 Laboratory technique.....	99
4.6.2 Summary of standard triaxial constant head permeability test.....	103

4.7 Chapter summary.....	106
<b>5 Field monitoring.....</b>	<b>108</b>
5.1 Chapter outline.....	108
5.2 Background.....	109
5.2.1 Theoretical concepts.....	109
5.2.2 Review of field-based studies.....	116
5.2.3 Methods used for measurement of volumetric water content in the field.....	120
5.3 Field monitoring station.....	121
5.3.1 Instrumentation.....	122
5.3.2 Installation of the field monitoring station.....	124
5.4 Observations of field-monitored rainfall and volumetric water content.....	127
5.4.1 Rainfall.....	127
5.4.2 Volumetric water content.....	134
5.5 Evaluation of the factors influencing volumetric water content response .....	146
5.5.1 Effect of rainfall features .....	146
5.5.2 Effect of seasonality.....	157
5.6 Chapter summary.....	160
<b>6 Numerical modelling in PLAXIS 2D .....</b>	<b>164</b>
6.1 Chapter outline.....	164
6.2 Review of numerical slope stability analysis methods.....	164
6.2.1 Limit equilibrium method .....	164
6.2.2 Finite element method.....	165
6.2.3 Numerical seepage analysis .....	166
6.2.4 Slope stability analysis with the finite element method .....	168
6.3 Review of numerical analyses of slope failures .....	168
6.4 Uncertainties in numerical modelling of landslides .....	173
6.5 Some limitations in numerical modelling of unsaturated soils .....	174
6.6 Fully coupled flow-deformation analysis in PLAXIS 2D.....	176
6.7 Numerical modelling approach.....	178
6.7.1 Part 1: Model calibration.....	180
6.7.2 Part 2: Stability analysis before Kanglang landslide (Dec 2017 - Jun 2018) .....	181

6.7.3 Part 3: Back-analysis of Kanglang landslide (July 2018).....	182
6.7.4 Part 4: Stability analysis without road cut.....	183
6.8 Setting up the model for numerical modelling in PLAXIS.....	183
6.8.1 Model geometry and finite element mesh .....	183
6.8.2 Material properties.....	186
6.8.3 Boundary and initial conditions.....	189
6.9 Results of the numerical analyses.....	190
6.9.1 Part 1: Model calibration.....	190
6.9.2 Part 2: Stability analysis before Kanglang landslide (Dec 2017 - Jun 2018).....	192
6.9.3 Part 3: Back-analysis of Kanglang landslide (July 2018).....	194
6.9.4 Part 4: Stability analysis without road cut.....	205
6.10 Chapter summary.....	208
<b>7 Discussions and conclusions.....</b>	<b>211</b>
7.1 Chapter outline.....	211
7.2 Discussions .....	211
7.2.1 Key issues related to local road construction in Nepal that can be conducive to landsliding during rainfall (Objective 1).....	213
7.2.2 Primary site-specific geotechnical data from field and laboratory testing generated for numerical modelling (Objective 2).....	217
7.2.3 Effects of atmospheric wetting and drying processes on the hydrologic response of surficial soils and their implications on slope stability (Objective 3).....	221
7.2.4 The influence of the road cut, rainfall, and their interaction on landsliding (Objective 4).....	225
7.3 Conclusions.....	229
7.4 Limitations of the study.....	231
7.5 Recommendations for future work.....	231
<b>References.....</b>	<b>233</b>
<b>Appendix A-1.....</b>	<b>261</b>
<b>Appendix A-2.....</b>	<b>262</b>
<b>Appendix A-3.....</b>	<b>270</b>

# List of figures

---

Figure 1.1 Research methodology. ....	5
Figure 2.1 Temporal variation in the landslide fatalities for the period 1978–2005 for Nepal. Modified after Petley et al. (2007), p. 30. ....	9
Figure 2.2 Map showing Daklang-Listi road; inset is the map of Nepal showing location of Daklang-Listi road within Sindhupalchok district. ....	17
Figure 2.3 Simplified geological map of Daklang-Listi road. Source: (DMG, 1994). ....	19
Figure 2.4 Average monthly rainfall measured at Gumthang meteorological station (1955 to 2018). Source: DHM (2018). ....	20
Figure 2.5 Construction of Daklang-Listi road, looking North (27°53'49.20"N, 85°54'46.20"E) (*photo location shown in Figure 2.6). ....	21
Figure 2.6 Distribution of landslides along Daklang-Listi road in December 2017. The coloured circular points on the map show subsequent photo locations including Figure 2.5. The arrows marked next to these points show the direction that the photographs were taken from. ....	23
Figure 2.7 Steep road-cut slope adjacent to the settlement area along Daklang-Listi road (27°53'30.0"N 85°54'09.2"E). ....	24
Figure 2.8 Steep road cut along Daklang-Listi road (27°53'11.1"N 85°53'25.4"E). ....	24
Figure 2.9 Gabion wall constructed to support a cut slope along Daklang-Listi road (27°53'43.2"N 85°54'48.0"E). ....	25
Figure 2.10 Removal of vegetation along Daklang-listi road (27°53'25.0"N 85°54'02.8"E). ....	26
Figure 2.11 Improper surface and subsurface flow management along Daklang-Listi road (27°53'24.3"N 85°53'18.5"E). ....	27
Figure 2.12 Measurement of the depth of landslide scar. ....	28
Figure 2.13 Distribution of landslides along Daklang-Listi road in August 2018. ....	29
Figure 2.14 Typical slope failures in relation to a road cutting. Modified after Hearn (2011, p. 51). ....	30
Figure 2.15 Failure types in relation to the road. Modified after (Hearn, 2011, p. 51). ....	31
Figure 2.16 Failure in cut slope extending to hillslope (27°53'8.20"N 85°52'45.30"E). ....	32

Figure 2.17 Failure in cut slope only (27°53'06.5"N 85°52'47.2"E). .....	32
Figure 2.18 Failure in original valley slope due to surface runoff (27°53'11.70"N 85°53'28.10"E). .....	33
Figure 2.19 Failure in original valley slope due to surface runoff (27°53'19.5"N 85°52'42.8"E). .....	33
Figure 2.20 Failure in hillslope (27°53'17.53"N 85°53'29.45"E). .....	34
Figure 2.21 Measured cut slope angles at the failed slopes along the Daklang-Listi road...35	
Figure 2.22 Gabion wall overtopped by landslide debris (27°53'43.2"N 85°54'48.0"E). ....	36
Figure 2.23 Impacts of slope failures on the road. ....	37
Figure 2.24 Land-use/land-cover in the vicinity of slope failures. ....	37
Figure 3.1 Road-cut slope at Kanglang landslide before failure (December 2017) (27°53'32.0"N, 85°54'28.5"E). .....	43
Figure 3.2 Kanglang landslide (August 2018) (27°53'32.0"N, 85°54'28.5"E).....	44
Figure 3.3 Photograph of rotary drilling equipment used in this study. ....	46
Figure 3.4 Photograph of Kanglang landslide showing the approximate location of boreholes (BH-1 and BH-2). .....	47
Figure 3.5 Location of Kanglang landslide in the Daklang-Listi road (left), location of trial pit and boreholes (BH-1, BH-2) (right). .....	48
Figure 3.6 180 mm thick weathered cobble extracted by the SPT sampler in BH-1 at 3 m.50	
Figure 3.7 SPT ( $N_{160}$ ) profile and material characteristics in BH-1. ....	51
Figure 3.8 SPT ( $N_{160}$ ) profile and material characteristics in BH-2. ....	52
Figure 3.9 Soil stratification as observed in the trial pit. ....	54
Figure 3.10 Method used for obtaining core samples (a) core inserted into the bottom of the trial pit, (b) both ends of the core sealed with paraffin wax after sampling, (c) core sample ready for transportation. ....	55
Figure 4.1 Critical state defined in the deviator stress versus mean effective stress plane. ....	61
Figure 4.2 Critical state defined in the specific volume versus mean effective stress plane. ....	61
Figure 4.3 Typical soil-water retention curve showing hydraulic hysteresis during drying and wetting. Modified after Toll (2012, chap. 4). .....	67



Figure 4.4 Components of the Durham University high suction tensiometer (not to scale). Modified after Lourenço et al. (2008).	69
Figure 4.5 Laser diffraction particle size analyser (LS 13 320).	75
Figure 4.6 Accupyc II 1340 gas pycnometer.	76
Figure 4.7 (a) Sample core obtained from the field, (b) sample extruded from the core.	76
Figure 4.8 Particle size distribution of trial pit samples.	78
Figure 4.9 Particle size distribution of borehole (BH-1) samples.	80
Figure 4.10 Comparison of particle size distributions of the trial pit samples (K4 and K6) and the borehole samples (B1 to B4) obtained from shallow depths (<1.45 m).	80
Figure 4.11 Plasticity chart for trial pit samples.	81
Figure 4.12 Set-up of triaxial cell in the landslide lab, Durham University.	84
Figure 4.13 Mould and rammer used to prepare samples (left), compacted sample for triaxial testing in the split-open mould (right).	85
Figure 4.14 Deviator stress versus axial strain.	89
Figure 4.15 Excess pore water pressure versus axial strain.	89
Figure 4.16 Effective stress paths.	90
Figure 4.17 Specific volume versus mean effective stress.	90
Figure 4.18 Set-up for suction measurement (figure not to scale).	93
Figure 4.19 Gravimetric water content versus suction.	94
Figure 4.20 Change in void ratio during drying.	95
Figure 4.21 Change in void ratio during wetting.	96
Figure 4.22 Volumetric water content versus suction for K3 samples.	98
Figure 4.23 Volumetric water content versus suction for K4 samples.	99
Figure 4.24 Recorded back and base flow volume for K3_P1.	102
Figure 4.25 Recorded back and base flow volume for K3_P2.	102
Figure 4.26 Recorded back and base flow volume for K3_P3.	102
Figure 4.27 Saturated coefficient of vertical permeability versus average effective confining pressure.	103
Figure 4.28 Saturated coefficient of vertical permeability versus void ratio.	104

Figure 5.1 Schematic representation of natural hydrologic cycle in an unsaturated soil environment. ....	109
Figure 5.2 Conceptual diagram showing the rate of change of infiltration, abstraction and runoff under constant rainfall. Modified after Premchitt et al. (1995). ....	110
Figure 5.3 Illustration of wetting front advancement in vertical soil column and corresponding water content distribution under constant ponding at the surface, based on Green and Ampt (1911) infiltration model. Modified after Lu and Likos (2004). ....	113
Figure 5.4 Variation of degree of saturation due to the advancement of wetting-front during infiltration. Modified after Lumb (1962). ....	114
Figure 5.5 Schematic diagram showing wetting front advancement in sloping ground. Modified after Chen and Young (2006). ....	116
Figure 5.6 Location of field monitoring station (27°53'28.79"N, 85°54'31.69"E) relative to Kanglang landslide. ....	122
Figure 5.7 10HS soil moisture smart sensor. Source: ONSET (2018b, n. Date accessed: 16-06-2020). ....	123
Figure 5.8 HOBO RX3000 remote monitoring station data logger. Source: ONSET (2019, n. Date accessed: 16-06-2020). ....	124
Figure 5.9(a) Schematic illustration of the field monitoring station (not to scale), (b) horizontal installation of 10HS soil moisture sensors on the vertical wall of trial pit at 0.3 m, 0.8 m and 1.2 m (c) complete set-up of the field monitoring station at Kanglang landslide (27°53'28.79"N, 85°54'31.69"E, 1460 m a.s.l.). ....	126
Figure 5.10 Daily rainfall measured during monitoring period from 27/03/2019 until 28/03/2020. ....	128
Figure 5.11 Distribution of daily rainfall (i) during the monitoring period (27/03/2019 to 28/03/2020) shown by the line-graph, (ii) during the monsoon (01/06/2019 to 30/09/2019) shown by bar-graph (dark), and (iii) during pre- and post-monsoon periods (27/03/2019 to 31/05/2019 and 01/10/2019 to 28/03/2020) shown by bar-graph (white). ....	129
Figure 5.12 Comparison of the monitored rainfall data from 27/03/2019 to 28/03/2020 with the 64-year average monthly rainfall (1955 – 2018) measured at Gumthang meteorological station. ....	130
Figure 5.13 Comparison of monthly rainfall measured at Kanglang landslide and Gumthang meteorological station from 01/04/2019 to 31/10/2019. ....	130

Figure 5.14 Relationship between monthly rainfall totals measured at the field-monitoring station in Kanglang and Gumthang meteorological station.....	131
Figure 5.15(a) Monthly distribution of rainfall events during the monitored period (27/03/2019 to 28/03/2020), (b) frequency statistic for total rainfall, (c) frequency statistic for rainfall duration, (d) frequency statistic for average hourly rainfall intensity, (e) frequency statistic for peak hourly rainfall intensity and (f) average rainfall intensity-duration relationships for the observed rainfall events in comparison to the landslide-triggering thresholds defined by Caine (1980) and Dahal and Hasegawa (2008).....	133
Figure 5.16 Average daily volumetric water content and daily rainfall recorded during monitoring period (27/03/2019 to 28/03/2020).....	136
Figure 5.17 Variation in average daily volumetric water content (VWC) with depth (from 27/03/2019 to 28/03/2020). Statistics denoted by the box plots are summarised in Table 5.3.....	137
Figure 5.18 (a) Variation in the degree of saturation with depth during continuous wetting (the numbers in the legend represent days starting from day 1 on 21/06/2019 to day 40 on 31/07/2019), (b) cumulative rainfall from day 1 on 21/06/2019 to day 40 on 31/07/2019. ....	139
Figure 5.19 Variation in the degree of saturation with depth during continuous drying (the numbers in the legend represent days starting from day 1 - 09/10/2019 to day 65 - 12/12/2019).....	140
Figure 5.20 Variation in average hourly volumetric water content and rainfall between 30/07/19 and 07/08/19 (left), and between 03/08/19 and 04/08/19 (right).....	142
Figure 5.21 Cross-correlation function for hourly rainfall and average hourly volumetric water content at 0.3 m.....	144
Figure 5.22 Cross-correlation function for hourly rainfall and average hourly volumetric water content at 0.8 m.....	145
Figure 5.23 Cross-correlation function for hourly rainfall and average hourly volumetric water content at 1.2 m.....	145
Figure 5.24 An example showing calculation of the percentage change in average hourly volumetric water content caused by a rainfall event. $VWC_{initial}$ is the initial volumetric water content before the rainfall initiation and $VWC_{max}$ is the maximum volumetric water content before the start of another rainfall event.....	147
Figure 5.25 Relationship between total rainfall and percentage change in average hourly volumetric water content at 0.3 m during 2019 monsoon.....	149

Figure 5.26 Relationship between total rainfall and percentage change in average hourly volumetric water content at 1.2 m during 2019 monsoon..... 149

Figure 5.27 Variation in rainfall and average hourly volumetric water content with depth during Rainfall event no. 45 (26/06/19 02:00-03:00) and Rainfall event no. 46 (26/06/19 13:00-14:00)..... 152

Figure 5.28 Variation in rainfall and average hourly volumetric water content with depth during Rainfall event no. 87 (28/07/2019 19:00 to 29/07/2019 01:00) and Rainfall event no. 90 (31/07/2019, 21:00 to 01/08/2019 03:00). ..... 152

Figure 5.29 Changes in average hourly volumetric water content and hourly rainfall during rainfall event no. 160 and 161 (between 13/12/2019 and 14/12/2019) and during rainfall event no. 166 (between 16/01/2020 and 17/01/2020)..... 159

Figure 6.1 Numerical modelling approach utilised in this study..... 179

Figure 6.2 Rainfall stations located near Kanglang landslide – i) Gumthang (27°51'19.12"N 85°51'34.75"E, 1846 m a.s.l.), ii) Bahrabise (27°47'19.25"N 85°53'59.95"E, 884 m a.s.l.), iii) Chautara (27°45'13.62"N 85°43'55.48"E, 1552 m a.s.l.) and iv) Dhap (27°54'5.13"N 85°37'57.00"E, 1347 m a.s.l.)..... 182

Figure 6.3 Geometry of the model for part 1 (model calibration), part 2 (stability analysis before Kanglang landslide (Dec 2017 - Jun 2018)) and part 3 (back-analysis of Kanglang landslide)..... 184

Figure 6.4 Finite element mesh for part 1 (model calibration), part 2 (stability analysis before Kanglang landslide (Dec 2017 - Jun 2018)) and part 3 (back-analysis of Kanglang landslide) (the vertical and horizontal axes show model dimensions in meters)..... 184

Figure 6.5 Geometry of the model for part 4 (stability analysis without road cut). ..... 185

Figure 6.6 Finite element mesh of the model for part 4 (stability analysis without road cut) (the vertical and horizontal axes show model dimensions in meters). ..... 185

Figure 6.7 Relationship between effective confining pressure and saturated permeability extrapolated from the laboratory results (chapter 4, Figure 4.27). ..... 187

Figure 6.8 Comparison between hourly volumetric water content measured in the field and simulated in PLAXIS at 0.3 m depth from the surface from 01/07/2019 00:00 to 11/07/2019 11:00..... 191

Figure 6.9 Comparison between hourly volumetric water content measured in the field and simulated in PLAXIS at 0.8 m depth from the surface from 01/07/2019 00:00 to 11/07/2019 11:00..... 191

Figure 6.10 Comparison between hourly volumetric water content measured in the field and simulated in PLAXIS at 1.2 m depth from the surface from 01/07/2019 00:00 to 11/07/2019 11:00..... 192

Figure 6.11 Variation of factor of safety from 01/12/2017 to 30/06/2018 ..... 193

Figure 6.12 Daily variation in effective degree of saturation and relative permeability starting from 01/12/2017 to 30/06/2018. .... 193

Figure 6.13 Daily variation in the factor of safety and relative permeability starting from 01/12/2017 to 30/06/2018..... 194

Figure 6.14 Variation in factor of safety with time from 01/07/2018 00:00 to 12/07/18 06:00. The numbers in the figure denote rainfall events\* (\*only the continuous rainfall events with more than 5 mm total rainfall are highlighted)..... 196

Figure 6.15 Relationship between rainfall duration and percentage decrease in the factor of safety..... 197

Figure 6.16 Suction contours at 267<sup>th</sup> hour (Figure 6.14) on 12/07/2018; suction profiles at sections A-A\* and B-B\* are shown in Figure 6.17 and Figure 6.18 (the vertical and horizontal axes show model dimensions in meters)..... 198

Figure 6.17 Variation of suction with depth during rainfall event no. 6 at section A-A\* (hours in the legend are shown with reference to Figure 6.14). .... 199

Figure 6.18 Variation of suction with depth during rainfall event no. 6 at section B-B\* (hours in the legend are shown with reference to Figure 6.14). .... 200

Figure 6.19 Total displacement contours at failure (FOS = 0.96) on 12/07/2018 (267<sup>th</sup> hour in Figure 6.14) (the vertical and horizontal axes show model dimensions in meters)..... 203

Figure 6.20 Cumulative total displacement measured near the cut slope (section C-C\*) from 01/07/2018 00:00 to 12/07/2018 06:00..... 203

Figure 6.21 Cumulative total displacement measured at the face of the cut slope (section C-C\*) from 11/07/2018 10:00 to 12/07/2018 06:00 highlighting the accelerated displacement during rainfall event no. 6. .... 204

Figure 6.22 Cumulative total displacement measured near the mid-slope (section D-D\*) from 01/07/2018 00:00 to 12/07/2018 06:00..... 204

Figure 6.23 Cumulative total displacement measured near the slope crest (Section E-E\*) from 01/07/2018 00:00 to 12/07/2018 06:00..... 205

Figure 6.24 Variation of factor of safety with time in the models with a road cut and without a road cut from 01/07/19 00:00 to 12/07/19 06:00. The numbers in the figure denote

rainfall events\* (\*only the continuous rainfall events with more than 5 mm total rainfall are highlighted)..... 207

# List of tables

---

Table 2.1 Causes and triggers of landslides. Modified after Petley (2010) and Hearn (2011). .....	11
Table 2.2 Recommended standard cutting height and slope gradient for cut slopes. Source: DoR (2003, chap. 3). .....	14
Table 2.3 Summary of the information recorded in the landslide information sheet.....	28
Table 3.1 Summary of the characteristics of Kanglang landslide .....	43
Table 3.2 Summary of the soil samples obtained from the field .....	55
Table 4.1 Summary of the soil properties obtained from laboratory testing.....	58
Table 4.2 Suction component and suction range for different suction measurement methods. Modified after Mendes (2011). .....	68
Table 4.3 Empirical equations for the soil-water retention curves.....	71
Table 4.4 Summary of the laboratory tests for physical soil properties.....	77
Table 4.5 Particle size distribution of samples obtained from the trial pit. ....	78
Table 4.6 Particle size distribution of the samples obtained from the borehole (BH-1).....	79
Table 4.7 Atterberg Limits of trial pit samples.....	81
Table 4.8 Particle density of soil samples.....	82
Table 4.9 In-situ soil properties obtained from core samples. ....	82
Table 4.10 Index properties of soil samples obtained from weight-volume relationships. 83	
Table 4.11 Initial conditions for saturated triaxial test samples. ....	85
Table 4.12 B-Values after saturation for triaxial tests.....	86
Table 4.13 Sample conditions after consolidation for triaxial tests. ....	87
Table 4.14 Initial condition of the samples for SWRC tests. ....	91
Table 4.15 Estimated curve fitting parameters for the van Genuchten (1980) model.....	97
Table 4.16 Initial condition of the sample for triaxial constant head permeability test....	100
Table 4.17 Sample conditions after consolidation for permeability tests. ....	101
Table 4.18 Results of the permeability test. ....	105

Table 5.1 Specifications of 10HS soil moisture sensors. Source: Decagon Devices (2010). .....	123
Table 5.2 Summary of daily rainfall measured during the monitoring period from 27/03/2019 to 28/03/2020.....	128
Table 5.3 Statistical summary of the box plot shown in Figure 5.17. ....	137
Table 5.4 Pearson correlation coefficients ( $r$ ) between rainfall features and percentage change in the volumetric water content (VWC) at 0.3 m, 0.8 m and 1.2 m. ....	147
Table 5.5 Summary of rainfall events selected to compare the effects of rainfall intensity and duration on volumetric water content changes.....	153
Table 5.6 Summary of the volumetric water content (VWC) changes caused by the selected rainfall events from Table 5.5 at 0.3 m, 0.8 m and 1.2 m. ....	154
Table 5.7 Summary of the rainfall events selected to compare the effect of seasonality on the volumetric water content (VWC) response. ....	157
Table 6.1 Summary of soil properties used for each layer for numerical modelling.....	188



# List of symbols

Symbol	Description	Dimension	SI unit
$\sigma'$	Effective stress	[ML <sup>-1</sup> T <sup>-2</sup> ]	kPa
$\sigma$	Total stress	[ML <sup>-1</sup> T <sup>-2</sup> ]	kPa
$u_w$	Pore water pressure	[ML <sup>-1</sup> T <sup>-2</sup> ]	kPa
$u_a$	Pore air pressure	[ML <sup>-1</sup> T <sup>-2</sup> ]	kPa
$\tau$	Shear strength	[ML <sup>-1</sup> T <sup>-2</sup> ]	kPa
$c'$	Effective cohesion	[ML <sup>-1</sup> T <sup>-2</sup> ]	kPa
$\phi'$	Effective angle of shearing resistance	-	degree
$\phi_{cs}'$	Critical state angle of shearing resistance	-	degree
$\phi^b$	Angle of shearing resistance of soil with respect to suction	-	degree
$p'$	Mean effective stress	[ML <sup>-1</sup> T <sup>-2</sup> ]	kPa
$p$	Mean total stress	[ML <sup>-1</sup> T <sup>-2</sup> ]	kPa
$q$	Deviator stress	[ML <sup>-1</sup> T <sup>-2</sup> ]	kPa
$\varepsilon_q$	Shear strain	-	%
$\varepsilon_a$	Axial strain	-	%
$\sigma_1, \sigma_2, \sigma_3$	Principal stresses	[ML <sup>-1</sup> T <sup>-2</sup> ]	kPa
$\sigma_1', \sigma_2', \sigma_3'$	Principal effective stresses	[ML <sup>-1</sup> T <sup>-2</sup> ]	kPa
$\nu$	Specific volume	-	-
$M$	Slope of the critical state line in $q - p'$ plot	-	-
$\Gamma$	Intercept of the critical state line in the $\nu - p'$ plot	-	-
$\lambda$	Slope of the critical state line on the $\nu - p'$ plot	-	-
$q_{flow}$	Flow rate of water, applied boundary flux	[LT <sup>-1</sup> ]	m/s
$Q_{flow}$	Mean rate of flow through the sample	[L <sup>3</sup> T <sup>-1</sup> ]	m <sup>3</sup> /s
$Q$	Total infiltration displacement or cumulative infiltration depth	[L]	m
$q_{inf}$	Rate of infiltration	[LT <sup>-1</sup> ]	m/s

Symbol	Description	Dimension	SI unit
$k$	Coefficient of permeability	[LT <sup>-1</sup> ]	m/s
$k_r$	Relative coefficient of permeability	-	-
$k_{unsat}$	Coefficient of permeability as a function of volumetric water content	[LT <sup>-1</sup> ]	m/s
$k_{sat}$	Saturated coefficient of permeability	[LT <sup>-1</sup> ]	m/s
$k_v$	Saturated coefficient of vertical permeability	[LT <sup>-1</sup> ]	m/s
$k_w$	Coefficient of permeability of soil behind the wetting front	[LT <sup>-1</sup> ]	m/s
$k_x$	Coefficients of permeability with respect to matric suction in x-direction	[LT <sup>-1</sup> ]	m/s
$k_y$	Coefficients of permeability with respect to matric suction in y- direction	[LT <sup>-1</sup> ]	m/s
$k_1$	Unsaturated coefficient of permeability equal to the rainfall intensity at time t	[LT <sup>-1</sup> ]	m/s
$k_{initial}$	Initial unsaturated coefficient of permeability equal to the initial surface flux	[LT <sup>-1</sup> ]	m/s
$e$	Void ratio	-	-
$k_0$	Coefficient of permeability corresponding to $\theta_0$	[LT <sup>-1</sup> ]	m/s
$i$	Hydraulic gradient	-	-
$\chi$	Bishop's effective stress parameter	-	-
$\theta$	Volumetric water content	[L <sup>3</sup> L <sup>-3</sup> ]	m <sup>3</sup> /m <sup>3</sup>
$\theta_e, \Theta$	Effective/normalised volumetric water content	-	-
$\theta_r$	Residual volumetric water content	[L <sup>3</sup> L <sup>-3</sup> ]	m <sup>3</sup> /m <sup>3</sup>
$\theta_s$	Volumetric water content at full saturation	[L <sup>3</sup> L <sup>-3</sup> ]	m <sup>3</sup> /m <sup>3</sup>
$\theta_0$	Volumetric water content behind the wetting front	[L <sup>3</sup> L <sup>-3</sup> ]	m <sup>3</sup> /m <sup>3</sup>
$\theta_i$	Volumetric water content beyond the wetting front	[L <sup>3</sup> L <sup>-3</sup> ]	m <sup>3</sup> /m <sup>3</sup>
$\theta_1$	Final volumetric water content at time $t$	[L <sup>3</sup> L <sup>-3</sup> ]	m <sup>3</sup> /m <sup>3</sup>
$\theta_{initial}$	Initial volumetric water content	[L <sup>3</sup> L <sup>-3</sup> ]	m <sup>3</sup> /m <sup>3</sup>
$S$	Degree of saturation	-	%

Symbol	Description	Dimension	SI unit
$S_e$	Effective degree of saturation	-	-
$S_r$	Residual degree of saturation	-	%
$\psi_r$	Matric suction at residual water content	[ML <sup>-1</sup> T <sup>-2</sup> ]	kPa
$\eta$	Index number of pore size distribution	-	-
$\alpha$	Fitting parameter dependent on the air-entry value	[L <sup>-1</sup> ] or [ML <sup>-1</sup> T <sup>-2</sup> ]	1/m or kPa
$n$	Fitting parameter dependent on the rate of soil drainage	-	-
$m$	Fitting parameter dependent on the residual water content	-	-
$g_a$	Fitting parameter related to the air-entry value (unit of pressure head), equivalent to $\alpha$	[L <sup>-1</sup> ]	1/m
$g_n$	Fitting parameter related to the slope of the soil water retention curve, equivalent to $n$	-	-
$g_c$	Fitting parameter equivalent to the $m$	-	-
$g_l$	Fitting parameter related to pore tortuosity and pore connectivity	-	-
$S$	Slope of the line tangent to the function passing through the inflection point	-	-
$L$	Sample height	[L]	m
$A$	Cross-sectional area of the sample	[L <sup>2</sup> ]	m <sup>2</sup>
$\Delta h$	Difference in the head of water between sample top and bottom	[L]	m
$\delta$	Temperature correction factor for the viscosity of water	-	-
$h$	Total hydraulic head	[L]	m
$S_s$	Saturated degree of saturation	-	%
$S_f$	Final degree of saturation	-	%
$S_0$	Initial degree of saturation	-	%
$S(\psi)$	Degree of saturation as a function of suction head	-	%
$s_f$	Matric potential head at the wetting front	[L]	m

Symbol	Description	Dimension	SI unit
$W$	Gravimetric water content	-	%
$\rho_{dry}$	Dry density of soil	[ML <sup>-3</sup> ]	Mg/m <sup>3</sup>
$\rho_{water}$	Density of water	[ML <sup>-3</sup> ]	Mg/m <sup>3</sup>
$\gamma_w$	Unit weight of water	[ML <sup>-2</sup> T <sup>-2</sup> ]	KN/m <sup>3</sup>
$\gamma_{unsat}$	Unsaturated unit weight of soil	[ML <sup>-2</sup> T <sup>-2</sup> ]	KN/m <sup>3</sup>
$\gamma_{sat}$	Saturated unit weight of soil	[ML <sup>-2</sup> T <sup>-2</sup> ]	KN/m <sup>3</sup>
$n$	Porosity	-	-
$G_s$	Specific gravity	-	-
$\psi$	Matric suction	[ML <sup>-1</sup> T <sup>-2</sup> ]	kPa
$E$	Elastic modulus	[ML <sup>-1</sup> T <sup>-2</sup> ]	MPa
$\nu$	Poissons ratio	-	-
$\psi_b$	Air-entry value or bubbling pressure	[ML <sup>-1</sup> T <sup>-2</sup> ]	kPa
$\psi_i$	Matric suction at the inflection point	[ML <sup>-1</sup> T <sup>-2</sup> ]	kPa
$h_m$	Matric suction head	[L]	m
$g$	Acceleration due to gravity	[LT <sup>-2</sup> ]	m/s <sup>2</sup>
$Z$	Elevation head above an arbitrary datum	[L]	m
$t$	Time	[T]	s
$z$	Depth of the wetting front	[L]	m
$z_f^*$	Depth of the wetting front normal to the ground surface	[L]	m
$\gamma$	Slope angle	-	degree
$H$	Ponding water head on sloping ground	[L]	m
$h_{ponding}$	Ponding depth normal to the ground surface	[L]	m
$N$	Number of observations	-	-
$T$	Row number	-	-
$K$	Lag	[T]	hr
$\bar{x}$	Mean of x (rainfall)	[L]	m
$\bar{y}$	Mean of y (average volumetric water content)	[L <sup>3</sup> L <sup>-3</sup> ]	m <sup>3</sup> /m <sup>3</sup>
$m_w$	Soil-water retention capacity	-	-

# Chapter 1

## Introduction

---

### 1.1 Background and motivation for study

Nepal is a mountainous country located in the central section of the young and active mountain range, the Himalayan arc. The mountainous terrain of Nepal is characterised by high relief, steep slopes, fractured and folded rocks, immature/unconsolidated soil, and rapid uplift and weathering (Fookes et al., 1985). In the active and evolving terrain, landslides are an inevitable natural process providing a mechanism to attain mass balance between tectonic uplift and erosion (Petley et al., 2007). Moreover, in Nepal, the period between June and September is marked by concentrated monsoon rainfall; almost 80% of the total annual rainfall is expected during this season. In such a setting that is prone to natural landslides, anthropogenic disturbances like road construction can further aggravate the occurrence of landslides (Hearn et al., 2003; Petley et al., 2007; Thapa, 2015).

For low- and middle-income countries like Nepal, roads are fundamental infrastructure for development. Better road access has socio-economic as well as socio-cultural benefits for communities living in the rural parts of Nepal (Beazley and Lassoie, 2017). The Government of Nepal and the international donors like the World Bank have been making continuous efforts since the 1950s to improve connectivity in the rural areas (Pokharel et al., 2015; World Bank, 2016; Government of Nepal: National Planning Commission, 2020). The local roads connecting rural parts of Nepal to economic trade centres have now expanded to ~60,000 km, which is a 1200% rise since 1998 (DoLIDAR, 2016; Sudmeier-rioux et al., 2019). The Government of Nepal further plans to expand the road density by ~140% increasing the road density to 1.3 km/km<sup>2</sup> by 2030 from 0.55 km/km<sup>2</sup> in 2015 under the sustainable development goal (SDG 9) to build resilient infrastructures in the country (Government of Nepal: National Planning Commission, 2017).

Studies have suggested that the expansion of the local road network in Nepal has become the key anthropogenic factor causing an increased number of landslides and landslide fatalities in Nepal (Petley et al., 2007; Dahal et al., 2010; Devkota et al., 2014; Froude and Petley, 2018; Mcadoo et al., 2018; Vuillez et al., 2018). This has been attributed to the non-engineered and almost haphazard cutting of hillslopes for road construction, which has been rising since the 1990s (UNDP, 2011).

The majority of construction and widening of local roads in Nepal are conducted during the dry season (World Bank, 2012; DSCWM, 2016; Beazley and Lassoie, 2017; Sudmeier-rioux et al., 2019). However, with the onset of the rainy season, shallow slope failures both above and below the road occur frequently and extensively along the local roads (Dahal et al., 2010; Dahal and Bhandary, 2013; Devkota et al., 2014). The occurrence of such frequent slope failures during the monsoon have adverse impacts on the livelihood and economy of the local communities, which contradicts the primary purpose of building local roads in the first place. Moreover, landslide material may be transported to the streams and rivers, which increases sedimentation problems that can damage infrastructure like bridges, hydropower plants, degrade water quality and also affect aquatic habitat (Merz et al., 2006; Sidle and Ziegler, 2012).

Despite the understanding that the presence of non-engineered local roads in the landscape increases the risk of landsliding in Nepal, far too less attention has been paid to understanding the physical process by which road cuts interact with rainfall to promote landsliding. The observation that steeply cut roadside slopes remain stable during the dry season but fail during rainfall tells us that we are dealing with unsaturated soils. Understanding the behaviour of unsaturated soil is hence crucial to evaluate how the transient changes in this zone lead to shallow landsliding during rainfall. However, the response of the road cut slopes to rainfall is not fully understood in Nepal, especially within the framework of unsaturated soil mechanics.

Extensive research has been conducted globally to analyse the mechanism of rainfall-induced landsliding using physically based numerical models under the framework of unsaturated soils (Zhang et al., 2011, 2018). However, to date, there has not been any studies in Nepal that focuses on understanding the behaviour of unsaturated soils to decode the physical mechanism by which slope cutting for road construction leads to a greater risk of rainfall-induced landsliding. This can be attributed to the complex physical environment, difficulties in access and limited financial resources that hinder the generation of geotechnical data necessary for physically based numerical modelling studies. The adoption of such models requires site-specific data related to slope geometry, hydro-mechanical soil properties, land-use and other external factors such as rainfall and evapotranspiration (Almeida et al., 2017). Collection of such detailed site-specific information can be challenging, especially in a data-scarce country like Nepal.

As the local roads in Nepal continue to expand across the country under the sustainable development goal (SDG 9) for 2016-2030, it has become more urgent than ever to understand the interaction between the two main factors of landsliding - rainfall and roads. Thus, in consideration of the existing knowledge gaps, this study attempts to analyse this

interaction numerically, under the framework of unsaturated soils, using an integrated methodology. This approach involves reconnaissance surveys to contextualise the research focus related to local road construction, field- and laboratory-testing and field-monitoring to generate a primary hydro-mechanical dataset and coupled flow-deformation analyses to explore the physical mechanism by which the interaction of rainfall with road cuts influences the stability of the hillslopes.

## 1.2 Overall aim and objectives

This study aims to improve understanding of how and why non-engineered slope cuttings can promote landsliding in the hillslopes during rainfall, using an integrated method in the data-scarce region of Nepal. To achieve this aim, this study sets out to fulfil the following objectives:

1. Investigate the issues related to local road construction in Nepal that can be conducive to landsliding during rainfall.
2. Generate site-specific input parameters (physical, mechanical, and hydraulic soil properties) in a data-scarce region for numerical modelling.
3. Understand the long-term hydrologic response of surficial soils to atmospheric drying and wetting processes and its implications on slope stability.
4. Evaluate the influence of the road cut, rainfall, and their interaction on landsliding.

The methodology adopted to fulfil the above objectives is described in the next section.

## 1.3 Methodology

The methodology adopted for the fulfilment of the objectives is shown schematically in Figure 1.1. The first objective - to investigate the underlying issues related to local road construction that could lead to landsliding was addressed by conducting a series of reconnaissance surveys in the case study area before and during the monsoon season of 2018. Based on the observational findings from the reconnaissance surveys, a landslide site that is representative of the predominant failure type in the case study area was selected for detailed investigation.

To fulfil the second objective, a site-specific geotechnical investigation was undertaken in the selected landslide site in March 2019. The investigation consisted of trial pit excavation and standard penetration tests (SPT). The SPT-values were used to empirically estimate the engineering properties of in-situ soils. Soil samples were collected from the site and brought to Durham University laboratory for testing. Physical soil properties including particle size

distribution, Atterberg limits, particle density, in-situ water content, dry density and void ratio were determined. Saturated triaxial tests were performed to estimate the mechanical strength properties. For hydrological soil properties, standard triaxial constant head permeability test was conducted to determine the saturated coefficient of permeability and high-capacity tensiometer was used to estimate suction for the soil-water retention curves. The soil parameters obtained from field and laboratory testing were used as input for numerical modelling to address the fourth objective.

During the field investigation in March 2019, a field-monitoring station was installed at the selected landslide site to address the third objective of this study. Three 10HS soil moisture sensors were installed inside the trial pit at three depths (0.3 m, 0.8 m and 1.2 m) and a tipping bucket rain gauge was installed adjacent to the trial pit. The year-long monitoring of volumetric water content and rainfall was used to understand the temporal changes in the hydrologic behaviour of shallow soils during dry and wet periods.

The fourth objective – evaluation of the influence of road cutting, rainfall, and their interaction on landsliding, was addressed by conducting fully coupled flow-deformation analyses in combination with safety analyses in PLAXIS 2D. The numerical model was calibrated against the volumetric water content measured at the site during the monitoring period. The calibrated model was then adopted to back-analyse the mechanism of failure of the selected landslide site.



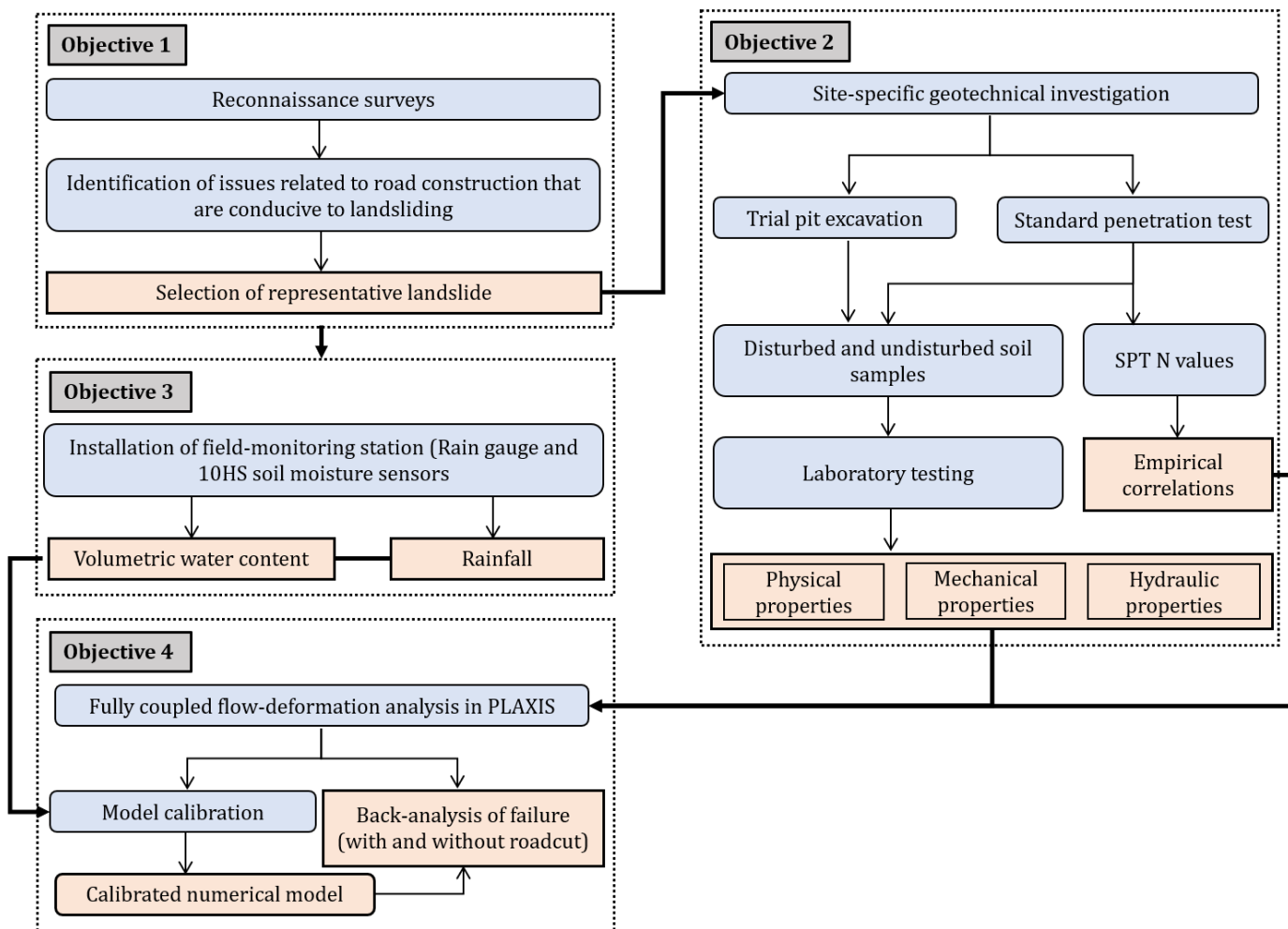


Figure 1.1 Research methodology.

## 1.4 Thesis structure

This thesis is divided into seven chapters, each focusing on a different aspect of this study. The theoretical concepts and the literature relevant to the content are described at the beginning of each chapter.

**Chapter 1** introduces this study by defining its context and motivation for the study. The overall aim, objectives and scope of this study are identified, and the methodologies adopted to fulfil the research objectives are presented.

**Chapter 2** starts by introducing the nature of landsliding in Nepal in relation to two landslide causing factors: rainfall and road construction. The discussions in the initial part of this chapter add to the motivation for conducting this study. In the second part, the case study area is introduced which is a district road located in Sindhupalchok, Province 3, Nepal. Following this, the observational findings gathered from the field reconnaissance surveys conducted in the case study area are presented, based on which a representative landslide site was selected for further detailed investigation. The selection approach used for the selection of the representative site is also described in this chapter.

**Chapter 3** presents the details of the site-specific geotechnical investigation conducted at the selected representative landslide (Kanglang landslide). The methods utilised for investigation and soil sampling and the results from the in-situ tests (standard penetration tests) are described.

**Chapter 4** presents the results of the laboratory testing conducted on the soil samples collected from Kanglang landslide. The results provide an understanding of the physical, mechanical and hydraulic properties of the soil in both saturated and unsaturated conditions.

**Chapter 5** focuses on the discussion of the year-long field-monitoring data obtained from the monitoring station installed at Kanglang landslide. The field-monitoring data consists of rainfall and volumetric water content at shallow depths down to 1.2 m. The discussion in this chapter focuses on better understanding the hydrologic changes that occur in shallow soils in response to seasonal drying and wetting.

**Chapter 6** describes the numerical analyses involving fully coupled flow-deformation analyses conducted using PLAXIS 2D. The numerical analyses consist of model calibration and back-analysis of the investigated slope (Kanglang landslide). The model calibration constitutes a comparison of the field-monitored data with the computational output. The back-analysis of failure involves coupled flow-deformation and safety analysis using the

calibrated numerical model to evaluate the influence of road-rainfall interaction on the stability of slope. The results of the numerical modelling also aim to provide an understanding of the effect road cut on the stability of hillslope during rainfall.

**Chapter 7** summarises the findings drawn from this study and presents the conclusions, limitations and recommendations for future study.

# Chapter 2

## Rainfall, roads, and landslides in Nepal

---

### 2.1 Chapter outline

The first part of this chapter begins with a discussion of the nature of landsliding in Nepal due to rainfall and local road construction, highlighting the need to further understand the increasing risk of rainfall-triggered landslides due to local road construction. The second part focuses on identifying the factors related to local road construction in Nepal which could contribute to landsliding during rainfall by using examples and observations from the reconnaissance surveys. The reconnaissance surveys were conducted along a newly widened local road before and during the monsoon of 2018 to compare the stability of roadside slopes and to identify common landslide types resulting from the interaction between roads and rainfall. Based on the findings from the reconnaissance surveys, a representative landslide site was selected for further investigation, the selection approach for which is presented in the final section of this chapter.

### 2.2 Background

Rainfall is one of the most common triggers of landslides in mountainous regions around the world. In the global fatal non-seismic landslide database compiled by Froude and Petley (2018), of 4862 landslide events recorded over 12 years (January 2004 – December 2016), more than 80% were triggered by rainfall. Nepal is located in the central part of the Himalayan arc, which is one of the hot-spots for fatal landslides; 10% of all rainfall-triggered fatal landslides in the global fatal non-seismic landslide database were recorded in Nepal (Froude and Petley, 2018). This is a significant fraction given that Nepal has less than 0.4% of the global population, whereas China and India have ~18% of the global population but have 15 to 16% of the fatal landslides.

Most parts of Nepal experience more than 80% of the total annual rainfall during the summer monsoon season between June and September (Shrestha, 2000). Due to concentrated rainfall in the geologically fragile mountain terrain, it is well recognised that rainfall is one of the main landslide triggering factors in Nepal (Upreti and Dhital, 1996;

Petley et al., 2007; Dahal and Hasegawa, 2008). Froude and Petley (2018) noted that 93% of the rainfall triggered landslides in Nepal within the global fatal non-seismic landslide database, occurred during the four months of summer monsoon season. Petley et al. (2007) also showed that 90% of fatal landslides and 92% of the landslide fatalities between 1978 and 2005 occurred during the monsoon (Figure 2.1).

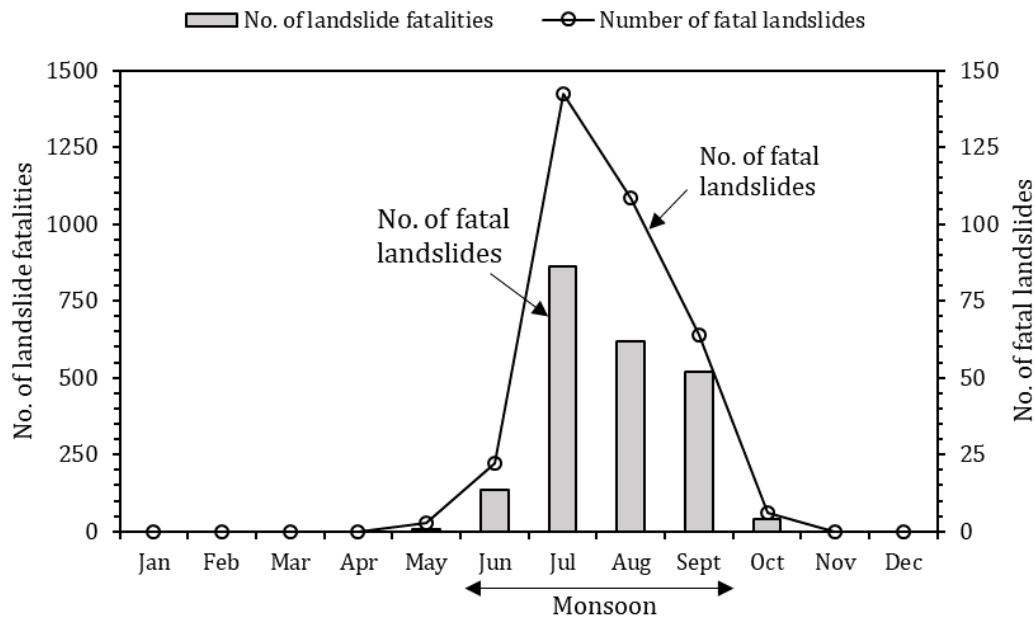


Figure 2.1 Temporal variation in the landslide fatalities for the period 1978–2005 for Nepal. Modified after Petley et al. (2007), p. 30.

There is also a growing body of research suggesting that the increasing number of rainfall-induced landslides and related fatalities in Nepal is related to the expansion of the local road network (LRN) (Petley et al., 2007; Dahal et al., 2010; Leibundgut et al., 2016; Mcadoo et al., 2018; Sudmeier-Rieux et al., 2018; Vuillez et al., 2018; Robson et al., 2021).

The local road network of Nepal includes district road core network and village roads and comes under the administration of the Department of Local Infrastructure Development and Agricultural Roads (DoLIDAR). According to the recent data published by DoLIDAR (2016), the local road network constitutes more than 80% of the total road length in Nepal (70,474 km). Between 1998 and 2016, extensive growth of local road network took place, increasing its total length by almost 1200% from 4,780 km to 57,632 km (Sudmeier-rioux et al., 2019). Petley et al. (2007) have shown that the local road expansion after the 1990s coincided with an increase in the number of fatal landslide and landslide fatalities in Nepal. With a larger dataset, Petley (2012) underlined another subsequent spike in fatal landslide number and related fatalities that occurred in Nepal after 2005. This time-frame coincided

with the end of the decade-long civil war in Nepal, after which road construction activities in the hill districts increased significantly (Lennartz, 2013).

According to Petley (2010), landslide disasters occur through a 'chain of events', which links the 'causes' and the external 'triggering factors' of landslides. Although there can be multiple 'causes' and 'triggering factors' that interact to induce landslides (Table 2.1), in this study, we view rainfall- and road-induced landslides as the consequence of an interaction between road construction (an anthropogenic landslide causal factor) and rainfall (the triggering factor). While studies have shown that rainfall and local road construction are the two key landslide causal factors in Nepal, there is still a gap in understanding of how rainfall and local roads interact to cause slope failures or landslides.

In this study, a newly widened local road located in the mountainous part of Nepal was selected for case study and the effects of road construction and monsoonal rainfall on roadside slope stability were evaluated. The selection of a newly widened road for case study allowed evaluation of i) the road construction method, ii) the stability of slopes immediately after road construction, iii) the road-related slope and water management issues that are conducive to landsliding and iv) the stability of roadside slopes under monsoonal rainfall.

Reconnaissance surveys were conducted along the selected local road, before and during the monsoon of 2018. The survey conducted before monsoon presented useful insights on the factors related to road construction that could be detrimental to slope stability during rainfall. Likewise, the observations from the reconnaissance survey undertaken during monsoon allowed the identification of predominant landslide type resulting from the interaction of a newly constructed road and rainfall. This chapter focuses on the discussion of the observational findings drawn from the reconnaissance surveys. To further understand the physical mechanism of the road- and rainfall-related slope failures using numerical modelling, a representative landslide site was selected from the study area. The approach utilised for selecting this representative site is discussed later in this chapter.

Table 2.1 Causes and triggers of landslides. Modified after Petley (2010) and Hearn (2011).

Causes	Triggering factors
<ul style="list-style-type: none"> <li>• Geological causes               <ul style="list-style-type: none"> <li>○ Weak and/or weathered materials</li> <li>○ Presence of adversely oriented joints or relict structures or failure surfaces</li> </ul> </li> </ul>	<ul style="list-style-type: none"> <li>• Rainfall</li> <li>• Earthquake</li> <li>• Human activities</li> </ul>
<ul style="list-style-type: none"> <li>• Morphological causes               <ul style="list-style-type: none"> <li>○ Slope height and slope angle</li> <li>○ Concavity or convexity of slopes</li> </ul> </li> </ul>	
<ul style="list-style-type: none"> <li>• Physical causes               <ul style="list-style-type: none"> <li>○ Shallow groundwater table</li> <li>○ Antecedent rainfall</li> </ul> </li> </ul>	
<ul style="list-style-type: none"> <li>• Anthropogenic causes               <ul style="list-style-type: none"> <li>○ Deforestation</li> <li>○ Road construction</li> <li>○ Leakage of pipes</li> </ul> </li> </ul>	

### 2.3 Local road construction in Nepal

Broadly, there are two methods adopted in Nepal for the construction of local roads: labour-based and equipment-based methods. The labour-based method promotes the use of light equipment and seeks to maximise the use of local labours and resources for road construction (Dahal et al., 2006). On the other hand, the equipment-based method uses earthwork equipment like bulldozers, rollers and excavators for slope cutting, trimming, and embankment and fill construction, with minimum utilisation of the labours (Dahal et al., 2006).

Initially, the equipment-based method was limited to the strategic road construction which constitutes highways and feeder roads (UNDP, 2011). Whereas, the labour-based method was utilised for rural infrastructure construction (UNDP, 2011). In the 1980s, the concept of green-road was introduced for the local road construction, which is a more organised, labour-based, participatory and environment-friendly method of constructing low-volume, single-lane rural roads (Sharma and Maskay, 1999). Hearn and Shakya (2017) have discussed the technical principles of the green roads approach and have presented comments on the suitability of the principles for a good road construction practice.

However, during the past 20 years, the use of the equipment-based method for local road construction has become hugely popular in Nepal (UNDP, 2011). This is mostly related to the cost and time associated with the equipment-based method (World Bank, 2012). As stated by DoLIDAR (2009), during local road construction, a job that a bulldozer can complete in a month could take up to five months for 150 labours working in 10 groups. Also, the cost of 25 bulldozers can be equivalent to 5 million workdays for labours for constructing a local road (DoLIDAR, 2009). Hence, the equipment-based method presents an enticing alternative to the traditional labour-based method for a quicker and cheaper means of road construction and this has contributed to the popularity of this method in Nepal (World Bank, 2012).

However, the equipment-based method of local road construction is often non-engineered and lack adequate planning, design and control on the use of heavy equipment (World Bank, 2012; Hearn and Shakya, 2017; Robson et al., 2021). As discussed in the study by UNDP, the roads built in this manner induce a greater risk of hillslope instability compared to the traditional labour-based methods. This is caused by, amongst other factors, steep slope cuts, steep gradients, lack of suitable drainage and slope protection, side-tipping of spoil, and lack of post-construction maintenance arrangements (UNDP, 2011). Due to such issues, non-engineered local roads in Nepal often become impassable during the first monsoon after construction (World Bank, 2012).

Studies from other developing parts of the world have also shown that the construction of roads can pose a greater risk of landsliding (Larsen and Parks, 1997; Guadagno et al., 2005; Dahal et al., 2010; Haigh and Rawat, 2011, 2012; Sidle and Ziegler, 2012; Sidle et al., 2014). This is mostly because of inadequate location planning and construction measures (Sidle and Ochiai, 2006). In Nepal, however, only a few studies have presented field-based evidences to support this observation.

Leibundgut et al. (2016) conducted a study within Phewa watershed located in the western mid-hills of Nepal, where the local roads were constructed extensively between 1979 and 2013 increasing the road length from 23 km to 310 km. As a consequence, landsliding phenomenon within the watershed aggravated during this period. This study found that the non-engineered road construction without suitable drainage provision caused accumulation and channelling of rain-water, which led to gulying, a greater release of soil volumes, roadside failures and shallow landslides. The authors also suggested that the presence of colluvial soils with low cohesion, high rates of weathering, steep slopes and intense rainfall within the study area created favourable conditions for landsliding to occur.



Vuillez et al. (2018) used aerial photographs, satellite images and conducted field studies to further understand the land use/land cover changes within the Phewa watershed, which was previously studied by Leibundgut et al. (2016). Their study found that during extreme rainfall events (216 to 315 mm in 24 hours), the occurrence of landslides was more prominent in areas that were either intersected by roads or were located in the vicinity of the roads.

Mcadoo et al. (2018) analysed the spatial distribution of landslides in Sindhupalchok district of Nepal using satellite images to evaluate if there is a link between roads and landslide occurrence. This study found that rainfall-induced landsliding can be twice as common in areas with poorly constructed roads as would be in areas without such roads.

The aforementioned field-based and statistical studies underline the increasing need to pay attention to the risk of rainfall-induced landsliding due to roads in Nepal. However, as stated in chapter 1, the physical mechanism by which the local roadside slopes interact with rainfall to cause landsliding is not well understood in Nepal. Whilst this study attempts to address this gap in understanding using numerical modelling technique (chapter 6), this chapter contributes to the fulfilment of this aim by setting out the scope of study by identifying the study-area and the key factors related to road construction that lead to an increased risk of rainfall-induced landsliding.

## 2.4 Effects of slope cutting for road construction on slope stability

Linear infrastructure such as roads and trails constructed by cutting the hillslopes affect slope stability by removing support and by changing natural hydrological pathways (Sidle and Ochiai, 2006). In the mountainous regions, there are essentially three main choices of cross-section for a new road construction: full-cut, full-fill and part-cut/part-fill (Hearn and Hunt, 2011). Since the full-cut cross-section requires minimum compaction of the road formation and eliminates the need for fill retaining walls, this method of road building can be relatively cheap (Hearn and Hunt, 2011). However, instabilities can occur along the full-cut road cross-sections if hillslopes are cut to a great height and steep angle, without due consideration of the underlying geological, groundwater and seepage conditions (Hearn and Hunt, 2011). The Department of Roads (DoR) in Nepal has published recommendations for standard cutting heights and cut slope gradients in different rock and soil types (Table 2.2) (DoR, 2003). A maximum cut slope gradient of 1:0.3 (vertical: horizontal) has been recommended for cutting in hard rock. For soils in general, the maximum recommended cut slope gradient is 1:0.8. However, often in Nepal, local roads are constructed by cutting hillslopes at steeper angles (DSCWM, 2016). According to Hearn

et al. (2003), the principal cause of road-induced landslides in Nepal is the excavation of slopes for road construction and widening.

It is worth noting that soil slopes cut at steep angles can remain stable after excavation as the construction of local roads in Nepal is usually undertaken during the dry season (Thapa, 2015; Sudmeier-rioux et al., 2019). During the dry season, the presence of matric suction in soils above the groundwater table allow slopes to remain stable for an extended period (Fredlund et al., 1978). However, while the development of soil suction during dry periods contributes additional slope stability, dissipation of the same due to infiltration, seepage, or groundwater rise could lead to slope failures (Ng and Shi, 1998).

Table 2.2 Recommended standard cutting height and slope gradient for cut slopes.  
Source: DoR (2003, chap. 3).

<b>Soil classification</b>		<b>Cutting height (m)</b>	<b>Cut slope gradient (vertical: horizontal)</b>
Hard rock			1:0.3 - 1:0.8
Soft rock			1:0.5 - 1:1.2
Sand	Loose, poorly graded		1:1.5
Sandy soil	Dense or well graded	< 5 m	1:0.8 - 1:1
		5 - 10 m	1:1 - 1:1.2
	Loose	< 5 m	1:1 - 1:1.2
		5 - 10 m	1:1.2 - 1:1.5
Sandy soil mixed with gravel or rock mass	Dense, well-graded	< 10 m	1:0.8 - 1:1
		10 - 15 m	1:1 - 1:1.2
	Loose, poorly graded	< 10 m	1:1 - 1:1.2
		10 - 15 m	1:1.2 - 1:1.5
Cohesive soil		< 10 m	1:0.8 - 1:1.2
Cohesive soil mixed with rock masses and cobbles		< 5 m	1:1 - 1:1.2
		5 - 10 m	1:1.2 - 1:1.5

Another issue related to full-cut cross-sections is that a larger volume of spoil is produced which requires safe disposal (Hearn and Hunt, 2011). According to Hearn and Shakya (2017), during mechanised or equipment-based construction of local roads in Nepal, the excavated spoil is simply side-casted along the length of the road (“cut to throw”). The spoil pushed downslope without attempting to incorporate it into the road prism has been termed as “silverfills” by Sidle and Ochiai (2006). Such a practice can result in highly unstable deposits and pose threat to lives and properties.

Additionally, cut slope excavation, as well as side-cast spoil, may strip natural vegetation in the slopes. The contribution of vegetation to slope stability is generally associated with root anchoring mechanism (mechanical effect) and with the promotion of the soil water extraction via evapotranspiration, which allows the generation of soil suction (hydrological effect) (Collison et al., 1995; Sidle and Ochiai, 2006; Wu et al., 2015; Liu et al., 2016; Gonzalez-Ollauri and Mickovski, 2017; Switała and Wu, 2018; Balzano et al., 2019). According to Sidle (1992), the removal of root anchoring could result in less stable conditions and lower rainfall thresholds for landsliding. Stripping natural vegetation from slopes during road construction can also cause rilling, which may eventually develop into deep gullies (Fookes et al., 1985). Moreover, the absence of vegetation that partly intercepts the rainfall, increases the amount of water reaching the soil and also increases the energy of rain-drop splash; both mechanisms can lead to slope instability and surface erosion (Jankauskas et al., 2008; Switała and Wu, 2018). The removal of native plant species can also promote the growth of non-native plant species, which may have a lesser ability to stabilise slopes (Walker and Shiels, 2013). However, studies have also discussed the adverse effects of vegetation on slope stability. For instance, the plant roots may increase soil infiltration capacity by creating macropores, vegetation adds surcharge and also increases the rate of evapotranspiration which can lead to drier soils and consequent desiccation cracks (Sidle and Ochiai, 2006). Also, Morgan (2007) have argued that the taller plants (>1 m) can create higher erosive forces of the raindrops falling through the plant canopy, as compared to shorter plants. This shows that the extent to which vegetation can be beneficial for slope stability depends on the characteristics of the plant and its root anchoring capacity. Additionally, the lithology, slope inclination, groundwater table depth, as well as the atmospheric conditions also influence the role of vegetation on slope stability (Switała and Wu, 2018).

When the cut slope angle is steeper than the values recommended in Table 2.2, the authorities in Nepal have suggested building slope protection structures to prevent or mitigate potential failure (DoR, 2003). Various types of low-cost toe support measures like gabion walls, stone masonry walls and composite masonry walls are deployed for this purpose on local roads in Nepal (Hearn et al., 2003; DoLIDAR, 2009; Dahal et al., 2010; Bhandary et al., 2013). The gabion walls are used extensively in the local road network as they can be built with low skilled labour using materials available locally, which significantly reduces the cost of construction (DoLIDAR, 2009). Besides, gabion walls are free-draining, can accommodate settlement without rupture and are flexible enough to sustain small slope failures (TRL, 1997; DoLIDAR, 2009). However, it is worth noting that the effectiveness of gabion walls depends on the shape, size and quality of the rocks. The use of weathered rocks

and rounded stones that are smaller than the mesh size can cause local deformation of the wall and undermine its effectiveness (Hearn, 2011).

In addition to removing toe support, the construction of roads can also induce landsliding by changing the natural hydrological pathways (Sidle and Ochiai, 2006; Fannin and Lorbach, 2007). Roads alter hydrological path in two ways: first, they intercept the precipitation on the road surface; and second, if the road construction exposes the interface through which subsurface flow occurs, the intercepted water flows along the road surface as runoff (Megahan, 1983; Sidle et al., 2006). Hence, water management on roads to control and divert surface and intercepted subsurface flow safely into natural channels is crucial to protect slopes from erosion and instabilities (DoR, 2003; Fannin and Lorbach, 2007). The guidelines for road slope protection works published by DoR, Nepal (DoR, 2003) recommends catch drain ditches and cascades for surface water management and horizontal drain holes and subsurface drains for subsurface water management as countermeasures against landslides. Drain ditches are the most common drainage measures constructed on the cut slope side of the road and under ideal conditions, they capture and divert the surface and subsurface water to a location like a cross-drain from where it can be discharged safely. In the absence of ditches, the surface runoff follows the contour of the road, which may eventually flow onto the downslope, or into channels, upon encountering a topographic low (Sidle et al., 2006).

## 2.5 Case study

A 13.7 km long stretch of a district road (Daklang-Listi-Bhairabkunda road) located in Sindhupalchok was selected for the case study. The selected road section extends from Daklang (27°53'36.54"N, 85°54'51.72"E, 1264 m above sea level (a.s.l.)) to Listi (27°53'37.97"N, 85°52'18.94"E, 2296 m a.s.l.) (hereafter termed as Daklang-Listi road) and connects the surrounding villages to the Araniko highway (Figure 2.2). The Araniko highway links the capital city Kathmandu to the Chinese border at Kodari and mostly follows the Bhote Koshi River which originates from Tibet and flows south along the Upper Bhote Koshi valley. Daklang-Listi road is one of the many local roads built in this area to connect to the Araniko highway after it came into operation in 1967 (Adhikari, 2001).

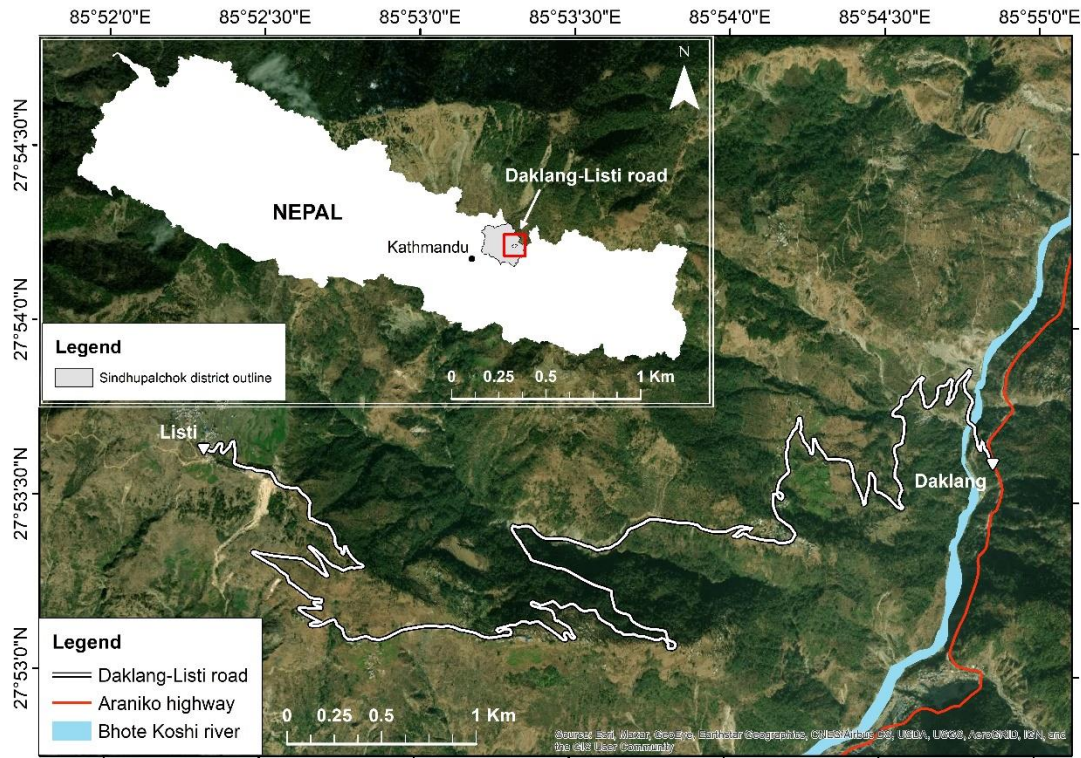


Figure 2.2 Map showing Daklang-Listi road; inset is the map of Nepal showing location of Daklang-Listi road within Sindhupalchok district.

### 2.5.1 Geological condition

Geologically, Nepal is divided into five longitudinal regions - Plains/Gangetic Alluvium (100 - 200 m a.s.l.), Siwalik/ Sub-Himalaya (700 - 1500 m a.s.l.), Lesser Himalaya (1500 - 2700 m a.s.l.), Higher Himalaya (2000 - 4000 m a.s.l.) and Tibetan Tethys (4000 - 8848 m a.s.l.). These regions are divided by the four major thrust faults: Main Frontal Thrust (MFT), Main Boundary Thrust (MBT), Main Central Thrust (MCT) and South Tibetan Detachment System (STDS).

The Daklang-Listi road is located in the Upper Bhote Koshi which is situated in the transitional zone between the Lesser Himalayan and the Higher Himalayan region, separated by the MCT. North of the MCT is the Higher Himalayan zone which is predominantly underlain by high-grade metamorphic rocks including gneiss, schist, quartzite and marble (Upreti, 2001). To the south of the MCT is the Lesser Himalayan region where the sedimentary and metasedimentary rocks including shale, sandstone, limestone, dolomite, slate, phyllite, schist, and quartzite are dominant (Upreti, 2001). The phyllitic rocks are most susceptible to landsliding, followed by the other rocks such as shale, schist, poorly cemented sandstone, limestone, and quartzite found in this area (Gerrard, 1994).

The Daklang-Listi road is located to the south of the MCT, the Lesser Himalayan region. As can be seen in Figure 2.3, this road traverses three geologic formations. The major part of the road passes through Lakharpata formation, which constitutes limestones, dolomitic limestones, quartzites and dolomites with intercalation of shales. Some sections of this road pass through Galyang formation constituting calcareous slates with dolomites and through Syanja formation consisting of calcareous quartzite, quartzitic limestones interbedded with shales. Furthermore, in some parts of the Lesser Himalayan zone, the slopes are overlain by thick, boulder rich soils (colluvium), which are prone to complex, large-scale landslides (Upreti, 2001).

The Upper Bhote Koshi region has rugged topography with steep slopes, a narrow gorge and high relief with altitude ranging between 760 m and 4100 m (Tanoli et al., 2017). Due to proximity to the tectonic thrust faults, the study area is prone to large earthquakes. The epicentre of the largest aftershock ( $M_w$  7.3) after 2015 Gorkha earthquake sequence was located less than 20 km from the Daklang-Listi road. According to Datta et al. (2018), Sindhupalchok was one of the most intensively affected districts during this earthquake sequence. In the coseismic landslide database compiled by Roback et al. (2018) and Kincey et al. (2020), a major concentration of coseismic landslides triggered by the 2015 Gorkha earthquake sequence can be seen within the study area.

Kincey et al. (2020) conducted a comprehensive study of the spatiotemporal evolution of landslides in the areas that were severely affected by the Gorkha-earthquake sequence including Sindhupalchok. By comparing the landslide inventory before, during and after the earthquake sequence, this study found that even after 3.5 years past the 2015 Gorkha earthquake, the number and area of the landslides had not returned to the pre-earthquake levels. The authors have argued the post-earthquake levels may never fully recover to the pre-event levels due to human-induced landscape disturbances like road building. Tian et al. (2020) studied the evolution of landslides along two critical highways in Nepal including the Araniko highway for three years after the 2015 Gorkha earthquake using field surveys and imagery. This study revealed that 56% of the investigated landslides (55) continued to evolve and enlarge through this period. Some landslides were also found to be changing mechanism, such as from debris slides to debris flows. Both Kincey et al. (2020) and Tian et al. (2020) provide evidences of a highly active and evolving post-earthquake landslide activity in the earthquake-impacted areas which includes Sindhupalchok. With a prolonged post-seismic recovery, the earthquake impacted regions continue to be under the threat of landslides. Hence, the Daklang-Listi road is located in a landslide-prone region not only because of a fragile geology and steep topography but also due to the active post-earthquake landslide activities.

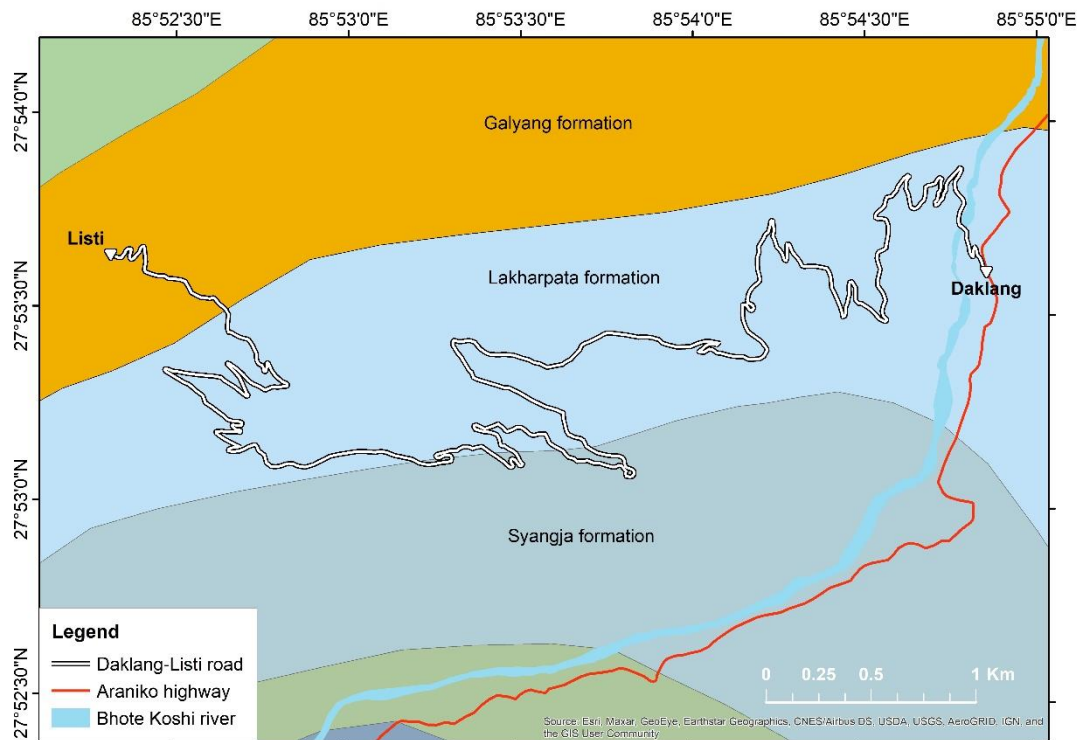


Figure 2.3 Simplified geological map of Daklang-Listi road. Source: (DMG, 1994).

### 2.5.2 Climate and rainfall

The climatic variation in Nepal mainly arises from the sharp altitudinal changes from approximately 60 m a.s.l. in the southern plains to 8848 m a.s.l. (Mt. Everest) within a relatively short north-south distance of 130 km to 260 km. Under the Köppen-Geiger climate classification system, a significant part of Sindhupalchok district experiences a warm temperate climate with dry winter and warm to hot and wet summer (Karki et al., 2016). At higher altitude, in the northern part of this district, a cold climate with dry winters and warm to cold summers as well as polar tundra and polar frost type of climate can be found (Karki et al., 2016).

The timing and amount of rainfall in Nepal is fundamentally controlled by the annual monsoon, in which the regional topography plays an effective role in controlling the rainfall distribution (Shrestha, 2000). With reference to the monsoonal system, there are four distinct seasons in Nepal: the pre-monsoon (March-May), the summer monsoon (June-September), the post-monsoon (October-November) and the winter (December-February). The pre-monsoon period can be warm - hot and dry and receives scattered rainfall. The summer monsoon is marked by heavy rainfall, with ~80% of the annual rainfall concentrated within this period. On the other hand, the post-monsoon season receives

substantially less rainfall and the winter season is generally dry and cold with some winter precipitation mainly in the north-western part of the country (Shrestha, 2000).

To understand the pattern of rainfall within the study area, the daily and monthly rainfall data recorded at the nearest meteorological station was obtained from the Department of Hydrology and Meteorology, Kathmandu (DHM, 2018). The nearest meteorological station is located in Gumthang (27°51'19.12"N, 85°51'34.75"E, 1846 m a.s.l.), which is approximately 6 km from the study area. The average monthly rainfall between 1955 and 2018 recorded at this station is shown in Figure 2.4. The 64-year average annual rainfall in Gumthang is 3600 mm, and according to Karki et al. (Karki et al., 2016), Gumthang receives the second-highest rainfall in Nepal after Lumle , north of Pokhara valley, which receives more than 5000 mm per year. Moreover, a clear monsoon-dominated rainfall pattern can be seen in Figure 2.4, with about 82% of the average annual rainfall (2950 mm) concentrated during the summer monsoon. The concentrated monsoonal rainfall in a relatively short period has been found to influence the incidence of landslides in Nepal (Upreti and Dhital, 1996).

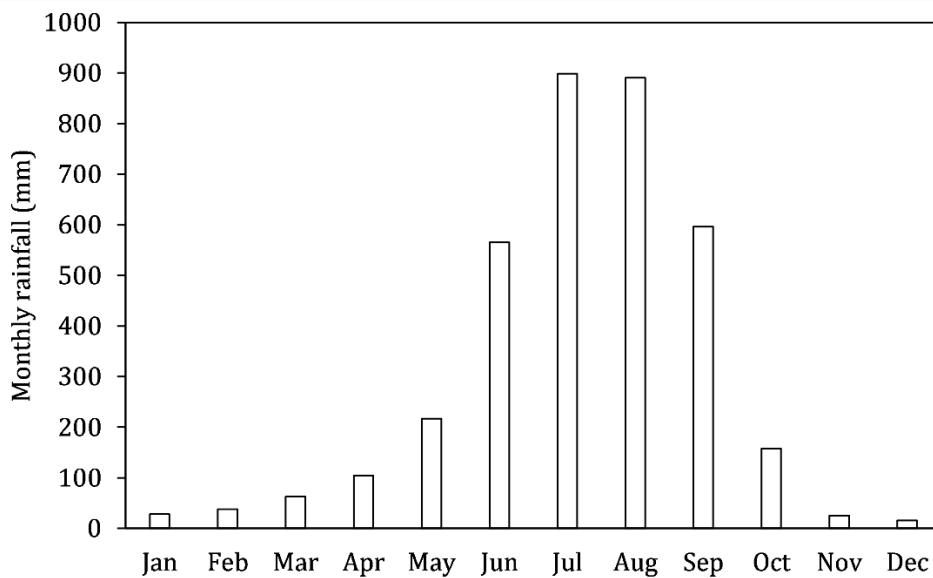


Figure 2.4 Average monthly rainfall measured at Gumthang meteorological station (1955 to 2018). Source: DHM (2018).



## 2.6 Reconnaissance surveys

Three reconnaissance field surveys were undertaken along the Daklang-Listi road to systematically and objectively evaluate the impacts that road construction can have on the landsliding phenomenon. In the following sub-sections, the observational findings from reconnaissance surveys conducted before and during monsoon are discussed.

### 2.6.1 Reconnaissance survey before monsoon

The first reconnaissance survey of the study area was undertaken in October 2017 to understand the local road construction method utilised in Nepal. During this survey, Daklang-Listi road was being widened by cutting into the hillslope using excavators (Figure 2.5). After slope cutting, the spoil with boulders was side-casted along the road as shown in Figure 2.5. It was discussed earlier in this chapter that such a method of road construction is typical for local roads in Nepal and can be detrimental to slope stability (Hearn and Shakya, 2017). Further, a “wait and see” working principle was adopted for the widening of the road (personal communication with the Site Engineer), which entailed slope excavation and landslide debris clearance (if necessary), without prior investigation of potential problematic locations.



Figure 2.5 Construction of Daklang-Listi road, looking North ( $27^{\circ}53'49.20''\text{N}$ ,  $85^{\circ}54'46.20''\text{E}$ ) (\*photo location shown in Figure 2.6).

To evaluate the immediate (post-construction) impacts of slope cutting on landslides, another reconnaissance survey was undertaken in December 2017. This was a problem identification survey that aimed to identify existing slope stability problems along the Daklang-Listi road and other critical issues related to local road construction that could promote landsliding during the monsoon. During this survey, a hand-held GPS was used to locate the existing landslides to assess if the number or frequency of landslides increased during the following monsoon. Although all the roadside slopes were not examined individually, field records were taken at locations where problematic issues related to slope cutting, surface and sub-surface water management, slope protection and spoil disposal were observed. Site photographs were also taken at these locations so that a comparison of the slope condition - before and during the monsoon can be made. It should be noted that specific slope assessment forms were not used during this survey, mainly because the objective was not to assess stability of individual road cut slopes, but to develop a general understanding of the typical problems associated with local road construction in Nepal.

In terms of the number of slope instabilities, the immediate effect of slope cutting was found to be sporadic; a total of 16 slope failures were recorded some of which existed before the road widening (Figure 2.6). Two possible explanations for this observation are i) there were no major slope failures during road widening and/or ii) the debris from the failed slopes had been removed before the survey was conducted. Nonetheless, road-related slope and water management issues that could potentially be conducive to landsliding during monsoon were identified during this survey.

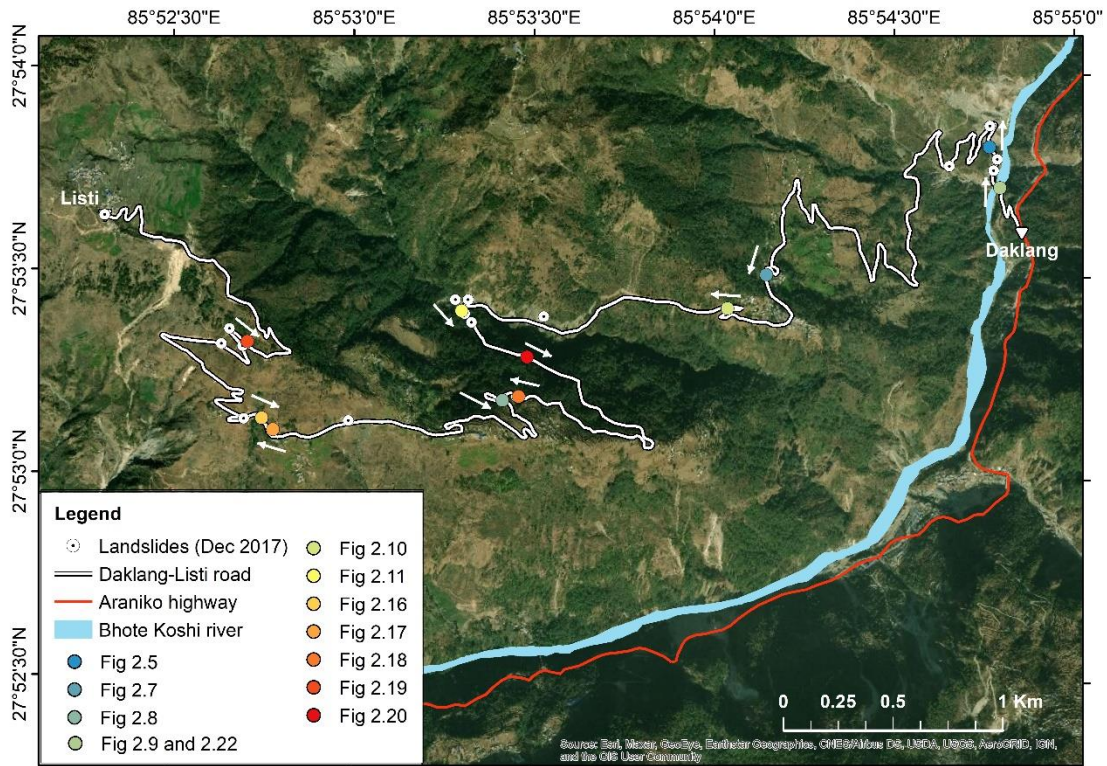


Figure 2.6 Distribution of landslides along Daklang-Listi road in December 2017. The coloured circular points on the map show subsequent photo locations including Figure 2.5. The arrows marked next to these points show the direction that the photographs were taken from.

One of the key observations made during the reconnaissance survey was that the roadside slopes at several locations along Daklang-Listi road were excavated at angles greater than those recommended by DoR (2003) (Table 2.2). Two examples of steep cut slopes along Daklang-Listi road are shown in Figure 2.7 and Figure 2.8. The typical angle of shearing resistance of the colluvial materials found in this area ranges from 25° to 45° (ICIMOD, 1991, p. 883). The stability of soil slopes at angles much greater than this can be attributed to the presence of soil suction (Eichenberger et al., 2011). Considering the fact that the soil suction can dissipate as a result of infiltration during rainfall (Fredlund and Rahardjo, 1993), unprotected soil slopes along Daklang-Listi road were left in a precariously stable state after widening the road. This aspect is evaluated in detail using numerical modelling method in chapter 6.





Figure 2.7 Steep road-cut slope adjacent to the settlement area along Daklang-Listi road ( $27^{\circ}53'30.0''\text{N}$   $85^{\circ}54'09.2''\text{E}$ ).



Figure 2.8 Steep road cut along Daklang-Listi road ( $27^{\circ}53'11.1''\text{N}$   $85^{\circ}53'25.4''\text{E}$ ).

In Figure 2.9, a section of Daklang-Listi road is shown where a three-step gabion wall had been constructed for slope protection. Seepage is evident at this section which indicates the presence of a shallow groundwater table. According to Hearn et al. (2003), in the colluvial



soil slopes where the groundwater table is located at shallow depth from the surface, the cut slope gradient should be between 1:0.8 and 1:1 and a cut height >6 m is not recommended. However, at this section, the height of the wall was >6 m and the cut slope gradient was much steeper ( $\sim 75^\circ$ ). In such a condition, the effectiveness of the gabion wall in supporting the back slope as well as the survivability of the gabion wall is uncertain during rainfall.

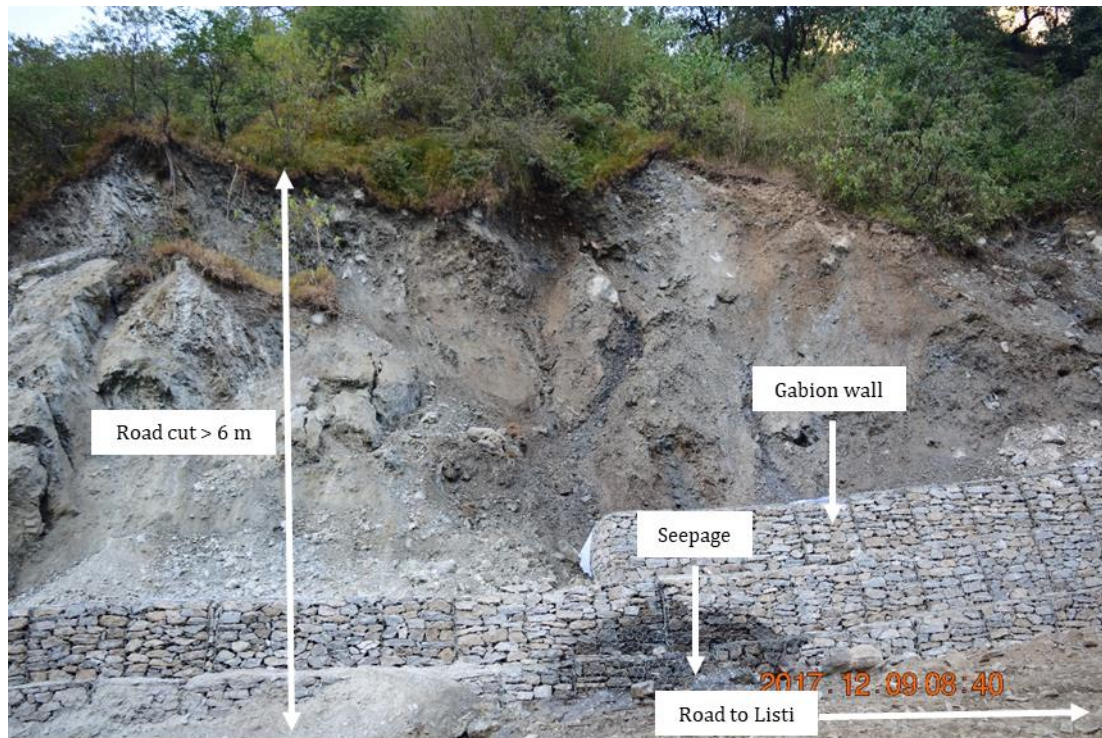


Figure 2.9 Gabion wall constructed to support a cut slope along Daklang-Listi road ( $27^\circ 53' 43.2''\text{N}$   $85^\circ 54' 48.0''\text{E}$ ).

Additionally, the side-casting of spoil during construction caused the stripping of natural vegetation, an example of which is shown in Figure 2.10. The preservation of vegetation is another issue in the slope management which was found to be overlooked during the widening of the investigated road.



Figure 2.10 Removal of vegetation along Daklang-listi road ( $27^{\circ}53'25.0''N$   $85^{\circ}54'02.8''E$ ).

The lack of simple drainage systems like roadside drain ditches along Daklang-Listi road was another critical observation made during the field survey in December 2017. An example of improper water management along the road is shown in Figure 2.11. In the figure, the surface runoff from upslope can be seen to be flowing on the roadway following the road gradient due to absence of the ditches before eventually discharging downslope upon encountering a topographic low. The subsurface water flow intercepted by the road cut can also be observed at this location which is discharged downslope from the topographic low in the absence of a drainage system (Figure 2.11). During periods of prolonged rainfall when the surface and subsurface discharge is high, the topographic low points such as that shown in Figure 2.11 can become preferential sites for gully erosion and landslide initiation (Sidle et al., 2006).

Hence, the reconnaissance surveys conducted before monsoon provided an understanding of the method used for local road construction and allowed the identification of the factors that could potentially cause slope failures during monsoon conditions. To evaluate the stability of the road cut slopes during the successive monsoon, a second reconnaissance survey was conducted, the findings of which are discussed in the next section.





Figure 2.11 Improper surface and subsurface flow management along Daklang-Listi road ( $27^{\circ}53'24.3''\text{N}$   $85^{\circ}53'18.5''\text{E}$ ).

### 2.6.2 Reconnaissance survey during monsoon

The observations from the preliminary reconnaissance surveys indicated that the road construction created precarious slopes along the Daklang-Listi road. To explore how the newly widened local road responded to the subsequent monsoonal rainfall and to identify common slope failure mechanism together with their impacts, a second reconnaissance survey was undertaken during the monsoon in August 2018.

A landslide information sheet (Appendix A-1) was prepared to record the distribution and characteristics of roadside slope failures along the Daklang-Listi road. The information collected during the reconnaissance survey has been summarised in Table 2.3. A hand-held GPS was used to mark the locations of the slope failures and the characteristic details about the failures and their impacts were recorded in the landslide information sheet in the field. The depth of the main landslide scarp and the road cut height and angle were obtained from direct measurements taken using measuring tape, laser distance meter and clinometer. The depth of the landslide scar was measured from the landslide crown to the top of the landslide deposit (Figure 2.12). The information collected in the field including the landslide features, geology, condition of the road and hydrological conditions (Table 2.3) were based on careful field observations. The land-cover and land-use in the vicinity of the landslides were also recorded to understand the impacts of road-related landslides on the surrounding

environment, communities and vice-versa. At some landslide locations, due to difficulties in access, the landslide scar lengths were estimated from the road. Since the aim of the survey was to identify landslide typologies and their impacts, accurate estimation of scar length was considered to be relatively less important.

Table 2.3 Summary of the information recorded in the landslide information sheet.

<b>Landslide features</b>	• Landslide type	• Age of failure
	• Geometry of the landslide	• Sign(s) of movement
	• Depth of landslide scar	• Activity state
	• Hillslope angle	• Slope failure type in relation to road
	• Triggering factor(s)	
<b>Soil and rock type</b>	• Material involved	• Nature of exposed rock
	• Principal soil type	• Weathering grade
	• Principal rock type	
<b>Road condition</b>	• Road type (cut/fill/cut & fill)	• Cut slope angle
	• Road construction method	• Impact on the road
	• Road alignment location	• Existing countermeasures
	• Road surface type	• Presence of cracks
	• Road cut height	
<b>Hydrological condition</b>	• Type of drainage	• Condition of drain (if any)
	• Type of roadside drain	• Any evidence of groundwater condition
<b>Land-over/land-use</b>	• Upslope from the road	
	• Downslope from the road	

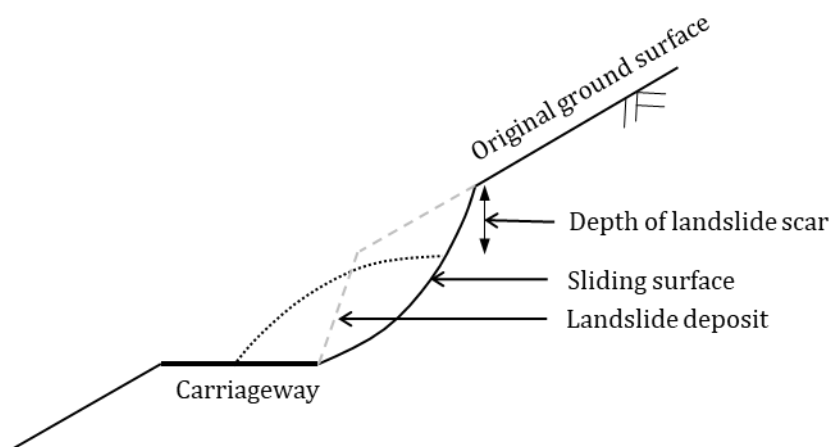


Figure 2.12 Measurement of the depth of landslide scar.



### 2.6.2.1 Distribution and characteristics of the landslides

Figure 2.13 shows the distribution of landslides along the investigated section of the Daklang-Listi road during the reconnaissance survey in August 2018. A total of 117 landslides were recorded, which averages almost 9 landslides per kilometre. In comparison to the dry period (December 2017) (Figure 2.6), the number of slope failures was almost an order of magnitude higher. Such high rates of slope failures along similar mountain roads have also been reported in the studies conducted in the neighbouring countries. For instance, Sidle et al. (2014) reported up to 64 landslides per kilometre per year along a newly widened mountain road in Yunnan, China. Bansal and Mathur (1976) cited in Sidle and Ochiai (2006, p. 189) reported 10 small and 0.1 large landslides in every kilometre of mountain road in the north-western Himalaya of India.

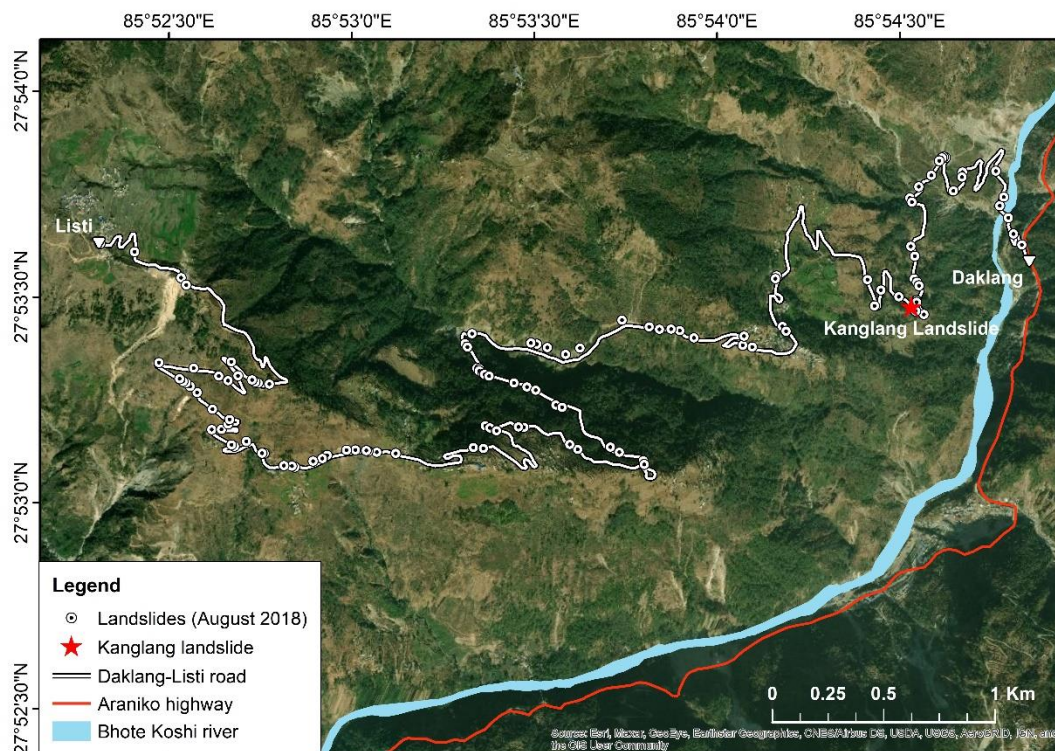


Figure 2.13 Distribution of landslides along Daklang-Listi road in August 2018.

### 2.6.2.2 Nature of the landslides

Based on the field data, the majority of the failures (102 slope failures) were observed on soil slopes, 88 of which were classified as 'slides' following the Varnes' landslides classification system (Varnes, 1958). In 56 landslides, the depth of the main scar was found to be relatively shallow (less than 1.5 m) and in 43 landslides the length of the main scarp was between 1.5 and 5 m. Only in 1 landslide, the depth of the main scar was greater than 5

m. According to Hearn (2011), it is common that up to 70% of the slope failures affecting any given mountain road are relatively shallow instabilities in the cut slopes. However, at some locations (17), the length of the main scarp had to be estimated from the road due to difficulties in access created by steep and unstable terrain. Furthermore, 93% of all failures along the Daklang-Listi road occurred on the road cut slope, which is expected as the Daklang-Listi road was widened solely by cutting into the hillslope, as mentioned in section 2.6.1. A small number of the failures were also recorded below the road, or on the valley side of the road.

To systematically evaluate the types of failure along the road, an attempt was made to classify the observed roadside slope failures based on the typical landslide shear surface configurations defined by Hearn (2011) for mountain roads. Since the Daklang-Listi road was widened by full cutting, the anticipated types of failure, modified after Hearn (2011), are shown in Figure 2.14. The '*failure in hillslope*' represents slope failures in the hillslope above the road cut but not on the road cut and the '*failure in cut slope only*' includes minor failures on the road cut slope surface. The '*failure in cut slope extending to hillslope*' comprises road cut slope failures that extend to the hillslope above the road cut. The '*deep failure beneath the road*' constitutes deeper slope failures extending below the road and the '*failure in original valley slope*' includes failures below the road. The '*river scour*' represents failures due to undercutting by the river and streams.

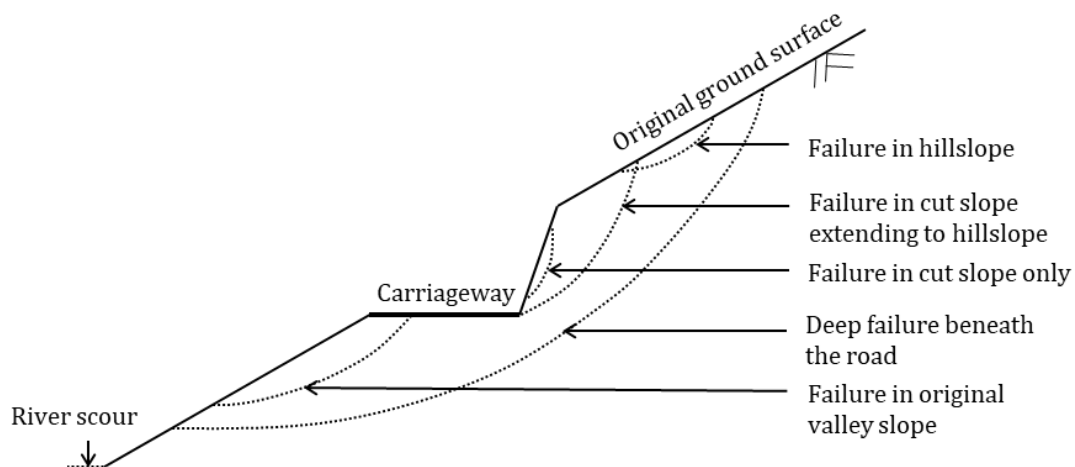


Figure 2.14 Typical slope failures in relation to a road cutting. Modified after Hearn (2011, p. 51).

The bar diagram in Figure 2.15 shows that the most common type of failure was '*failure in cut slope extending to hillslope*', followed by '*failure in cut slope only*', '*failure in valley slope*' and '*failure in hillslope*' respectively. An example of a '*failure in cut slope extending to hillslope*' is shown in Figure 2.16. It can be seen in this figure that the landslide scar is located

well above the road cut suggesting that the failure at the road cut may have allowed the soil above the road cut to slide, thereby affecting a larger area of the hillslope. Similarly, an example of the second common failure type observed in the field – ‘*failure in cut slope only*’ is shown in Figure 2.17. This type of failure was relatively less damaging to the slope and the surroundings as they affected only a small portion of the cut slope. The third most common failure type that was encountered along the Daklang-Listi road was ‘*failure in valley slope*’. Two examples of this type of failure are shown in Figure 2.18 and Figure 2.19. This type of failure was mainly caused by the flow of sediment-laden surface runoff. The failure of the valley slope was anticipated during the reconnaissance survey undertaken in December 2017 by noting the lack of subsurface/surface water management for the road (section 2.6.1). Among the other types of failure, the valley side slope failures were the most damaging as they caused partial or complete loss of the roadway. Lastly, only at two locations, ‘*failure in hillslope*’ was recorded although no damage to the road cut was seen. In Figure 2.20 an example of this type of failure is presented. Although the actual failure surface cannot be seen in this picture, the road cut appears to be intact and the landslide deposit and the flow path can be seen, which suggests that the failure may have occurred above the road cut. This type of failure was infrequent and created less disruption.

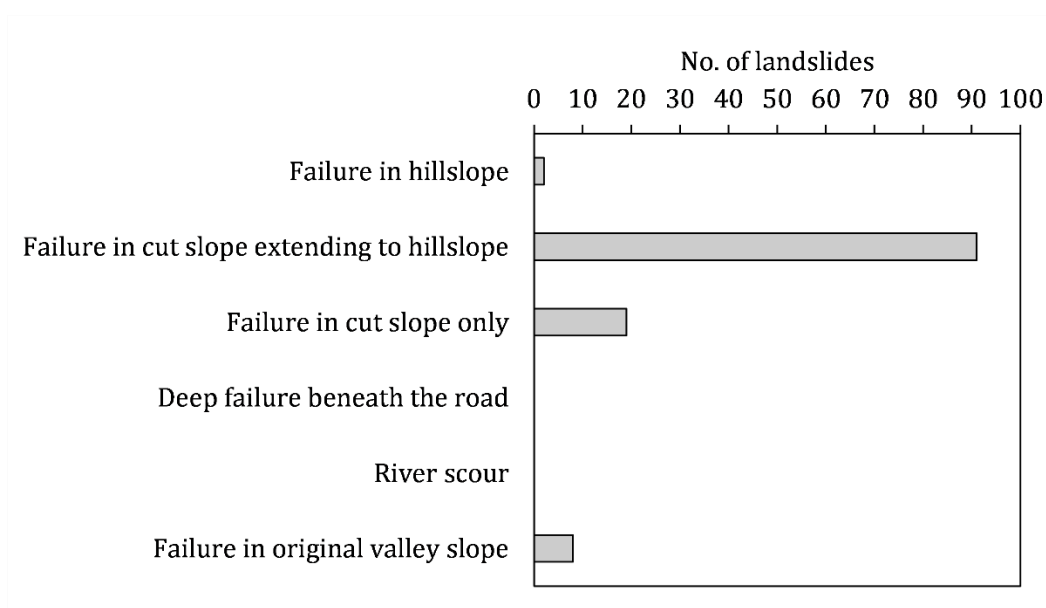


Figure 2.15 Failure types in relation to the road. Modified after Hearn (2011, chap. 51).





Figure 2.16 Failure in cut slope extending to hillslope (27°53'8.20"N 85°52'45.30"E).



Figure 2.17 Failure in cut slope only (27°53'06.5"N 85°52'47.2"E).





Figure 2.18 Failure in original valley slope due to surface runoff (27°53'11.70"N 85°53'28.10"E).



Figure 2.19 Failure in original valley slope due to surface runoff (27°53'19.5"N 85°52'42.8"E).



Figure 2.20 Failure in hillslope ( $27^{\circ}53'17.53''\text{N}$   $85^{\circ}53'29.45''\text{E}$ ).

The frequency distribution of the road cut angles measured adjacent to the landslides are shown in Figure 2.21. From the figure, it is evident that more than 95% of the landslides had occurred where the roadside slopes were excavated at angles greater than the maximum recommended cut slope angle in soils i.e.  $51^{\circ}$  (1:0.8) given by (DoR, 2003) (Table 2.2). It should be noted that this finding does not necessarily imply that the roadside slope failures could be prevented if the cut angles were less than the recommended maximum value. Also, the relative likelihood of landslides based on the cut slope angles cannot be commented on without studying all the roadside slopes including those that did not fail. Other factors related to local site condition like soil/rock types, soil/rock strength and moisture condition may have played a role in causing the slope failures. Nonetheless, considering only the slopes that failed, the observation from the field does suggest that the potential of failure could be higher in the slopes when they are excavated at steep angles for road construction or widening. Referring back to the 'causes' in the 'chain of events' discussed in section 2.2, the steepness of the road cut could perhaps be an important causal factor, which may not necessarily trigger the failure immediately after construction but may create favourable conditions for the slopes to fail given the onset of external triggers like rainfall.

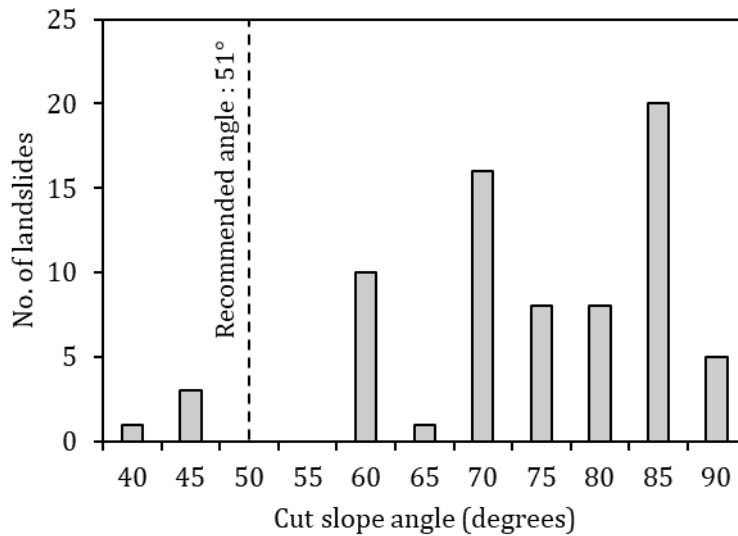


Figure 2.21 Measured cut slope angles at the failed slopes along the Daklang-Listi road.

As discussed previously, gabion walls and masonry walls are the most common countermeasures adopted for roadside slope stability in the local road network in Nepal. Along the investigated road, 9 slope failures were recorded despite the presence of countermeasures, whereas the other 102 slope failures had no protection. An example of a slope failure despite the presence of a gabion wall is shown in Figure 2.22. This slope was identified as being precarious and the gabion wall was anticipated to be ineffective for slope protection during the walk-over survey in December 2017 (Figure 2.9). The possible implication of this observation is that the slope protection measures are perhaps important to prevent landslides during rainy periods, but at the same time, may not be fully effective unless engineered carefully considering the local factors like cut slope geometry, strength and seepage conditions.





Figure 2.22 Gabion wall overtopped by landslide debris (27°53'43.2"N 85°54'48.0"E).

### 2.6.2.3 Impacts of landslides

The findings of the reconnaissance field survey were used to understand the impacts of the roadside slope failures. As shown in Figure 2.23, the landslide deposits caused complete or partial blockage of the road at 37 and 73 locations, respectively. Likewise, the valley-side failures caused the complete or partial failure of the roadway at 8 locations. As a result of the extensive landslides along the Daklang-Listi road, the road was unserviceable during the monsoon resulting in socio-economic difficulties for the local communities. The Daklang-Listi road is only a representation of the 42,805 km of the local roads (74% of the total LRN in Nepal) which are not serviceable during monsoon due to poor road conditions and frequent slope failures (Devkota et al., 2014; DoLIDAR, 2016).

Furthermore, the landslide impact information collected during the reconnaissance survey showed that the roadside slope failures caused damage to the agricultural lands, roads, houses and forests in their vicinity (Figure 2.24). Since the Daklang-Listi road was constructed by cutting the agricultural terraces at several locations, the roadside slope failures caused the most damage to agricultural land (Figure 2.24), which had an adverse economic impact on the local farmers.

In addition, the damage to the agricultural lands due to seasonal road-related landslides has led to farmland abandonment in Nepal (Chaudhary et al., 2020). Oven (2009) studied the impacts of landslides on the communities in the Upper Bhote Koshi region, including Listi, by conducting household surveys. The survey results showed that landslide activities led to



temporary or permanent abandonment of the farmlands in the study area. Confounding this, the abandonment of farmlands further leads to a loss of traditional instability and runoff control measures which includes the construction of terraces and raisers, waterways and retention walls that are commonly adopted in mountainous areas (Khanal and Watanabe, 2006). As a result of the abandonment, farmland terraces gradually deteriorate, leading to collapse, increased runoff, modified subsurface pathways and concentrated flows along the furrows, eventually causing rills, gullies and landslides (Khanal and Watanabe, 2006; Chaudhary et al., 2020). Thus, besides the direct socio-economic impacts, the impact of road-related landslides can be an increased susceptibility to rainfall-induced landslides due to farmland abandonment.

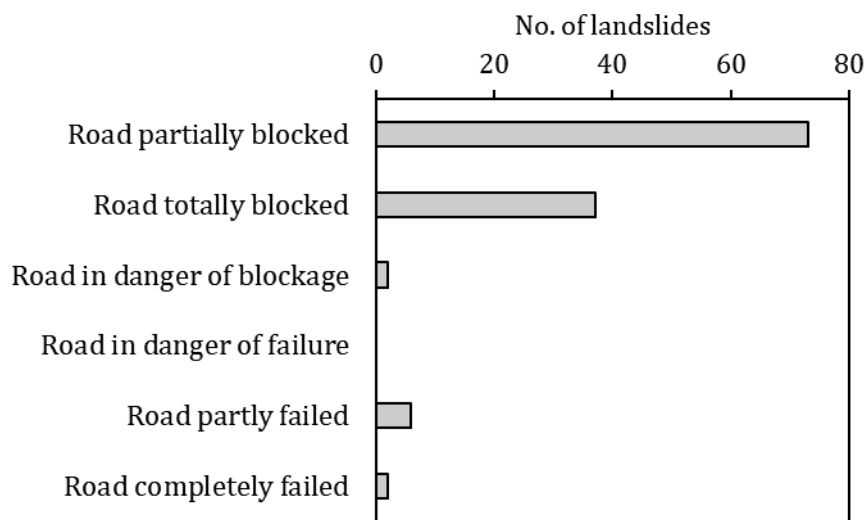


Figure 2.23 Impacts of slope failures on the road.

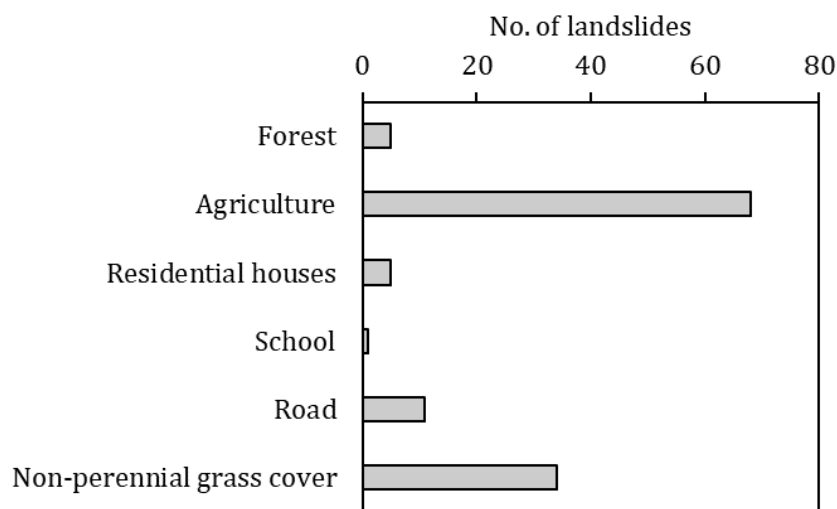


Figure 2.24 Land-use/land-cover in the vicinity of slope failures.

## 2.7 Site selection for further investigation

The observations from the reconnaissance surveys showed that extensive roadside slope failures occurred along the newly widened Daklang-Listi road during the monsoon. For a detailed investigation of the failure mechanism of a road cut slope subjected to rainfall using numerical analysis (chapter 6), a representative landslide that occurred along the Daklang-Listi road was selected. The approach defined below was adopted for the selection of the representative landslide.

Firstly, from the 117 slope failures that occurred along Daklang-Listi road during the monsoon, a common failure type was identified. Based on the field records, 56% of the slope failures were shallow in depth (<1.5 m), 87% of the slope failures were in soil, 86% of the slope failures were classified as slides (Varnes, 1978), 93% of the slope failures occurred in the cut slope and 76% of the slope failures were '*failure in cut slope extending to hillslope*'. Hence, the common failure type along the Daklang-Listi road was identified as a 'shallow soil slide in the road cut slope which extended into the hillslope above the road cut.' This type of failure was found at 75 locations along the road. Among them, a representative landslide site was selected for detailed geotechnical investigation, taking into account the following criteria.

1. Representativeness - The selected landslide site should represent common failure type encountered along the Daklang-Listi road.
2. Triggered by the first monsoonal rainfall after the excavation of slope for road widening - The primary focus of this study is to evaluate the failure mechanism of a landslide triggered by the interaction of road and rainfall. Selecting a slope that remained stable after road widening in 2017 but failed during the following monsoon in 2018 would provide insights into how the rainfall and road cutting interact to trigger slope failure.
3. Good mobile network reception - As discussed earlier in chapter 1, one of the objectives of this study is to install a field monitoring station for long-term monitoring of soil water content and rainfall. To retrieve data remotely from the data logger, suitable mobile network reception was necessary.
4. Safe accessibility around the site for ground investigation, sample collection and transportation and installation of field monitoring instruments.
5. Permission from the landowner for access and investigation - This was crucial not only to access the site for investigation but also for the safety of the field monitoring station.

Based on the above criteria, a landslide located near Kanglang village, hereafter referred to as Kanglang landslide (27°53'32.0"N, 85°54'28.5"E) was selected for further investigation (Figure 2.13). At the location of this landslide, a steep (~70°) road cut slope was formed to accommodate the wider road. The slope had remained stable after road widening in December 2017 but eventually failed during rainfall in July 2018, as confirmed by the landowner (criteria 2). The failure of this cut slope affected a larger area of the hillslope above the road cut (criteria 1). This site was safe to access and had good mobile network reception (criteria 3 and 4). Lastly, permission for in-situ tests and installation of monitoring station was obtained from the owner of the site (criteria-5).

Since Kanglang landslide represents the most common slope failure type encountered along the Daklang-Listi road and fits into the other criteria described above, this landslide was selected for a detailed investigation. It may be argued that uncertainties will exist in the representativeness of the selected site due to site-selection bias. Generally, such uncertainties can be minimised by increasing the number of study sites or by adopting a systematic approach for site-selection. Although increasing the number of study sites is useful, this can be difficult given the limitations in time and resources. Hence, as described above, in this study, a systematic approach was adopted where a complete inventory of existing roadside slope failures was carefully evaluated to identify the common slope failure type. A representative slope failure was then selected based on the pre-defined 5-step criteria described above. By adopting this approach, uncertainty due to site-selection bias was minimised.

## 2.8 Chapter summary

The key points from this chapter are summarised below:

1. The concentrated monsoon rainfall has been demonstrated as one of the main triggers of landslides in Nepal. There is also increasing evidence that the expansion of the non-engineered local road network has further aggravated the frequency of rainfall-induced landsliding.
2. The primary reason for the rise in the road-related landslides in Nepal is found to be rooted in the proliferation of non-engineered equipment-based methods for cheaper and quicker road construction. The roads built in this manner often lack adequate planning, design and control on the use of heavy equipment, consequently inducing a greater risk of hillslope instability.
3. Some studies conducted in Nepal have discussed the issue of increased landslide risk in areas with non-engineered local roads and underlined the increasing need to

pay attention to the risk of rainfall-induced landsliding due to roads. However, little attention has been given to understanding of the interaction of local road with rainfall that can cause landsliding.

4. This chapter introduced the case study of a district road (Daklang-Listi road) situated in central Nepal. Daklang-Listi road is located in a tectonically active mountainous region characterised by rugged topography with steep slopes, high relief and narrow gorge. This region was severely affected during the 2015 Gorkha earthquake sequence because of which the landslide activity in this area has been reported to be still highly active and evolving.
5. A series of reconnaissance surveys was undertaken along the Daklang-Listi road in 2017 and 2018 with the aim of understanding i) the method employed in local road construction in Nepal ii) the stability of slopes immediately after road construction, iii) road-related slope and water management issues that are conducive to landsliding, and iv) the stability of roadside slopes under monsoon rainfall.
6. The reconnaissance surveys conducted before the monsoon in October 2017 provided first-hand evidence of how local roads in Nepal are widened. The construction method involved slope cutting using excavators and side-tipping of excavated materials without prior investigation of the potential problematic locations.
7. The field observations from the reconnaissance surveys in December 2017 and August 2018 showed that steep road excavation, side-tipping of spoil, vegetation removal, inadequate and ineffective slope protection measures and lack of drainage system were the key factors related to local road construction which can contribute to landsliding during the monsoon.
8. The reconnaissance survey undertaken during the monsoon (August 2018) revealed that the number of slope failures along the Daklang-Listi road increased by an order of magnitude within seven months of road widening. The extensive landsliding along the investigated road was found to be largely, if not entirely, pre-conditioned to failure by the road widening works. This observation highlights that the frequency of slope failures can increase significantly along non-engineered local roads within a short period of time when exposed to concentrated monsoonal rainfall.
9. The most common type of failure recorded along the Daklang-Listi road during monsoon was "*failure in cut slope extending to the hillslope*". The other failure type - "*failure in valley slope*" caused mainly by debris-carrying runoff was most damaging as such failures caused a partial or complete loss of the carriageway.

10. The majority of the roadside slope failures caused complete or partial blockage of the road making this road unserviceable during the monsoon. The slope failures caused most damage to agricultural lands located proximal to the road. Landsliding due to road construction has previously been reported to be one of the main reasons for farmland abandonment. The abandonment of agricultural land in mountainous terrain is also known to have an influence on the increased susceptibility to landslide occurrence.
11. Based on the findings of the reconnaissance surveys conducted during the monsoon, a representative landslide located in Kanglang village along the Daklang-Listi road (Kanglang landslide) was selected for a detailed analysis of the failure mechanism using numerical modelling.

# Chapter 3

## Geotechnical field investigation

---

### 3.1 Chapter outline

From the previous chapter, a representative landslide was selected for further exploration of the causes and mechanism of failure using field investigation and numerical analysis. This chapter focuses on the field investigation which was carried out at the selected location (Kanglang landslide) in March 2019. The initial part of this chapter describes the selected landslide and the rationale for field investigation. This is followed by a description of the methods utilised in this study, which constitutes borehole drilling, penetration tests and trial pit excavation. The observations and the findings from this work are presented later in this chapter.

### 3.2 General information about Kanglang landslide

Kanglang landslide (27°53'32.0"N, 85°54'28.5"E) is located at km 02+420 of the Daklang-Listi road at an elevation of 1440 m<sup>1</sup> a.s.l. (chapter 2, Figure 2.14). The slope is underlain by colluvial deposit with isolated boulders. The average hillslope angle at this location is ~22°, which was estimated using the digital elevation map of Sindhupalchok. The natural slope at this location was excavated to widen the road, forming a steep (~70°) cut slope in December 2017 which is shown in Figure 3.1. Within seven months of road widening, during the monsoon (July 2018), failure of the cut slope occurred which extended above the road cut into the hillslope and affected a larger area. Figure 3.2 shows the failed slope at this location observed during the reconnaissance survey in August 2018. Based on the landslide classification given by Varnes (1958), Kanglang landslide can be classified as a translational slide with a sliding depth of approximately 1.5 m. The general characteristics of this landslide are summarised in Table 3.1.

---

<sup>1</sup> The elevations in this study were recorded using a hand-held GPS (Garmin 60CSx). This GPS provides an approximate estimation of the elevation with an accuracy of <10 m.

Table 3.1 Summary of the characteristics of Kanglang landslide

Length	~25 m
Width	~45 m
Depth of sliding surface	~1.5 m
Failure type	Translational slide
Aspect	North-east
Elevation	[1440 m (toe) m to 1460 m (crown)]
Cut slope angle	~70°
Hillslope angle	~22°



Figure 3.1 Road-cut slope at Kanglang landslide before failure (December 2017) (27°53'32.0"N, 85°54'28.5"E).



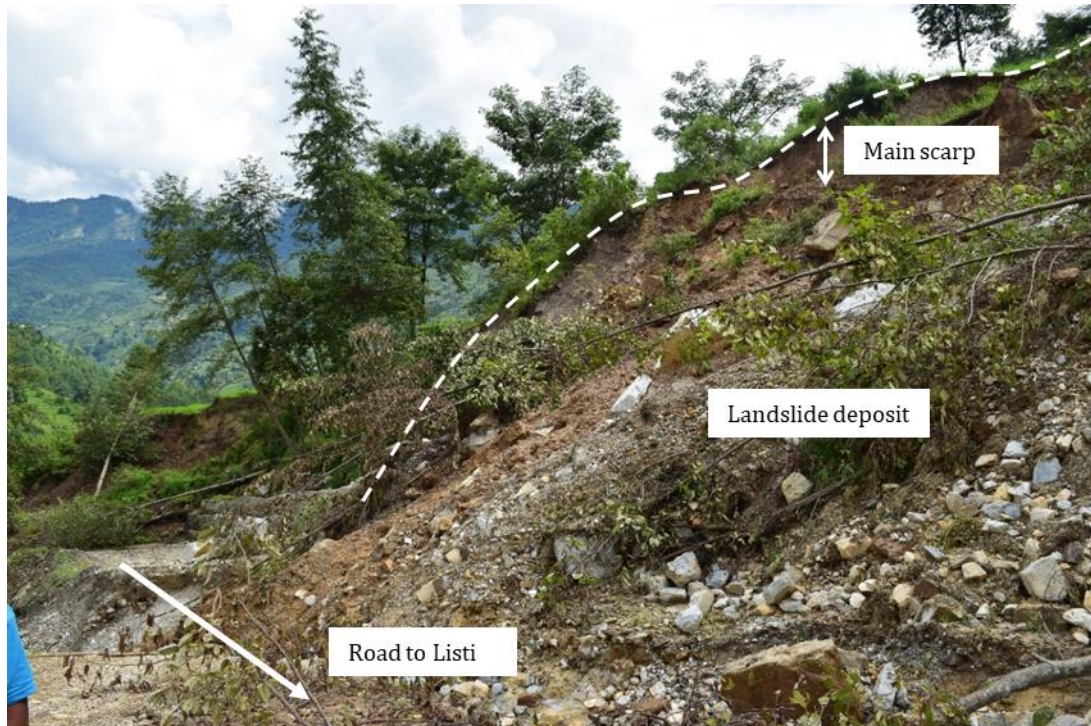


Figure 3.2 Kanglang landslide (August 2018) ( $27^{\circ}53'32.0''\text{N}$ ,  $85^{\circ}54'28.5''\text{E}$ ).

### 3.3 Objectives of geotechnical field investigation

Geotechnical field investigations are conducted to obtain information on the slope materials and the ground water condition which are essential for evaluating the potential causes and mechanism of the slope failures. In this study, a geotechnical investigation was undertaken at Kanglang landslide, the main objectives of which were:

1. to perform in-situ tests for determination of the nature and vertical stratification of the subsoil near the failed area
2. to obtain soil samples for laboratory testing
3. to determine the position of the groundwater table

The information obtained from the field about the subsoil stratification and groundwater conditions was used to create a representative slope profile for the numerical analysis (chapter 6). The soil samples obtained from the field were tested in the laboratory to obtain their physical, mechanical and hydraulic properties, which will be discussed in detail in chapter 4.



### 3.4 Selection of methods for investigation

There are various methods used for subsoil exploration which are reviewed in detail by McGuffey et al. (2014). Trial pit excavation and borehole drilling are the conventional and widely used methods of ground investigation (Hearn et al., 2003). The excavation of trial pits using hand tools or backhoes is an efficient and economical method of investigation that is suitable for most soil types (Clayton et al., 1995; Craig, 2004). Trial pits provide useful two-dimensional information on the shallow soil and rock conditions and the presence of existing or potential slip surfaces (if any) (Hearn and Massey, 2009). In colluvial deposits, the visual inspection of the trial pit wall can provide a better understanding of the subsoil condition than examination of the samples obtained from boreholes (Turner and Schuster, 1996, p. 546). Additionally, a larger volume of disturbed and undisturbed samples can be collected from the trial pits for laboratory testing (Craig, 2004; McGuffey et al., 2014). However, this method is limited to shallow depths. BS 5930:2015 (BSI, 2015) recommends a maximum 4 to 5 m depth for trial pit excavation although depths greater than 1.2 m are unsafe for a person to enter (for sampling and logging). Trial pit excavation to greater depths necessitates the use of appropriate temporary support and risk assessment as per BS 5930:2015 (BSI, 2015), which makes excavation of trial pits to greater depths and below the groundwater table both uneconomical and risky (McGuffey et al., 2014). Since the objective of trial pit excavation in this study was to obtain information on the near-surface soil condition, trial pit excavation to greater depths (>1.5 m) was not pursued.

For continuous subsoil exploration to greater depths, borehole drilling methods like auger boring, rotary drilling, wash boring and percussion drilling are used (Jackson and Dhir, 1996). In-situ tests can be performed in the borehole during drilling, which can provide information on the subsoil profile (Jackson and Dhir, 1996). The standard penetration test (SPT) is one of the most commonly used in-situ tests used for various geotechnical applications (Jackson and Dhir, 1996; Terzaghi et al., 1996). The simplicity of the test procedure and the equipment employed in SPT are the few main reasons for its popularity. Besides being simple, disturbed samples can be obtained during the test, which can be used for geotechnical soil characterisation (Sivrikaya and Toğrol, 2006). Additionally, several soil properties can be inferred from the measured SPT values using empirical relationships. For instance, SPT N-value has been used in correlations with the relative density and angle of shearing resistance (Meyerhof, 1957; Peck et al., 1974; Skempton, 1986; Hatanaka and Uchida, 1996; Jackson and Dhir, 1996; Terzaghi et al., 1996) and with the modulus of elasticity (Jackson and Dhir, 1996).

Thus, a combination of trial pit excavation, borehole drilling and standard penetration testing was adopted for field investigation of Kanglang landside. The standard penetration tests were conducted at every 1 m depth unless obstructed by boulders/cobbles during borehole drilling. The choice of investigation method to fulfil the objectives stated in section 3.3 was made considering the equipment accessibility to the site and the limitations in time and budget. Borehole drilling and SPT were performed in coordination with Clay Engineering Consultancy Private Limited, Kathmandu, Nepal. Disturbed and undisturbed samples were also obtained during field investigation for determining their physical, mechanical and hydraulic properties in the laboratory (chapter 4).

### 3.5 Geotechnical field investigation in Kanglang landslide

#### 3.5.1 Borehole drilling

The rotary drilling method was utilised in this study as a means of advancing the borehole to conduct in-situ tests at various depths. This method is faster compared to the other methods like auger boring and wash boring and causes relatively less disturbance to the soil beneath the borehole (Craig, 2004). A portable rotary drilling rig was used to drill the boreholes, which is shown in Figure 3.3. Temporary borehole casings were also inserted in the borehole to prevent the ground from collapsing.



Figure 3.3 Photograph of rotary drilling equipment used in this study.

### 3.5.1.1 Drilling location

Two 100 mm diameter boreholes (BH-1 and BH-2) were drilled at Kanglang landslide. The location of the boreholes is shown in Figure 3.4 and Figure 3.5. BH-1 ( $27^{\circ}53'28.8''\text{N}$ ,  $85^{\circ}54'32.2''\text{E}$ , 1460 m a.s.l.) was drilled near the landslide crown to evaluate the subsoil and groundwater condition of the failed area. To obtain an approximate cross-sectional stratification across the slope before the failure, BH-2 ( $27^{\circ}53'28.95''\text{N}$ ,  $85^{\circ}54'33.42''\text{E}$ , 1440 m a.s.l.) was drilled at the toe of the landslide.



Figure 3.4 Photograph of Kanglang landslide showing the approximate location of boreholes (BH-1 and BH-2).



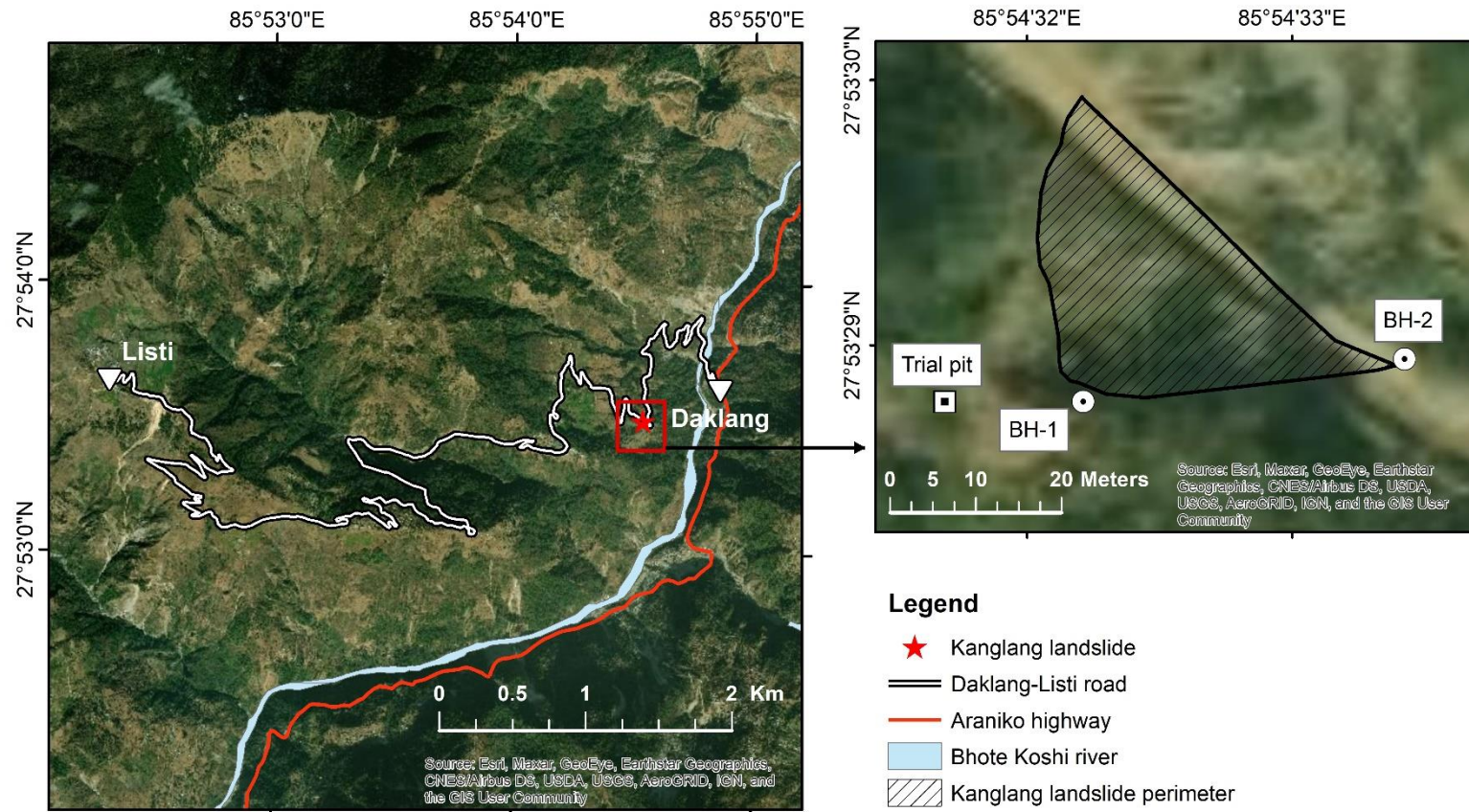


Figure 3.5 Location of Kanglang landslide in the Daklang-Listi road (left), location of trial pit and boreholes (BH-1, BH-2) (right).

### 3.5.2 Standard penetration test in BH-1

Standard penetration testing in BH-1 was conducted in accordance with BS EN ISO 22476-3 (BSI, 2005). Within BH-1, the upper 3 m of the soil was characterised as medium dense light reddish brown sandy-silty soil. At 3 m, a thin (~180 mm) layer of dark grey coarse material, perhaps a weathered cobble, was encountered (Figure 3.6). At 4 and 5 m, the colour and composition of the soil were found to be similar to that in the upper layers (0 to 2 m). However, during drilling, boulder- and cobble-sized materials were encountered at 5.8 m and 6.3 m. Because of this, standard penetration testing was not conducted at 6 m. To prevent damage to the cutting shoe of the SPT sampler by coarser materials in the borehole, the sampler was replaced by a solid 60° cone (SPT (cone)) as recommended in BS 5930: 2015 (BSI, 2015). The number of blows required for 300 mm penetration with the cone was converted to SPT N-value using the correlation proposed by Mohan et al. (1970) for fine to medium sands. According to this study, the ratio between the cone value and the SPT N-value is 1.5 for 1 to 4 m depth and is 1.75 for 4 to 9 m depth. At 7 m depth, samples were not extracted because the SPT sampler was replaced by the cone. The soil description at this depth was recorded based on the soil slurry carried to the surface by the circulating water which consisted of brownish-grey sandy soil. Moreover, the groundwater table was not encountered down to 7 m depth within BH-1 during drilling.

The recorded SPT N-values were corrected using the factors given by Skempton (1986) (energy correction  $\eta_H = 0.9$ , sampler correction  $\eta_s = 1.2$ , borehole diameter correction  $\eta_B = 1$ , rod length correction  $\eta_R = 0.75$  (up to 4 m rod length) and 0.85 (up to 4-6 m rod length)). The energy correction of 0.9 was applied considering the fact that the hammer was dropped manually for the SPT, as suggested by Skempton (1986). Additionally, the overburden pressure corrections as recommended by Liao and Whitman (1986) were applied to obtain the corrected SPT values ( $(N_1)_{60}$ ). The corrected SPT value  $(N_1)_{60}$  for BH-1 is plotted in Figure 3.7. As shown in this figure, the SPT values range from 11 to 19 (with a mean of 14), indicating the presence of medium dense soil as per Skempton (1986). Due to presence of the weathered material at 3 m (Figure 3.6), the SPT value at this depth was relatively higher (19) than in the upper layers.

As discussed in section 3.4, the SPT N-values have been used in correlations for angle of shearing resistance and elastic modulus. In this study, the empirical correlation proposed by Hatanaka and Uchida (1996) for sandy soils was adopted to estimate the angle of shearing resistance. Although there are several SPT N-value correlations for the angle of shearing resistance such as that given by Peck et al. (1974) and Bowles (1996), they do not

take into account the effect of overburden pressure or confining pressure on the SPT N-values. Hence, the correlation given by Hatanaka and Uchida (1996) for sandy soils that takes into account the effect of confining stress on the SPT N-value was adopted. Based on this correlation, the angle of shearing resistance of soil within the borehole ranges from 35° to 40° (37° on average). This agrees with the geotechnical investigation result presented by Adhikari (2001) where the author investigated a landslide in a colluvial slope that is located approximately 30 km from the study area. Interestingly, the angle of shearing resistance of the soil in BH-1 is much lower than the cut slope angle at Kanglang landslide. This suggests that some other factor such as (apparent) cohesion supported the steep cut slope, while the rainfall may have acted as a triggering factor for the failure. Furthermore, based on the empirical correlation between SPT value and elastic modulus given by Bowles (1996), the elastic modulus of the soil within BH-1 was estimated to range from 6 to 8 MPa.



Figure 3.6 180 mm thick weathered cobble extracted by the SPT sampler in BH-1 at 3 m.

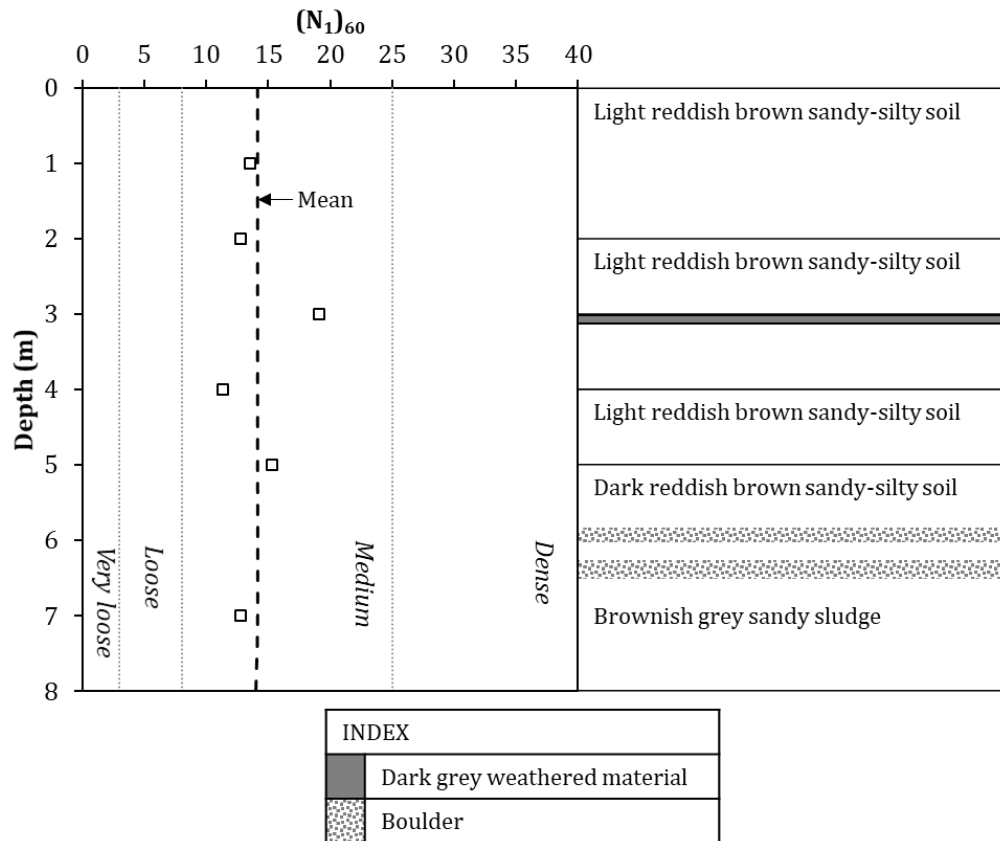


Figure 3.7 SPT  $(N_1)_{60}$  profile and material characteristics in BH-1.

### 3.5.3 Standard penetration test with 60° cone in BH-2

During the course of drilling in BH-2, several boulders, cobbles and gravels of various sizes were encountered (Figure 3.8). Hence, in BH-2, the split-spoon sampler was replaced by a solid 60° cone as recommended in BS 5930: 2015 (BSI, 2015). Due to obstructions during drilling, SPT (cone) could not be performed at regular intervals. The soil characteristics were recorded based on the soil slurry carried to the surface by the circulating water. The recorded number of blows with the solid cone was converted into SPT N-value using the empirical correlation proposed by Mohan et al. (1970). Corrections were then applied as per Skempton (1986) (energy correction  $\eta_H = 0.9$ , borehole diameter correction  $\eta_B = 1$ , rod length correction  $\eta_R = 0.75$  (up to 4 m rod length) and 0.85 (up to 4-6 m rod length)). In addition, the overburden pressure corrections given by Liao and Whitman (1986) was applied to obtain the corrected SPT values  $((N_1)_{60})$ .

The variation of  $(N_1)_{60}$  values with depth and the description of soil layers in BH-2 is shown in Figure 3.8. The upper 1 m consisted of gravelly soil, which includes the earthen material that had been deposited in-place to form carriageway for the road. Boulders were

encountered at 1 m, 2.6 m, and 3.7 m and the SPT (cone) were performed at 1.9 m, 3.2 m and 4.2 m. Below 1.9 m and 3.2 m, the soil was characterised as light brownish-grey medium dense soil as per Skempton (1986). From the SPT (cone) a high  $(N_1)_{60}$  value (34) was obtained at 4.2 m, which indicated the presence of a denser strata below this depth. Based on the empirical relationships given by Hatanaka and Uchida (1996) and Bowles (1996), the angle of shearing resistance and the elastic modulus of the soils in BH-2 range from 36 to 46° and 6 to 13 MPa respectively. Within the depth of the borehole (BH-2), the groundwater table was not encountered.

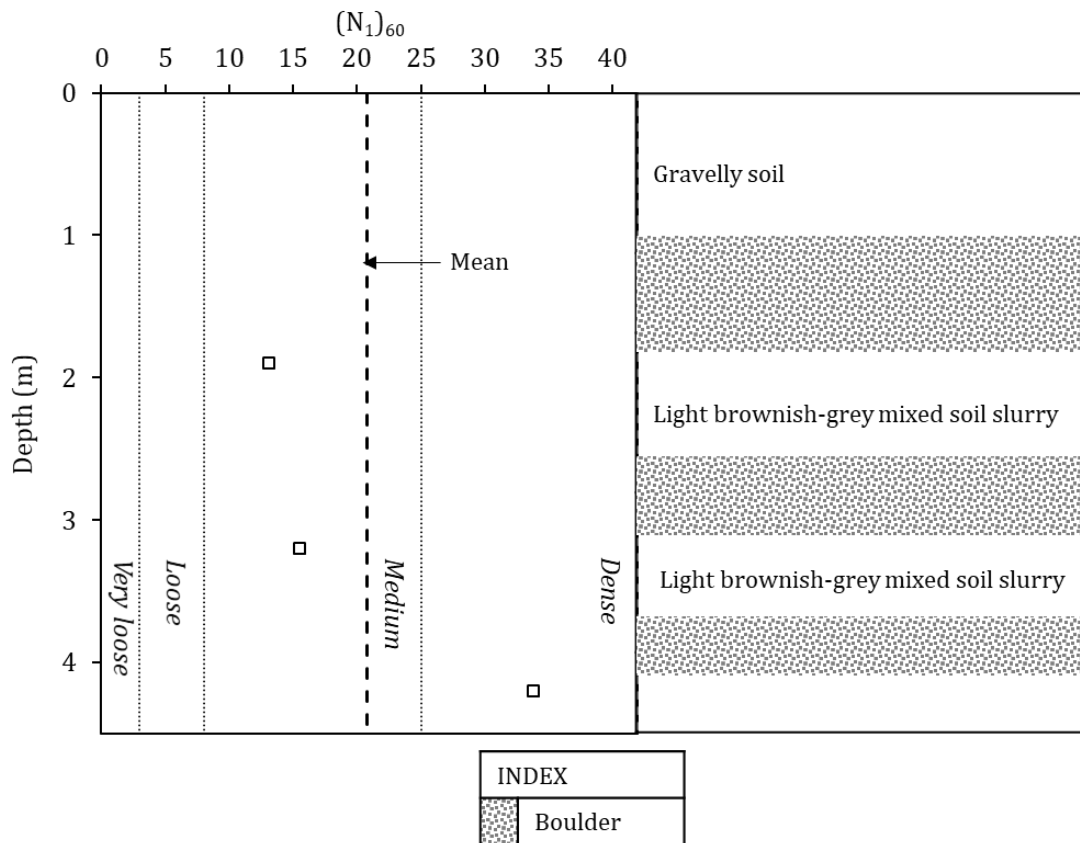


Figure 3.8 SPT  $(N_1)_{60}$  profile and material characteristics in BH-2.

### 3.5.4 Trial pit excavation

#### 3.5.4.1 Trial pit location

In this study, the purpose of trial pit excavation was two-fold. First was to log the near-surface soil conditions and collect representative soil samples and second was to install soil moisture sensors for long-term field monitoring (chapter 5). Since the location near the landslide crown appeared unstable/unsafe for the instruments, a safe location with similar



soil condition, approximately 10 m west of the landslide crown was chosen for the trial pit (27°53'28.79"N, 85°54'31.69"E, 1460 m a.s.l.) (Figure 3.5).

#### *3.5.4.2 Method of excavation and back-filling*

The trial pit (1.5 m × 1.0 m) was excavated manually using hand tools to 1.5 m depth as per BS ISO 18400-102:2017 (BSI, 2017a). After careful logging, sampling and installing instruments (chapter 5) in the trial pit, the excavated materials were reinstated as carefully as possible to the depth from which they were obtained. The backfilled soil was compacted manually in small layers to achieve the approximate density of the surrounding soils. The initial surface layer of soil was kept separate from other excavated material and was replaced on the top after backfilling.

#### *3.5.4.3 Observations from the trial pit*

Figure 3.9 shows the soil stratification exposed in the wall of the trial pit. The materials excavated from the trial pit were predominantly fine and when mixed with small amount of water, the materials exhibited dilatancy, slight grittiness and lustre, which indicated the presence of silty and sandy particles (BSI, 2018a). The topsoil (down to 0.25 m) was characterised as greyish-brown loose soil. This layer appeared different from the underlying layers, which may be due to the presence of organic materials and weathering. Beneath this layer, the soil was described as reddish-brown sandy-silty soil. Below 0.5 m, the soil was slightly wet which is why the soil below this depth appears darker than that between 0.25 and 0.5 m in Figure 3.9. This suggest that the effect of atmospheric drying was greater in the upper 0.25 m and decreased with increasing depth from the ground surface. Moreover, it is worth noting that based on the field observations, the characteristics of the samples obtained from the trial pit were similar to those obtained from the SPT sampler in BH-1 in terms of colour and composition. This observation will be further verified using particle size analysis in chapter 4.

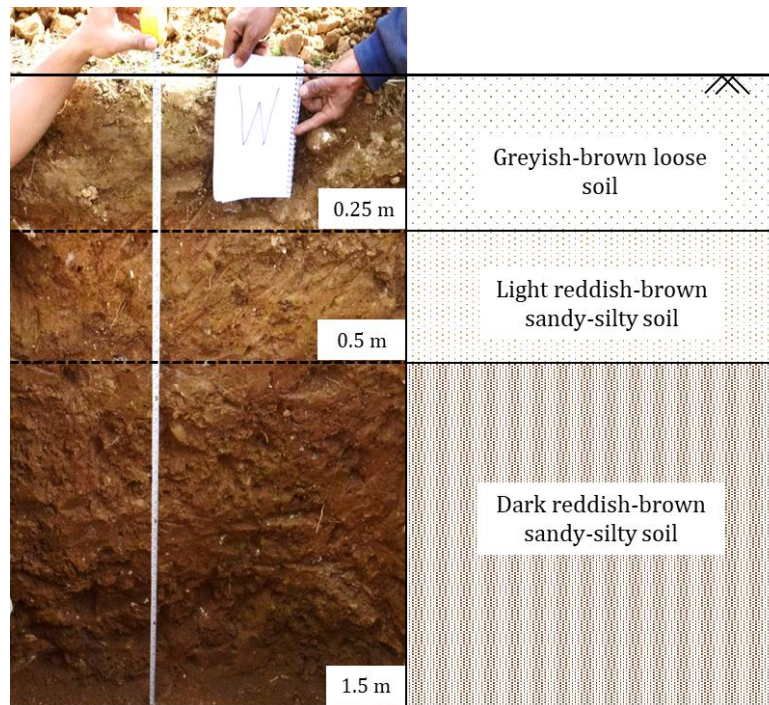


Figure 3.9 Soil stratification as observed in the trial pit.

### 3.6 Sampling, storage, and transportation of the samples

Table 3.2 presents a summary of the samples that were collected from the field. Disturbed soil samples were extracted from BH-1 using the split-spoon sampler and disturbed bag samples were obtained from the trial pit. The disturbed bag samples were used to prepare reconstituted samples for laboratory testing. Additionally, core samples were obtained using open-ended steel sampling tubes (37 to 38 mm diameter) from the bottom of the trial pit for determining the in-situ soil properties like water content, bulk density and dry density. To prevent the loss of moisture, the core samples were sealed using paraffin wax at both ends and were wrapped using plastic film as shown in Figure 3.10. This method of obtaining core samples is suitable for fine soils that do not contain gravel and possess some cohesion for the sample not to fall out (BSI, 2015). Once the samples were collected, sample labelling and handling and transportation to the laboratory in Durham University were undertaken in accordance with BS ISO 18400-105:2017 (BSI, 2017b), which provides the guidelines for preparing, preserving, and transporting samples to the laboratory so as to minimise any potential changes before examination.

Table 3.2 Summary of the soil samples obtained from the field.

Location	Depth	Type of sample
<b>BH-1</b>	1 m	Disturbed sample
	2 m	Disturbed sample
	3 m	Disturbed sample
	4 m	Disturbed sample
	5 m	Disturbed sample
<b>Trial pit</b>	0 to 0.3 m	Disturbed bag sample
	0.3 to 0.5 m	Disturbed bag sample
	0.5 to 0.75 m	Disturbed bag sample
	0.75 to 1 m	Disturbed bag sample
	0.5 m	Sealed core sample
	1 m	Sealed core sample
	1.5 m	Sealed core sample

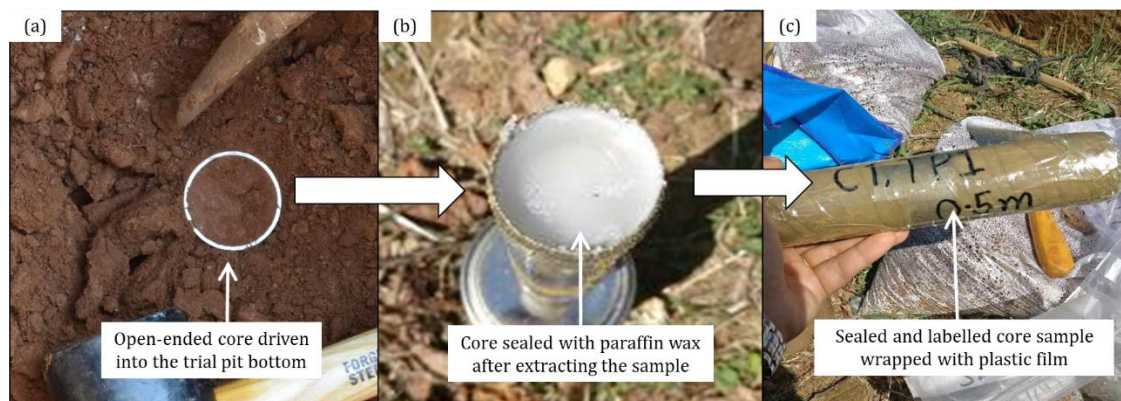


Figure 3.10 Method used for obtaining core samples (a) core inserted into the bottom of the trial pit, (b) both ends of the core sealed with paraffin wax after sampling, (c) core sample ready for transportation.

### 3.7 Chapter summary

This chapter provided information about the representative landslide site (Kanglang landslide) and the methods adopted for geotechnical investigation at this location. The key points from this chapter are summarised below:

1. The roadside cut slope at the selected landslide site was excavated at a steep angle ( $\sim 70^\circ$ ) in December 2017 to widen the Daklang-Listi road. The cut slope failed in July 2018 during the monsoon and became extended further into the hillslope which affected a larger area.
2. A combination of borehole drilling, standard penetration tests and trial pit excavation was adopted for geotechnical investigation of Kanglang landslide. The objectives of the investigation were to obtain information on the subsoil and groundwater conditions and to collect soil samples for laboratory testing.
3. Two boreholes (BH-1 and BH-2) were drilled using rotary drilling method and standard penetration tests (SPT) were performed at various depths during drilling. The standard penetration test was modified by replacing the split-spoon sampler with a  $60^\circ$  solid cone (SPT (cone)) for driving in gravelly soils as recommended in BS 5930: 2015 (BSI, 2015).
4. Corrections for the energy, sampler, rod length, borehole diameter and overburden pressure were applied to the field measured SPT N-values to obtain the standardised N-value  $(N_1)_{60}$  value.
5. The  $(N_1)_{60}$  profiles obtained from BH-1 and BH-2 show that the failed slope is underlain by a fairly uniform colluvial deposit consisting of reddish-brown medium dense sandy-silty soil with isolated boulders, cobbles and gravel.
6. The average  $(N_1)_{60}$  value of 14 in BH-1 and 20 in BH-2 correspond to the angle of shearing resistance of  $37^\circ$  and  $39^\circ$  respectively based on the empirical relationship given by Hatanaka and Uchida (1996) for sandy soils. Similarly, based on the empirical equation given by Bowles (1996), the average elastic modulus of the soils in BH-1 and BH-2 ranged from 6 MPa and 8 MPa respectively.
7. Groundwater table was not encountered in both BH-1 (down to 7 m) and BH-2 (down to 4.2 m).
8. A trial pit was manually excavated to 1.5 m depth near the failed area to evaluate the surficial soil conditions and to obtain representative soil samples for laboratory testing. In the trial pit, the colour of the upper layer (0 to 0.25 m) was found to be different than the layers below (in terms of colour and density), which may be due to the presence of organic materials and weathering in this layer. In addition, the soil below 0.5 m appeared slightly wetter than the layers above. Together, these

observations suggested that the effect of atmospheric drying decreased with increasing depth from the ground surface.

9. The colour and composition of the samples obtained from the trial pit were found to be similar to those obtained from BH-1, which will be verified further using particle size analysis (chapter 4).
10. Disturbed soil samples and core samples were obtained from the trial pit and BH-1 and were transported to the geotechnical laboratory in Durham University for testing. The core samples were sealed in the field to prevent the loss of moisture. These samples were used to determine the in-situ water content and densities in the laboratory, which will be discussed later in chapter 4.

# Chapter 4

## Determination of soil properties

### 4.1 Chapter outline

To conduct a reliable assessment of soil behaviour from the numerical models, it is crucial to select appropriate soil parameters that closely represent the in-situ subsoil conditions. This chapter hence sets out to determine the physical, mechanical, and hydraulic soil properties that are representative of the site conditions at Kanglang landslide. At the beginning of this chapter, the theoretical concepts related to the mechanical and hydraulic behaviour of soils in both saturated and unsaturated conditions are reviewed, which leads to the identification of the key properties that govern soil behaviour. For the determination of these key properties of the soil samples obtained from Kanglang landslide (chapter 3), laboratory testing was conducted. Table 4.1 presents a summary of the laboratory tests that were carried out during this study. The second part of this chapter describes the laboratory testing methodology and findings from the tests. The soil properties determined from this chapter have been used to define the material parameters in the numerical model, which will be discussed further in chapter 6.

Table 4.1 Summary of the soil properties obtained from laboratory testing.

<b>Soil properties</b>	
<b>Physical properties</b>	Particle size distribution
	Atterberg limits
	In-situ water content and bulk density
	Particle density
	Dry density, void ratio, saturated density, porosity
<b>Mechanical properties</b>	Shear strength parameters
<b>Hydraulic properties</b>	Soil-water retention curve
	Saturated permeability

## 4.2 Theoretical concepts

### 4.2.1 Mechanical behaviour of saturated soils

The mechanical behaviour of saturated soils- the shear strength characteristics and the volume change process are governed by one stress state variable: effective stress (Equation 4.1). Any change in the effective stress caused by changes in total stress and/or pore water pressure leads to alteration of the equilibrium state of saturated soils (Terzaghi, 1936). By combining the effective stress formulation with the Mohr-Coulomb failure criterion, the shear strength of the saturated soils can be obtained (Equation 4.2).

$$\sigma' = \sigma - u_w \quad (4.1)$$

$$\tau = c' + \sigma' \tan \phi' \quad (4.2)$$

Where

$\sigma'$  = normal effective stress

$\sigma$  = normal total stress

$u_w$  = pore water pressure

$\tau$  = shear strength

$c'$  = effective cohesion

$\phi'$  = effective angle of shearing resistance (peak, residual or critical state)

#### 4.2.1.1 Critical state framework for saturated soils

The critical state framework can be used to explain the stress-strain and volume change behaviour of saturated soils. This framework is based on the understanding that any soil when sheared continuously after reaching the peak will ultimately attain a critical state irrespective of its initial condition (Schofield and Wroth, 1968). At the critical state, the soils will have undergone large deformations, such that the soil has lost its initial structure. After the critical state condition is attained, with a further increment of shear deformation, the void ratio or the effective stresses of the soil remains constant, as shown by Equation 4.3 (Schofield and Wroth, 1968). The critical state can be defined using the critical state line (CSL), which can be plotted in  $q - p'$  space and  $v - p'$  space as shown in Figure 4.1 and Figure 4.2 respectively. From the two-dimensional plots, the critical state line can be defined by Equations 4.8 and 4.9.



$$\frac{\partial p'}{\partial \varepsilon_q} = \frac{\partial q}{\partial \varepsilon_q} = \frac{\partial v}{\partial \varepsilon_q} \quad (4.3)$$

Where  $p'$ ,  $q$  and  $v$  are the three state variables that are used to define the critical state which are given as:

$$p' = \frac{\sigma_1 + \sigma_2 + \sigma_3}{3} - u_w = p - u_w \quad (4.4)$$

$$q = \sigma_1 - \sigma_3 = \sigma_1' - \sigma_3' \quad (4.5)$$

$$v = 1 + e \quad (4.6)$$

Where

$p'$  = mean effective stress

$p$  = mean total stress

$q$  = deviator stress

$\varepsilon_q$  = shear strain

$\sigma_1$ ,  $\sigma_2$  and  $\sigma_3$  = principal stresses

$\sigma_1'$ ,  $\sigma_2'$  and  $\sigma_3'$  = principal effective stresses

$v$  = specific volume

$e$  = void ratio

Under the triaxial test conditions where  $\sigma_2'$  and  $\sigma_3'$  are equal, Equation 4.2 becomes:

$$p' = \frac{\sigma_1 + 2\sigma_3}{3} - u_w = p - u_w \quad (4.7)$$

$$q = M p' \quad (4.8)$$

$$v = \Gamma - \lambda \ln p' \quad (4.9)$$

Where

$M$  = slope of the critical state line in  $q - p'$  plot

$\Gamma$  = intercept of the critical state line in the  $v - p'$  plot

$\lambda$  = slope of the critical state line on the  $v - p'$  plot

From the slope of the  $q-p'$  plot ( $M$ ), the critical state angle of shearing resistance ( $\phi'_{cs}$ ) of soil is determined using Equation 4.10.

$$M = \frac{6 \sin \phi'_{cs}}{3 - \sin \phi'_{cs}} \quad (4.10)$$

Where

$\phi'_{cs}$  = critical state angle of shearing resistance of soil

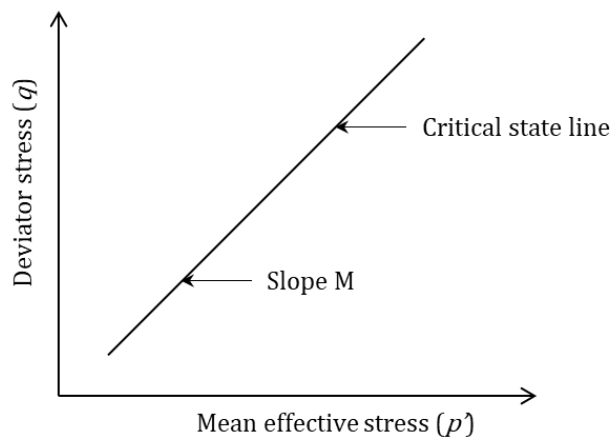


Figure 4.1 Critical state defined in the deviator stress versus mean effective stress plane.

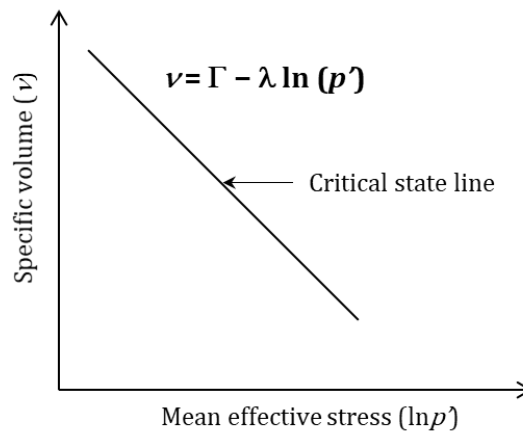


Figure 4.2 Critical state defined in the specific volume versus mean effective stress plane.

In this study, triaxial compression tests were conducted to evaluate the mechanical behaviour of the saturated soil. From these tests, the effective stress-strain behaviour, the

development of pore water pressure and the critical state parameters were evaluated. Further discussions on the test procedure are presented later in this chapter.

#### 4.2.2 Hydraulic behaviour of saturated soils

The hydraulic behaviour of saturated soils is governed by Darcy's law which is written as Equation 4.11. The key parameter here, the coefficient of permeability (hydraulic conductivity) determines the ability of soil to conduct water through its macropores and is a function of void ratio (and effective stress level) (Lambe and Whitman, 1969).

The coefficient of permeability of saturated soils is commonly determined in the laboratory using various methods such as falling head and constant head tests by controlling and measuring the one-dimensional water flow through a sample (BSI, 2019). This parameter can also be estimated using empirical relationships with the particle size distribution such as that given by Hazen (1892), Taylor (1948) and Chapuis (2004) or using field-based in-situ tests like borehole tests and infiltrometer tests (BSI, 2012a, 2012b). In this study, the saturated coefficient of permeability was estimated using triaxial constant head permeability tests (section 4.6). This method is suitable for soils of low to intermediate permeability like clay and silts (BSI, 1990).

$$q_{flow} = -ki \quad (4.11)$$

Where

$q_{flow}$  = flow rate of water

$k$  = coefficient of permeability or hydraulic conductivity of soil

$i$  = hydraulic gradient

#### 4.2.3 Mechanical behaviour of unsaturated soils

In the unsaturated or vadose zone, the water phase is held by soil suction. Hence, when considering the mechanical behaviour of an initially unsaturated soil slope subjected to rainfall, it is essential to incorporate the effects of soil suction. The soil suction consists of matric suction and osmotic suction (Krahn and Fredlund, 1971). The matric suction is associated with the capillarity and adsorption forces at the interfaces (menisci) between air and water (Fredlund and Rahardjo, 1993; Lu and Likos, 2004). It is affected by the particle and the pore size distribution in soils. On the other hand, the osmotic suction is related to

the presence of solutes, generally salt in the pore water (Barbour and Fredlund, 1989). In the stability analysis of unsaturated soil slopes under rainfall, the matric suction component is considered to be of most importance (Fredlund and Rahardjo, 1993).

One of the earliest constitutive equations defining the mechanical behaviour of unsaturated soils was proposed by Bishop (1959), referred to as Bishop's effective stress equation (Equation 4.12). This equation is an extension of Terzaghi's effective stress concept (Equation 4.1), with an additional term  $u_a$  for the pore air pressure. Based on this equation, the mechanical behaviour of unsaturated soils can be defined using two stress state variables: the net normal stress  $(\sigma - u_a)$  and matric suction  $(u_a - u_w)$  as shown in Equation 4.12. Combining Equation 4.12 with the Mohr-Coulomb failure criterion, the shear strength of unsaturated soil can be expressed as Equation 4.13.

$$\sigma' = (\sigma - u_a) + \chi(u_a - u_w) \quad (4.12)$$

$$\tau = c' + (\sigma - u_a) \tan \phi' + \chi(u_a - u_w) \tan \phi' \quad (4.13)$$

Where

$(u_a - u_w)$  = matric suction, which is the difference between pore air pressure ( $u_a$ ) and pore water pressure ( $u_w$ )

$\chi$  = Bishop's effective stress parameter originally related to the degree of saturation

The parameter  $\chi$  can be simply put as a scaling parameter, which determines the contribution of matric suction to the shear strength of unsaturated soils. There have been several attempts to estimate the equivalent of  $\chi$  for the shear strength of unsaturated soils, which have been reviewed by Leong (2019). One of the earliest studies by Bishop and Blight (1963) explored  $\chi$  as a function of the degree of saturation. Under this consideration, Bishop's effective stress converges to Terzaghi's effective stress when the soil is saturated. It is certainly logical to relate  $\chi$  to a volumetric parameter of soil such as degree of saturation because the matric suction is directly related to the volume of water present in the soil voids. Various experimental studies have also shown that  $\chi$  can be replaced by the degree of saturation or effective degree of saturation (Vanapalli et al., 1996; Öberg and Sällfors, 1997; Alonso et al., 2010; Casini et al., 2011). However, other studies have questioned the use of a soil parameter (degree of saturation) to define the stress state of the unsaturated soils (Jennings and Burland, 1962; Fredlund et al., 1978; Khalili and Khabbaz, 1998). Fredlund et al. (1978) proposed an extended Mohr-Coulomb criterion to formulate the

shear strength of unsaturated soils using two independent stress state variables (Equation 4.14).

$$\tau = c' + (\sigma - u_a) \tan \phi' + (u_a - u_w) \tan \phi^b \quad (4.14)$$

Where

$\phi'$  = effective angle of shearing resistance of soil with respect to the changes in normal stress  $(\sigma - u_a)$

$\phi^b$  = angle of shearing resistance of soil with respect to suction  $(u_a - u_w)$

Nonetheless, conducting laboratory tests to obtain the unsaturated soil strength properties may not be feasible in all conditions. As an alternative, Vanapalli et al. (1996) proposed empirical equations to obtain the shear strength of unsaturated soils (Equations 4.15 and 4.16). These equations combine the shear strength properties of the saturated soils and the effective degree of saturation ( $S_e$ ) or the effective or normalised volumetric water content ( $\theta_e$ ), which can be obtained from the soil-water retention curve (SWRC) (section 4.2.4.1).

The same concept is utilised in PLAXIS for fully coupled flow-deformation problems, which is elaborated later in chapter 6. In such analyses, the pore air pressure is considered negligible and the effective stress parameter  $\chi$  is substituted by the effective degree of saturation (Galavi et al., 2009; Galavi, 2010). It is recognised here that the simple concept of using a single stress variable for unsaturated soil may not be suitable for all degrees of saturation. However, in the modelling of rainfall-induced landslides, the degrees of saturation are naturally high, and the air phase is discontinuous. In such conditions, Bishop's effective stress concept can provide a realistic prediction of the unsaturated soil behaviour (Toll et al., 2019). Toll (2020) also showed that the Bishop's effective stress concept is valid for clayey soils when the degree of saturation is 75% or greater, although may be questionable when the degree of saturation is lower. Hence, in this study, the effective shear strength parameters of saturated soil and soil-water retention curves were determined to model the behaviour of unsaturated soils.

$$\tau = c' + (\sigma - u_a) \cdot \tan \phi' + \theta_e \cdot (u_a - u_w) \cdot \tan \phi' \quad (4.15)$$

$$\tau = c' + (\sigma - u_a) \cdot \tan \phi' + S_e \cdot (u_a - u_w) \cdot \tan \phi' \quad (4.16)$$

Where

$$\theta_e = \left( \frac{\theta - \theta_r}{\theta_s - \theta_r} \right) \text{ and } S_e = \left( \frac{S - S_r}{100 - S_r} \right)$$

$\theta$  and  $S$  = volumetric water content and degree of saturation

$\theta_r$  and  $S_r$  = residual volumetric water content and residual degree of saturation

$\theta_s$  and  $S_s$  = volumetric water content at full saturation and saturated degree of saturation

#### 4.2.4 Hydraulic behaviour of unsaturated soils

Darcy's law which governs the flow of water in saturated soil also applies in unsaturated condition (Buckingham, 1907; Lorenzo Adolph Richards, 1931; Childs and Collis-George, 1950). However, in unsaturated soil, the soil permeability depends not only on the void ratio but also on the water content (or the matric suction) (Fredlund and Rahardjo, 1993). Water can be visualised as flowing through a web of inter-connected, continuous conduits (pore spaces) in soil (Fredlund and Rahardjo, 1993). During desaturation, as the air gradually replaces the water, the water phase becomes discontinuous. This causes an increased tortuosity to the flow path that increases further with the increase in suction. Ultimately, it causes a decrease in the ability of soil to conduct water (Childs, 1969). Hence, the percentage of water-filled voids is an important factor that affects the permeability and ultimately, the hydraulic behaviour of unsaturated soils.

This understanding brings us to the three main hydraulic properties of unsaturated soil: water content, suction and permeability. These properties are inter-related and together, they govern the hydraulic behaviour of unsaturated soils. The relationship between water content and suction is described using the soil-water retention curve and that between water content (or suction) and permeability is defined using the unsaturated permeability function. These inter-relationships are discussed in the following sub-sections.

##### 4.2.4.1 Soil-water retention curve (SWRC)

The soil-water retention curve also known as the soil-water characteristic curve (SWCC) is the graphical expression of the relationship between soil suction and water content. In the SWRC, the soil suction may be expressed as total suction or matric suction and the soil water content may be expressed as gravimetric water content, volumetric water content or degree of saturation. The relationship between gravimetric water content, volumetric water content or degree of saturation are shown in Equation 4.17. To take into account the combined effect of the changes in void ratio and water content, the SWRC is often plotted using a volumetric unit of water content like the degree of saturation or

volumetric water content. Nonetheless, all the expressions of SWRC tell us about the capacity of soil to retain water as the water content changes when subjected to different values of suction during drying and wetting (Vanapalli et al., 1999). The determination of the soil-water retention curve is crucial when dealing with unsaturated soils. It is not only because it provides an understanding of the relationship between suction and water content, but also because it can be used to estimate other important unsaturated soil properties like shear strength (section 4.2.3) and permeability function (van Genuchten, 1980; Fredlund and Xing, 1994; Vanapalli et al., 1996) (section 4.2.4.2), without conducting rather difficult and time-consuming unsaturated testing.

$$\theta = \frac{W \cdot \rho_{dry}}{\rho_{water}} = S \cdot n = \frac{S \cdot e}{1 + e} = \frac{w \cdot G_s}{1 + e} \quad (4.17)$$

Where

$\theta$  = volumetric water content

$W$  = gravimetric water content

$\rho_{dry}$  = dry density of soil

$\rho_{water}$  = density of water

$S$  = degree of saturation

$n$  = porosity

$e$  = void ratio

$G_s$  = specific gravity

- Nature of the soil-water retention curve

The shape of the soil-water retention curve can be influenced by several factors such as soil type, soil texture, mineralogy, soil structure, compaction method, initial water content and stress history (Vanapalli et al., 1999). In general, the texture of the soils- fine or coarse influences the shape and range of the SWRC (Melgarejo Corredor, 2004). A typical sigmoidal (S-shaped) SWRC constituting three identifiable states i) boundary effect stage, ii) transition stage, and iii) residual stage has been shown by Vanapalli et al. (1999). In the boundary effect stage, the soil is in a saturated condition. The magnitude of suction at this stage is not sufficient to drain the pores and as a result, the initial increase in suction causes negligible changes in the degree of saturation (Blight, 1967). The end of the boundary effect stage is marked by the air-entry value (AEV), which is the suction at which air enters the largest pores of the soil. When the AEV is exceeded, water in the voids starts to be replaced



by air. This marks the transition zone, where the soil starts to de-saturate significantly leading to an increase in suction. At the end of the transition stage, the soil enters the residual zone beyond which it becomes increasingly difficult to remove water from the soil. Consequently, even large increases in suction lead to an only small change in water content. After the residual water content is reached, any changes in the matric suction will not have a significant contribution towards the increase in the shear strength of soil (Vanapalli et al., 1996).

In Figure 4.3, two complete SWRCs representing the primary drying and the primary wetting curve are shown where the saturated volumetric water content of the wetting curve is lower than the starting water content of the drying curve and the soil has a higher suction during drying than during wetting for the same amount of water content. This is a fundamental characteristic of the SWRC known as the hydraulic hysteresis. The hysteretic behaviour can result from several factors such as the non-uniform geometry of the pores (the 'ink-bottle' effect), different liquid-solid contact angles for advancing and receding water meniscus and entrapped air and volume change (swelling and shrinking) during wetting and drying (Hillel, 1998). If a partially dried soil starts to wet, the soil follows the intermediate curve called the scanning curve until the primary wetting curve is reached. Similarly, if a partially wetted soil starts to dry, the soil follows the scanning curves. In this manner, primary drying and wetting curves are considered to define an envelope within which soil exists (Toll, 2012). In the natural environment, soils undergo continuous wetting and drying without reaching fully dried or fully saturated conditions. Thus, the scanning curves are likely to be representative of the actual in-situ soil behaviour (Hillel, 1998).

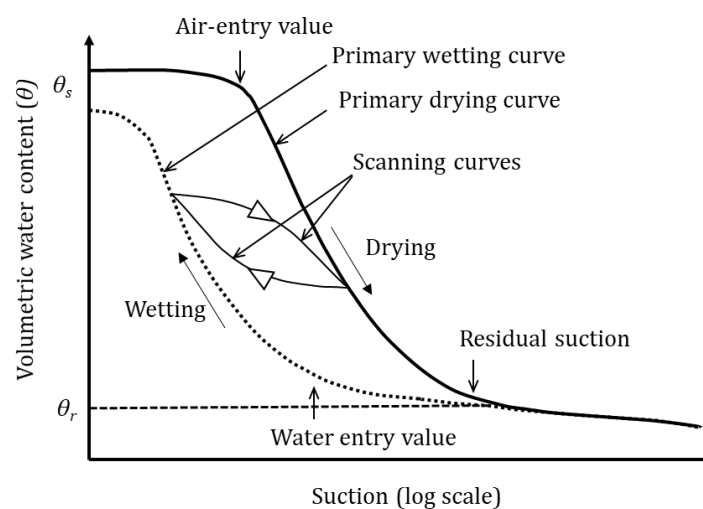


Figure 4.3 Typical soil-water retention curve showing hydraulic hysteresis during drying and wetting. Modified after Toll (2012, chap. 4).

- Suction measurement techniques

To obtain the soil-water retention curve, it is necessary to select a suitable technique for suction measurement. The selection of a suitable technique generally depends on the range of suctions that is expected in the laboratory or the field. To cover an entire range of suction that may be encountered, sometimes a combination of different techniques may also be used (Boso et al., 2006; Pan et al., 2010).

Table 4.2 presents a summary of the various suction measurement techniques and their approximate ranges. The tensiometer provides a direct measurement of matric suction, whereas psychrometers and filter paper methods provide indirect measurements of suction using calibration with other properties like relative humidity and soil moisture (Vanapalli et al., 2002). Since the tensiometer measures suction directly, the errors related to calibration can be avoided, which may be inevitable in the indirect methods. Additionally, the tensiometers are portable and have a faster response than other indirect methods (Toll et al., 2013).

Considering the aforementioned advantages, the high-capacity tensiometer developed at Durham University (Lourenço et al., 2006; Toll et al., 2013) (Figure 4.4) was used in this study to measure soil suction in the laboratory. This tensiometer has been reported to be capable of measuring suctions up to 2 MPa (Lourenço et al., 2008). It consists of a porous ceramic disc with high air-entry value ( $\sim 1.5$  MPa), behind which there is a small reservoir of water followed by a ceramic transducer. When the tensiometer is placed in contact with a soil sample, the water in the porous disc starts to equilibrate with the pore water pressure in the soil. After equilibration, the pore water pressure is transmitted to the pressure transducer for measurement of suction (Lourenço et al., 2008).

Table 4.2 Suction component and suction range for different suction measurement methods. Modified after Mendes (2011).

<b>Suction component</b>	<b>Method</b>	<b>Suction range (kPa)</b>
<b>Total Suction</b>	Thermocouple psychrometer	300 - 7000
	Transistor psychrometer	100 - 18000
	Non-contact filter paper	400 - 30000
<b>Matric Suction</b>	Contact filter paper	30 - 30000
	Pressure plate	0 - 1500
	Tensiometer	0 - 1600

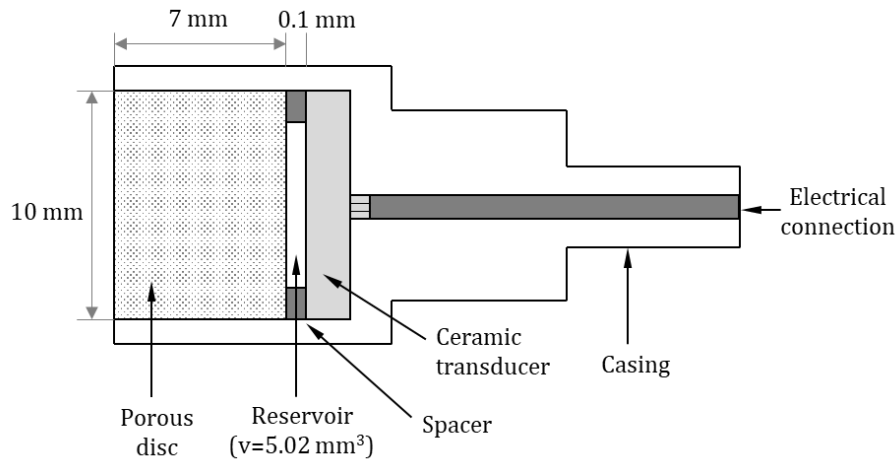


Figure 4.4 Components of the Durham University high suction tensiometer (not to scale). Modified after Lourenço et al. (2008).

- Soil-water retention curve with the high-capacity tensiometer

The technique of obtaining the soil-water retention curve using high-capacity tensiometer can be employed in two ways: discrete (staged) method and continuous method (Toll et al., 2013). In the discrete method, the sample is dried (or wetted) in stages and is allowed to equalise after each period of drying (or wetting). After equalisation, suction is measured at constant water content and volumetric measurements of the sample are made. In contrast, in the continuous method, the sample and the tensiometer are placed on a balance allowing continuous measurement of the suction and the sample mass (Lourenço et al., 2007).

In the study conducted by Lourenço et al. (2007), the two methods (discrete and continuous) were compared, which showed that the soil-water retention curves obtained by continuous drying showed higher suction than that obtained by discrete drying at the same water content. The absence of suction equalisation stage during continuous drying was considered to be the reason for the discrepancy (Lourenço et al., 2007). On the other hand, some studies have reported that similar results can be obtained from both staged and continuous methods (Boso et al., 2006; Osinski et al., 2016). Nonetheless, experimental errors related to the measurement of sample mass, volume and suction can occur in either method. That said, ambient conditions around the test set-up to minimise the effects of evaporation and careful measurements of sample mass and volume can refine the accuracy of the soil-water retention curves. In this study, the soil-water retention curve was determined using the discrete procedure with the high-capacity tensiometer (section 4.5).

- Empirical equations for soil-water retention curve

For obtaining a soil-water retention curve, several measurements of suction, water content and volume changes may be necessary in the laboratory. To fit the discrete laboratory measurements to obtain a continuous soil-water retention curve, several empirical equations have been proposed, some of which are shown in Table 4.3. The empirical equations of SWRC in Table 4.3 are expressed in terms of normalised water content and have either two or three fitting parameters with one describing the air-entry value of the soil. The van Genuchten (1980) model (Equation 4.20) is one of the most commonly used SWRC equations (Fredlund et al., 2011). The three fitting parameters present in this equation are reduced to two using a fixed relationship between  $m$  and  $n$  ( $m=1-1/n$ ) based on Mualem (1976). In PLAXIS, this model is used to describe the hydraulic behaviour of unsaturated soils (Galavi, 2010). Hence, in this study, the experimental data points obtained for SWRC measurement were fitted to the van Genuchten (1980) model (section 4.5.3).

Table 4.3 Empirical equations for the soil-water retention curves.

Reference	Equation	Description
Gardner (1958)	$\Theta = \frac{1}{1 + \left(\frac{\psi}{\alpha}\right)^n}$	$\psi$ = matric suction $\alpha$ = fitting parameter dependent on AEV $n$ = fitting parameter dependent on the rate of soil drainage
(Brooks and Corey, 1964)	$\Theta = \left(\frac{\psi_b}{\psi}\right)^\eta$	$\psi_b$ = AEV or bubbling pressure $\eta$ = index number of pore size distribution
(van Genuchten, 1980)	$\Theta = \frac{1}{\left[1 + (\alpha \cdot \psi)^n\right]^m}$	$\psi$ = matric suction $\alpha$ = fitting parameter dependent on AEV $n$ = fitting parameter dependent on the rate of soil drainage $m$ = fitting parameter dependent on residual water content = $1 - \frac{1}{n}$
(Fredlund and Xing, 1994)	$\Theta = C(\psi) \frac{\theta_s}{\left\{ \ln \left[ e + \left(\frac{\psi}{\alpha}\right)^n \right] \right\}^m}$ $C(\psi) = \left[ 1 - \frac{\ln \left( 1 + \frac{\psi}{\psi_r} \right)}{\ln \left( 1 + \frac{1000000}{\psi_r} \right)} \right]$	$\psi$ = matric suction $\alpha$ = fitting parameter dependent on AEV $m = 3.67 \ln \left( \frac{\theta_s}{\theta_i} \right)$ $n = \frac{1.31^{m+1}}{m\theta_i} 3.72 \times s \times \psi_i$ $\psi_i$ = matric suction at the inflection point $\psi_r$ = matric suction at residual water content $s$ = slope of the line tangent to the function that passes through the inflection point

$$\Theta = \text{normalised volumetric water content} = \frac{\theta - \theta_r}{\theta_s - \theta_r}$$

#### 4.2.4.2 Unsaturated permeability function

The unsaturated permeability function describes the variation of soil permeability with changes in the void ratio and water content (or degree of saturation). Determination of the unsaturated soil permeability in the laboratory is considered difficult, expensive, and time-consuming (van Genuchten, 1980; Lam et al., 1987; Leong and Rahardjo, 1997; Toll et al., 2014). Alternatively, the permeability of unsaturated soil is commonly estimated using indirect methods. There are three indirect methods for determining the permeability function which include empirical models, macroscopic models, and statistical models (Leong and Rahardjo, 1997).

The empirical models are based on the recognition that there is a relationship between the characteristics of the soil-water retention curve and the permeability function. Several empirical equations have been developed in which the permeability function for unsaturated soils is estimated as a function of saturated permeability and volumetric water content or as a function of saturated permeability and matric suction as reviewed by Leong and Rahardjo (1997). However, this method has been found to be less suitable for problems involving a wide range of change of degree of saturation (Md. Rahim, 2016). On the other hand, the macroscopic models are used to develop analytical expression for the unsaturated permeability function (Mualem, 1986). These models assume that laminar flow at the microscopic level is comparable to the flow in the porous medium (macroscopic level) (Leong and Rahardjo, 1997). Based on this assumption, the microscopic flow behaviour is related to the macroscopic variables of average flow velocity, hydraulic gradient and permeability (Leong and Rahardjo, 1997). All macroscopic models relate the unsaturated permeability function to the degree of saturation of the soils. However, this model is criticised for disregarding the effect of the pore-size distribution of the soils (Brooks and Corey, 1964).

The most rigorous and popular models for predicting the unsaturated permeability function are the statistical models. The statistical models are based on the understanding that the soil-water retention curve, as well as the permeability function, are primarily determined by the pore-size distribution of the soil (Fredlund et al., 1994). In the statistical models, the unsaturated permeability is determined using the SWRC parameters and the saturated coefficient of permeability. The commonly used model developed by van Genuchten (1980) is given in Equation 4.22 and 4.23. In this model, the saturated permeability is used in

combination with the SWRC fitting parameters to obtain the unsaturated permeability at different values of suction. This model is also adopted in PLAXIS to describe the permeability of unsaturated soils. Nonetheless, it should be noted here that there may be errors related to SWRC determination in the laboratory, which can potentially lead to discrepancies in the unsaturated permeability function. Toll et al. (2019) have suggested that the permeability function may require experimental validation to prevent major discrepancies.

$$k_r = \Theta^{0.5} \left[ 1 - (1 - \Theta^{1/m})^m \right]^2 \quad (4.22)$$

$$k_{unsat} = k_{sat} \cdot k_r = k_{sat} \cdot \Theta^{0.5} \left[ 1 - (1 - \Theta^{1/m})^m \right]^2 \quad (4.23)$$

Combining Equation 4.22 with Equation 4.20, the unsaturated permeability can be expressed in terms of pressure head (Equation 4.24):

$$k_{unsat} = k_{sat} \cdot k_r = k_{sat} \cdot \frac{\left[ 1 - (\alpha \cdot \psi^{(n-1)}) (1 + (\alpha \cdot \psi^n)^{-m}) \right]^2}{\left[ 1 + (\alpha \cdot \psi^n) \right]^{m/2}} \quad (4.24)$$

Where

$k_r$  = relative coefficient of permeability

$\Theta$  = normalised volumetric water content

$k_{unsat}$  = coefficient of permeability as a function of volumetric water content

$k_{sat}$  = saturated coefficient of permeability

$\psi$  = matric suction

$\alpha, n$  and  $m$  = SWRC curve fitting parameters;  $m = 1 - (1/n)$



## 4.3 Determination of physical soil properties

In this section, the laboratory tests conducted to determine the physical properties of the soil samples obtained from Kanglang landslide are discussed. Firstly, the laboratory techniques are described briefly which is followed by the summary of the test results.

### 4.3.1 Laboratory techniques

#### 4.3.1.1 Particle size distribution test

Mechanical sieving and sedimentation are conventional methods for particle size analysis. However, in recent years, the laser diffraction method is increasingly being used (Fisher et al., 2017). The laser diffraction method works on the principle that the particles of different size diffract light through different angles; the angle of diffraction being inversely proportional to the size of the particle. The intensity of the diffracted beam at any angle hence corresponds to the number of particles with a specific cross-sectional area in its optical path (Di Stefano et al., 2010).

Some studies have argued that the laser diffraction method can underestimate the clay fraction due to the irregular shape of the soil particles as opposed to the assumption that they are perfectly spherical (Loizeau et al., 1994; Blott et al., 2004; Di Stefano et al., 2010). However, the assumption of particle sphericity is also a known source of error in the conventional sedimentation method, which can lead to overestimation of the fine silt and clay fractions (Blott et al., 2004). In addition, the method of calibration of sieves can also affect the results of traditional sieve analysis (Konert and Vandenberghe, 1997). This shows that both the traditional sieve-sedimentation method and the laser diffraction methods have potential sources of error and no one method is superior to the other. Nonetheless, the laser diffraction method is a non-destructive method which is much quicker and requires less sample than the traditional method and has shown to provide reliable and reproducible results (Blott et al., 2004; Fisher et al., 2017). Hence, in this study, particle size analysis was conducted using the commercial laser diffraction particle size analyser (LS 13 320) with a measurement range from 0.04  $\mu\text{m}$  to 2 mm (Figure 4.5).



Figure 4.5 Laser diffraction particle size analyser (LS 13 320).

#### 4.3.1.2 Atterberg limits

The Atterberg limit tests are performed to predict the water content range over which the soil exhibits plastic behaviour for their identification and comparison (Terzaghi et al., 1996). As recommended by BS EN ISO 17892-12:2018 (BSI, 2018b), the liquid limits of the soil samples were obtained using the fall cone method, which is known to provide results with better repeatability. Similarly, the plastic limits were determined using the rolling thread method as recommended in BS EN ISO 17892-12:2018 (BSI, 2018b).

#### 4.3.1.3 Particle density

The particle density of soil is related to the mineralogy or chemical composition of the soil. Determination of this parameter is required to obtain key soil properties, notably void ratio, degree of saturation and dry density. In this study, the gas pycnometer method (Figure 4.6) was used to measure the particle density of the soil samples. This method uses a non-destructive gas displacement technique to measure the volume of the soil solids. Compared to the commonly used liquid pycnometers, this method is quicker and eliminates the problem associated with air entrapment.



Figure 4.6 Accupyc II 1340 gas pycnometer.

#### 4.3.1.4 In-situ soil properties

To determine the in-situ water content and bulk density, the sealed core samples obtained from the trial pit located near Kanglang landslide (chapter 3) were extruded in the laboratory (Figure 4.7). The measured in-situ water content and bulk density in combination with the particle density (section 4.3.1.3) were then used to obtain the other in-situ soil properties like dry density, void ratio, porosity and degree of saturation using the standard weight-volume relationships. The reconstituted samples for the triaxial, permeability and SWRC tests were prepared based on the estimated in-situ dry density.



Figure 4.7 (a) Sample core obtained from the field, (b) sample extruded from the core.

The aforementioned tests for physical soil properties which consist of particle size distributions, Atterberg limits, particle densities and in-situ soil properties were conducted following the standard procedures outlined in the British Standards as shown in Table 4.4.

Table 4.4 Summary of the laboratory tests for physical soil properties.

<b>Physical properties</b>	<b>Method</b>	<b>British standard</b>
Particle size distribution	Laser diffraction method	BS EN ISO 17892-4
Atterberg limits	Fall cone and rolling thread methods	BS EN ISO 17892-12
Particle density	Gas pycnometer method	BS 1377-2 (BS EN ISO 17892-3)
Water content, bulk density, dry density, void ratio, saturated density and porosity	Weight-volume relationships	BS EN ISO 17892-1, BS EN ISO 17892-2

### 4.3.2 Summary of index properties

#### 4.3.2.1 Particle size distribution

The particle size distributions of the samples obtained from the trial pit are summarised in Table 4.5 and Figure 4.8. In all tested samples down to 1.5 m of depth, the clay content was found to be low (<12%) and silt-sized particles dominated the distribution. As shown in Table 4.5, the percentage of fine materials was greater than 35% in all tested samples, which classifies them as fine soils as per BS 5930:2015 (BSI, 2015). Based on the particle size distribution, the soil samples were classified as Sandy SILT or SILT.

Furthermore, the particle size distribution of the samples obtained from the borehole (BH-1), which was drilled near the crown of Kanglang landslide is shown in Table 4.6 and Figure 4.9. Similar to the samples obtained from the trial pit, the borehole samples contained low clay content (<8%) with higher percentages of silt-sized particles (43 to 70%). Based on the particle size distributions, the soil samples down to 5.45 m were classified as SILT or sandy SILT. An exception to this is the sample obtained from 3 to 3.3 m, which represents the weathered boulder encountered during borehole drilling (Figure 3.6). Below 5.7 m, the samples were found to contain relatively higher sand fraction (67 to 71%) which classifies them as Very Silty SAND (BSI, 2015).

It is worth noting here that the particle size distributions of the trial pit samples K4 obtained from 0.75 to 1 m depth and core sample K6 obtained from 1 m depth are similar to that obtained from shallow depth (0 to 1.45 m) within the borehole (BH-1) (B1 to B4), which are

shown in Figure 4.10. Based on the particle size distributions, it can be said that the samples obtained from the trial pit were representative of the soil near the failed area of Kanglang landslide.

Table 4.5 Particle size distribution of samples obtained from the trial pit.

Depth (m)	ID	% < Volume				Soil description	Remarks
		Clay	Silt	Sand	Fines		
0 - 0.3	K1	7	46	47	53	Sandy SILT	Bag sample
0.3 - 0.5	K2	9	57	34	66	SILT	Bag sample
0.5 - 0.75	K3	12	62	26	74	SILT	Bag sample
0.75 - 1	K4	7	56	37	63	Sandy SILT	Bag sample
0.5	K5	12	63	25	75	SILT	Core sample
1.0	K6	8	60	32	68	SILT	Core sample
1.5	K7	8	54	38	62	Sandy SILT	Core sample

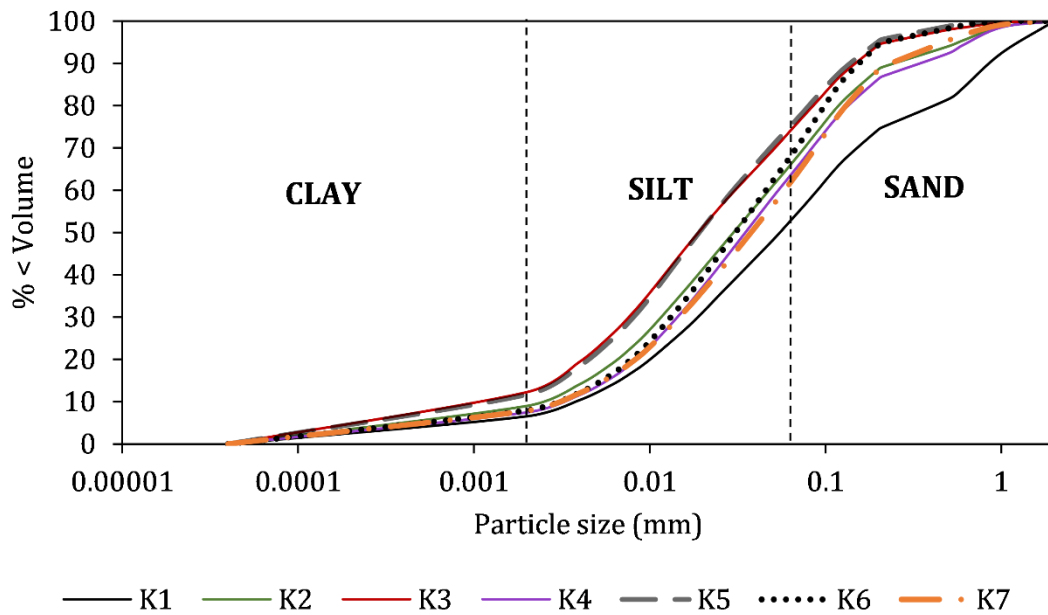


Figure 4.8 Particle size distribution of trial pit samples.

Table 4.6 Particle size distribution of the samples obtained from the borehole (BH-1).

Depth (m)	ID	% < Volume				Soil description
		Clay	Silt	Sand	Fines	
0 - 1	B1	8	60	33	67	SILT
1 - 1.15	B2	5	51	44	56	Sandy SILT
1.15 - 1.3	B3	6	58	36	64	Sandy SILT
1.3 - 1.45	B4	7	62	31	69	SILT
2.2 - 2.3	B5	3	43	54	46	Sandy SILT
2.3 - 2.4	B6	4	46	51	49	Sandy SILT
2.4 - 2.45	B7	4	55	41	59	Sandy SILT
3 - 3.3	B8	2	30	68	32	Very Silty SAND
3.3 - 3.4	B9	4	56	40	60	Sandy SILT
3.4 - 3.45	B10	5	70	25	75	SILT
4 - 4.3	B11	2	47	50	50	Sandy SILT
4.3 - 4.4	B12	5	62	33	67	SILT
5.2 - 5.3	B13	3	48	49	51	Sandy SILT
5.3 - 5.4	B14	3	50	47	53	Sandy SILT
5.4 - 5.45	B15	5	54	41	59	Sandy SILT
5.7 - 6	B16	2	31	67	33	Very Silty SAND
6.3 - 6.6	B17	2	27	71	29	Very Silty SAND

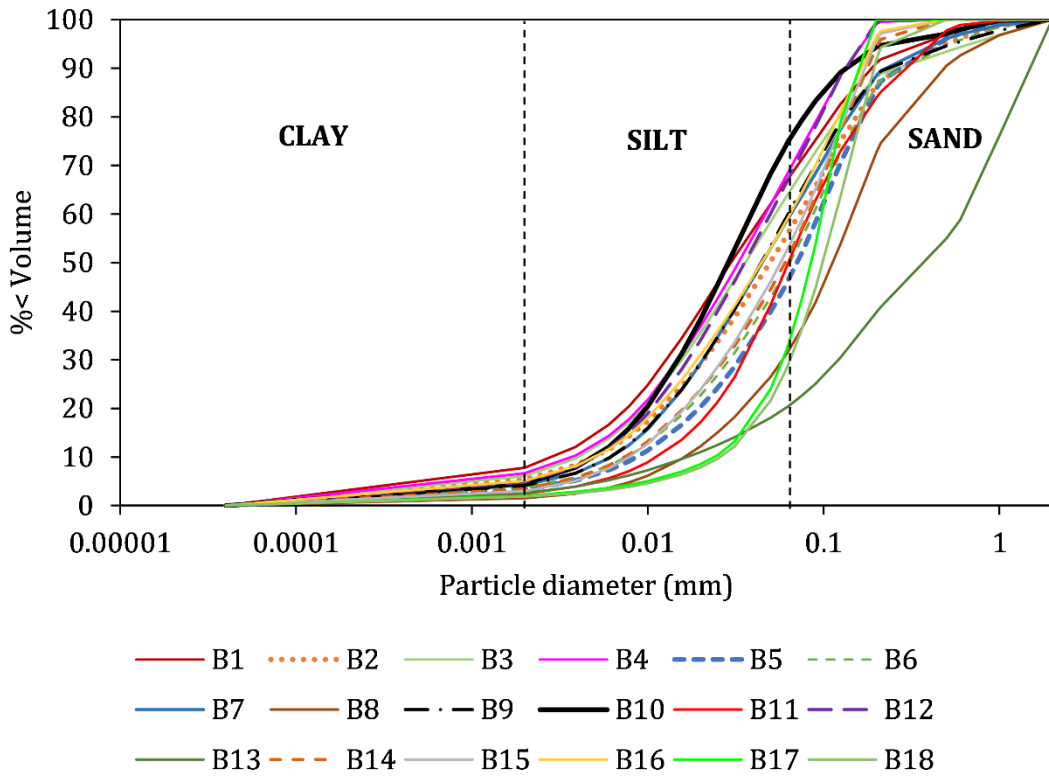


Figure 4.9 Particle size distribution of borehole (BH-1) samples.

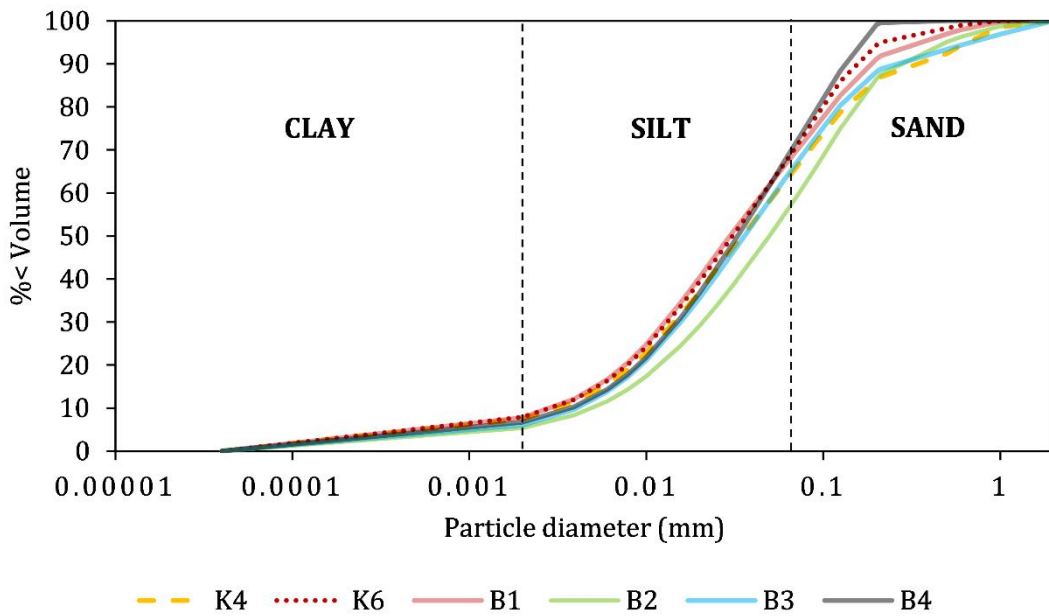


Figure 4.10 Comparison of particle size distributions of the trial pit samples (K4 and K6) and the borehole samples (B1 to B4) obtained from shallow depths (<1.45 m).



4.3.2.2 Atterberg limits

Figure 4.11 and Table 4.7 show the results of the Atterberg limit tests undertaken on the bag samples obtained from the trial pit. In Figure 4.11, all four samples down to 1 m possess similar properties as they overlap close to the A-line. The samples exhibited intermediate plasticity with a plasticity index from 13.8 to 16.6%. Although the samples behaved plastic enough to be plotted above the A-line in the plasticity chart, the higher silt and sand fractions as shown in Table 4.5 separated them from what can be considered as clay. Nonetheless, based on the plasticity chart, the finer fraction (<0.425 mm) of the samples can be classified as CLAYS of intermediate plasticity.

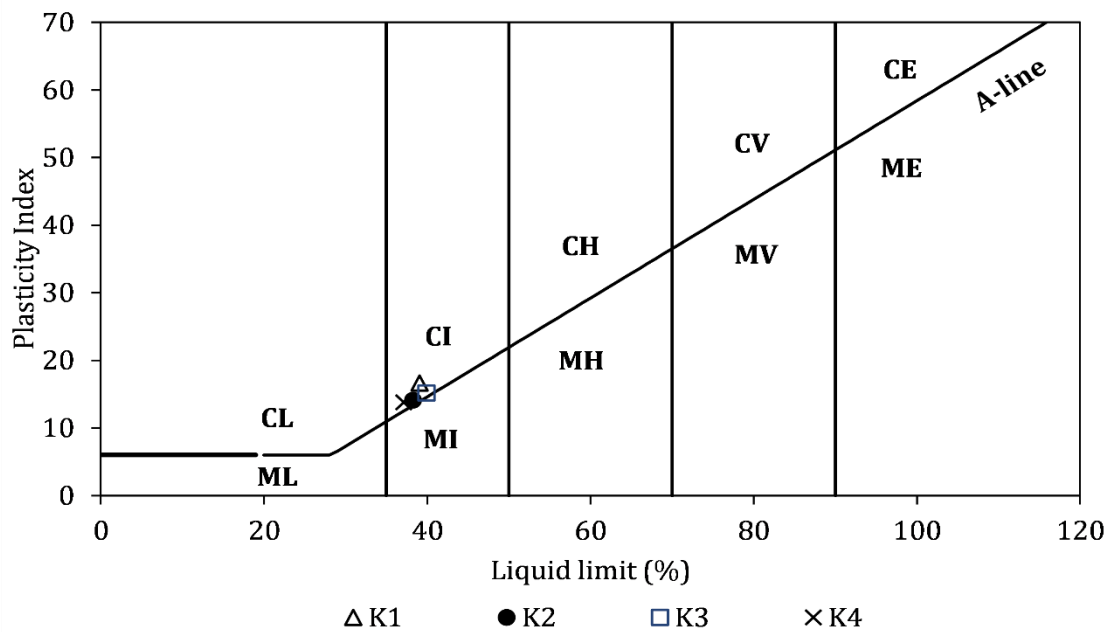


Figure 4.11 Plasticity chart for trial pit samples.

Table 4.7 Atterberg Limits of trial pit samples.

Depth (m)	ID	Liquid Limit (%)	Plastic Limit (%)	Plasticity Index (%)
0 - 0.3	K1	39.1	22.5	16.6
0.3 - 0.5	K2	38.3	24.2	14.1
0.5 - 0.75	K3	39.9	24.7	15.2
0.75 - 1.0	K4	37.1	23.4	13.8

4.3.2.3 Particle density

The particle densities of the soil samples obtained from the trial pit are shown in Table 4.8. The colour of the samples (reddish-brown to brown) indicated the presence of iron in

the soil. To confirm this, a hand-held x-ray fluorescence (XRF) analyser was used. High iron content from 47000 to 49200 ppm (~5%) was detected by the XRF analyser. Thus, the traces of iron found in the soil samples could have resulted in a relatively high particle density ranging from 2.72 to 2.78 Mg/m<sup>3</sup>.

Table 4.8 Particle density of soil samples.

Depth (m)	ID	Particle density (Mg/m <sup>3</sup> )	Remarks
0 - 0.3	K1	2.76	Bag sample
0.3 - 0.5	K2	2.72	Bag sample
0.5 - 0.75	K3	2.72	Bag sample
0.75 - 1	K4	2.78	Bag sample
0.5	K5	2.72	Core sample
1.0	K6	2.78	Core sample
1.5	K7	2.75	Core sample

#### 4.3.2.4 In-situ soil properties

The bulk density and the water content of the core samples obtained from the study site are presented in Table 4.9. The in-situ water content was found to be much less than the plastic limit which suggests that the soils were in an unsaturated state when sampling was conducted in March 2019 (Rahardjo et al., 2002). Additionally, using the weight-volume relationships, the dry density, void ratio, porosity, degree of saturation and saturated density of the core samples were obtained, which are shown in Table 4.10. From the table, it can be seen that the soil near the surface was loose (higher void ratio) than that at greater depths from the surface, which could be the result of the surficial cracks. Similarly, the soil at greater depth from the surface was found to have a greater degree of saturation (~64%) than that near the surface. Such a trend is expected because the atmospheric drying process mainly affects the soils at shallow depth.

Table 4.9 In-situ soil properties obtained from core samples.

Depth (m)	ID	Bulk density (Mg/m <sup>3</sup> )	In-situ water content (%)
0.5	K5	1.57	18.0
1.0	K6	1.85	17.7
1.5	K7	1.98	13.3

Table 4.10 Index properties of soil samples obtained from weight-volume relationships.

Depth (m)	ID	Dry density (Mg/m <sup>3</sup> )	Void ratio	Porosity (%)	Degree of saturation (%)	Saturated density (Mg/m <sup>3</sup> )
0.5	K5	1.33	1.04	51.0	47.1	1.84
1.0	K6	1.57	0.77	43.4	64.0	2.01
1.5	K7	1.75	0.57	36.4	64.2	2.11

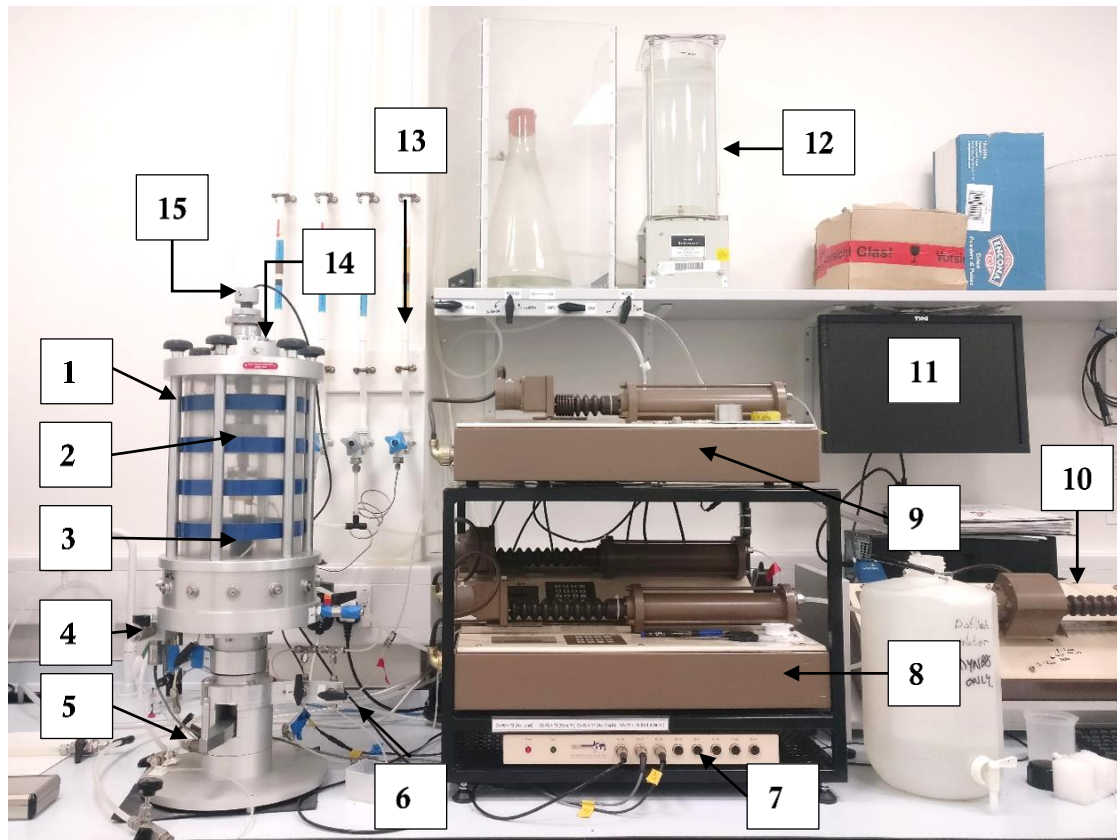
## 4.4 Determination of mechanical soil properties

### 4.4.1 Laboratory technique

To evaluate the mechanical behaviour of the saturated soil samples, consolidated undrained (CU) triaxial compression tests were performed in accordance with BS EN ISO 17892-9:2018 (BSI, 2018a). Since the soil samples obtained from shallow depths in the trial pit and the borehole (BH-1) exhibited similar index properties, one set of triaxial test conducted at different confining pressures was considered to be adequate for this study. The triaxial testing set-up used in this study is shown in Figure 4.12.

### 4.4.2 Sample preparation

Three samples were prepared from the bag samples obtained from 0.5 to 0.75 m depth (K3) for testing. To prepare samples for the triaxial tests, the soil was air-dried and sieved through a 2 mm test sieve to remove the larger particles. The sieved samples were then mixed with distilled water to achieve the desired water content. The first sample (K3\_T3) was mixed to 10% water content and later to speed up the saturation process, the other two samples (K3\_T1 and K3\_T2) were mixed to 15% water content. After mixing, the samples were compacted in a split mould using a 2.5 kg metal rammer (Figure 4.13) to achieve the desired dry density (1.3 Mg/m<sup>3</sup>). To ensure uniform compaction, the samples were compacted in 8 layers of ~95 mm thickness. The initial conditions of the triaxial samples before testing are shown in Table 4.11.



**LEGEND**

- 1 Triaxial cell
- 2 Load cell
- 3 Sample
- 4 Pore pressure transducer
- 5 Displacement
- 6 Drainage outlet
- 7 Data acquisition unit
- 8 Cell pressure controller
- 9 Back pressure controller
- 10 Lower chamber pressure controller/axial load controller
- 11 PC for data logging and test control
- 12 De-aerator
- 13 CO<sub>2</sub> supply
- 14 Displacement transducer
- 15 Loading ram

Figure 4.12 Set-up of triaxial cell in the landslide lab, Durham University.

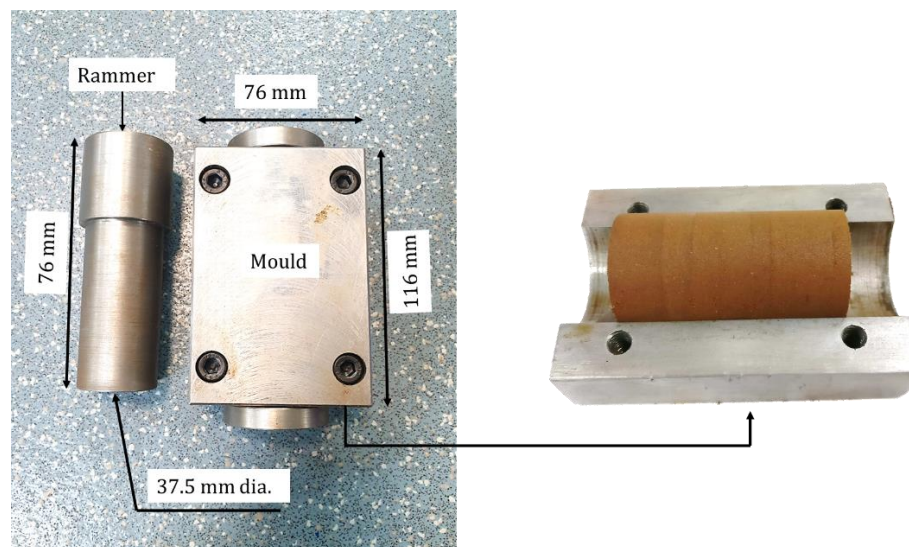


Figure 4.13 Mould and rammer used to prepare samples (left), compacted sample for triaxial testing in the split-open mould (right).

Table 4.11 Initial conditions for saturated triaxial test samples.

Depth (m)	ID	H (mm)	D (mm)	Initial volume (mm <sup>3</sup> )	Dry density (Mg/m <sup>3</sup> )	Water content (%)	Void ratio	Degree of saturation (%)
0.5 to 0.75	K3_T1	75.5	38.04	85806.04	1.34	15	1.03	39.6
	K3_T2	75.5	38.04	85806.04	1.34	15	1.03	39.7
	K3_T3	75.5	38.04	85806.04	1.34	10	1.03	26.0

### 4.4.3 Triaxial test stages

The triaxial test was conducted in three stages: saturation, consolidation and shearing, which are discussed below:

#### 4.4.3.1 Saturation

To saturate the sample, firstly, CO<sub>2</sub> was flushed from its bottom for at least 3 hours to replace any air trapped in the voids. Secondly, de-aired water was flushed through the sample for at least 12 hours to replace the CO<sub>2</sub> with water. After flushing water, the samples were subjected to 5 kPa effective pressure by increasing the cell pressure to 205 kPa and applying a back pressure of 200 kPa from the sample top for approximately 2 hours to dissolve any air if present. To ensure that the sample was saturated, a B-value check was undertaken. During this check, the cell pressure was increased by 100 kPa and the subsequent increase in the pore water pressure was recorded. The B-value is given as:

$$\text{B-value} = \frac{\text{change in pore water pressure}}{\text{change in cell pressure}} \quad (4.25)$$

Ideally, B-value should be 1 when the sample is fully saturated but in practice, B-value  $\geq$  0.95 is considered satisfactory (BSI, 2018c). The B-values obtained for the triaxial tests are shown in Table 4.12. After satisfactory completion of the B-value check, the next stage of the test was started.

Table 4.12 B-Values after saturation for triaxial tests.

Depth (m)	ID	B-value
0.5 to 0.75	K3_T1	0.95
	K3_T2	0.98
	K3_T3	0.98

#### 4.4.3.2 Consolidation

The samples were consolidated isotropically to attain the desired effective consolidation pressures (ECP) of 25 kPa, 75 kPa and 100 kPa. The desired effective stress was imposed on the samples by either increasing the cell pressure (constant back pressure) or by decreasing the back pressure (constant cell pressure). The consolidation stage was terminated when the excess pore water pressure measured at the base of the sample had

dissipated and no significant volume change was recorded. Table 4.13 shows that the volume of the samples and the void ratio decreased after consolidation. The change in the sample volume during consolidation was calculated from the change of water volume in the back-pressure controller and the water content in the samples were back-calculated by weighing the oven-dried soils at the end of each test.

Table 4.13 Sample conditions after consolidation for triaxial tests.

Depth (m)	ID	ECP (kPa)	Volume (mm <sup>3</sup> )	Dry density (Mg/m <sup>3</sup> )	Water content (%)	Void ratio
0.5 to 0.75	K3_T1	25	78649.68	1.46	31.8	0.86
	K3_T2	75	77872.68	1.47	31.2	0.85
	K3_T3	100	77486.68	1.49	30.8	0.84

#### 4.4.3.3 Shearing

To shear the samples, the axial strain was increased up to 25% of the consolidated sample height in 5 to 6 hours (strain-controlled test), maintaining a strain rate of 0.05 to 0.06 mm/min. The rate of deformation during shear was slow enough to allow the non-uniform pore pressure to equalise. During the test, the drainage valve was closed to maintain the undrained condition.

#### 4.4.4 Summary of the triaxial compression test results

##### 4.4.4.1 Stress-strain behaviour

Figure 4.14 and Figure 4.15 illustrate the stress-strain curves and the excess pore water pressure curves generated for the three test samples (K3\_T1, K3\_T2, and K3\_T3). The stress-strain plot and the excess pore water pressure plot show typical contractive behaviour for relatively loose or normally consolidated soils in saturated triaxial tests. In samples K3\_T1 and K3\_T2, the deviator stress increased sharply and reached maximum strength at low axial strain (<5%) and exhibited plastic behaviour afterwards. The sample K3\_T3 however, showed weak strain hardening before reaching a constant value. This may be due to the application of higher confining pressure, which led to a greater contraction of the soil grains compared to that at lower confining pressures.

As discussed in section 4.2.1, when the soils attain the critical state, with a further increment of shear strain after reaching the peak, the effective stress remains constant. It can be seen from Figure 4.15 that the changes in the pore water pressures (and hence, the effective

stresses) became negligible towards the end of the tests. Based on this observation, it is likely that the critical state was being approached in all three tests. The effective stress path followed by the samples during shear is shown in Figure 4.16. This figure illustrates the changes in the mean effective stress and shear stress during mobilisation of the shearing resistance. A critical state line with a stress ratio ( $M$ ) of 1.47 (Equation 4.8) has been drawn on this figure, which is equivalent to a critical state angle of shearing resistance of  $36^\circ$ . This is comparable to the angle of shearing resistance of  $35^\circ$  to  $40^\circ$  corresponding to SPT  $(N_1)_{60}$  values in BH-1 (11 to 19) as per Hatanaka and Uchida (1996) which was discussed in chapter 3.

In Figure 4.16, the sample K3\_T1 which was subjected to lower consolidation pressure can be seen to climb up to the critical state line almost vertically. On the contrary, the samples confined at higher pressures (K3\_T2 and K3\_T3), indicated greater contraction, resulting in the development of positive pore water pressures and consequent reduction in the effective stress ( $p'$ ). The magnitude of the positive pore water pressure for K3\_T3 is greater due to higher consolidation pressure applied to the sample. For K3\_T3, as the stress path approached the projection of the critical state line, a change in direction can be seen, indicating dilation with increasing shear strain. Under the critical state framework, the samples should form a unique relationship between the specific volume ( $v$ ) (or void ratio) and the mean effective stress ( $p'$ ). In Figure 4.17, the specific volume of the tested samples is plotted against  $\ln(p')$ . Since the volume change was prevented during shear, the specific volume of the samples remains unchanged during shearing. In the  $v$ - $\ln(p')$  space, the critical state line can be described by  $\Gamma = 2.06$  and  $\lambda = 0.064$  (Equation 4.9).



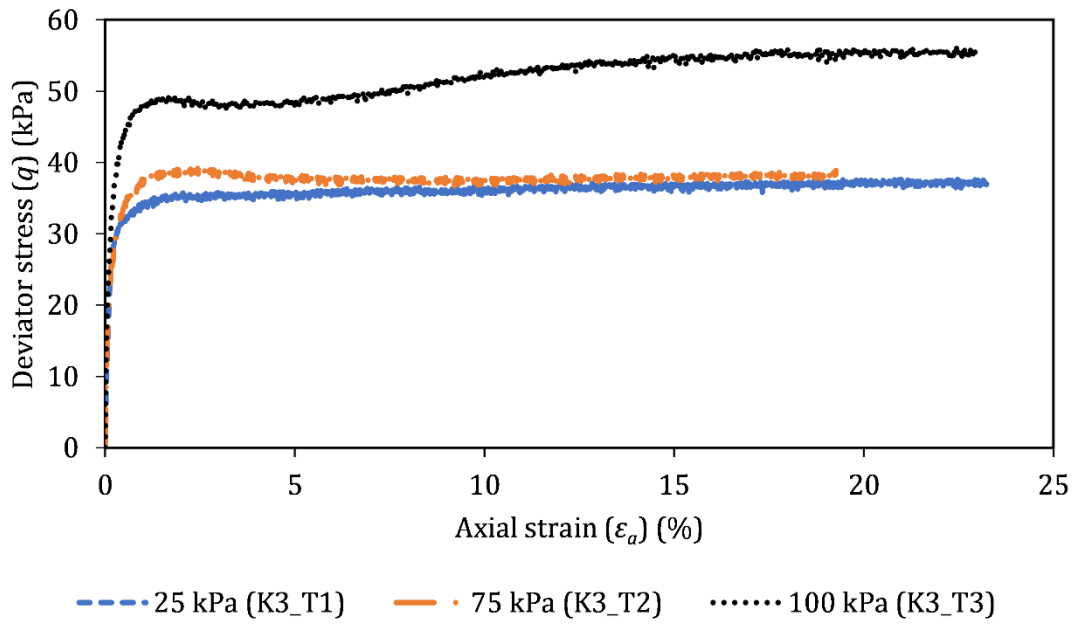


Figure 4.14 Deviator stress versus axial strain.

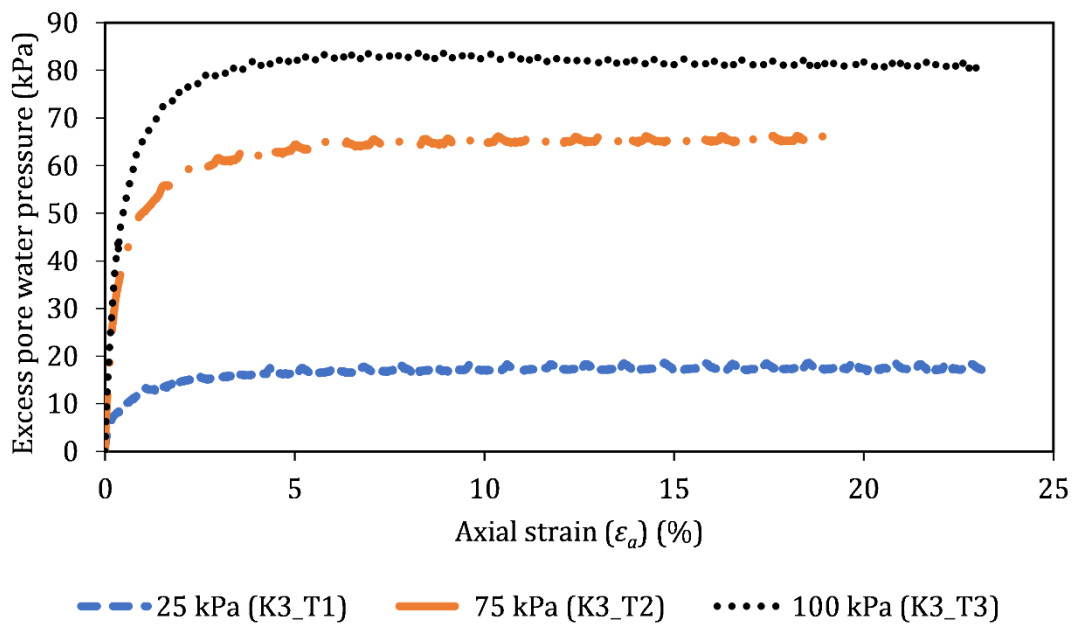


Figure 4.15 Excess pore water pressure versus axial strain.

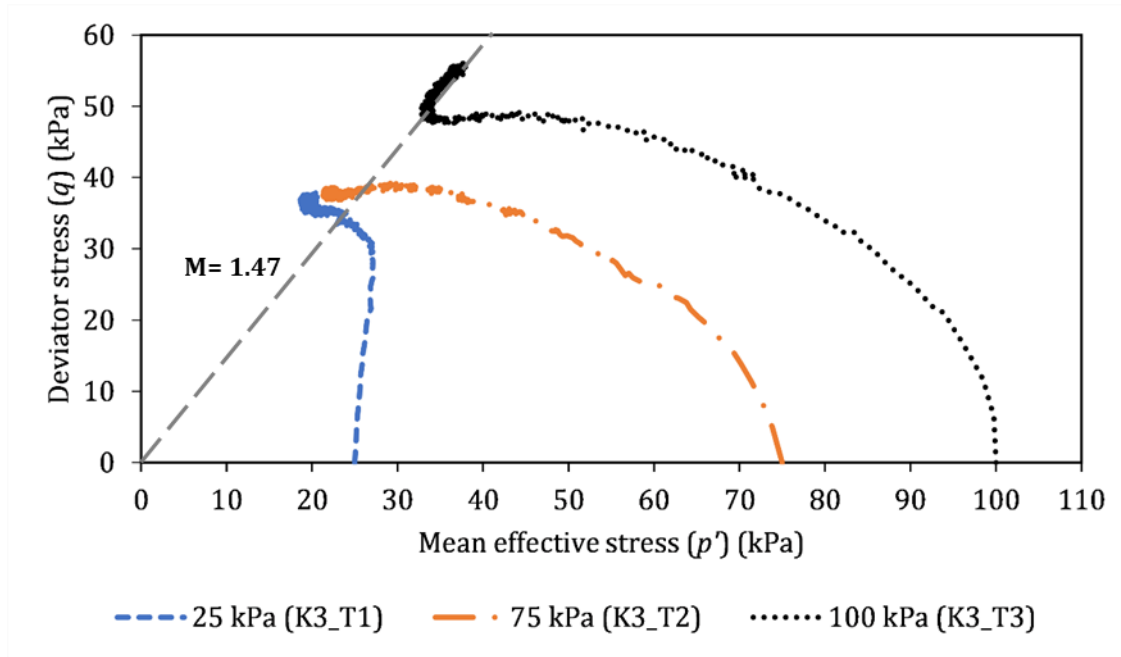


Figure 4.16 Effective stress paths.

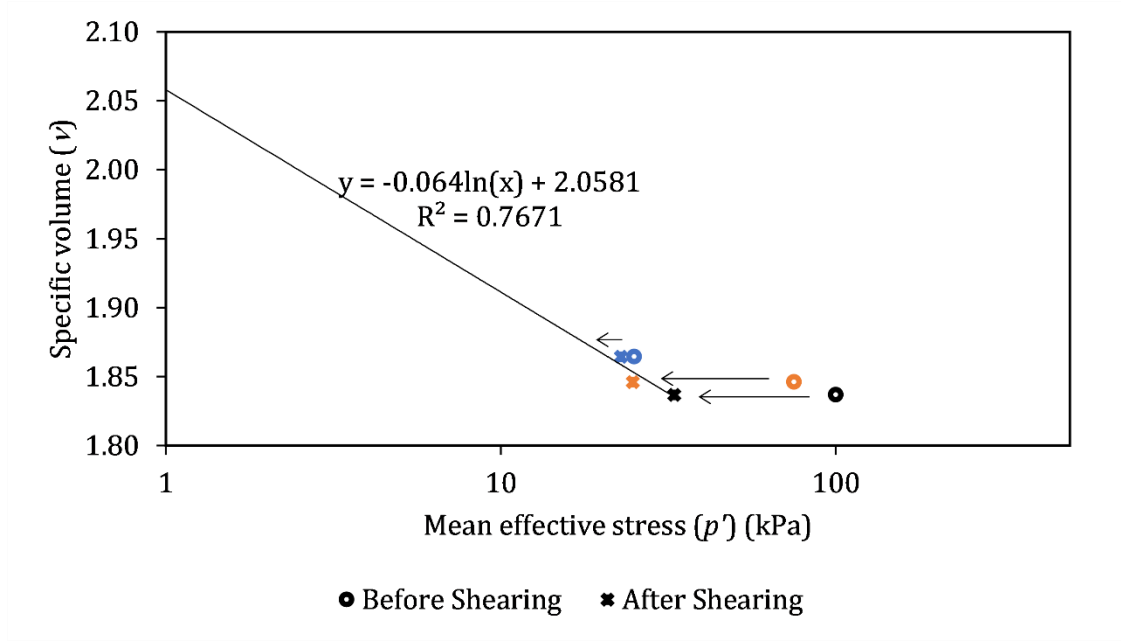


Figure 4.17 Specific volume versus mean effective stress.

#### 4.5 Determination of soil-water retention curve

As noted earlier in section 4.2.4.1, the discrete procedure outlined by Lourenço et al. (2007) for obtaining the soil-water retention curve with a high-capacity tensiometer was used in this study.

#### 4.5.1 Sample preparation

To prepare the samples for soil-water retention curve measurement, the soil samples were air-dried in the laboratory for at least 48 hours and sieved through a 2 mm test sieve to remove the larger particles. The initial conditions of the samples prepared for the SWRC test are shown in Table 4.14. Two samples were prepared from each depth (0.3 to 0.5 m) and (0.75 to 1 m), one for the drying path and another for the wetting path. For obtaining the primary drying path, it is essential to start the drying process from a fully saturated condition. If the sample is not fully saturated, the curve may not be the primary drying path, but a scanning curve representing an intermediate state between the drying and the wetting paths (Md. Rahim, 2016). Thus, the sieved soils were mixed with water to obtain a degree of saturation close to 98% to allow the samples to hold their shape outside the mould. The mixture was then sealed in a plastic container for at least 24 hours to allow uniform adsorption of water. The samples were prepared by compacting the samples in a steel mould with two endplates. The samples were wrapped in cling film and sealed in an air-tight container for 48 hours for equalisation before the suction measurements were made.

Table 4.14 Initial condition of the samples for SWRC tests.

Sample ID	0.3 to 0.5 m		0.75 to 1 m	
	K3_S1	K3_S2	K4_S1	K4_S2
Height (mm)	25.5	26.4	27.7	28.0
Diameter (mm)	102.6	101.0	103.2	103.1
GWC (%)	28.7	28.9	25.6	26.2
Total mass (g)	411.2	411.9	467	470.9
Mass of dry soil (g)	319.6	319.4	371.8	373.3
Dry density (Mg/m <sup>3</sup> )	1.52	1.51	1.61	1.60
Void ratio	0.79	0.80	0.73	0.74
Porosity (%)	44.2	44.4	42.3	42.6
Degree of saturation (%)	98.4	98.6	97.2	98.0
VWC (%)	43.5	43.8	41.1	41.7
Remarks	Wetting	Drying & wetting-scanning	Drying & wetting-scanning	Wetting

#### 4.5.2 Laboratory technique

The procedure for obtaining the drying path of the soil-water retention curve consisted of four distinct steps, which are summarised below:

1. Drying: The samples (K3\_S2 and K4\_S1) were allowed to dry naturally in the temperature and humidity-controlled laboratory. During drying, the samples were weighed frequently to control the amount of water lost by evaporation.
2. Equalisation: After a certain amount of water was lost by drying, the samples were wrapped in cling film and placed in re-sealable plastic bags. The samples were then kept on a raised platform inside plastic boxes containing a small volume of water. The boxes were then sealed with cling film to create an insulating environment for equalisation. During wrapping, special care was taken to prevent air from being trapped in the cling film to minimise evaporation from the sample. The samples were left for at least 24 hours for equalisation.
3. Suction-measurement: After equalisation, each sample was placed on a base pad and a lightweight brass disc ( $\phi 100$  mm) with a hole at the centre was positioned on the sample top. The tensiometer was brought in contact with the sample through the hole in the brass disc, which held the tensiometer in place during measurement. The base pad, the sample, the brass disc and the tensiometer were then placed on an electronic balance for continuous measurement of the mass. Figure 4.18 shows the test set-up used for suction measurement. To ensure proper contact between the sample and tensiometer, a thin paste of fine material was applied onto the contact surface. The suction in the sample was measured until a uniform value indicating equalisation of pressure was obtained.
4. Mass and volume measurement: After the suction measurement was completed, the samples were weighed, and the height and the diameter of the samples were measured using a digital calliper with  $\pm 0.01$  mm accuracy to determine their volumes.

The process from (i) to (iv) was repeated multiple times to obtain the data points required to define the drying path. The tests were terminated when the suction started to increase beyond 550 kPa to avoid cavitation. After obtaining the data points for the drying curve, the same samples were wetted in stages to obtain the wetting-scanning curves. To wet the samples, distilled water was sprayed carefully on all sides of the samples until the targeted masses were achieved.

Similarly, to obtain the wetting path of the SWRC, the samples (K3\_S1 and K4\_S2) were first dried from the saturated state until the gravimetric water contents were less than 1.5%. After drying, the samples were wetted in stages using a spray bottle to obtain the data points required for the wetting curve. The same procedure described above from (ii) to (iv) was repeated after each wetting stage. During wetting, first suction measurements were not taken until the GWC reached close to 10% to prevent potential cavitation. After this, the samples were wetted in stages and corresponding suction measurements were made. The measurements for the wetting curves were terminated when the suction readings dropped below 10 kPa. All tests were conducted in a temperature and humidity-controlled laboratory with an average of 20°C temperature. After the tests were completed, the samples were weighed and placed in the oven at 104°C for 48 hours to measure their final water content.

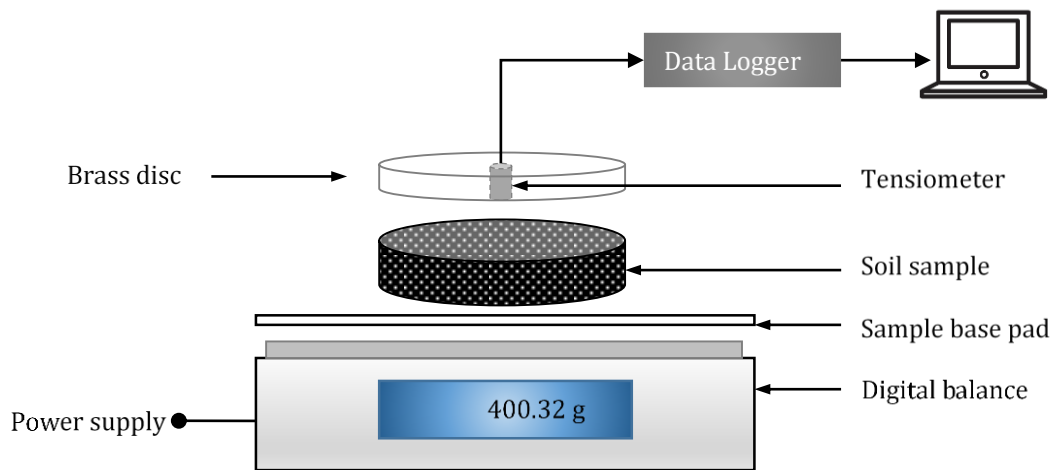


Figure 4.18 Set-up for suction measurement (figure not to scale).

### 4.5.3 Summary of soil-water retention curve measurements

#### 4.5.3.1 Gravimetric water content (GWC) versus suction

The soil-water retention curves plotted between the gravimetric water content and the matric suction for all four samples (Table 4.14) are shown in Figure 4.19. This figure illustrates the hysteretic behaviour of soil during drying and wetting for both samples (K3 and K4). The particle size distribution of the samples K3 and K4 as shown in Table 4.5 are very similar to one another, which explains the similar rate of saturation and desaturation that is evident in Figure 4.19. The drying curve, the wetting curve and the wetting-scanning curve of K3 samples are located above the respective curves of the K4 samples. This may be because the K3 samples obtained from shallow depth have a higher void ratio as compared

to the K4 samples. The shrinkage and swelling of soils during drying and wetting can cause changes in the amount of water that can be held within the soil, which ultimately changes the gravimetric water content of the soil. This means that the changes in the gravimetric water content illustrated in Figure 4.19 could be attributed to the changes in volume during drying and wetting (Toll et al., 2015). Hence, it is desirable to evaluate soil-water retention properties in terms of volumetric measurements (section 4.5.3.3).

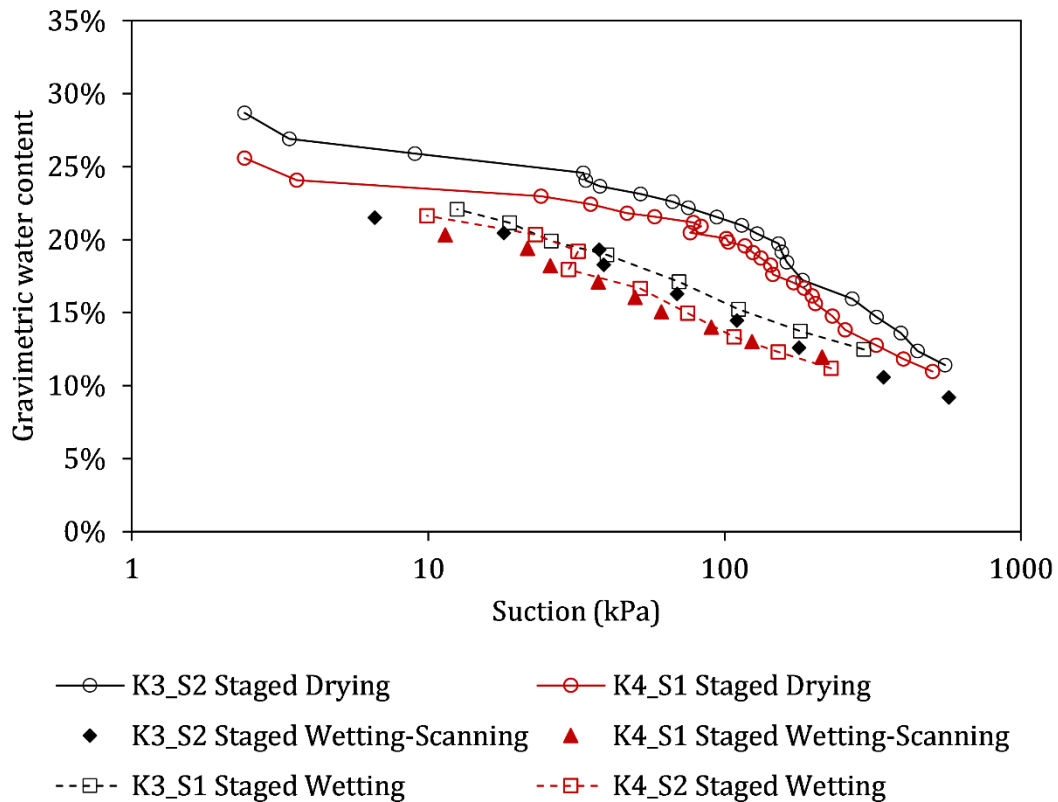


Figure 4.19 Gravimetric water content versus suction.

#### 4.5.3.2 Void ratio versus gravimetric water content

In Figure 4.20 the change in void ratio during drying is plotted against the gravimetric water content. As shown in the figure, the void ratio reduced significantly during drying in both samples, especially during the initial stages. As the water content dropped to ~20%, the decrease in void ratio with drying became less significant. Greater reduction of void ratio in the K3 samples can be linked to the higher initial void ratio when compared with the K4 samples. In contrast, the change in void ratio during wetting and wetting-scanning was not as prominent for either sample as shown in Figure 4.21. In this figure, the wetting paths leading to the saturation lines are almost horizontal, indicating that the volume change in samples (swelling) during wetting was not significant. This behaviour may have resulted from the method of wetting and/or the duration and conditions adopted for suction

equalisation, which may have inhibited uniform distribution of pore water. Nonetheless, Md. Rahim (2016) also reported similar behaviour of soil during the wetting process, which was associated with a stiffer elastic response of the soil.

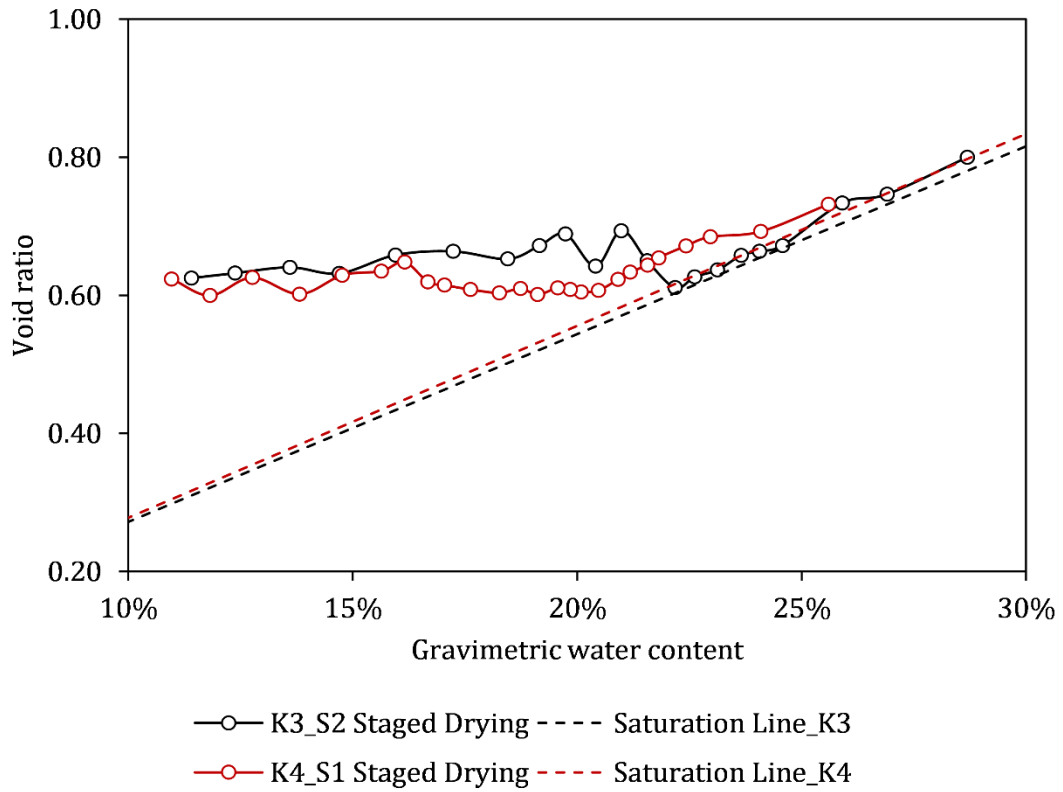


Figure 4.20 Change in void ratio during drying.

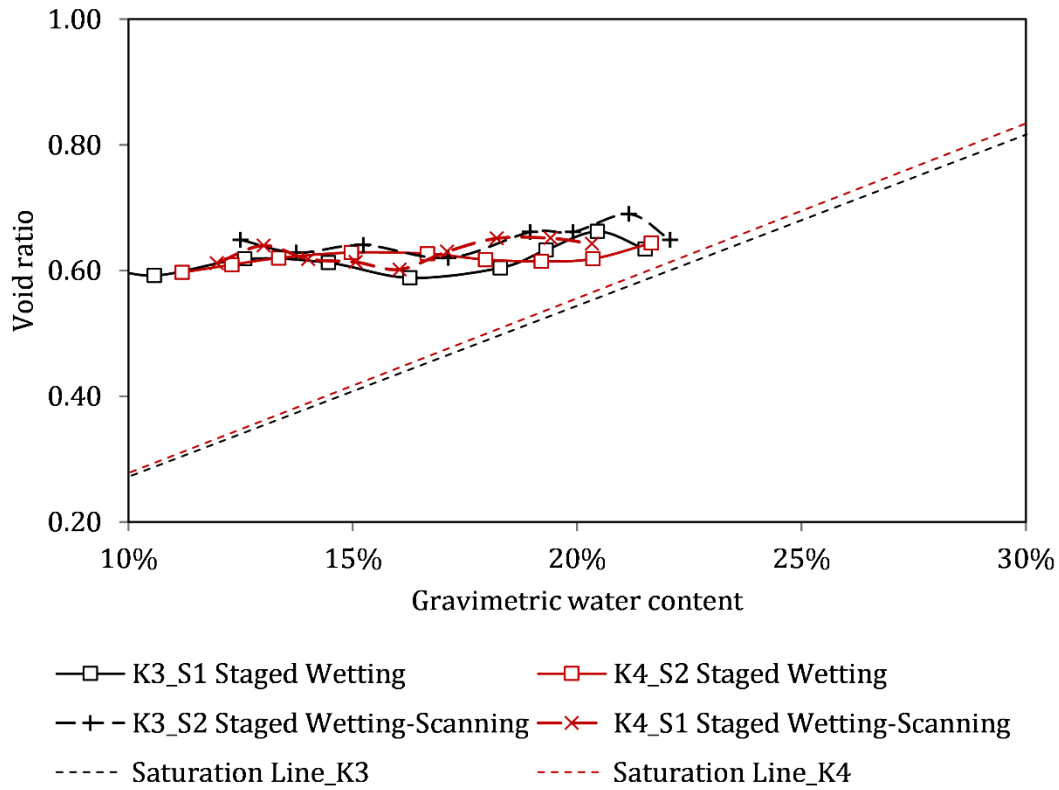


Figure 4.21 Change in void ratio during wetting.

#### 4.5.3.3 Volumetric water content (VWC) versus suction

The relationship between volumetric water content and suction during drying and wetting for K3 and K4 samples are shown in Figure 4.22 and Figure 4.23 respectively. To define the relationship between matric suction and volumetric water content over a larger range, the van Genuchten model (van Genuchten, 1980) (Equation 4.20) was fitted to the experimental data. The fitting parameters for the model ( $\alpha$ ,  $n$  and  $m$ ) are shown in Table 4.15. The air-entry values (AEV) shown in this table have been converted to the unit of kPa ( $AEV = \alpha^{-1} \times 10$ ). The fitting parameters were obtained using a web-based, SWRC fitting program developed by Seki (2007).

In general, the experimental data showed a good fit with the model. As would be expected, the wetting-scanning curve obtained by wetting the sample immediately after terminating the drying stage reached the primary wetting curve, which can be seen in Figure 4.22 and Figure 4.23. As shown in Table 4.15, the air-entry value of the K4 sample is higher than the K3 sample. This may be because the void ratio of the former is lower which would mean higher suction would be needed to overcome the influence of the pore size after which the soil starts drying effectively. The other parameter ‘ $n$ ’ represents the slope of the curves or the rate of drying or wetting. From the fitted data, it can be seen that the K3 samples have a



lower ' $n$ ' value than the K4 samples during drying, meaning the former dried at a slower rate than the later. This could be because the K4 samples contained relatively higher sand-sized particles (37%) than that in the K3 samples (34%).

As noted by Toll (2012), the air-entry values of clean silty soil tend to be lower than 100 kPa, and this increases with the increase in finer-sized particles. As the sample from 0.75-1 m consisted of 7% clay-sized particles, the air-entry value can be expected to be slightly greater than that for clean silty soils. Further, based on the UNSODA database (Leij et al., 1996) compiled by Tuller and Or (2004), the ' $n$ ' value for SILT is approximately 1.53. The difference between this value and the measured ' $n$ ' values from the laboratory is <14%. Hence, it can be said that the measured SWRC fitting parameters were found to be within reasonable range for the given soil textures.

Table 4.15 Estimated curve fitting parameters for the van Genuchten (1980) model.

Depth (m)	van Genuchten model fitting parameters			Air-entry value (kPa)	Remarks	
	$\alpha$	$n$	$m$			
0.3 to 0.5	K3_S1	0.272	1.315	0.271	-	Wetting path
	K3_S2	0.121	1.372	0.240	83	Drying path
0.75 to 1.0	K4_S1	0.063	1.650	0.394	158	Drying path
	K4_S2	0.226	1.405	0.288	-	Wetting path

$\alpha$  is expressed as the unit of pressure head (1/m)

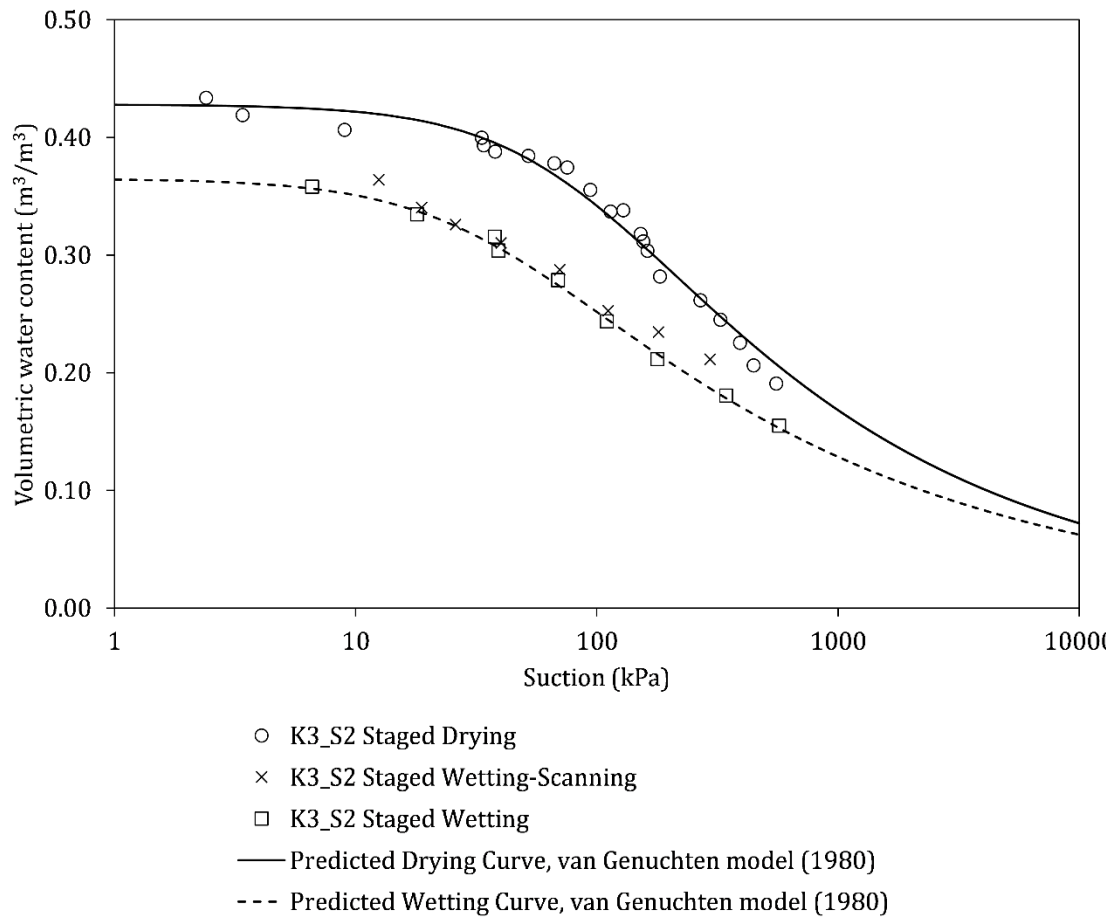


Figure 4.22 Volumetric water content versus suction for K3 samples.

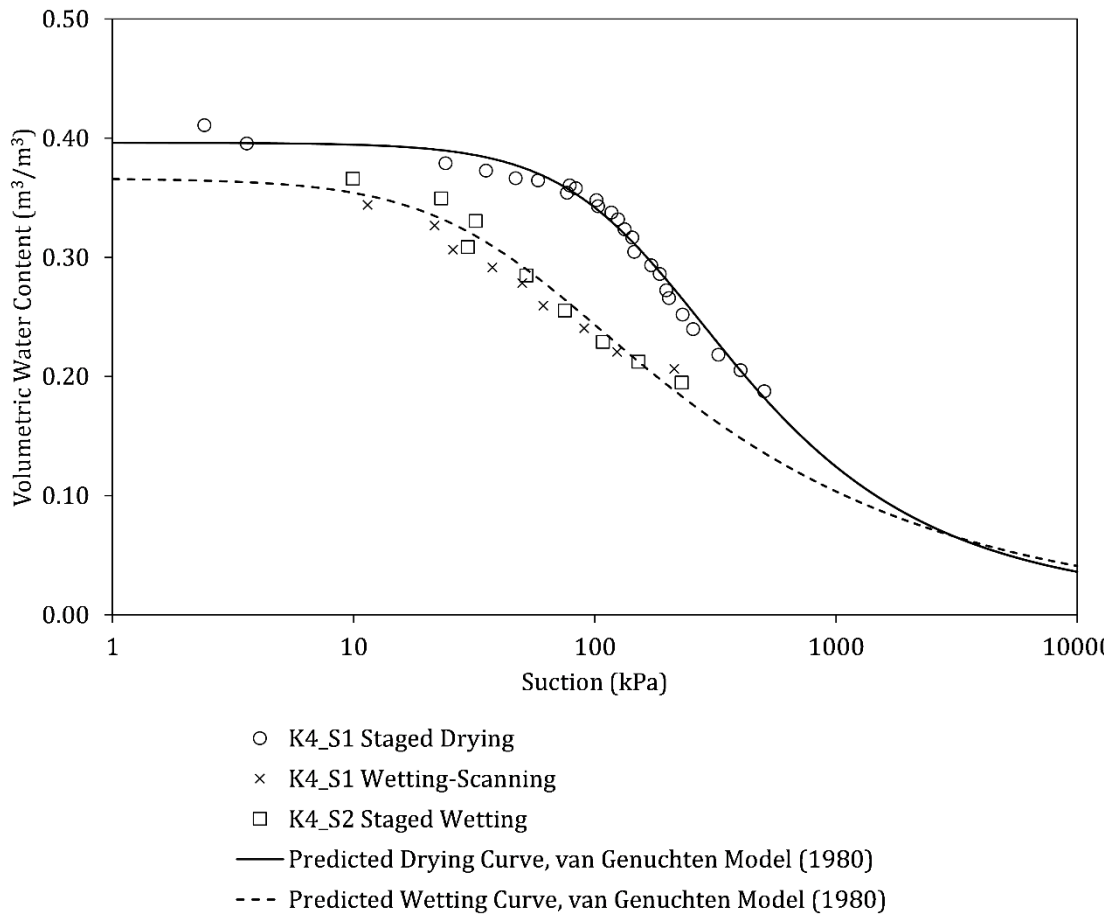


Figure 4.23 Volumetric water content versus suction for K4 samples.

## 4.6 Determination of saturated coefficient of permeability

### 4.6.1 Laboratory technique

The standard triaxial constant head permeability test was conducted in accordance with BS EN ISO 17892-11:2019 (BSI, 2019) to determine the saturated coefficient of permeability. The triaxial set-up shown in Figure 4.12 with an additional base pressure controller was used for this test. The base pressure controller was connected to the sample bottom to control the pressure and to measure the volume of water leaving the sample. Like during the triaxial test, the sample was fully saturated and consolidated before the permeability test. During the permeability test, a constant hydraulic gradient was maintained between the sample top and bottom to ensure a constant flow through the sample. The volume of water entering and leaving the sample was recorded continuously during the permeability test, which was used to determine the coefficient of vertical permeability using the Equation 4.26.

$$k_v = \frac{Q_{flow} \times L}{A \times \Delta h} \times \delta \quad (4.26)$$

Where

$k_v$  = saturated coefficient of vertical permeability

$Q_{flow}$  = mean rate of flow through the sample

$L$  = sample height

$A$  = cross-sectional area of the sample

$\Delta h$  = difference in the head of water between sample top and bottom

$\delta$  = temperature correction factor for the viscosity of water (= 1.002 at 20°C)

#### 4.6.1.1 Sample preparation

The method of preparing samples of saturated permeability test was the same as that for the triaxial test (please refer to section 4.4.2). The initial condition of the sample for the permeability test is outlined in Table 4.16.

Table 4.16 Initial condition of the sample for triaxial constant head permeability test.

Depth (m)	ID	H (mm)	D (mm)	Initial volume (mm <sup>3</sup> )	Dry density (Mg/m <sup>3</sup> )	Water content (%)	Void ratio	Degree of saturation (%)
0.5 to 0.75	K3	75.5	38.04	85806.04	1.4	15	1.0	40.5

#### 4.6.1.2 Stages in the triaxial constant head permeability test

The triaxial constant head permeability test was conducted in three stages: saturation, consolidation and constant head permeability test, which are described below:

- Saturation

The saturation procedure was the same as that outlined in section 4.4.3.1 for the triaxial test. B-value of 0.98 was obtained, which indicated satisfactory saturation of the samples.

- Consolidation

The samples were consolidated isotropically to the consolidation pressures of 100 kPa, 200 kPa and 300 kPa. At the end of each consolidation phase, after the pore water pressures had equalised, the permeability test was performed. In Table 4.17, the condition of the samples after each consolidation phase is presented. With the increase in the effective consolidation pressure (ECP), a gradual decrease in the void ratio can be seen in this table.

Table 4.17 Sample conditions after consolidation for permeability tests.

Depth (m)	ID	ECP (kPa)	Volume (mm <sup>3</sup> )	Dry density (Mg/m <sup>3</sup> )	Water content (%)	Void ratio
0.5 to 0.75	K3_P1	100	79492.04	1.46	31.5%	0.86
	K3_P2	200	76599.04	1.52	29.1%	0.79
	K3_P3	300	75446.04	1.54	28.1%	0.76

- Constant head permeability test

For the permeability test, water was allowed to flow downward through the consolidated sample under a constant hydraulic head. A pressure difference of 20 kPa was maintained across the sample by using the back pressure and base pressure systems connected to the top and bottom of the sample respectively. The volume of water entering and leaving the sample was recorded continuously during the test.

The permeability test was continued until the two plots of inflow (back volume) and outflow (base volume) from the sample were linear which are shown in Figure 4.24, Figure 4.25 and Figure 4.26. When the measurement of permeability at one consolidation pressure was completed and the pore water pressure had equalised, the sample was consolidated at a higher pressure and the test was repeated. In this way, the coefficient of permeability was obtained at three different effective confining stresses. From the inflow and outflow plots (Figure 4.24 to Figure 4.26), the mean rate of flow ( $Q_{flow}$ ) was calculated and using Equation 4.26, the coefficient of vertical permeability of soil was determined.

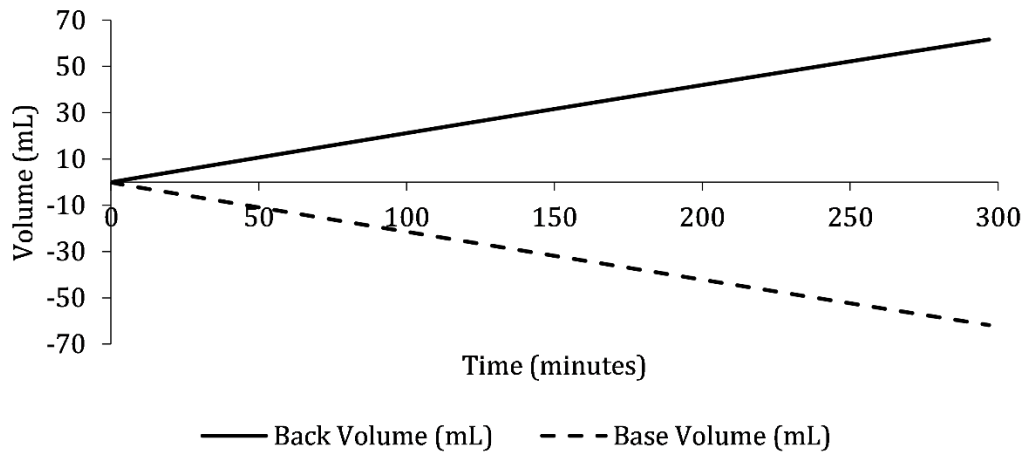


Figure 4.24 Recorded back and base flow volume for K3\_P1.

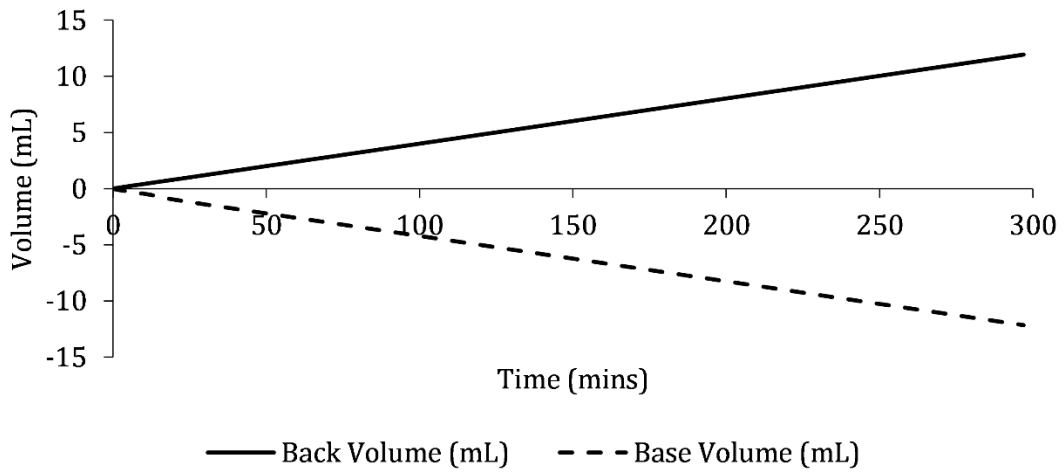


Figure 4.25 Recorded back and base flow volume for K3\_P2.

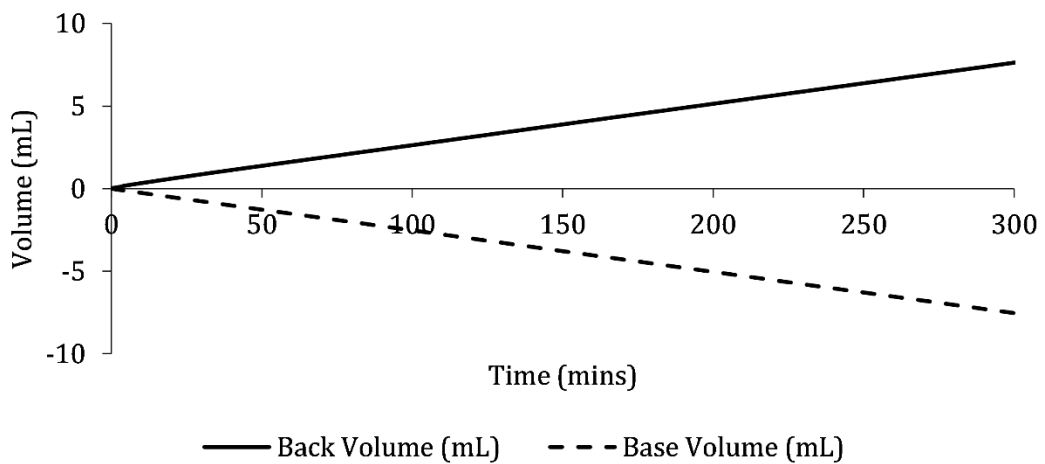


Figure 4.26 Recorded back and base flow volume for K3\_P3.

#### 4.6.2 Summary of standard triaxial constant head permeability test

The results of the permeability test are summarised in Table 4.18. At increasing confining pressures, the permeability of the sample varied between  $1.15 \times 10^{-7}$  m/s and  $1.43 \times 10^{-8}$  m/s. This range of permeability is typical for silts and silty sands (Lu and Likos, 2004). The variation of vertical permeability against effective confining pressure is plotted in Figure 4.27. A non-linear decrease in the permeability with increasing confining pressure can be seen in this figure. A significant drop ( $\sim 79\%$ ) in the permeability can be seen when the effective confining pressure increased by 100 kPa (K3\_P1 to K3\_P2). However, during subsequent increment of the same magnitude (K3\_P2 to K3\_P3), the change was found to be relatively less significant ( $\sim 9\%$ ). This may be interpreted in combination with Figure 4.28 where the permeability is plotted against the void ratio. From this figure, it is clear that the higher void ratio of soil at lower confining pressure (100 kPa) may have allowed greater permeability. However, further consolidation of the sample led to a decrease in the void ratio, which may have impeded the flow, thereby reducing the soil permeability.

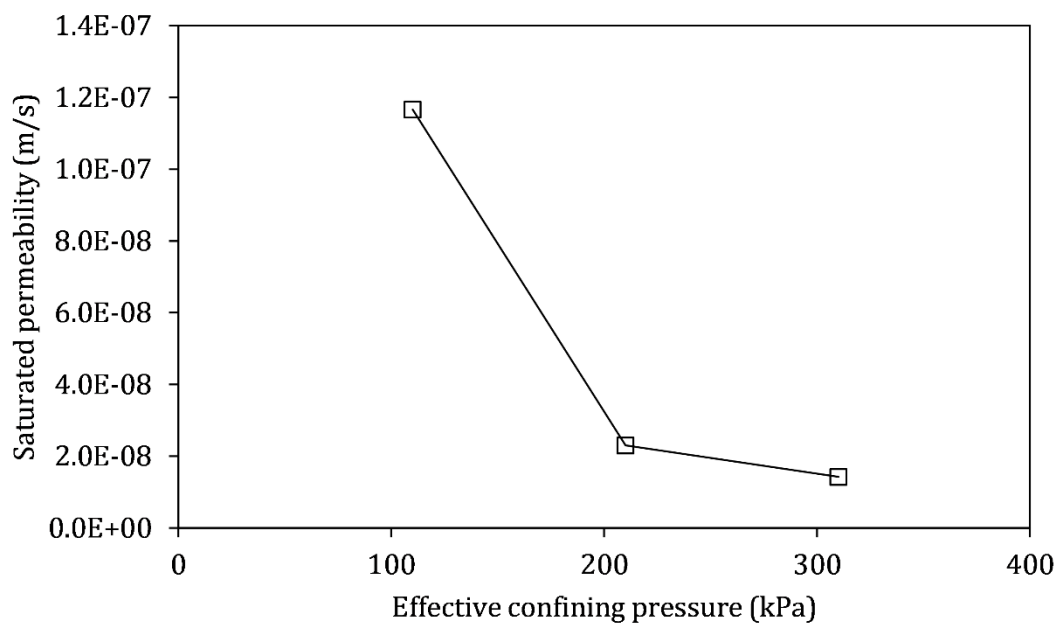


Figure 4.27 Saturated coefficient of vertical permeability versus average effective confining pressure.

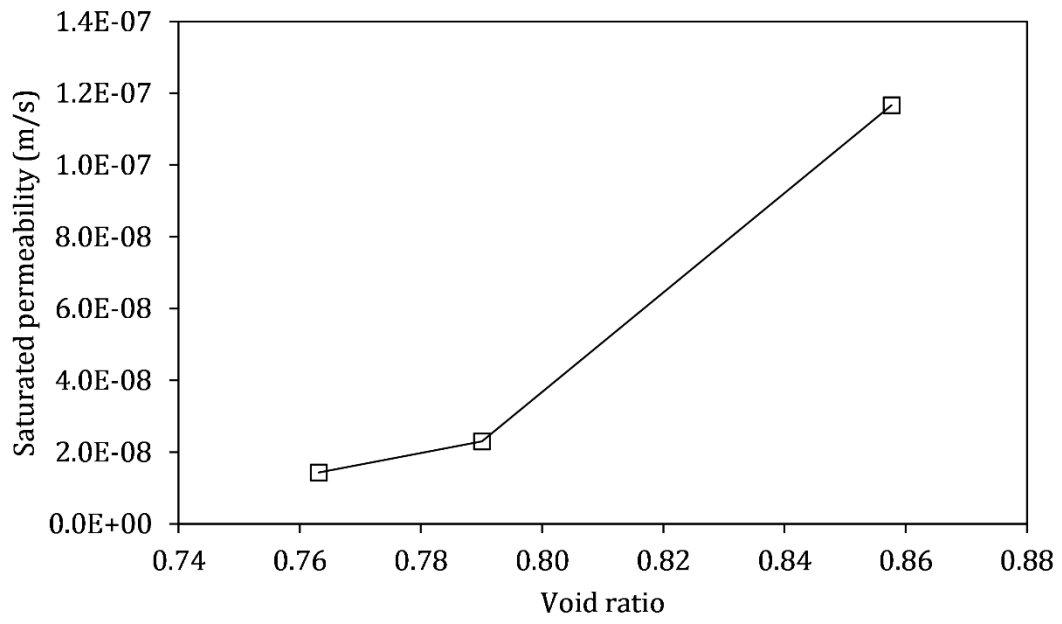


Figure 4.28 Saturated coefficient of vertical permeability versus void ratio.



Table 4.18 Results of the permeability test.

Depth (m)	ID	ECP (kPa)	Pressure difference (kPa)	Average effective confining pressure (kPa)	Void ratio	Inflow rate (mL/min)	Outflow rate (mL/min)	Average flow rate (mL/min)	Cross-sectional area (mm <sup>2</sup> )	Vertical permeability (m/s)
0.5 to 0.75	K3_P1	100	20	110	0.86	0.2073	0.0275	0.2074	1080.8	1.15E-07
	K3_P2	200	20	210	0.79	0.0402	0.0404	0.0403	1054.5	2.39E-08
	K3_P3	300	20	310	0.76	0.0251	0.0251	0.0251	1044.0	1.43E-08

## 4.7 Chapter summary

In the initial part of this chapter, theoretical concepts related to the mechanical and hydrological behaviour of saturated and unsaturated soils were discussed. From the laboratory tests, the following conclusions have been made:

1. The particle size distribution of the samples obtained from the study site showed lower clay contents (<12%) and higher silt- (27-70%) and sand- (25-71%) sized fractions. In the Atterberg limit tests, the finer fraction of the samples (<0.425 mm) exhibited intermediate plasticity (13.8-16.6%) and plotted close to the A-line.
2. The samples obtained from the trial pit near Kanglang landslide and the borehole drilled next to the crown of this landslide exhibited similar particle size distributions. This suggested that the samples obtained from the trial pit are representative of the soil near the failed area.
3. The particle density of the soil samples ranged from 2.72 to 2.78 Mg/m<sup>3</sup>; the colour of the samples and the measurements from hand-held x-ray fluorescence (XRF) analyser confirmed the presence of iron in the soil, which may have resulted in a higher particle density.
4. From the sealed cores brought from the study site, in-situ water content was determined. Since the samples were obtained in March 2019, which is a relatively dry period, the in-situ water content was found to be less than the plastic limit of the soils. This suggests that the soils were in an unsaturated condition when the sampling was undertaken.
5. Using the in-situ water content, bulk density and particle density, other in-situ index properties like dry density, void ratio, porosity, degree of saturation and saturated density were calculated. A decreasing trend of void ratio and the increasing trends of dry density and degree of saturation was observed with the increase in distance from the ground surface. This trend is perhaps, expected because of the presence of surficial cracks and also due to a greater effect of atmospheric drying near the ground surface.
6. From the saturated triaxial tests (CU), the critical state parameters were determined:  $M = 1.47$ ,  $\Gamma = 2.06$  and  $\lambda = 0.064$ . From the  $p'$ - $q$  plot, the angle of shearing resistance of the soil samples at the critical state was estimated as 36°. This is comparable to the angle of shearing resistance estimated from the SPT  $(N_1)_{60}$  value recorded in the borehole (BH-1) which was drilled near the crown of Kanglang landslide (chapter 3).
7. For the soil-water retention curves, suction was measured using the high capacity tensiometer and the volumetric measurements were taken using a digital calliper.

The discrete procedure that allows equalisation of suction after each measurement was employed to obtain the soil-water retention curves. A total of four samples from two different depths (0.3 to 0.5 m) (K3) and (0.75 to 1 m) (K4) were tested. One from each depth was used for drying path and another for the wetting path. To prevent potential cavitation of the tensiometer, the suction measurement was terminated when the suction in the samples exceeded 550 kPa.

8. To understand the volume changes during drying and wetting, the change of void ratio with the change in gravimetric water content was examined. This showed that the change in void ratio during wetting was less profound than the change during drying of the samples.
9. Since the volume changes during drying and wetting of the samples can play a major influence on the soil water retention behaviour, the soil-water retention curves were plotted in terms of volumetric water contents. The van Genuchten model was fitted to the experimental data points and the curve fitting parameters ( $\alpha$ ,  $n$  and  $m$ ) were estimated numerically. From the plots, the air-entry value of K3 was estimated to be 83 kPa during drying and that for K4 was estimated to be 158 kPa during drying. Higher air-entry value of K4 samples is expected because of a lower void ratio. In general, the experimental data fitted fairly well with the van Genuchten model, which indicates that the model can predict the water retention behaviour to a reasonable accuracy at a lower range of suction (<1000 kPa).
10. To obtain the saturated coefficient of permeability of the soil samples, the standard triaxial constant head test was conducted by creating a pressure difference of 20 kPa across the sample. The coefficient of vertical permeability was measured at three different effective confining stresses and it was found to vary between  $1.15 \times 10^{-7}$  m/s and  $1.43 \times 10^{-8}$  m/s. A non-linear decrease in the soil permeability was also observed with increasing effective stress.

The laboratory tests provided a good estimation of the physical soil properties as well as the saturated and unsaturated, mechanical and hydrological soil properties. Further discussions of the findings from this chapter are presented in the last chapter (chapter 7). The soil parameters estimated from this chapter were used to define the material parameters for numerical modelling in chapter 6.

# Chapter 5

## Field monitoring

---

### 5.1 Chapter outline

A real-time field monitoring station was established near the crown of Kanglang landslide in March 2019 to monitor rainfall and volumetric water content (VWC) of the soil at shallow depths. The purpose of conducting field monitoring was two-fold: first, to evaluate the changes in volumetric water contents due to rainfall and drying, and second, to use the field-monitored volumetric water content to calibrate of the numerical model. This chapter focuses on the first purpose, whilst the calibration of the numerical model is elaborated in chapter 6.

In the first part of this chapter, the theoretical concepts related to flow in unsaturated soils, soil-atmospheric interaction and infiltration models are described to discuss the basic mechanisms involved in infiltration. This is followed by a review of the field-based studies and methods used for evaluating hydrological changes in unsaturated soils during rainfall. The second part focuses on the presentation of the location of monitoring station and the methods of installation. The final part of this chapter centres around the field-monitored data, focusing on the following aspects:

- i. Presentation of the daily, monthly and annual rainfall distribution in the study area.
- ii. Assessment of the daily and hourly changes in volumetric water content at different depths in response to rainfall.
- iii. Evaluation of the effects of atmospheric processes like drying and wetting on the soil water condition.
- iv. Assessment of the effects of seasonality and rainfall characteristics on the volumetric water content response of soil at different depths.

## 5.2 Background

### 5.2.1 Theoretical concepts

#### 5.2.1.1 Soil-atmosphere interaction

A schematic representation of the natural processes that occur in an unsaturated soil slope environment is shown in Figure 5.1. The unsaturated zone responds continuously to the transient environmental processes such as rainfall and evapotranspiration. These processes influence the depth of the unsaturated zone (or the depth of the groundwater table) (Lu and Likos, 2004). Infiltration is one of the primary components of the natural hydrologic cycle which determines the degree to which rainfall affects slope stability. Studies have shown that the majority of rainfall-induced shallow slope instabilities above the groundwater table occur due to infiltration resulting in a loss of suction (or generation of positive pore water pressures) (Lumb, 1975; Fredlund, 1987; Tsaparas et al., 2002; Springman et al., 2003; Godt et al., 2009; Tang et al., 2018; Rahardjo et al., 2019).

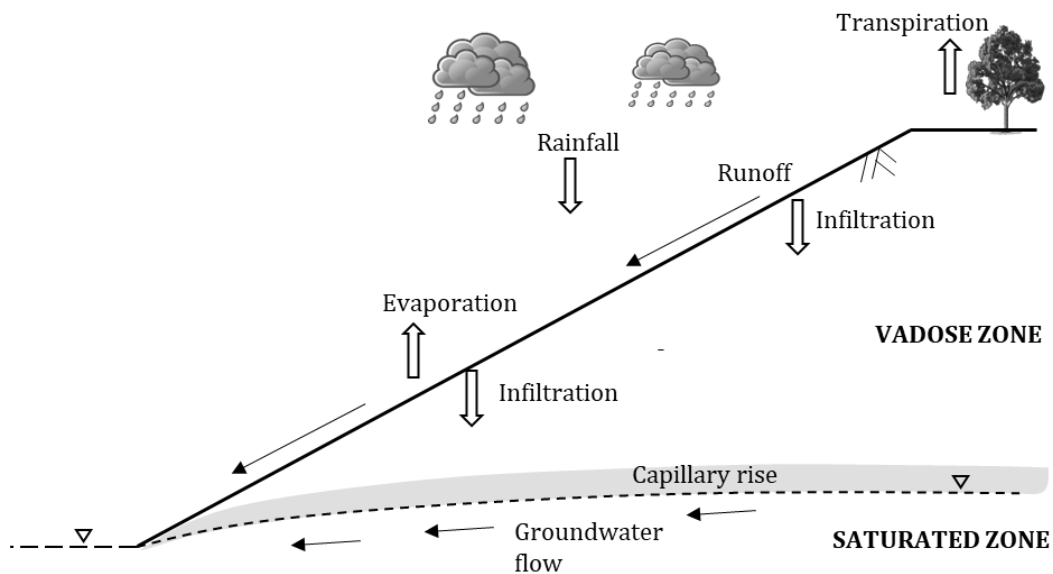


Figure 5.1 Schematic representation of natural hydrologic cycle in an unsaturated soil environment.

Rainfall is divided into three components when it reaches the ground: initial abstraction, infiltration and runoff. Premchitt et al. (1995) presented a qualitative representation of this division under an idealised scenario of constant total rainfall (Figure 5.2). This figure shows that a large portion of the rain is taken up by initial abstraction in the beginning of rainfall, which constitutes vegetation interception and depression storage. The amount of vegetation interception depends on the type and density of vegetation, antecedent rainfall

conditions and total rainfall (Penman, 1963) and the depression storage depends on the soil type, topography, land use and environmental conditions (Abd Elbasit et al., 2019). With increasing time, the interception of rainfall by vegetation and depression storage declines to a negligible time rate. The infiltration on the other hand, initially increases to a maximum and eventually decreases to a constant rate. This is most likely to occur if the soil in the upper layers becomes saturated and those in the lower layers have lower permeability preventing infiltration (Tsaparas, 2002). Under a constant rainfall total, the decrease in the rate of initial abstraction and infiltration leads to an increase in the surface runoff (Premchitt et al., 1995). In practical applications, infiltration is considered difficult to assess mainly because of the soil heterogeneity and interaction between surface and subsurface flow (Kwok and Tung, 2003). Hence, very often, infiltration is estimated by subtracting the runoff, vegetation interception and depression storage from the recorded total rainfall (Premchitt et al., 1995). However, a better approach would be to measure the water content changes in the ground, as will be described in this chapter.

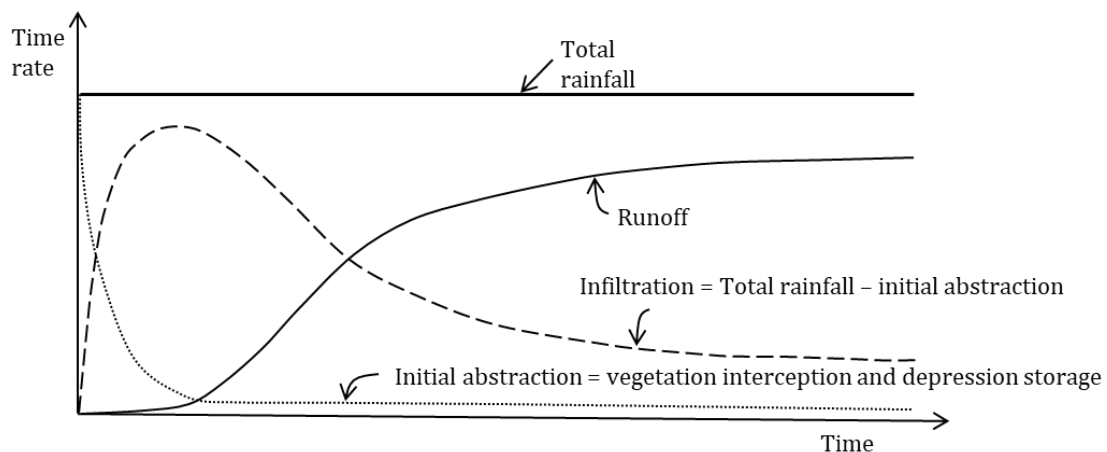


Figure 5.2 Conceptual diagram showing the rate of change of infiltration, abstraction and runoff under constant rainfall. Modified after Premchitt et al. (1995).

#### 5.2.1.2 Flow in unsaturated soil

The starting point for understanding the role of infiltration on the slope stability is to understand the basic mechanisms of water flow and pore water pressure distribution within the flow regime. It is known that regardless of the saturated or unsaturated state of the soil, water flows under the influence of hydraulic gradient, which is the sum of elevation head, pressure head and velocity head (Bernoulli's theorem) (Das, 2008). Since the seepage velocity in soils is small, the hydraulic gradient is taken as the sum of the former two components as shown in Equation 5.1.

$$h = h_m + Z = \frac{u_w}{\rho_{water}g} + Z \quad (5.1)$$

Where

$h$  = total hydraulic head

$h_m$  = matric suction head

$u_w$  = pore water pressure

$\rho_{water}$  = density of water

$g$  = acceleration due to gravity

$Z$  = elevation head

As discussed in the chapter 4, by considering the coefficient of permeability as a function of the water content (or matric suction), Darcy's law can be extended to define the flow in unsaturated soils (Buckingham, 1907; Lorenzo Adolph Richards, 1931; Childs and Collis-George, 1950). Hence, using Equation 5.1, the flow through unsaturated soil can be written as Equation 5.2.

$$q_{flow} = -k \cdot \frac{dh}{dZ} = -k \left( \frac{dh_m}{dZ} + 1 \right) \quad (5.2)$$

Where

$q_{flow}$  = flow rate of water

$k$  = coefficient of permeability

$\frac{dh}{dZ}$  = total hydraulic gradient in z-direction

$\frac{dh_m}{dZ}$  = matric suction gradient in z-direction

### 5.2.1.3 One-dimensional infiltration models

When water infiltrates into the ground, a zone of saturation is created whose lower limit is widely referred to as the wetting front. Based on this concept, physical infiltration models have been developed (Green and Ampt, 1911; Lumb, 1962; Mein and Larson, 1973;

Sun et al., 1998; Chen and Young, 2006). One of the earliest infiltration models was developed by Green and Ampt (1911). This model utilises Darcy's law to describe an idealised process of infiltration from a ponded surface into a homogenous, initially unsaturated soil. Under this model, infiltration occurs under the influence of gravity and the matric suction head, forming a sharp, piston-shaped wetting front as shown in Figure 5.3. It is assumed that the permeability of soil is constant through the wetting front and that the matric suction of soil beyond the wetting front remains unchanged. Based on the assumptions of this model, the total infiltration displacement ( $Q$ ) for a unit cross-sectional area at time  $t$  is given by Equation 5.3 and the rate of transient vertical infiltration ( $q_{inf}$ ) is written as Equation 5.4 and 5.5.

$$Q = (\theta_0 - \theta_i)z \quad (5.3)$$

$$q_{inf} = \frac{dQ}{dt} = \frac{(\theta_0 - \theta_i)dz}{dt} \quad (5.4)$$

$$q_{inf} = -k_w \frac{dh}{dz} = k_w \left( 1 + \frac{h_0 - h_i}{z} \right) \quad (5.5)$$

Where

$Q$  = total infiltration displacement or cumulative infiltration depth

$\theta_0$  = volumetric water content behind the wetting front

$\theta_i$  = volumetric water content beyond the wetting front

$q_{inf}$  = rate of infiltration

$t$  = time

$k_w$  = coefficient of permeability of soil behind the wetting front

$z$  = depth of the wetting front

$h$  = difference between total head at the wetting front ( $h_i - z$ ) and that behind the wetting front ( $h_0$ )

The combination of Equation 5.4 and 5.5 gives Equation 5.6 and by integrating this equation and applying an initial condition where  $z$  and  $t$  are zero, Equation 5.7 is obtained. This equation is used to estimate the arrival time of the advancing wetting front.



$$\frac{dz}{dt} = \frac{k_0}{\theta_0 - \theta_i} \left( 1 + \frac{h_0 - h_i}{z} \right) \quad (5.6)$$

$$t = \frac{(\theta_0 - \theta_i)}{k_0} \left[ z - (h_0 - h_i) \ln \left( 1 + \frac{z}{h_0 - h_i} \right) \right] \quad (5.7)$$

Where

$k_0$  = coefficient of permeability corresponding to  $\theta_0$

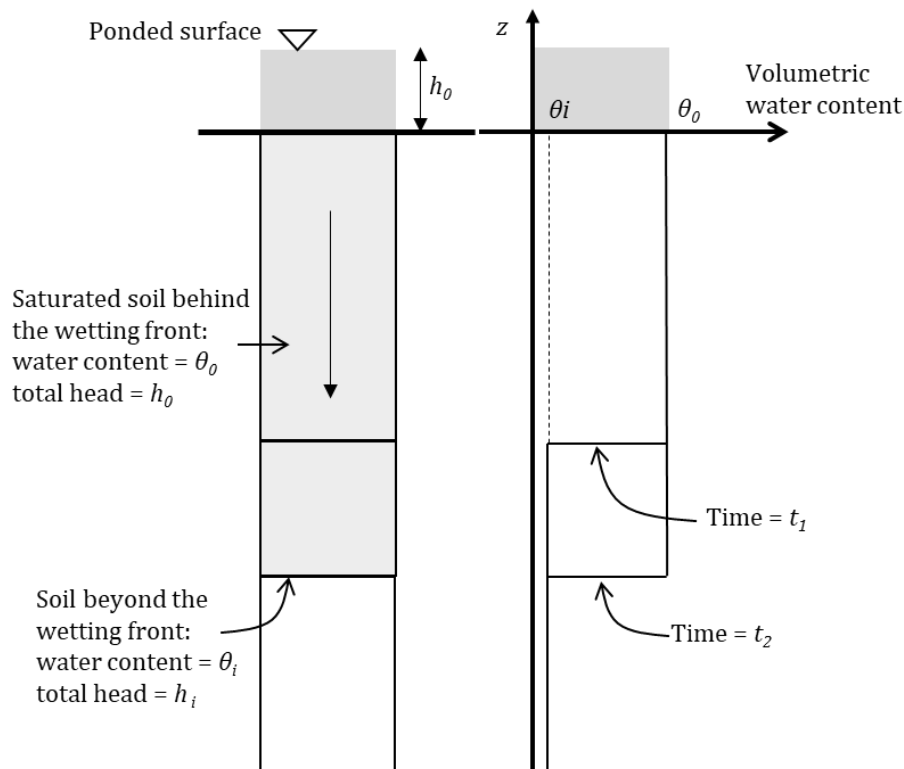


Figure 5.3 Illustration of wetting front advancement in vertical soil column and corresponding water content distribution under constant ponding at the surface, based on Green and Ampt (1911) infiltration model. Modified after Lu and Likos (2004).

Lumb (1962) also used the wetting front concept in relation to slope failure investigation in Hong Kong. As in the Green and Ampt (1911) infiltration model, the saturated zone is considered to propagate downwards forming a sharp wetting front as shown in Figure 5.4 and the permeability of soil within the wetting front is considered to be constant. The depth of the wetting front is calculated using Equation 5.8. This equation assumes that the soil near the ground surface becomes saturated during rainfall and the rainfall intensity at the surface is equal to the saturated soil permeability.

$$z = \frac{k_{sat} t}{n(S_f - S_0)} \quad (5.8)$$

Where

$k_{sat}$  = saturated coefficient of permeability

$t$  = elapsed time

$n$  = porosity of soil

$S_f$  = final degree of saturation

$S_0$  = initial degree of saturation

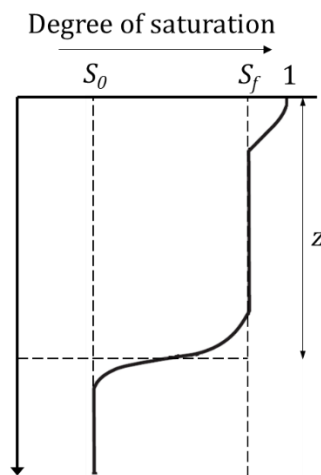


Figure 5.4 Variation of degree of saturation due to the advancement of wetting-front during infiltration. Modified after Lumb (1962).

The wetting front equation proposed by Lumb (1962) was modified by Sun et al. (1998) to incorporate the conditions when the rainfall intensity is less than the saturated coefficient of permeability. Based on this model, the depth of the wetting front is defined by Equation 5.9.

$$z = \frac{(k_1 - k_{initial})t}{\theta_1 - \theta_{initial}} \quad (5.9)$$

Where

$z$  = depth of the wetting front

$t$  = rainfall duration or time

$k_1$  = unsaturated coefficient of permeability equal to the rainfall intensity at time  $t$

$k_{initial}$  = initial unsaturated coefficient of permeability equal to the initial surface flux

$\theta_1$  = final volumetric water content at time  $t$

$\theta_{initial}$  = initial volumetric water content

The previous models assume that the ground surface is horizontal. However, infiltration into sloping ground may be of interest, especially for slope stability problems. The Green and Ampt (1911) model was extended by Chen and Young (2006) to formulate the infiltration rate in a homogenous sloping surface. Under a ponding condition at the surface, as per Chen and Young (2006) (Figure 5.5). The depth of wetting front can be calculated using Equation 5.10 and the arrival time of the wetting front is defined using Equation 5.11.

$$Q = (\theta_0 - \theta_i) z_f^* \quad (5.10)$$

$$t = \frac{(\theta_0 - \theta_i)}{k_w \cos \gamma} \left[ z_f^* - \frac{(s_f + H)}{\cos \gamma} \ln \frac{z_f^* \cos \gamma + s_f + H}{s_f + H} \right] \quad (5.11)$$

Where

$Q$  = cumulative infiltration depth

$\theta_0$  = volumetric water content behind the wetting front

$\theta_i$  = volumetric water content beyond the wetting front

$z_f^*$  = depth of the wetting front normal to the ground surface

$t$  = arrival time of the wetting front

$k_w$  = coefficient of permeability of soil behind the wetting front

$\gamma$  = slope angle

$s_f$  = matric potential head at the wetting front

$h_{ponding}$  = ponding depth normal to the ground surface

$H$  = ponding water head on sloping ground =  $h_{ponding} \cos \gamma$

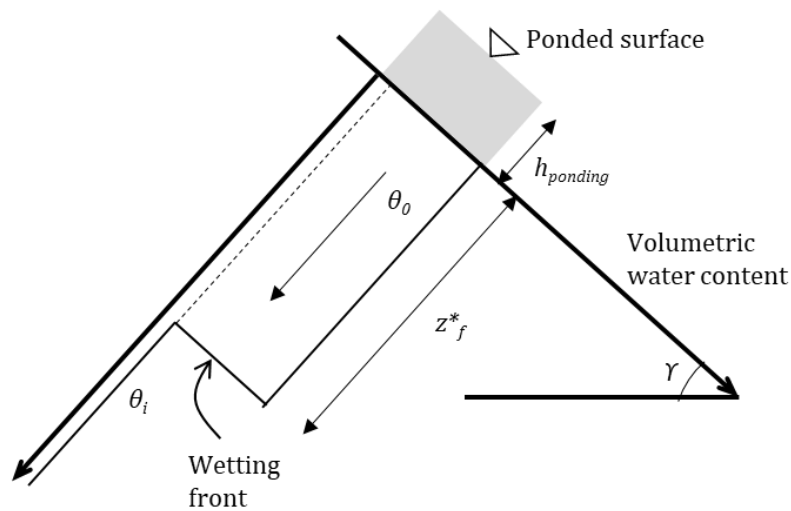


Figure 5.5 Schematic diagram showing wetting front advancement in sloping ground. Modified after Chen and Young (2006).

These infiltration models can provide useful insights into the depth and arrival time of the wetting front during infiltration. However, they are based on assumptions of soil homogeneity, constant permeability and water content within the wetting front and constant suction head at the wetting front. While the assumptions simplify the models, they may not provide an accurate reflection of reality. In reality, the infiltration mechanism is influenced by several factors including soil heterogeneity, unsaturated soil permeability, rainfall characteristics, temperature, vegetation and depression storage (Premchitt et al., 1995; Ng and Shi, 1998; Tsaparas, 2002; Godt et al., 2012; Assouline, 2013), which are not considered. To understand the infiltration process and its consequent effects on the pore water pressure distribution and slope stability, several studies have utilised field measurements and numerical modelling. In the next section, a review of the field-based studies is presented.

### 5.2.2 Review of field-based studies

Globally, several studies have utilised long-term field-monitoring to understand the infiltration mechanisms and resulting changes in pore water pressure and slope stability in both natural and man-made slopes. Such field-monitoring programs typically involve measurement of soil water content, pore water pressure, temperature, air pressure and precipitation.

Rahardjo et al. (2005) instrumented an experimental cut slope in Singapore, underlain by residual soil derived from the weathering of a sedimentary formation. The runoff, pore water pressure and soil water content changes were monitored during both simulated and

natural rainfall events. This study found that about 40 to 100% of the rainfall total can contribute to infiltration, depending on the rainfall intensity, duration and antecedent soil water condition. This study also suggested that the amount of rainfall contributing to infiltration decreased with an increase in the rainfall total; events with a larger rainfall total (>40 mm) was found to contribute more towards runoff generation than to infiltration. Similar observations were reported by Tsaparas et al. (2003) where the authors investigated the infiltration characteristics using field measurements at the same location. Tsaparas et al. (2003) also showed that a high rainfall total does not necessarily translate into high infiltration, but the rainfall is likely to infiltrate if the soil near the ground surface is dry due to low antecedent rainfall conditions. Rahardjo et al. (2005) also found that the change in the volumetric water content in the slope during rainfall was influenced by the number of dry days that preceded the rainfall event.

Tu et al. (2009) employed the application of artificial rainfall on an instrumented road cut slope in Northwest China for understanding the infiltration mechanism and pore water pressure response. Real-time measurements of soil water content, ground water level, pore water pressure, air pressure and rainfall were undertaken. This study showed that the active zone of infiltration and evaporation was within 0.7 m of the ground surface in loess during rainfall with a maximum intensity of 40 mm/day. The depth of wetting front and consequent increase in volumetric water content and decrease soil suction was found to increase with the increase in rainfall intensity and duration.

A similar experimental study was undertaken by Li et al. (2005) in a natural saprolite hillslope underlain by completely decomposed to moderately decomposed granite in Hong Kong. Field measurements of volumetric water content and matric suction were examined to understand the wetting front movement during rainfall. This study found that approximately 70% of the total rainfall can infiltrate and change the soil water content at shallow depths; the maximum depth of the wetting front was found to be limited within the upper 3 m of soil. The observations from this study also showed that although low-intensity rainfall increased the volumetric water content of the soil in the upper 2 m, only high-intensity rainfall (~194.5 mm/day) could lead to the development of a transient perched water table at this depth.

Hawke and McConchie (2011) conducted real-time monitoring of volumetric water content, suction and positive pore water pressures within the Lake Tutira catchment, New Zealand that is prone to shallow landsliding. The monitored data showed that the soil water content at 0.25 m depth responded instantaneously to any rainfall over ~10 mm/day and this response became more sensitive during the dry periods as a result of evapotranspiration. This study also pointed out that the drying of soil due to evapotranspiration was much

slower than the wetting of soil during rainfall. An interesting observation from this study was that despite the high sensitivity of soil at 0.25 m to rainfall, larger rainfall (~40 mm/day) was required to detect a response of volumetric water content at 0.5 m and no noticeable changes in volumetric water content were detected at 1 m and below. The authors explained this behaviour by relating it to the porosity of the soil. Since the soil near the surface had a higher porosity, it captured the available moisture resulting in rapid changes during rainfall. This left little moisture for percolation to the lower layers that already have a reduced porosity much of which is occupied by pre-existing moisture. As a result, changes in the volumetric water content of soils in the lower layers were much less during rainfall. Toll (2006) explains this behaviour in terms of soil permeability for tropical residual soils in Singapore. According to Toll (2006), during rainfall, infiltration creates a zone near the ground surface that has a high degree of saturation and high permeability. At the lower layers however, the degree of saturation and permeability of soil are relatively small. This encourages the water to flow down the slope within this near-surface zone instead of flowing to greater depths. As a result, relatively small changes in pore water pressure can be observed at greater depths than near to the ground surface due to infiltration.

Smith et al. (2013) evaluated three years of field measurements of rainfall, volumetric water content, suction and positive pore water pressures in the Oregon coast range, USA. The data showed strong seasonal variations in volumetric water content and pore water pressures. The volumetric water content and pore water pressure generally increased with the onset of the rainy season and remained high throughout this period. The sensors located at shallow depths recorded maximum seasonal variations, almost double that recorded by deeper sensors. Moreover, this study showed that the lag time in response to rainfall and drying was proportional to sensor depth; as the depth of the sensor increased, their response time to rainfall also increased.

Comegna et al. (2016) discussed the hydrological response of a pyroclastic soil slope in Cervinara, Italy using a field-monitored record of rainfall, suction and volumetric water content. In this study, the authors highlighted that the hydrological response of soil during rainfall is linked to the initial soil moisture conditions. Since the rainfall-based empirical landslide failure thresholds do not take into account the initial condition of the soil, the authors argued that they have limited reliability for landslide assessments.

All the studies discussed above have utilised field measurements of both volumetric water content and pore water pressures. However, when the measurement of pore water pressure is not feasible, the field measurement of volumetric water content alone can also provide useful information on the hydrologic response of soil slopes (Tohari, 2018). For instance,

Chae and Kim (2012) successfully used field measurements of volumetric water content and rainfall in Deoksan, Korea, to estimate the infiltration velocity and its relationship with cumulative rainfall. The infiltration velocity was calculated as the ratio of the vertical distance between surface and sensor depth and the difference in time between rainfall arrival time and the time of maximum volumetric water content. This study showed that the infiltration velocity decreased with the increase in cumulative rainfall and slope angle. Similarly, Harris et al. (2012) instrumented a failed road cut slope in Auckland, New Zealand, with volumetric water content sensors and rain gauge to monitor the hydrological response of slope. The pattern of volumetric water content changes observed in this study was similar to that reported by Hawke and McConchie (2011). Additionally, the volumetric water content and rainfall data obtained from the field was used to calibrate the numerical model for the back-analysis of failure mechanism.

From the above discussion, it is evident that volumetric water content is a soil parameter that is commonly measured in the field. By monitoring the volumetric water content, the infiltration pattern occurring in unsaturated soils can be evaluated. Additionally, by analysing the long-term variations in volumetric water content during rainfall, the effects of various rainfall patterns, as well as antecedent conditions, on hydrological soil response can be assessed. Furthermore, the instruments used for volumetric water content are relatively easy to install and maintain. According to Chae and Kim (2012), the volumetric water content response during infiltration is much quicker than the pore water pressure response, although this may vary depending on the type of sensor adopted. Hence, the measurement of volumetric water content in the field is not only useful but appealing because of the advantages related to instrumentation.

In the context of Nepal, it is known that shallow landslides occur extensively across the country every year during the monsoon (Dahal et al., 2009; Dahal, 2012; Thapa, 2015). Studies have tried to identify critical rainfall thresholds for landslide occurrence using statistical methods. One of the earliest studies undertaken by Caine and Mool (1982) in the Kolpu Khola catchment, central Nepal, suggested that the landslide threshold due to a 24-hour rainfall is ~100 mm. This threshold is based on the empirical rainfall threshold for slope failures (debris flows initiated as shallow planar slides) derived by Caine (1980), which can be written in terms of rainfall depth ( $d$ ) and rainfall duration ( $D$ ) ( $d=14.82D^{0.61}$ ) or in terms of rainfall intensity ( $I$ ) and duration ( $D$ ) ( $I=14.82D^{-0.39}$ ). Dahal et al. (2009) suggested that continuous rainfall lasting for 1 to 2 days is considered responsible for shallow slope failures in the Lesser Himalaya region. Another study conducted by Dahal and Hasegawa (2008) has shown that the probability of landslides is highest when the daily rainfall exceeds 144 mm. This rainfall threshold was derived empirically by using the

rainfall data corresponding to 193 landslides that occurred in Nepal between 1951 and 2006, which is written in terms of rainfall intensity and duration as  $I=73.9D^{-0.79}$ .

However, as discussed before, the hydraulic behaviour of slopes during rainfall can vary depending on the initial conditions, topography, rainfall patterns, seasonality and local heterogeneity. Hence, the occurrence of landslides in a larger area is unlikely to be successfully predicted using a single rainfall total or intensity-based thresholds. As noted by Toll et al. (2011, p. 1) *“it is not rainfall per se that causes a slope to fail; rather it is a change in pore water pressure in the soil resulting from rainfall infiltration”*. A study undertaken by Gerrard and Gardner (2000) in the Likhu Khola drainage basin located north of Kathmandu has suggested that the landslides occur as a result of gradual increase in water content and pore water pressures and not due to high-intensity, short-duration rainfall events. This agrees with the numerical study conducted by Tsaparas et al. (2002) in Singapore. However, in Nepal, field-monitoring based evidence showing the effects of transient infiltration on water content and pore water pressure response in unsaturated soils is scarce. This has limited the understanding of the rainfall-induced failures occurring in initially unsaturated soil slopes in Nepal. Hence, in this study, volumetric water content sensors were installed in the field to monitor the water content changes in the soil in response to rainfall and drying. Using the field-monitoring data, the effects of various factors on volumetric water content response were evaluated.

### 5.2.3 Methods used for measurement of volumetric water content in the field

Different methods for the direct measurement of soil water content have been developed over the last two decades (Robinson et al., 2008). The most common method is using electromagnetic methods for continuous measurement of in-situ soil water contents (Mittelbach et al., 2012). The electromagnetic methods utilise the high relative dielectric permittivity of water ( $\sim 80$  at  $20^\circ\text{C}$ ) to measure the water content of soils. When the electromagnetic method-based sensors are installed in the ground, they measure the charge storage capacity of the soil. Since the charge storage capacity of water is much greater than that of other soil constituents like air (permittivity  $\sim 1$ ) and sediments (permittivity  $\sim 5$ ), any changes in permittivity recorded by the sensor can be related to the changes in the water content (Topp, 2003). These sensors are based on either time domain reflectometry (TDR) or frequency domain reflectometry (FDR), or capacitance.

TDR sensors operate by releasing an electromagnetic impulse along the sensor probes inserted into the soil. This signal travels to the ends of the probes and is reflected back and the travel time is measured. The travel time is related to the permittivity of the medium and



hence, to the water content in the soil (Topp, 2003). Similarly, the FDR sensor also releases an electromagnetic signal along the sensor rods and instead of measuring time, it measures the oscillating frequency of the electromagnetic impulse that is influenced by the capacitance which depends on the dielectric permittivity of the soil (Czarnomski et al., 2005). The capacitance-based technique uses soil as a capacitor element and relates the charge storing capacity of the soil to the water content (Topp, 2003). In the capacitance-based sensors, two parallel probes act as the electrodes (one positively charged, and the other negatively charged). By charging and discharging the positive electrode, an electromagnetic field is created around the probes, whose charging time is related to the capacitance of the medium between the electrodes (Decagon Devices, 2010). Since the capacitance is related to the dielectric permittivity, when the sensor is installed in the ground, the dielectric permittivity of the soil can be obtained which is then correlated with the volume of water present in the soil (Decagon Devices, 2010).

The TDR-based sensors are known for their accuracy, however, they are expensive (Mittelbach et al., 2012). These sensors can also be difficult to install and use more power for operation (METER Environment, 2017). Similarly, the FDR-based sensors can also be complicated to install and require additional power for operation (Czarnomski et al., 2005). On the other hand, capacitance-based sensors can be installed easily and have low power requirements. Other advantages of these sensors include a large volume of influence, fast response time and low cost compared to other sensors (METER Environment, 2017). Hence, in this study, capacitance-based 10HS sensors were installed in the field.

### 5.3 Field monitoring station

The field monitoring station was installed near the crown of Kanglang landslide in March 2019. The three components of the field monitoring station were: i) 10HS soil moisture sensors to measure the volumetric water content of the soil, ii) rain gauge to measure rainfall, and iii) data logger to log and transfer the recorded data.

To ensure that the monitored data reflected the real behaviour of the landslide under study, it was crucial to establish the monitoring station in a suitable location. Generally, the field instrumentation for landslide monitoring is carried out near the landslide crown or where signs of movement are visible on the surface. However, other factors also needed consideration while selecting the location for field instrumentation. These included safety and survivability of the instruments for long-term operation, mobile network reception for data transfer, accessibility for installation and maintenance and permission from the landowner for access and installation.

Considering these factors, the monitoring station was installed approximately 10 m west of the landslide crown (27°53'28.79"N, 85°54'31.69"E, 1460 m a.s.l.) (Figure 5.6). Next to the monitoring station, a trial pit (1.5 m × 1.0 m × 1.5 m) was excavated to install the soil moisture sensors. The excavation of this trial pit was discussed in chapter 3 (section 3.5.4). The samples collected from this trial pit were brought to the laboratory for geotechnical characterisation and testing. The colour and textural properties of the soil samples obtained from this trial pit and from the borehole located next to the landslide crown (BH-1) (chapter 3) were found to be similar (chapter 4, section 4.3.2). This suggested that the location selected for field instrumentation is representative of the failed section of the slope.

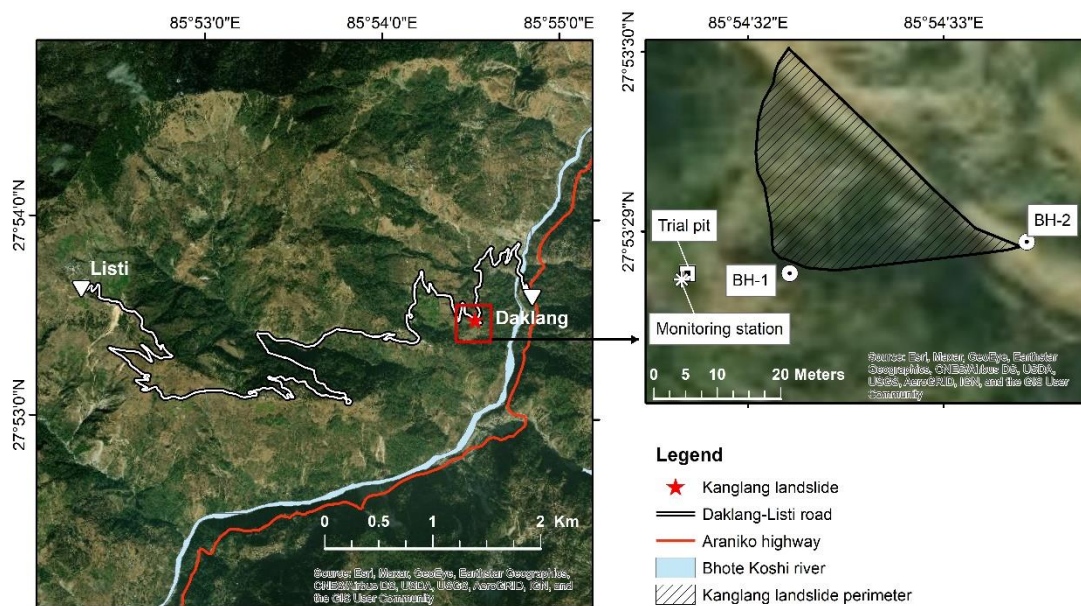


Figure 5.6 Location of field monitoring station (27°53'28.79"N, 85°54'31.69"E) relative to Kanglang landslide.

### 5.3.1 Instrumentation

#### 5.3.1.1 10HS soil moisture sensor

The 10HS soil moisture sensor (Figure 5.7) uses the capacitance-based technique to measure the volumetric water content of the soil. The sensor consists of two parallel prongs that are 100 mm in length and 9.8 mm in width, separated by a 12.1 mm space. The specifications of the 10HS sensor are summarised in Table 5.1.

The sensitivity of the 10HS sensors can be influenced by the soil type, which suggests the need for individual soil calibration (Kargas and Soulis, 2012; Vaz et al., 2013). With the manufacturer's standard calibration equation for mineral soils, the sensors provide direct

measurements of the volumetric water content with  $\pm 3.3\%$  VWC ( $0.033 \text{ m}^3/\text{m}^3$ ) accuracy (Decagon Devices, 2010). In this study, the focus was placed on evaluating the relative changes in volumetric water content in response to wetting and drying, rather than estimating the absolute values of the volumetric water content. Hence, soil-specific calibration was not performed in this study. The volumetric water content estimated using the manufacturer's standard calibration equation was considered to be satisfactory as the volumetric water contents measured by the sensors at the time of installation ( $0.27 \text{ m}^3/\text{m}^3$  at 0.3 m,  $0.26 \text{ m}^3/\text{m}^3$  at 0.8 m,  $0.32 \text{ m}^3/\text{m}^3$  at 1.2 m) was found to be comparable to that of the undisturbed soil samples obtained from the field ( $0.24 \text{ m}^3/\text{m}^3$  at 0.5 m,  $0.28 \text{ m}^3/\text{m}^3$  at 1 m).



Figure 5.7 10HS soil moisture smart sensor. Source: ONSET (2018b, n. Date accessed: 16-06-2020).

Table 5.1 Specifications of 10HS soil moisture sensors. Source: Decagon Devices (2010).

Dimensions	160 mm × 32 mm × 2 mm
Measurement range	0 to $0.57 \text{ m}^3/\text{m}^3$
Resolution	$0.0008 \text{ m}^3/\text{m}^3$
Accuracy	$\pm 0.033 \text{ m}^3/\text{m}^3$ ( $\pm 3.3\%$ ) for mineral soils
Volume of influence	1 litre
Measurement time	10 milliseconds
Operating temperature	0 to 50 °C
Frequency	70 MHz

#### 5.3.1.2 Rain gauge

A tipping bucket-type rain gauge (HOBO® S-RGB-M002) was installed at the monitoring station. This rain gauge measures rainfall with a resolution of 0.2 mm and 1% accuracy up to 127 mm/hour (ONSET, 2018a). Heating system was not provided on the rain gauge as snow is not expected at the study site.

### 5.3.1.3 Data logger

A data logger (HOBO RX3000 remote monitoring station data logger) shown in Figure 5.8 was installed in the field to record data from the 10HS sensors and the rain gauge. It has a rugged weatherproof enclosure which is suited for remote outdoor monitoring (ONSET, 2019). A sampling interval ( $\geq 1$  second) and a logging interval (1 minute to 18 hours) can be configured in this logger. The logger takes multiple measurements at the specified sampling interval within a given logging interval and then records their average as a single logged data point (ONSET, 2019). In this study, the data logger was programmed to log the data at 1-minute intervals. For the power supply, a 5-Watt solar panel (SOLAR-xW) was connected to the data logger and a 4 Volt, 10 Ahr, rechargeable sealed lead-acid battery was fitted inside the box for power back-up. With a cellular connection, the logged data was accessed remotely using the online Hobolink platform.



Figure 5.8 HOBO RX3000 remote monitoring station data logger. Source: ONSET (2019, n. Date accessed: 16-06-2020).

### 5.3.2 Installation of the field monitoring station

Figure 5.9 (a) presents the schematic diagram of the field monitoring station installed near Kanglang landslide. On the undisturbed vertical wall of the trial pit (chapter 3, section 3.5.4), the 10HS soil moisture sensors were installed horizontally at depths of 0.3 m, 0.8 m, and 1.2 m below the ground surface, as shown in Figure 5.9 (b). Installation of the sensors within the undisturbed vertical wall is crucial to allow a natural flow of water and to avoid the possibility of preferential flow paths reaching the sensors. During installation, if the sensors hit any obstructions such as stones or plant roots, the electrodes could be damaged. To prevent this, a dummy metallic sensor with thickness and length the same as that of the sensor prong was pushed into the pit wall at the desired depths before inserting the actual sensor. After inserting the sensors, the trial pit was carefully backfilled with the excavated materials in layers to achieve the approximate density of the surrounding soils. The cabling was placed inside a PVC pipe to protect them from external factors like water and animals

and was connected to the data logger. A wooden frame, as shown in Figure 5.9 (c), was positioned approximately 1 m from the trial pit, on which the rain gauge and data logger were mounted. The solar panel was also installed facing a south-east direction to power the data logger. The monitoring station was enclosed using a barbed wire fence to protect from potential damage, as shown in Figure 5.9 (c).



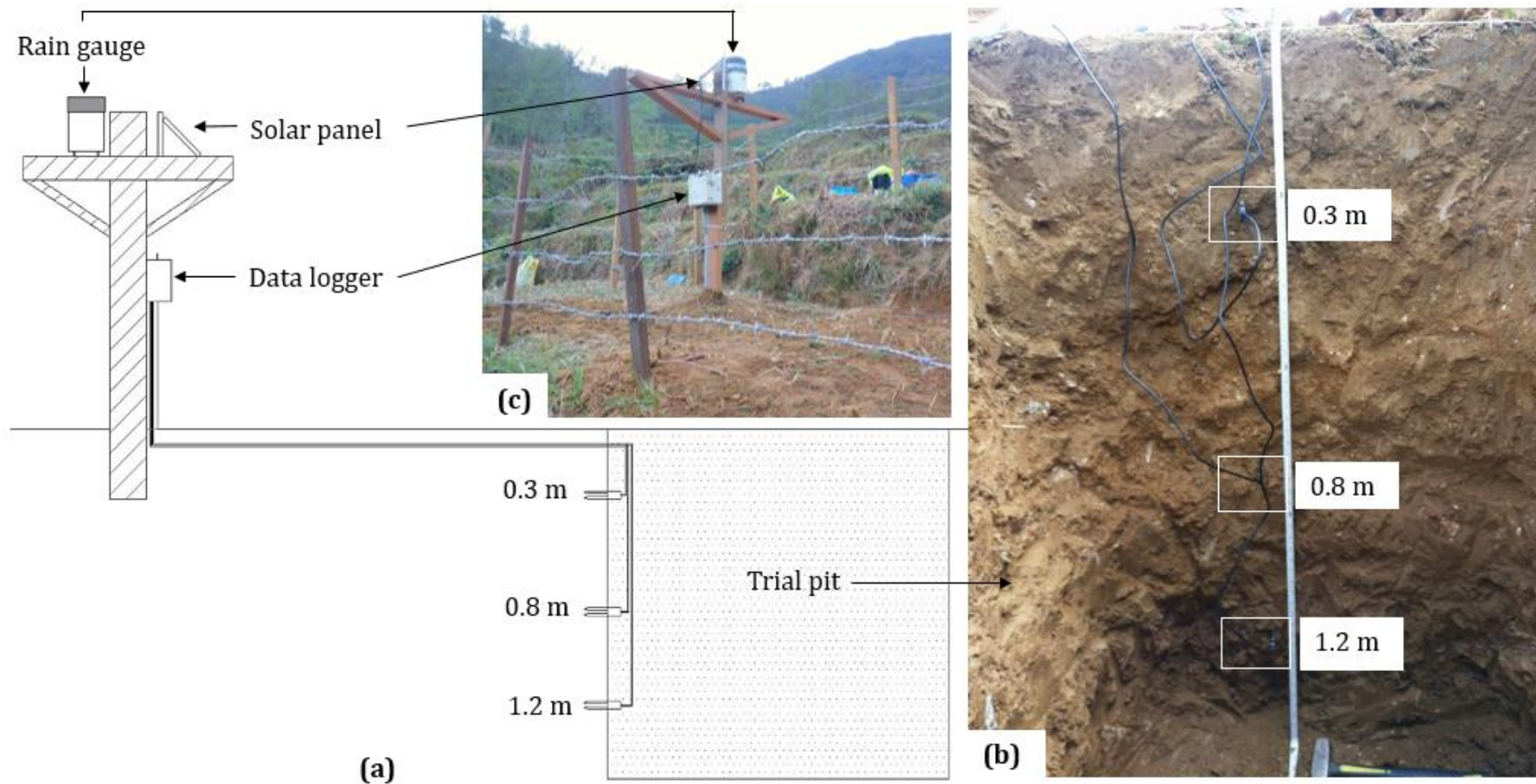


Figure 5.9(a) Schematic illustration of the field monitoring station (not to scale), (b) horizontal installation of 10HS soil moisture sensors on the vertical wall of trial pit at 0.3 m, 0.8 m and 1.2 m (c) complete set-up of the field monitoring station at Kanglang landslide ( $27^{\circ}53'28.79''\text{N}$ ,  $85^{\circ}54'31.69''\text{E}$ , 1460 m a.s.l.).

## 5.4 Observations of field-monitored rainfall and volumetric water content

The rainfall and volumetric water content of the soil at Kanglang landslide were monitored continuously from 27 March 2019 to 28 March 2020. A complete year-long record of rainfall and volumetric water content measurements was evaluated on an annual, monthly, daily and hourly basis, which are discussed in the following sections.

### 5.4.1 Rainfall

#### 5.4.1.1 Daily rainfall

The time series of daily rainfall measured over the year-long monitored period is presented in Figure 5.10. As shown in this figure, a total rainfall of 2690.4 mm was recorded which constituted 199 wet days and 169 dry days based on a threshold of >0.2 mm rainfall per day. As expected, the monsoon season was the wettest period of the year when ~81% of the total rainfall was recorded. During the monsoon, rainfall was recorded almost every day with only 6 individual dry days. The longest consecutive wet period lasted for 74 days from 14/06/2019 to 26/08/2019. On the other hand, after the monsoon, the longest dry period with less than 0.4 mm rainfall was recorded from 08/10/2019, which lasted for 65 days until 13/12/2019. Further information on the daily rainfall is presented in Table 5.2.

In Table 5.2 and Figure 5.11, the daily rainfall data has been divided into two groups: the period between 01/06/2019 and 30/09/2019 has been termed as 'monsoon' and the remaining time before the monsoon (27/03/2019 to 31/05/2019) and after the monsoon (01/10/2019 to 28/03/2020) has been termed as the 'pre-' and 'post-monsoon' periods.

An examination of the frequency distribution of daily rainfall totals during the monitoring period (Figure 5.11) showed that the frequency of smaller daily rainfall totals was greatest, decreasing almost in an exponential manner with increasing total daily rainfall. For comparison, the histograms of daily rainfall totals during the monsoon and the pre- and post-monsoon are shown in Figure 5.11. In this figure, the difference in the skewness of the two histograms, also shown in Table 5.2, is evident. The figure suggests that the number of days with smaller rainfall totals (<5 mm) was greater during the pre- and post-monsoon period than during the monsoon period. Nonetheless, during both periods, with the increase in the magnitude of daily rainfall, the frequency decreased in an exponential manner.

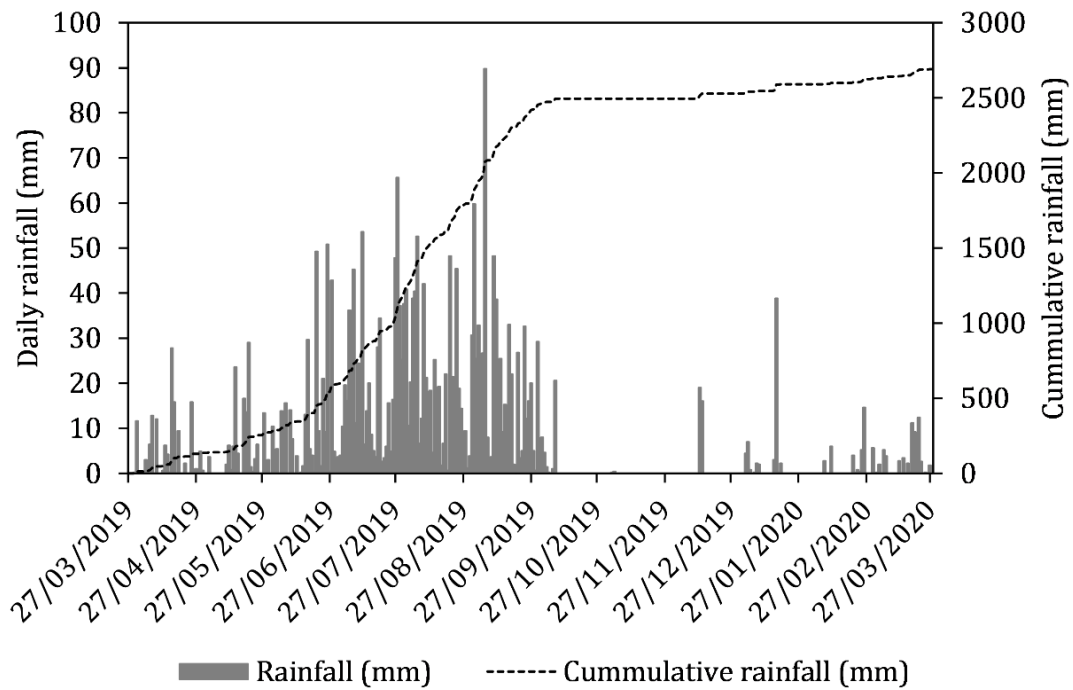


Figure 5.10 Daily rainfall measured during monitoring period from 27/03/2019 until 28/03/2020.

Table 5.2 Summary of daily rainfall measured during the monitoring period from 27/03/2019 to 28/03/2020.

	<b>Monsoon (2019)</b>	<b>Pre- and post-monsoon (2019/2020)</b>
Total number of days	122	246
Number of wet days	116	83
Number of dry days	6	163
Total rainfall (mm)	2181.4	509.0
Average daily rainfall (mm)	18.8	6.1
Maximum daily rainfall (mm)	89.8	38.8
Skewness	1.3	2.1



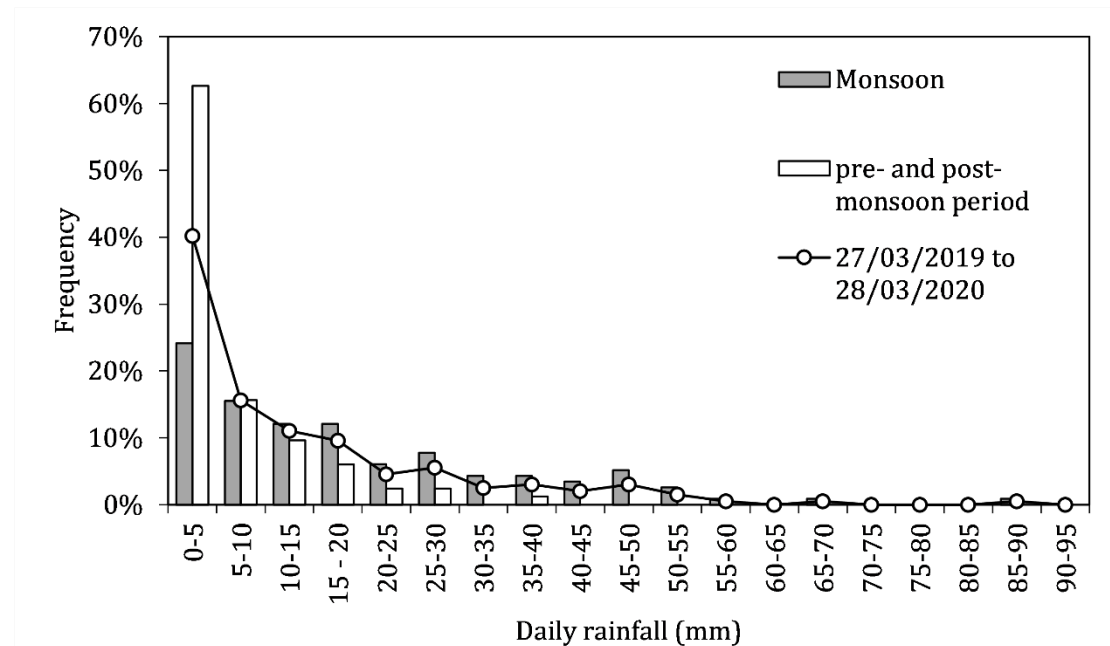


Figure 5.11 Distribution of daily rainfall (i) during the monitoring period (27/03/2019 to 28/03/2020) shown by the line-graph, (ii) during the monsoon (01/06/2019 to 30/09/2019) shown by bar-graph (dark), and (iii) during pre- and post-monsoon periods (27/03/2019 to 31/05/2019 and 01/10/2019 to 28/03/2020) shown by bar-graph (white).

To compare the observed rainfall with the average rainfall in this area, rainfall data from 1955 to 2018 (64 years) measured at the nearest meteorological station in Gumthang, Sindhupalchok (27°51'19.1"N, 85°51'34.7"E, 1846 m a.s.l) was obtained from Department of Hydrology and Meteorology, Nepal (DHM, 2018). In Figure 5.12 a clear monsoon-dominated rainfall pattern is evident in both the 64-year average and monitored rainfall totals. The total rainfall during the monitoring period was approximately 75% of the average annual rainfall in this area (3599 mm), which suggests that the year 2019 was relatively dry. The monitored rainfall during the dry months of 2019 and 2020 was comparable to that of the 64-year average monthly rainfall. However, it is worth noticing that the total monthly rainfall was nearly constant throughout the monsoon period in 2019 at the monitoring station, while a notable decrease after August can be seen in the 64-year rainfall record from Gumthang station. This discrepancy is most likely due to the distance and the difference in elevation, topography and local conditions between the two locations as the Gumthang station is located at ~6 km distance and ~390 m above the study site. For comparison, the monthly rainfall totals (from April to October 2019) recorded at the field monitoring station and that measured at Gumthang are plotted together in Figure 5.13. Interestingly, the rainfall at Kanglang was found to be greater than that at Gumthang in June and July 2019. This could be the result of localised rainfall events that occurred at the field-monitoring station in Kanglang. In August and September 2019, both stations recorded a

similar monthly rainfall totals. From the limited available data, a fairly strong correlation was obtained between the two datasets which is shown in Figure 5.14. This correlation also indicated that the rainfall at the field monitoring station was slightly greater than that measured at Gumthang. With a larger dataset, this relationship could be explored further. However, this was not pursued due to lack of data availability.

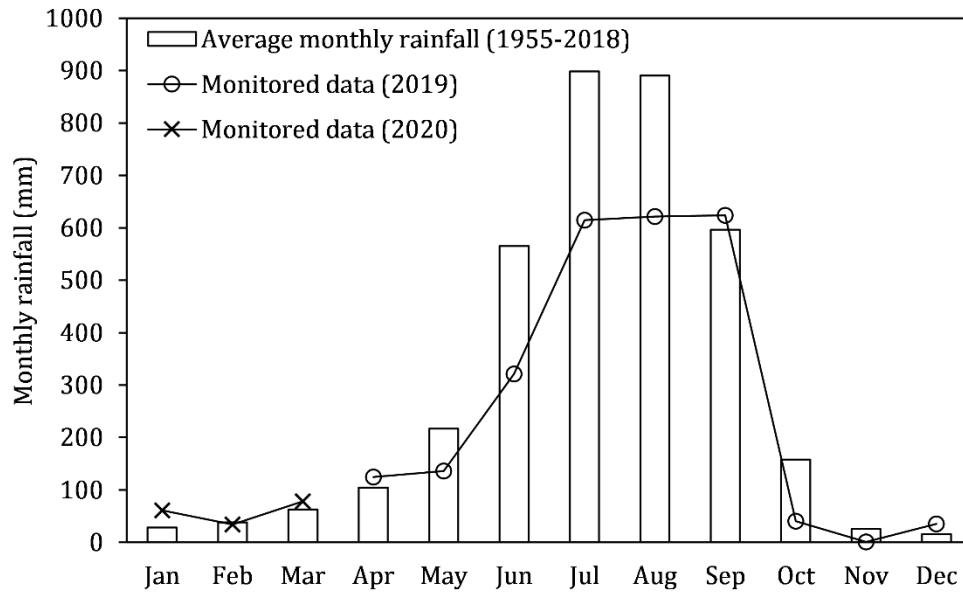


Figure 5.12 Comparison of the monitored rainfall data from 27/03/2019 to 28/03/2020 with the 64-year average monthly rainfall (1955 – 2018) measured at Gumthang meteorological station.

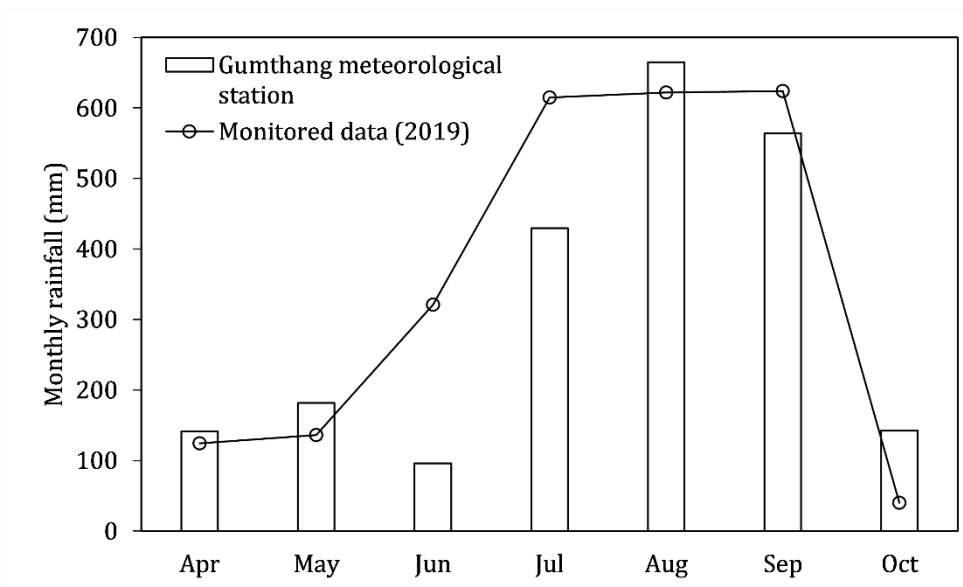


Figure 5.13 Comparison of monthly rainfall measured at Kanglang landslide and Gumthang meteorological station from 01/04/2019 to 31/10/2019.

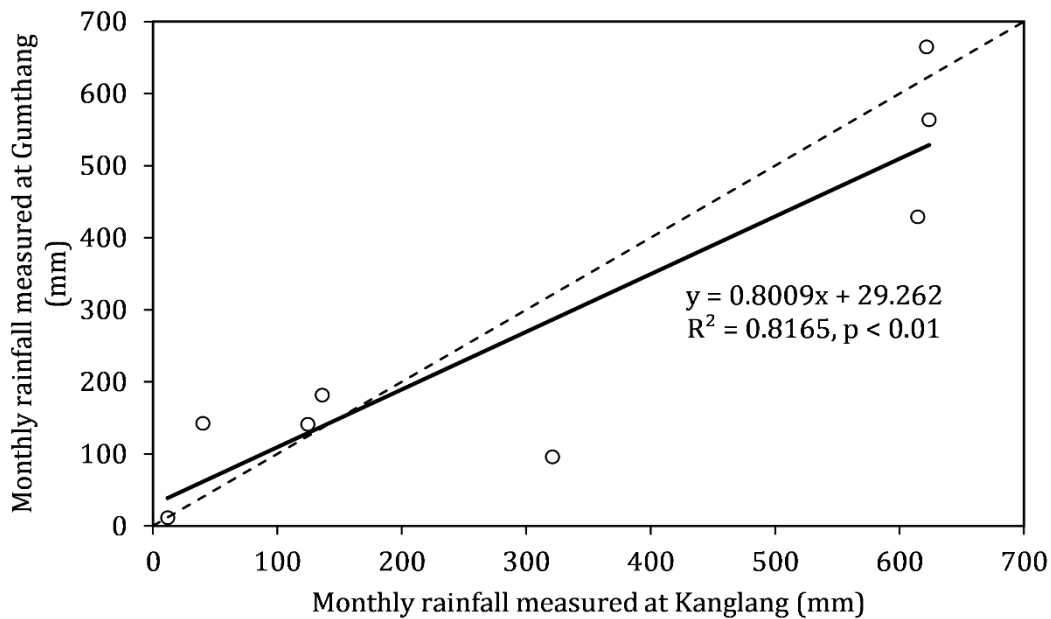


Figure 5.14 Relationship between monthly rainfall totals measured at the field-monitoring station in Kanglang and Gumthang meteorological station.

#### 5.4.1.2 Rainfall events distribution

To evaluate the effects of rainfall on the volumetric water content changes, individual rainfall events were identified from the hourly rainfall data recorded in the field from 27/03/2019 to 28/03/2020. Continuous rainfall that accumulated more than 2 mm rainfall without any interruption was classified as an individual rainfall event. Altogether 182 rainfall events were identified. The rainfall events constituted 2577 mm of rainfall (182 rainfall events), which is ~96% of the total annual precipitation measured in the field. The details about the individual rainfall events are summarised in Appendix A-2.

As shown in Figure 5.15 (a), the highest and lowest number of discrete rainfall events were recorded in July 2019 (41 events) and December 2019 (2 events) respectively. Overall, ~70% of the rainfall events were recorded during the monsoon season. Moreover, the total rainfall accumulated during a single rainfall event ranged from 2.2 mm to 90.8 mm. The histogram for total rainfall (Figure 5.15 (b)) shows that a maximum number of rainfall events (96 events) constituted less than 10 mm of total rainfall. This figure also highlights the fact that the number of events decreased in an exponential manner with the increase in total rainfall, and that the occurrence of relatively extreme events was rare during the monitored period.

Similarly, the histogram for total rainfall duration (Figure 5.15 (c)) shows that the majority of the rainfall events (144 events) lasted for less than 6 hours. This figure also follows a

similar trend indicating that the occurrence of extreme events such as those lasting for 10 hours or more were rare during the monitoring period. In Figure 5.15 (d), the distribution of rainfall events based on the average hourly rainfall intensity is shown. The average hourly rainfall intensity was obtained by dividing the total rainfall during a rainfall event by its duration. For the rainfall events, the average rainfall intensity ranged from 0.4 to 13.3 mm/hr. It can be seen from this figure that low-intensity rainfall events (<4mm/hr) occurred more frequently. Additionally, the maximum hourly rainfall intensities during the rainfall events ranged from 5 to 40 mm/hr and the occurrence of the events with a high peak hourly intensity was much less frequent, as can be seen in Figure 5.15 (e). In Figure 5.15 (f), the observed rainfall events are plotted in terms of their average rainfall intensities and durations. As can be noted from this figure, the landslide-triggering rainfall threshold defined by Caine (1980) was exceeded by 11 rainfall events, whereas none exceeded the threshold defined by Dahal and Hasegawa (2008).

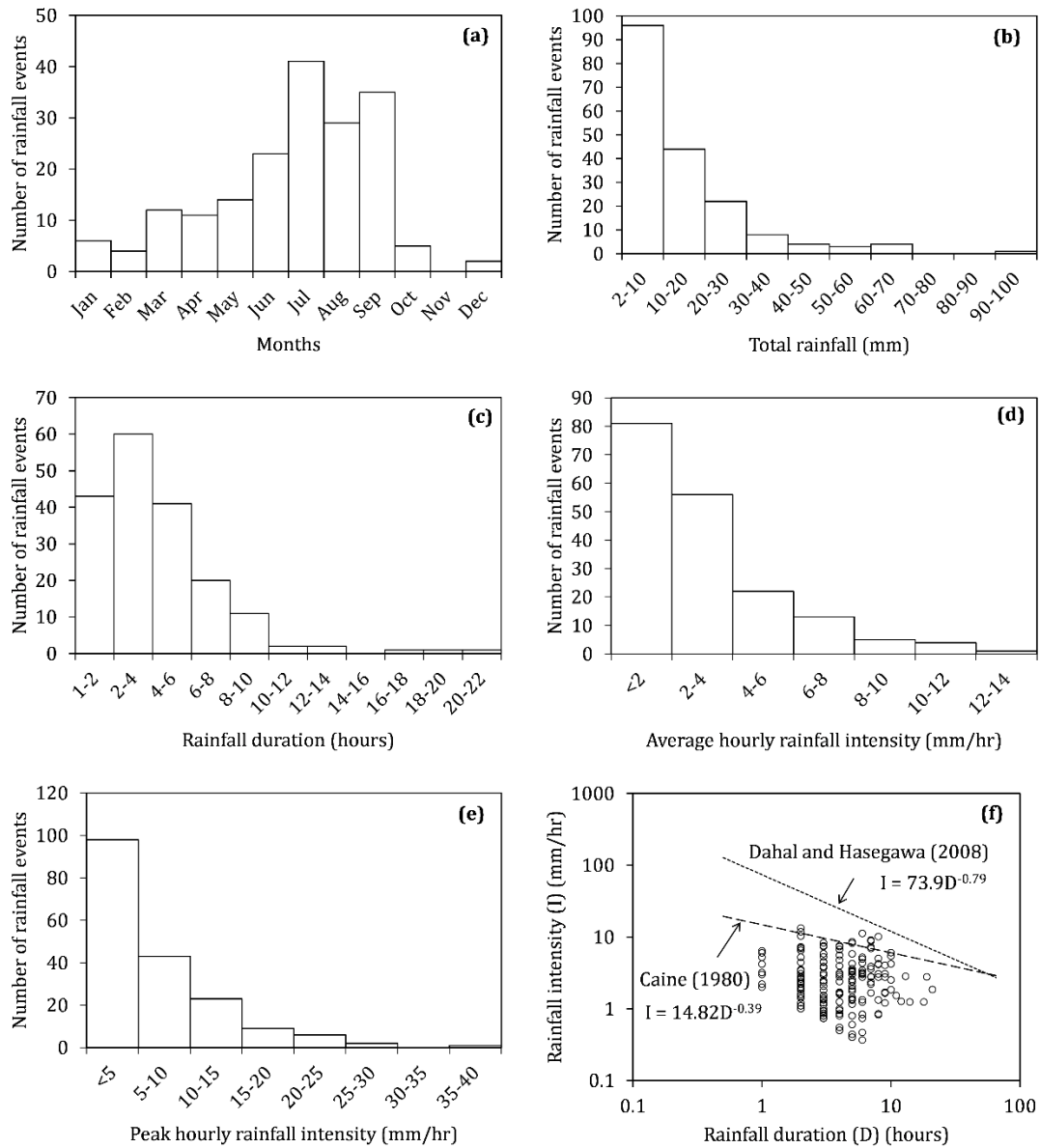


Figure 5.15(a) Monthly distribution of rainfall events during the monitored period (27/03/2019 to 28/03/2020), (b) frequency statistic for total rainfall, (c) frequency statistic for rainfall duration, (d) frequency statistic for average hourly rainfall intensity, (e) frequency statistic for peak hourly rainfall intensity and (f) average rainfall intensity-duration relationships for the observed rainfall events in comparison to the landslide-triggering thresholds defined by Caine (1980) and Dahal and Hasegawa (2008).

## 5.4.2 Volumetric water content

### 5.4.2.1 Average daily volumetric water content

The temporal variation in the average daily volumetric water content of the soil at 0.3 m, 0.8 m and 1.2 m due to atmospheric drying and wetting process during the monitoring period is shown in Figure 5.16. The first thing that can be noticed from the figure is that even with a relatively small increase in depth, the pattern of volumetric water content fluctuations differed significantly. Additionally, the pattern of change in volumetric water content can also be seen to be affected by the seasonal changes.

During the relatively dry months before and after the monsoon, the fluctuations in volumetric water content at 0.3 m were found to be directly associated with rainfall and atmospheric drying processes. Such a quick response to wetting and drying can be attributed to the presence of surficial cracks that dominate the coefficient of permeability of the soil at the surface. Compared to the fluctuations at 0.3 m, the variations in volumetric water content of the soil at 1.2 m was different during the pre- and post- monsoon periods. From Figure 5.16 it can be seen that during these periods, volumetric water content at 1.2 m remained relatively stable and consistently higher than that in the upper layers. At 0.8 m, the volumetric water content increments during the pre- and post- monsoon periods did not occur immediately after rainfall. At this depth, a slight increase in volumetric water content was observed during the pre-monsoon period and a gradual decline in volumetric water content was found during the prolonged dry period in the post-monsoon season; however, both were not as pronounced as that at 0.3 m. An unusual drop in the volumetric water content at 0.8 m occurred on 10/02/2020. After this drop, prominent fluctuations in volumetric water content were recorded at this depth than at 0.3 m, which indicated malfunctioning of the instrument.

During the monsoon (June to September), the volumetric water content of soil at all three depths fluctuated continuously. At 1.2 m, the first notable increase in volumetric water content came after the rainfall events in late June 2019, which was preceded by similar notable changes at 0.8 m and 0.3 m. A saturation line representing the soil porosity at 1.2 m is shown in Figure 5.16. The soil porosity at 1.2 m was estimated by linear interpolation using the known porosity of soil at 0.5 m, 1 m, and 1.5 m (Table 4.10) ( $d = -6.84n + 3.98$ ,  $R^2 = 0.99$ , where  $d$  and  $n$  are soil depth and porosity respectively). It can be seen in Figure 5.16 that the soil at 1.2 m did not reach full saturation even during the monsoon which could be because the infiltrating water advanced below this depth, as indicated by the fluctuations in volumetric water content observed at 1.2 m.

The box plot shown in Figure 5.17 further highlights the observation that the maximum changes in volumetric water content occurred at 0.3 m and 0.8 m compared to those at 1.2 m. This figure shows that the average daily volumetric water content at all depths attained a maximum value during the monsoon period. It is interesting to see that the standard deviation of volumetric water content at 0.3 m and 0.8 m are the same (Table 5.3), which suggests that the fluctuations in volumetric water content from their respective mean were comparable at these depths. The volumetric water content at 1.2 m which was already higher throughout the year increased to  $0.36 \text{ m}^3/\text{m}^3$  during the monsoon. This implies that the soil at this depth was approaching saturation as defined by the soil porosity ( $\sim 0.4$ ) at this depth.

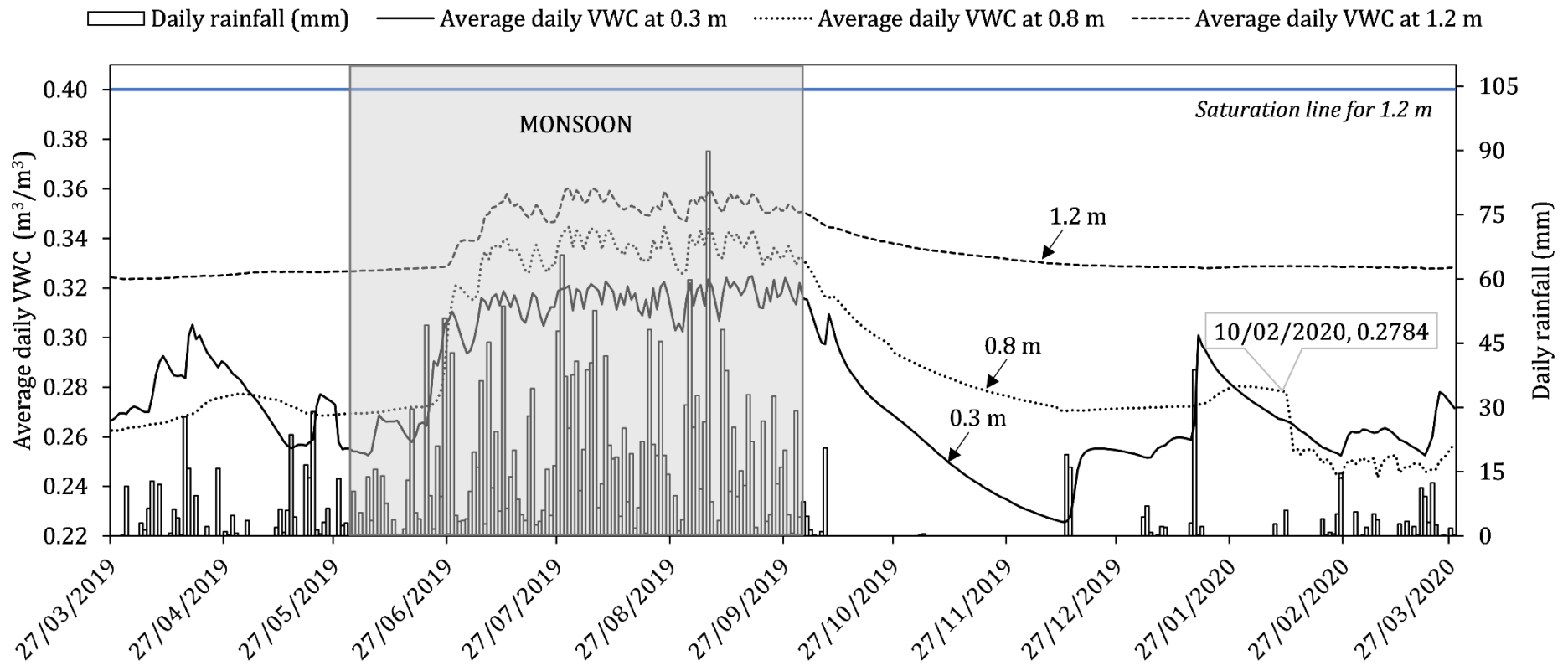


Figure 5.16 Average daily volumetric water content and daily rainfall recorded during monitoring period (27/03/2019 to 28/03/2020).



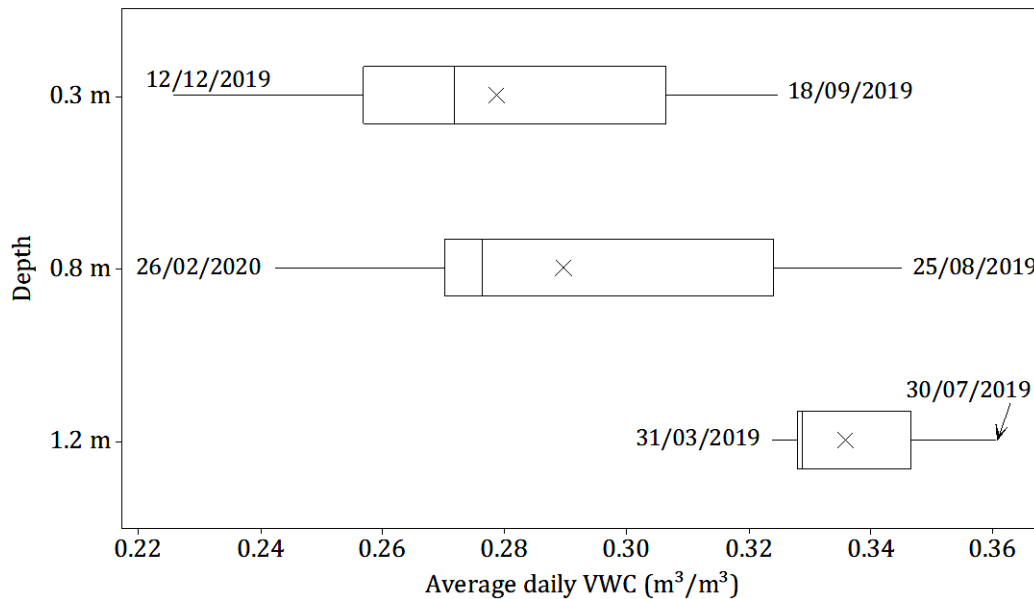


Figure 5.17 Variation in average daily volumetric water content (VWC) with depth (from 27/03/2019 to 28/03/2020). Statistics denoted by the box plots are summarised in Table 5.3.

Table 5.3 Statistical summary of the box plot shown in Figure 5.17.

Depth (m)	Average daily VWC (m <sup>3</sup> /m <sup>3</sup> )						Standard deviation
	Mean	Maximum	Minimum	Q1	Median	Q3	
0.3	0.28	0.33	0.23	0.26	0.27	0.31	0.03
0.8	0.29	0.35	0.24	0.27	0.28	0.32	0.03
1.2	0.34	0.36	0.32	0.33	0.33	0.35	0.01

Q1: first quartile and Q3: third quartile

#### 5.4.2.2 Effect of atmospheric drying and wetting on the hydrological soil response

To understand the soil-water movement in response to atmospheric drying and wetting, the change in the degree of saturation with depth during a prolonged dry and wet period was assessed. The degree of saturation was obtained from the measured average daily volumetric water content assuming that the porosity of the soil remained unchanged.

During the 40-day long continuous rainfall period from 21/06/2019 to 30/07/2019, the degree of saturation at 0.3 m, 0.8 m and 1.2 m increased by ~21%, ~27% and ~10% respectively, as shown in Figure 5.18. Moreover, a gradual downward movement of the wetting front in unsaturated soil with time due to rainfall can also be visualised in this plot.

Although the degree of saturation at 1.2 m changed relatively less ( $\sim 10\%$ ) than the upper layers, the advancement of the wetting front to 1.2 m increased the degree of saturation to nearly 90% ( $VWC = 0.36 \text{ m}^3/\text{m}^3$ ) at the end of the wet period. Referring back to chapter 4 (Table 4.10), the porosity of soil at 1.5 m is 0.364. If the pattern of infiltration illustrated in Figure 5.18 is continuous down to 1.5 m, the soil at this depth may have reached full saturation during this wetting period. These observations suggest that during prolonged wet periods, water can infiltrate to 1.2 m or more leading to an increased degree of saturation ( $>90\%$ ). Such a progressive saturation of soil could cause dissipation of matric suction, reduction of shear strength and ultimately, cause shallow slope failures (Pradhan et al., 2020).

Similarly, the longest dry period from 09/10/2019 to 12/12/2019 (65 days) was selected to evaluate the effect of atmospheric drying on the soil water content. As shown in Figure 5.19, during this period, the degree of saturation at 0.3 m decreased by  $\sim 27\%$  and at 0.8 m, the degree of saturation reduced by  $\sim 14\%$ . The interesting observation from Figure 5.19 is that the decrease in the degree of saturation at 1.2 m was  $\sim 4\%$ , which is significantly lower than that in the upper layers. From this observation, it can be said that the effect of atmospheric drying was significant at shallow depth (0.3 m), however, this became less pronounced as the depth increased. Such an interaction between soil and atmosphere explains the consistently high volumetric water content recorded at 1.2 m throughout the monitoring period (Figure 5.16).

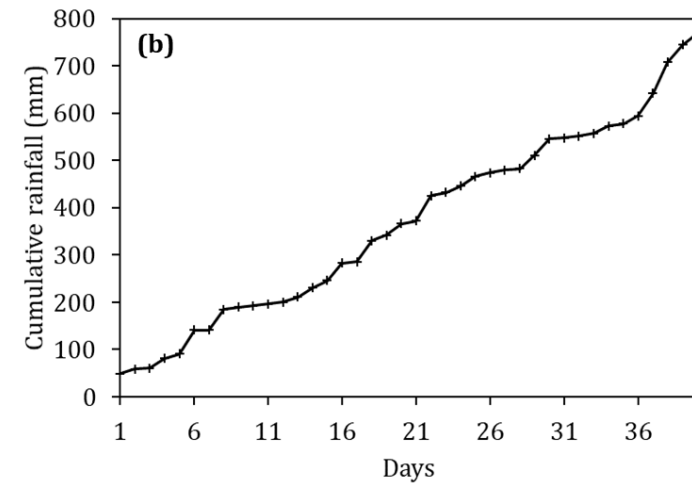
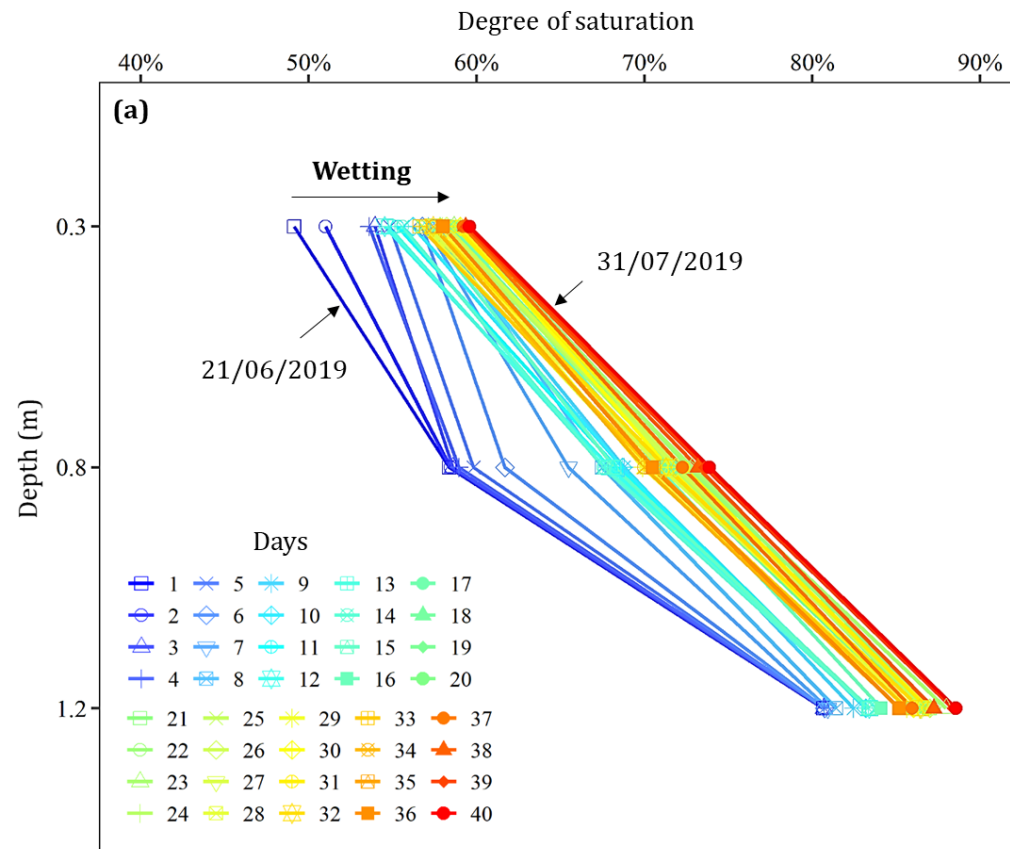


Figure 5.18 (a) Variation in the degree of saturation with depth during continuous wetting (the numbers in the legend represent days starting from day 1 on 21/06/2019 to day 40 on 31/07/2019), (b) cumulative rainfall from day 1 on 21/06/2019 to day 40 on 31/07/2019.

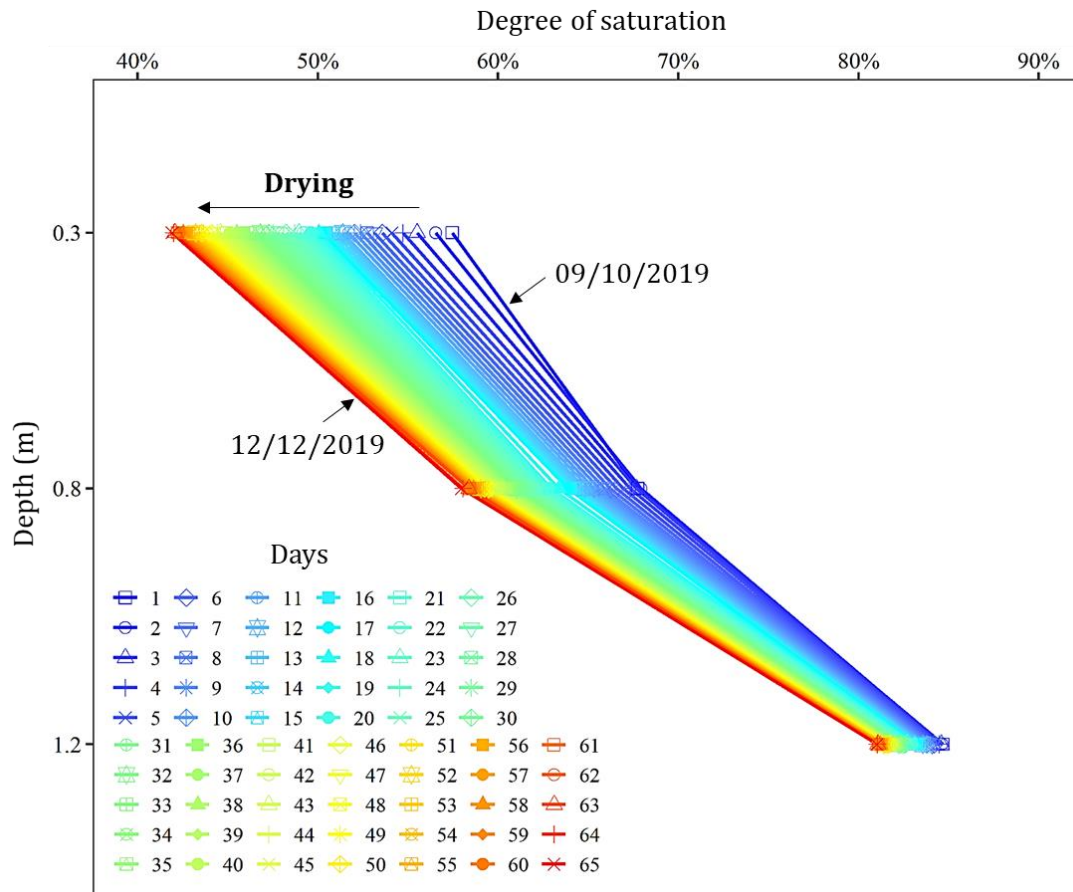


Figure 5.19 Variation in the degree of saturation with depth during continuous drying (the numbers in the legend represent days starting from day 1 - 09/10/2019 to day 65 - 12/12/2019).

#### 5.4.2.3 Hourly changes in volumetric water content

The evaluation of average daily volumetric water content in section 5.4.2.1 provided a useful understanding of the long-term and seasonal variations in water content. However, the volumetric water content when averaged over a day may distort the actual condition if, for example, in a certain day a few hours of rainfall was followed by long hours of drying or vice-versa. Hence, it is necessary to evaluate the hydrological changes at a smaller temporal scale to capture the hydrological changes induced by individual rainfall events. In this section, the hourly changes in the volumetric water content in response to discrete rainfall events are discussed.

As discussed in the previous sections, the volumetric water content fluctuated continuously at all three measured depths during the monsoon. To evaluate the hourly changes in the volumetric water content, the variations observed during the mid-monsoon period between 30/07/2019 and 07/08/2019 is shown in Figure 5.20 (left). From this figure, it is clear that the increase in volumetric water content was strictly related to infiltration. The sensor located at 0.3 m responded first after a rainfall event, which was followed sequentially by

the sensors located at 0.8 m and 1.2 m. Also, the response times of the sensors were found to be related to the rainfall characteristics. Overall, the three sensors located at increasing depths from the surface effectively captured the infiltration pattern down to 1.2 m during rainfall.

Furthermore, in Figure 5.20 (right), the 13-hour long rainfall event between 03/08/2019 and 04/08/2019 is highlighted. It can be seen in the figure that during this rainfall event, the volumetric water content at 0.3 m increased at first, almost 5 hours after rainfall started. The volumetric water content at 0.3 m continued to rise for the next six hours before starting to decrease. This decrease was followed by a gradual rise in the volumetric water content at 0.8 m. For the next five hours, the volumetric water content at 0.8 m kept increasing and when it stopped, the volumetric water content at 1.2 m started to rise. This shows that the lag time of volumetric water content response at 0.3 m, 0.8 m and 1.2 m during/after a rainfall event increased with depth. Visually, from Figure 5.20 (right) it can be said that it would take around 15 to 16 hours for the rainfall to infiltrate to 1.2 m. However, it should be noted that the lag in the response time may be influenced by the rainfall intensity and duration, as well as by the soil's hydraulic properties. To assess if similar time-lags were recurrent during the monitored period, cross-correlation analysis was conducted, which is discussed in the next section.

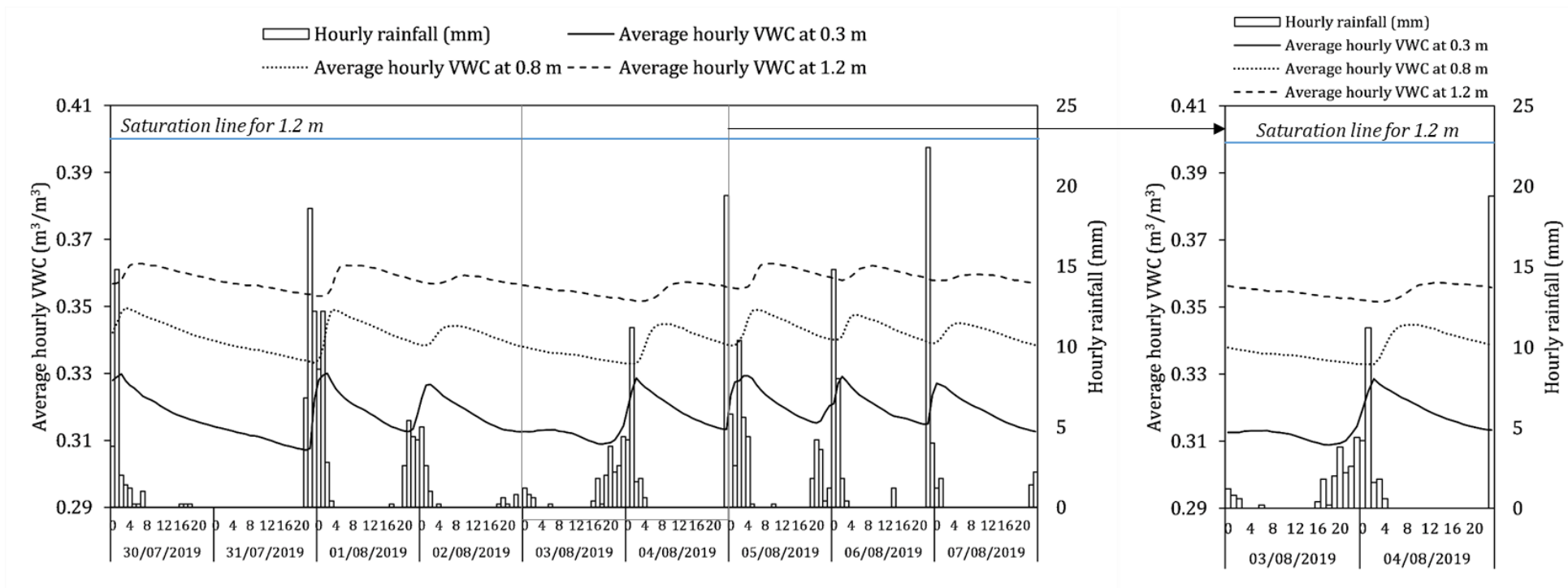


Figure 5.20 Variation in average hourly volumetric water content and rainfall between 30/07/19 and 07/08/19 (left), and between 03/08/19 and 04/08/19 (right).

#### 5.4.2.4 Cross-correlation analysis

The observation of hourly changes in volumetric water content showed that the soil water response was linked directly to rainfall, but the response was not instantaneous. During rainfall, the sensor located closest to the ground surface (0.3 m) responded first and a time-lag of 5 to 6 hours was observed for the infiltrating water to increase the volumetric water content at 0.8 m and 1.2 m successively. To further explore the relationship between rainfall and volumetric water content response, and to see if the time-lag evaluated visually from Figure 5.20 was recurrent over the monsoon, a cross-correlation analysis was undertaken. By conducting the cross-correlation analysis, the time-delay between rainfall and volumetric water response at increasing depths from the surface was quantified.

The cross-correlation function (CCF) is useful to describe the relationship between two input time series at a certain time period apart. Previous studies have used this function to evaluate the relationship between rainfall and groundwater level fluctuations (Chae et al., 2010; Nawawitphisit, 2014; Cai and Ofterdinger, 2016) and between rainfall and soil moisture changes (Mahmood et al., 2012). The cross-correlation function is obtained by dividing the covariance of the two variables by the product of their standard deviations. The CCF between the two time series  $x_T$  and  $y_{T+K}$  is written as Equation 5.12.

$$CCF = \frac{\sum_{T=1}^{N-K} (x_T - \bar{x})(y_{T+K} - \bar{y})}{S_x S_y} \quad (5.12)$$

Where

$N$  = number of observations

$T$  = row number

$K$  = lag

$\bar{x}$  = mean of x

$\bar{y}$  = mean of y

$$S_x = \sqrt{\sum_{T=1}^N (x_T - \bar{x})^2}$$

$$S_y = \sqrt{\sum_{T=1}^N (y_T - \bar{y})^2}$$

In this study, the cross-correlation function was obtained between rainfall ( $x_T$ ) and average hourly volumetric water content at 0.3 m 0.8 m and 1.2 m depths ( $y_{T+K}$ ) measured during the monsoon season, when maximum fluctuations in volumetric water content and rainfall were recorded. The correlation between the two time-series is considered significant if the following expression (Equation 5.13) was satisfied.

$$CCF > \frac{2}{\sqrt{N - |K|}} \quad (5.13)$$

The correlation between hourly rainfall and average hourly volumetric water content at 0.3 m was found to be statistically significant at a lag time of 2 to 5 hours (highest correlation of 0.164 at 3-hour lag) (Figure 5.21). This agrees with the observation made in Figure 5.20 (right), where the volumetric water content at 0.3 m increased after approximately 5 hours of rainfall. Furthermore, as shown in Figure 5.22, at 0.8 m, the strongest correlation was recorded at a longer time-lag of 7 to 10 hours. Similarly, the correlation between rainfall and volumetric water content at 1.2 m was strongest at a time-lag of 11 to 15 hours shown in Figure 5.23. The increase in the response time with increasing depth from the ground surface shown by cross-correlation analyses shows good agreement with discussions in the previous section referring to Figure 5.20.

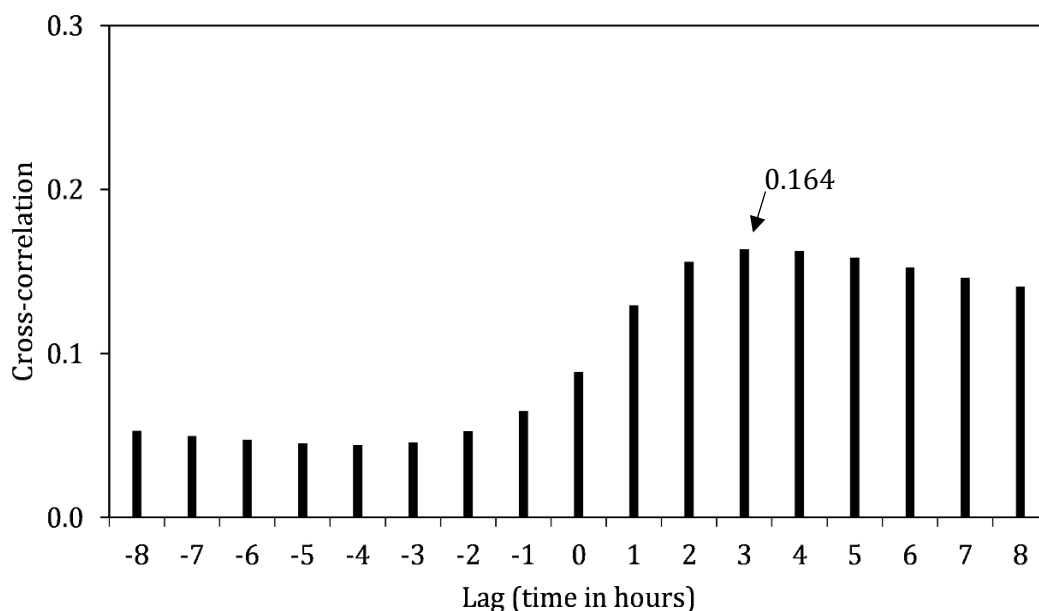


Figure 5.21 Cross-correlation function for hourly rainfall and average hourly volumetric water content at 0.3 m.



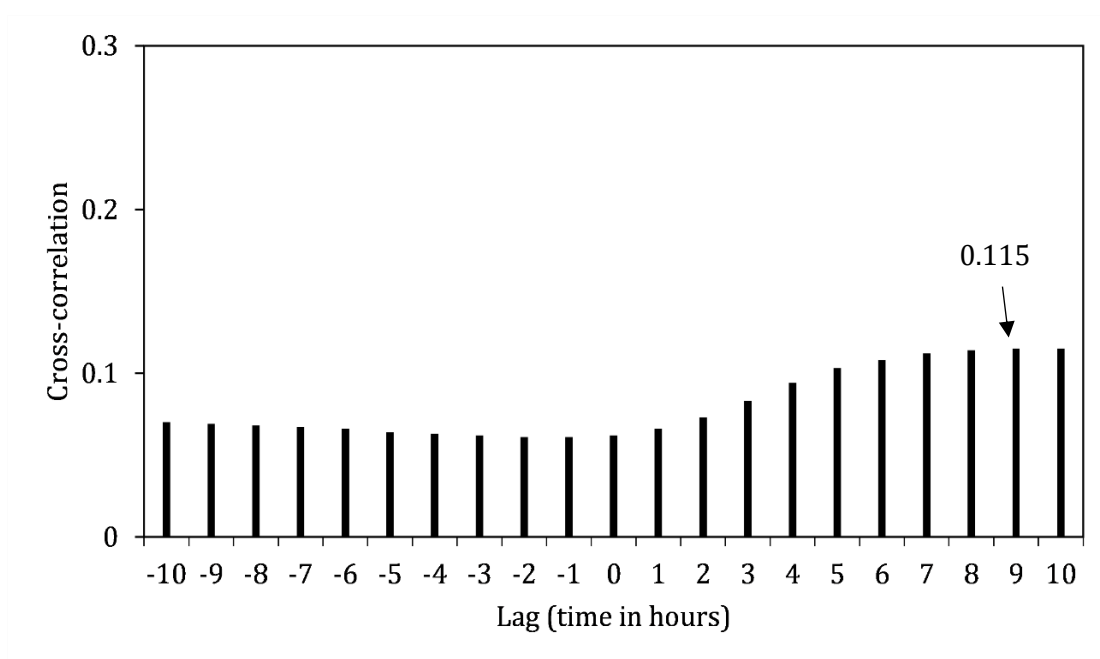


Figure 5.22 Cross-correlation function for hourly rainfall and average hourly volumetric water content at 0.8 m.

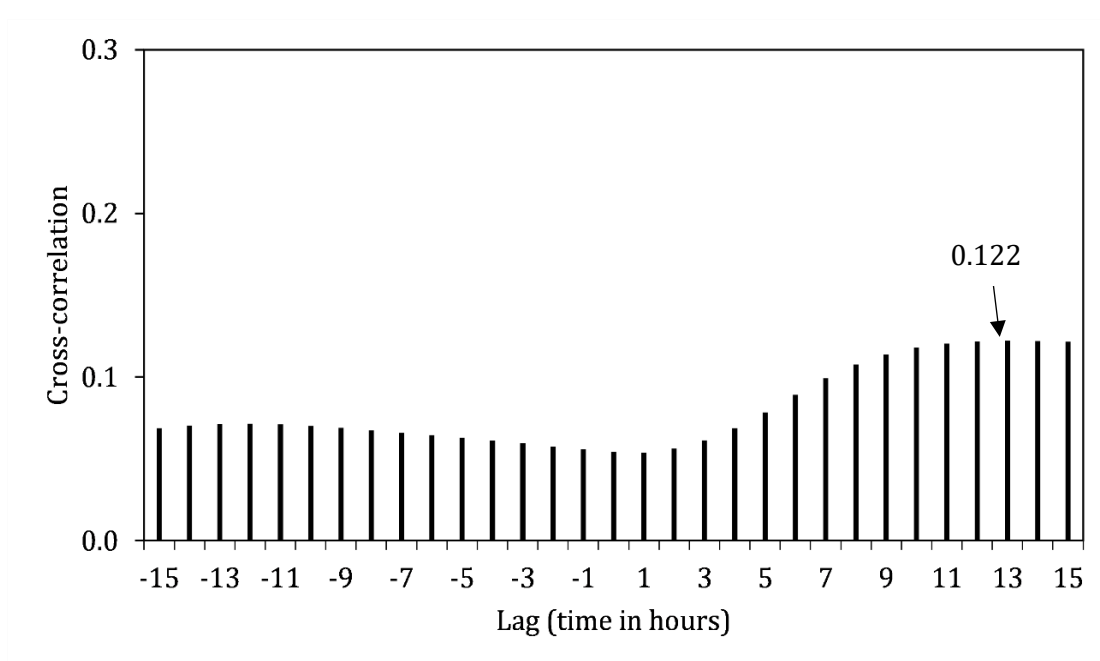


Figure 5.23 Cross-correlation function for hourly rainfall and average hourly volumetric water content at 1.2 m.

## 5.5 Evaluation of the factors influencing volumetric water content response

### 5.5.1 Effect of rainfall features

From the previous sections, it is clear that the volumetric water content at all measured depths fluctuated continuously during monsoonal rainfall. In addition to this, it can be seen in Figure 5.16 and Figure 5.20 that the magnitude of these fluctuations varied during different rainfall events. To evaluate if the magnitude of these fluctuations was related to the rainfall features, firstly, the percentage changes in volumetric water content caused by individual rainfall events (section 5.4.1.2) were quantified. The percentage change was calculated using the initial volumetric water content ( $VWC_{initial}$ ) (before the start of rainfall event) and the maximum volumetric water content ( $VWC_{max}$ ) (until the start of the subsequent rainfall event), as shown in Figure 5.24. The maximum volumetric water content was calculated in this manner because a time-lag between rainfall initiation and corresponding soil moisture response was observed throughout the monitoring period (section 5.4.2.4).

After calculating the percentage change in volumetric water content caused by individual rainfall events, correlation analysis was conducted to explore their association with rainfall parameters. Only the rainfall events that occurred during the monsoon (128 rainfall events) were taken into account. The other events were not taken into consideration to eliminate any effects of seasonality, which will be discussed in the next section. By doing so, the abrupt changes in volumetric water content which were observed in the upper 0.3 m during intermittent rainfall events in the post-monsoon period (Figure 5.16) could be disregarded.

The features of the rainfall events including total rainfall, peak hourly intensity, average rainfall intensity, minimum hourly intensity and rainfall duration were correlated to the percentage change in the volumetric water content at 0.3 m, 0.8 m and 1.2 m (Table 5.4). The highest statistically significant positive correlation ( $r = 0.72$  to  $0.78$ ,  $p < 0.0001$ ) was obtained for the relationship between total rainfall and percentage change in volumetric water content at all three depths (Table 5.4).

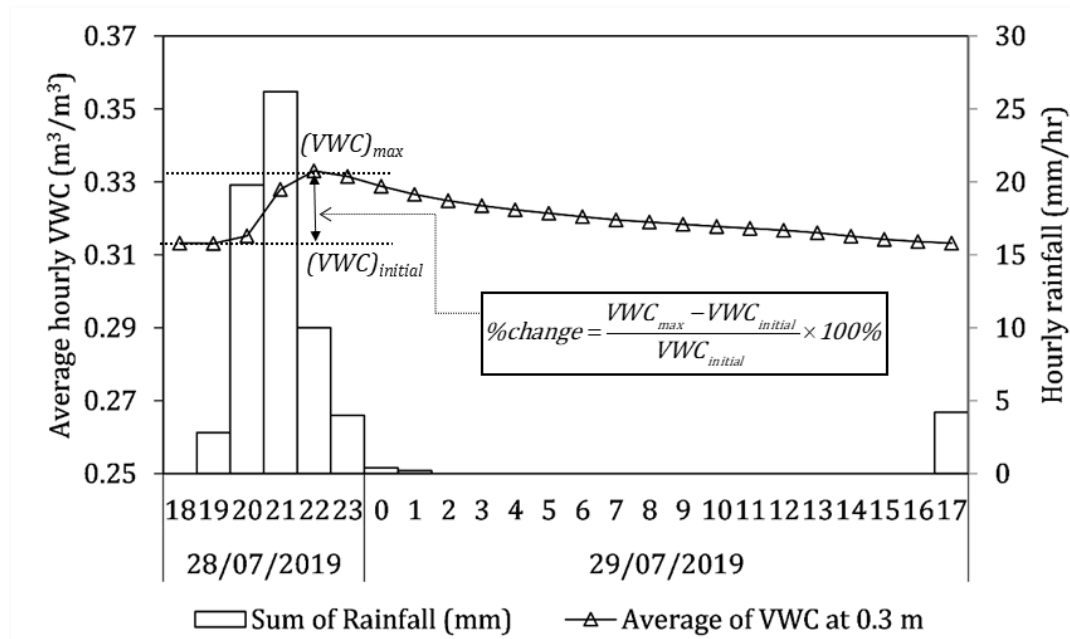


Figure 5.24 An example showing calculation of the percentage change in average hourly volumetric water content caused by a rainfall event.  $VWC_{initial}$  is the initial volumetric water content before the rainfall initiation and  $VWC_{max}$  is the maximum volumetric water content before the start of another rainfall event.

Table 5.4 Pearson correlation coefficients (r) between rainfall features and percentage change in the volumetric water content (VWC) at 0.3 m, 0.8 m and 1.2 m.

	Total rain (mm)	Peak intensity (mm/hr)	Minimum intensity (mm/hr)	Average intensity (mm/hr)	Rainfall duration (hr)
Percentage change in VWC at 0.3 m	0.78 (p<0.0001)	0.69 (p<0.0001)	0.00 (p=0.9746)	0.61 (p<0.0001)	0.42 (p<0.0001)
Percentage change in VWC at 0.8 m	0.76 (p<0.0001)	0.68 (p<0.0001)	0.028 (p=0.8581)	0.66 (p<0.0001)	0.38 (p<0.0001)
Percentage change in VWC at 1.2 m	0.72 (p<0.0001)	0.5 (p<0.0001)	-0.01 (p=0.2803)	0.4 (p<0.0001)	0.48 (p<0.0001)

### 5.5.1.1 Empirical relationship between total rainfall and percentage change in volumetric water content

Following the previous discussion that a fairly strong correlation exists between the total rainfall and corresponding volumetric water content change during the monsoon, simple regression analyses were conducted to estimate the dependency of water content changes on total rainfall. Figure 5.25 shows the percentage change in volumetric water content at 0.3 m as a logarithmic function of the total rainfall amount. Although there is a considerable scatter, a fairly significant positive correlation ( $R^2 = 0.64$  with  $p < 0.0001$ ) can be seen between the two variables. The scatter in the dataset is perhaps due to the effect of initial soil water conditions and rainfall characteristics that are not incorporated in the model. The fitted line shows that at 0.3 m, at least  $\sim 3$  mm rain would be required to initiate an increase in volumetric water content; any rainfall smaller than this would be abstracted by the vegetation at the ground surface. The trend evident in this plot shows that the percentage change in volumetric water content increased rapidly with the increase in rainfall amount. However, at greater rainfall totals, a limiting condition was reached where the direct association between rainfall total and volumetric water content change became less clear. This could be because the rainfall events with greater rainfall totals contributed less to infiltration (Tsaparas et al., 2003; Rahardjo et al., 2005), resulting in a relatively lesser increase in volumetric water content. Similarly, a good linear relationship was obtained between rainfall total and percentage change in volumetric water content at 1.2 m ( $R^2 = 0.52$  with  $p < 0.0001$ ) (Figure 5.26). The fitted linear regression presented in Figure 5.26 shows that at least 4.1 mm of rainfall would be necessary to trigger a change in volumetric water content at 1.2 m.

Overall, the regression analyses showed that the total rainfall can be used as a good predictor of the volumetric water content changes within the unsaturated soils. However, it should be noted that this empirical model does not take into account the effects of various rainfall patterns like duration and peak intensity, varying soil properties and topographic influences. They could be addressed in a more complex model, but this is beyond the scope of this study. These factors that were not taken into account in the model could have resulted in the scatter in the data points as seen in Figure 5.25 and Figure 5.26, which could make transferring this model to a different location difficult.

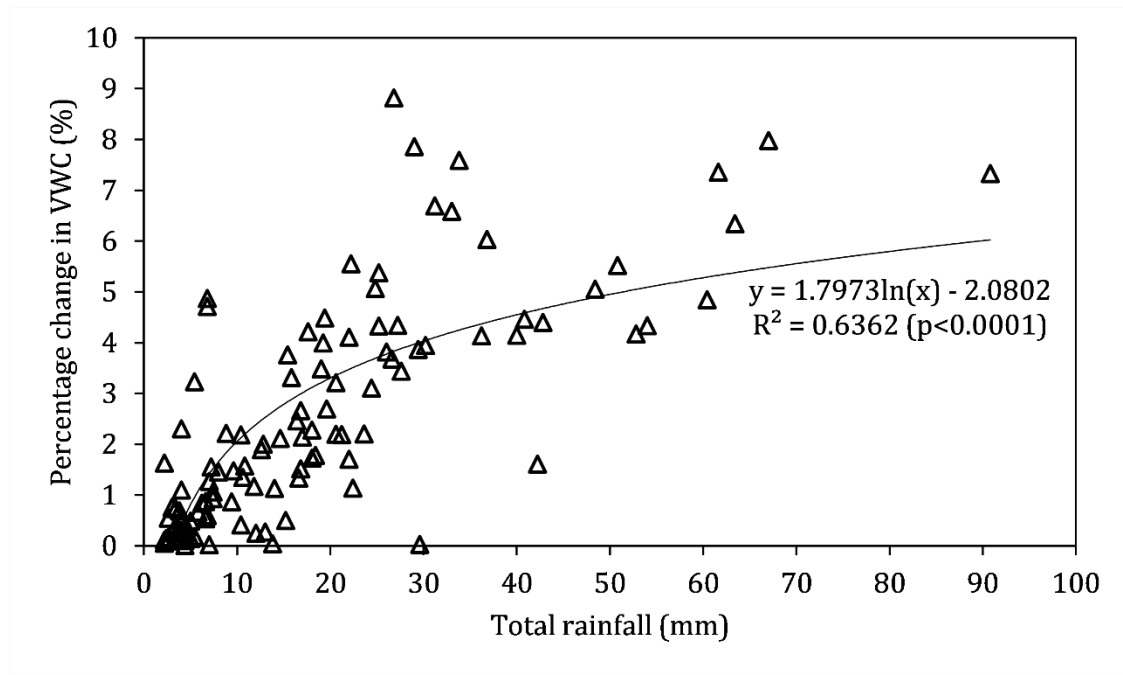


Figure 5.25 Relationship between total rainfall and percentage change in average hourly volumetric water content at 0.3 m during 2019 monsoon.

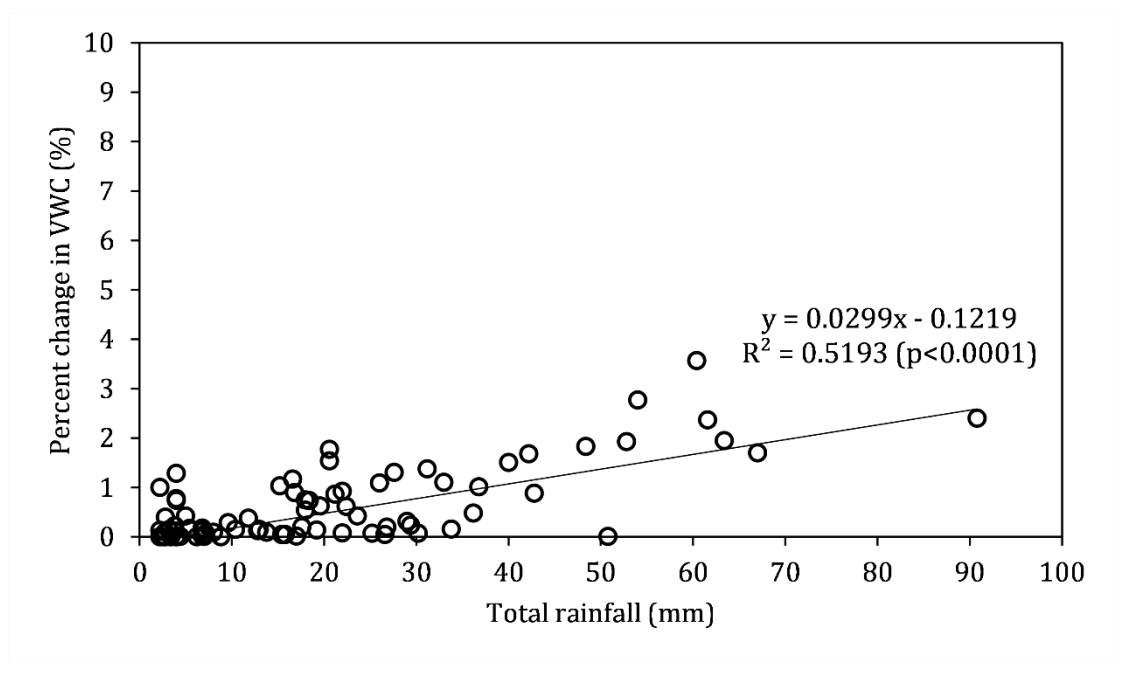


Figure 5.26 Relationship between total rainfall and percentage change in average hourly volumetric water content at 1.2 m during 2019 monsoon.

5.5.1.2 Effect of average rainfall intensity and total duration on volumetric water content

In this study, to understand the influence of rainfall duration, events with the same or similar rainfall intensities were compared. In the same manner, to evaluate the effect of rainfall intensity, events having the same or similar rainfall duration were compared. For

this comparison, twenty-five rainfall events were selected. For the selection of the twenty-five rainfall events, firstly, all rainfall events were distributed into seven 'average rainfall intensity categories' based on the histogram of the average rainfall intensities (Figure 5.15 (d)). From every intensity category, four rainfall events were selected and divided into two groups (Group 1 and Group 2) according to their average rainfall intensities. The two rainfall events in every group were chosen in such a way that they would have the same average rainfall intensity but significantly different rainfall durations. Within each intensity-category, if there were more than two events with same average rainfall intensity, the events having the biggest difference in rainfall duration were chosen. As the number of events with higher average intensity was less, comparisons were made between the rainfall events with the closest average intensity. A summary of the selected rainfall events is given in Table 5.5. Other information about the rainfall events is given in Appendix A-2. Dividing the rainfall events in this manner allowed an evaluation of the effect of rainfall intensity, as well as duration, on the changes in the volumetric water content. The percentage change in average hourly volumetric water content measured during each rainfall event at 0.3 m, 0.8 m and 1.2 m are presented in Table 5.6.

Considering the rainfall threshold for landsliding suggested by Dahal and Hasegawa (2008), which is 144 mm/day (6 mm/hr), the rainfall events that have an average hourly intensity of less than 6 mm/hr were considered to be low-intensity rainfall. In the same way, the events with an average hourly intensity of 6 mm/hr or higher were considered as high-intensity events. As for duration, no specific boundary for short and long events was specified, but the comparisons were made in a relative manner.

- **Low-intensity rainfall events ( $\leq 6$  mm/hr)**

To evaluate the effect of rainfall duration on the volumetric water content response during low-intensity rainfall events, pairs of rainfall events with the same intensity, such as rainfall event no. 83 and 144, 40 and 135, 69 and 103, 68 and 63, 101 and 89 and 27 and 53 were compared. This comparison showed that the low-intensity rainfall events that lasted for a longer duration (6 to 19 hours) caused ~7% change in volumetric water content at 0.3 m, ~5% change at 0.8 m and ~2% change at 1.2 m. On the other hand, low-intensity, short-duration events like rainfall event no. 40, 69 and 27 that lasted only for two to three hours, caused minimal changes (<3% at 0.3 m) in the volumetric water content. This indicates that the low-intensity rainfall events which persist for a longer duration allow rainwater to infiltrate into greater depths, thereby increasing the volumetric water content.

- **High-intensity rainfall events (>6 mm/hr)**

The high-intensity, short-duration rainfall events which lasted for two to three hours (rainfall event nos. 35, 112, 85, 46 and 45) caused a slightly greater increase in the volumetric water content at all depths in comparison to the low-intensity, short-duration events (Table 5.6). An exception found in this observation was related to event no. 46, when ~9% increase in volumetric water content was recorded at 0.8 m which was greater than that at 0.3 m (Figure 5.27). This unusual increase was perhaps due to infiltration from two consecutive rainfall events at the beginning of the monsoon and not due to the rainfall event no. 46 alone, which can also be seen in Figure 5.27.

It was found that the high-intensity rainfall events that lasted for a longer duration ( $\geq 6$  hours) caused the highest changes in volumetric water content. During such events, the volumetric water content increased by ~5 to 8% at 0.3 m, ~3 to 5% at 0.8 m and by ~2% at 1.2 m. This shows that the high-intensity rainfall events that last for a longer period have a greater tendency to cause a higher increase in the volumetric water content at greater depths. Furthermore, rainfall event no. 87 and 90 in Table 5.6 have the same average rainfall intensity and rainfall duration. Although rainfall event no. 87 had a slightly higher total rain, it caused relatively smaller changes in the volumetric water content at all depths. This discrepancy is most likely due to the nature of rainfall distribution shown in Figure 5.28. During rainfall event no. 87, a peak-intensity of more than 25 mm/hr was recorded before it dropped to less than 4mm/hr in the last two hours. Consequently, the volumetric water content at 0.3 m increased rapidly in response to the rainfall but decreased quickly as the hourly rainfall intensity declined. On the other hand, rainfall event no. 90 had a sustained high intensity rainfall for the first five hours, which allowed rainwater to percolate to greater depths (down to 1.2 m) and caused a greater increase of volumetric water content at 0.8 m than that during rainfall event no. 87. This shows that high-intensity, long-duration rainfall caused a significant increase in the volumetric water content when the high rainfall intensity sustained for a longer duration.

The above discussions suggest that the shorter duration events caused minimum changes in the volumetric water content. In contrast, longer duration rainfall events, even with a lower intensity induced a relatively higher increase in the volumetric water content down to 1.2 m. The high-intensity, long-duration rainfall events triggered notable increase in the volumetric water content down to 1.2 m and this increment was found to be more pronounced during sustained high intensity rainfall.

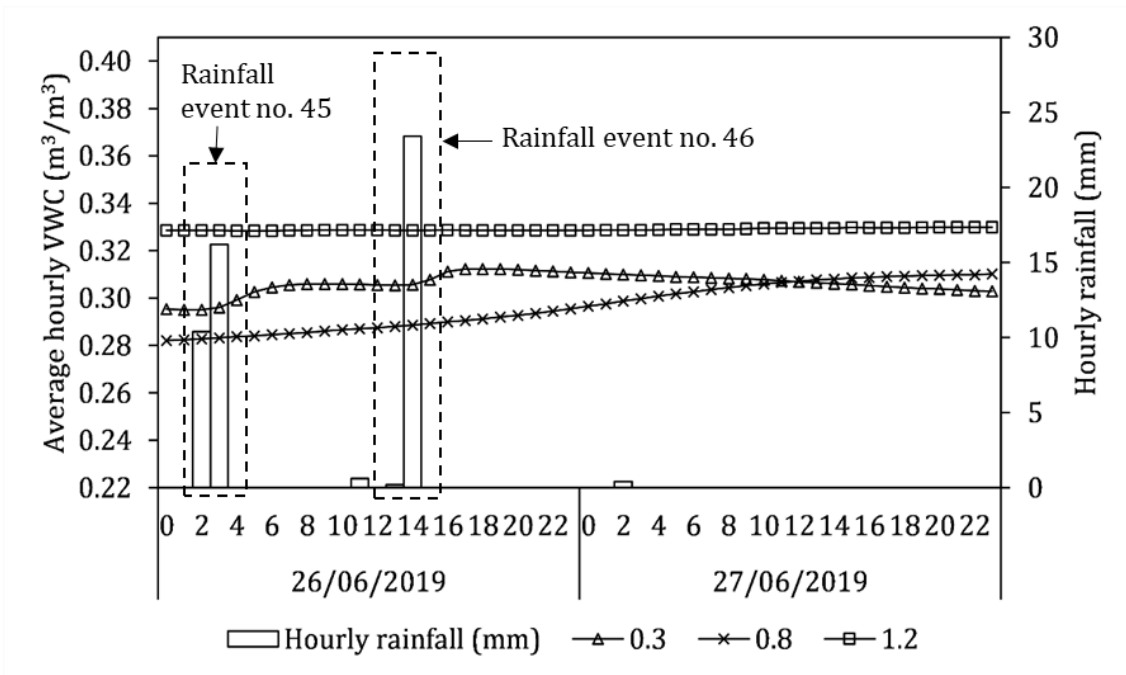


Figure 5.27 Variation in rainfall and average hourly volumetric water content with depth during Rainfall event no. 45 (26/06/19 02:00-03:00) and Rainfall event no. 46 (26/06/19 13:00-14:00).

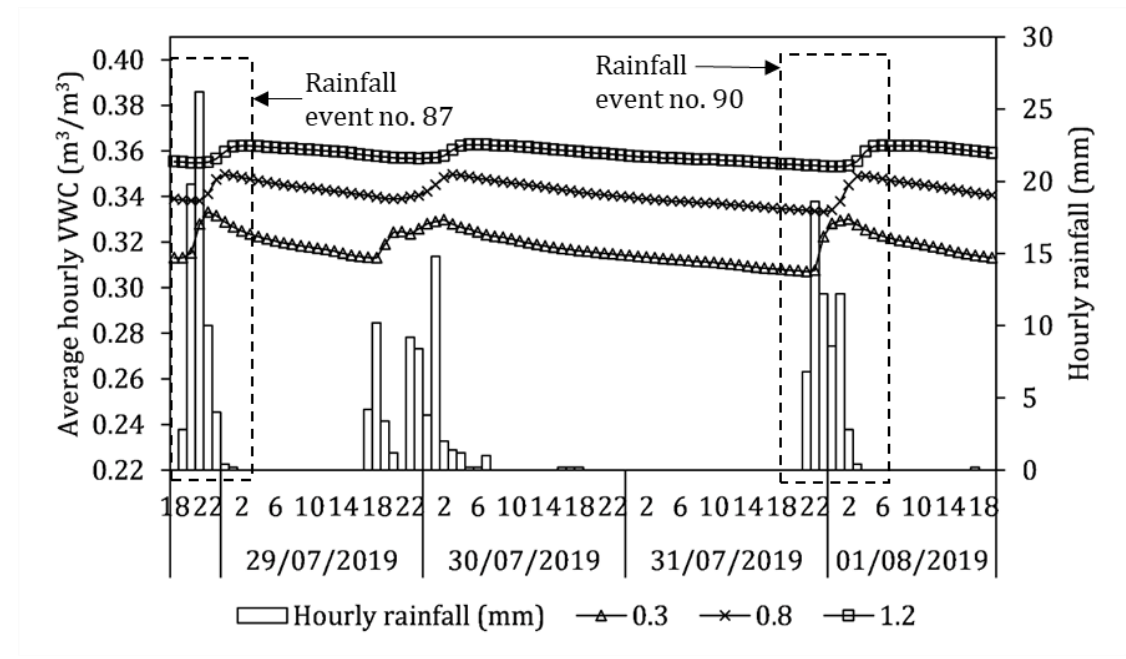


Figure 5.28 Variation in rainfall and average hourly volumetric water content with depth during Rainfall event no. 87 (28/07/2019 19:00 to 29/07/2019 01:00) and Rainfall event no. 90 (31/07/2019, 21:00 to 01/08/2019 03:00).



Table 5.5 Summary of rainfall events selected to compare the effects of rainfall intensity and duration on volumetric water content changes.

Average rainfall intensity categories	Group 1		Group 2	
0-2 mm/hr	<b>1.2 mm/hr</b>		<b>1.8 mm/hr</b>	
	Rainfall event no. 83 (7.4 mm in 6hrs)	Rainfall event no. 144 (22.4 mm in 18hrs)	Rainfall event no. 40 (5.4 mm in 3hrs)	Rainfall event no. 135 (18.4 mm in 10hrs)
2-4 mm/hr	<b>2.3 mm/hr</b>		<b>2.8 mm/hr</b>	
	Rainfall event no. 69 (7 mm in 3hrs)	Rainfall event no. 103 (16.4 mm in 7hrs)	Rainfall event no. 68 (19.6 mm in 7hrs)	Rainfall event no. 63 (52.8 mm in 19hrs)
4-6 mm/hr	<b>4.2 mm/hr</b>		<b>5.2 mm/hr</b>	
	Rainfall event no. 101 (21.2 mm in 5hrs)	Rainfall event no. 89 (42.2 mm in 10hrs)	Rainfall event no. 27 (10.4 mm in 2hrs)	Rainfall event no. 53 (31.2 mm in 6hrs)
6-8 mm/hr	<b>6.9 mm/hr</b>		<b>7.3 to 7.4 mm/hr</b>	
	Rainfall event no. 35 (13.8 mm in 2hrs)	Rainfall event no. 94 (48.4 mm in 7hrs)	Rainfall event no. 111 (22 mm in 3hrs)	Rainfall event no. 96 (29.4 mm in 4hrs)
8-10 mm/hr	<b>8.2 to 8.6 mm/hr</b>		<b>8.8 to 9 mm/hr</b>	
	Rainfall event no. 47 (42.8 mm in 5hrs)	Rainfall event no. 56 (40.8 mm in 5hrs)	Rainfall event no. 87 (63.4 mm in 7hrs)	Rainfall event no. 90 (61.6 mm in 7hrs)
10-12 mm/hr	<b>10.1 to 10.3 mm/hr</b>		<b>11.2 to 11.8 mm/hr</b>	
	Rainfall event no. 85 (20.6 mm in 2 hrs)	Rainfall event no. 123 (90.8 mm in 8hrs)	Rainfall event no. 46 (23.6 mm in 2hrs)	Rainfall event no. 112 (67 mm in 6hrs)
12-14 mm/hr	<b>13.3 mm/hr</b>		N/A	
	Rainfall event no. 45 (26.6 mm in 2hrs)			

Table 5.6 Summary of the volumetric water content (VWC) changes caused by the selected rainfall events from Table 5.5 at 0.3 m, 0.8 m and 1.2 m.

Average rainfall intensity categories	Group 1				Group 2			
	0-2 mm/hr	1.2 mm/hr				1.8 mm/hr		
Rainfall event no. 83 (7.4 mm in 6hrs)		Rainfall event no. 144 (22.4 mm in 18hrs)		Rainfall event no. 40 (5.4 mm in 3hrs)		Rainfall event no. 135 (18.4 mm in 10hrs)		
Depth		Percentage change in VWC	Depth	Percentage change in VWC	Depth	Percentage change in VWC	Depth	Percentage change in VWC
0.3 m		1%	0.3 m	1%	0.3 m	3%	0.3 m	2%
0.8 m		0%	0.8 m	1%	0.8 m	0%	0.8 m	2%
1.2 m	0%	1.2 m	1%	1.2 m	0%	1.2 m	1%	
2-4 mm/hr	2.3 mm/hr				2.8 mm/hr			
	Rainfall event no. 69 (7 mm in 3hrs)		Rainfall event no. 103 (16.4 mm in 7hrs)		Rainfall event no. 68 (19.6 mm in 7hrs)		Rainfall event no. 63 (52.8 mm in 19hrs)	
	Depth	Percentage change in VWC	Depth	Percentage change in VWC	Depth	Percentage change in VWC	Depth	Percentage change in VWC
	0.3 m	1%	0.3 m	3%	0.3 m	3%	0.3 m	4%
	0.8 m	0%	0.8 m	1%	0.8 m	2%	0.8 m	4%
1.2 m	0%	1.2 m	0%	1.2 m	1%	1.2 m	2%	

Average rainfall intensity categories	Group 1				Group 2			
	4-6 mm/hr	4.2 mm/hr				5.2 mm/hr		
Rainfall event no. 101 (21.2 mm in 5hrs)		Rainfall event no. 89 (42.2 mm in 10hrs)		Rainfall event no. 27 (10.4 mm in 2hrs)		Rainfall event no. 53 (31.2 mm in 6hrs)		
Depth		Percentage change in VWC	Depth	Percentage change in VWC	Depth	Percentage change in VWC	Depth	Percentage change in VWC
0.3 m		2%	0.3 m	2%	0.3 m	0%	0.3 m	7%
0.8 m		1%	0.8 m	3%	0.8 m	0%	0.8 m	5%
1.2 m		1%	1.2 m	2%	1.2 m	0%	1.2 m	1%
6-8 mm/hr	6.9 mm/hr				7.3 to 7.4 mm/hr			
	Rainfall event no. 35 (13.8 mm in 2hrs)		Rainfall event no. 94 (48.4 mm in 7hrs)		Rainfall event no. 111 (22 mm in 3hrs)		Rainfall event no. 96 (29.4 mm in 4hrs)	
	Depth	Percentage change in VWC	Depth	Percentage change in VWC	Depth	Percentage change in VWC	Depth	Percentage change in VWC
	0.3 m	2%	0.3 m	5%	0.3 m	4%	0.3 m	4%
	0.8 m	3%	0.8 m	3%	0.8 m	1%	0.8 m	2%
	1.2 m	2%	1.2 m	2%	1.2 m	0%	1.2 m	0%

Average rainfall intensity categories	Group 1				Group 2			
	8-10 mm/hr	8.2 to 8.6 mm/hr				8.8 to 9 mm/hr		
Rainfall event no. 47 (42.8 mm in 5hrs)		Rainfall event no. 56 (40.8 mm in 5hrs)		Rainfall event no. 87 (63.4 mm in 7hrs)		Rainfall event no. 90 (61.6 mm in 7hrs)		
Depth		Percentage change in VWC	Depth	Percentage change in VWC	Depth	Percentage change in VWC	Depth	Percentage change in VWC
0.3 m		4%	0.3 m	5%	0.3 m	6%	0.3 m	7%
0.8 m		3%	0.8 m	1%	0.8 m	3%	0.8 m	5%
1.2 m	1%	1.2 m	0%	1.2 m	2%	1.2 m	2%	
10-12 mm/hr	10.1 to 10.3 mm/hr				11.2 to 11.8 mm/hr			
	Rainfall event no. 85 (20.6 mm in 2 hrs)		Rainfall event no. 123 (90.8 mm in 8hrs)		Rainfall event no. 46 (23.6 mm in 2hrs)		Rainfall event no. 112 (67 mm in 6hrs)	
	Depth	Percentage change in VWC	Depth	Percentage change in VWC	Depth	Percentage change in VWC	Depth	Percentage change in VWC
	0.3 m	2%	0.3 m	7%	0.3 m	2%	0.3 m	8%
	0.8 m	3%	0.8 m	5%	0.8 m	9%	0.8 m	4%
1.2 m	2%	1.2 m	2%	1.2 m	0%	1.2 m	2%	
12-14 mm/hr	13.3 mm/hr				N/A			
	Rainfall event no. 45 (26.6 mm in 2hrs)							
	Depth		Percentage change in VWC					
	0.3 m		4%					
	0.8 m		2%					
1.2 m		0%						

### 5.5.2 Effect of seasonality

The variation in average daily volumetric water content during the year-long monitoring period (Figure 5.16) showed that the pattern of volumetric water content change can be significantly different during the monsoon and the relatively dry months of the year. To explore the effect of seasonality on the volumetric water content changes, the three main rainfall events from the post-monsoon period which showed a maximum response to rainfall were compared. Table 5.7 presents a summary of these events.

Table 5.7 Summary of the rainfall events selected to compare the effect of seasonality on the volumetric water content (VWC) response.

	<b>Rainfall event no. 160</b>	<b>Rainfall event no. 161</b>	<b>Rainfall event no. 166</b>
Total rainfall (mm)	15.2	18.6	38.8
Rainfall duration (hr)	9	6	21
Average hourly rainfall intensity (mm/hr)	1.7	3.1	1.8
Percentage change in VWC at 0.3 m	1%	13%	17%
Percentage change in VWC at 0.8 m	0%	0%	0%
Percentage change in VWC at 1.2 m	0%	0%	0%

It can be seen in Figure 5.29 that rainfall events no. 160 and 161 caused a rather slow, but significant increase (~13%) in the volumetric water content at 0.3 m. These rainfall events were preceded by a 65 day long dry period that caused a major decrease in the degree of saturation (27%) shown in Figure 5.19. The decrease in the degree of saturation (and the consequent increase of suction) may have reduced the unsaturated soil permeability, causing a noticeable time-lag of ~18 hours (from the start of rainfall event no. 160) in volumetric water content response at 0.3 m. This observed time-lag is much higher than during the monsoon period (2 to 5 hours), when the volumetric water content was relatively high (section 5.4.2.4). The reduced permeability due to drying could have also inhibited percolation of rainwater to greater depths. Hence, negligible changes in volumetric water content occurred at 0.8 m and 1.2 m during these rainfall events. Similarly, a low-intensity (1.8 mm/hr) rainfall event which lasted for 21 hours (rainfall event no. 166) led to a sharp ~17% increase in the volumetric water content at 0.3 m (Table 5.7 and Figure 5.29). A time-lag of about 18 hours from the start of the rainfall event was also observed for this increment and after the end of the rainfall event, the volumetric water content at 0.3 m declined and yet, no changes in volumetric water content were recorded at 0.8 m and 1.2 m.

By assessing all rainfall events that occurred during the pre-and post-monsoon period, it was found that the maximum increase in volumetric water content during a single rainfall event was ~17% and ~3% at 0.3 m and 0.8 m, respectively, while that at 1.2 m was insignificant. On the other hand, the rainfall events that occurred during the monsoon caused a maximum of ~9%, ~8% and ~4% increase in volumetric water content at 0.3 m, 0.8 m and 1.2 m respectively. Hence, during intermittent rainfall events in the dry season, the upper layers of the soil may have captured the available moisture causing a sharp increase in the volumetric water content. The reduction in the degree of saturation due to prolonged drying and the consequent increase in soil suction could have also resulted in lower permeability of the soil at greater depths. Together, this may have not only resulted in a longer time-lag for the volumetric water content response at 0.3 m but may have also prevented rainwater infiltration to greater depths.

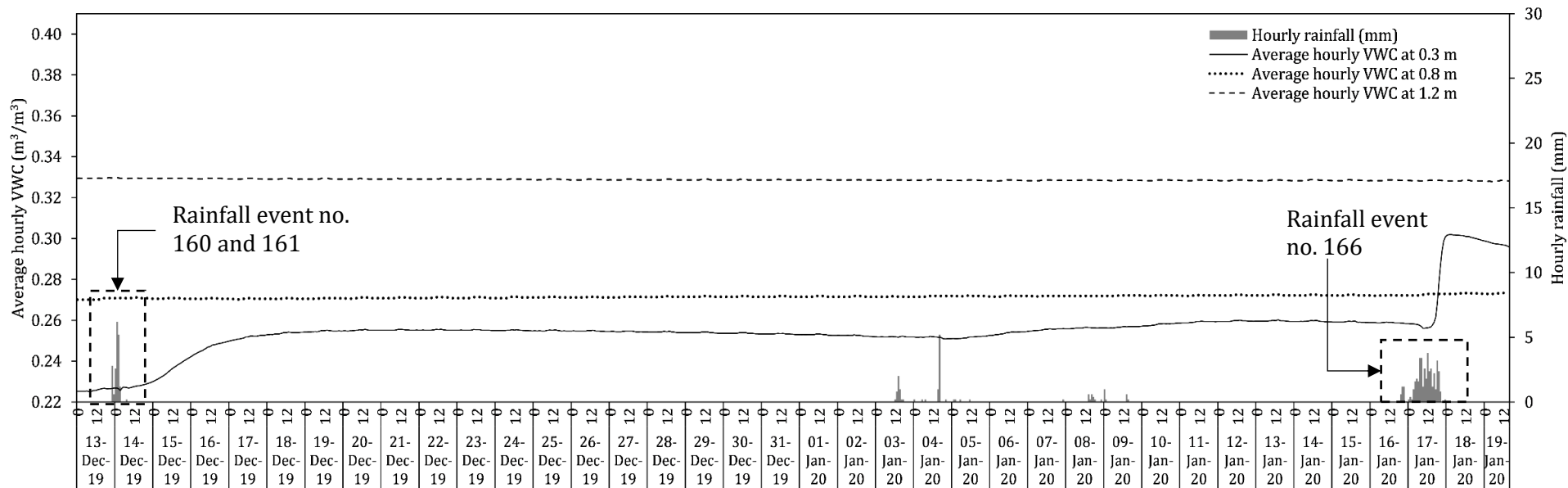


Figure 5.29 Changes in average hourly volumetric water content and hourly rainfall during rainfall event no. 160 and 161 (between 13/12/2019 and 14/12/2019) and during rainfall event no. 166 (between 16/01/2020 and 17/01/2020).

## 5.6 Chapter summary

The initial part of this chapter described the theoretical concepts related to the flow of water in soils, the interaction of unsaturated zone with the atmosphere and the infiltration models based on the wetting front concept. This was followed by a review of the field studies that have been conducted to understand the hydrological response of soil during rainfall.

The field monitoring station installed near Kanglang landslide during this study provided a year-long record of rainfall and volumetric water content from 27/03/2019 to 28/03/2020. The summary of this dataset is presented below:

### **Rainfall**

1. Total rainfall of 2690.4 mm was recorded during the monitoring period which constituted 199 wet days and 169 dry days. As expected, during the four months of the monsoon, ~81% of the total annual rainfall was recorded. Rainfall occurred almost every day during the monsoon, and for the majority of days the total rainfall was greater than 5 mm. On the other hand, during the pre- and post- monsoon seasons, more than 60% of rainy days accumulated less than 5 mm rainfall.
2. The monthly rainfall totals recorded at the monitoring station from April 2019 to October 2019 were compared to those obtained from the nearby meteorological station in Gumthang. The rainfall recorded at the monitoring station was notably greater than that recorded at Gumthang in June and July 2019. This could be the result of localised rainfall events during the monitoring period. A reasonable correlation was found between the monthly rainfall totals measured at the field-monitoring station and Gumthang meteorological station.
3. 182 individual rainfall events were identified during the monitoring period, the majority (~70%) of which were recorded during the monsoon. The distribution of the rainfall events showed that the extreme events with high total rainfall (>40 mm), long duration (>10 hours) and high hourly rainfall intensity (>25 mm/hr) were relatively infrequent during the monitored period. The individual rainfall events were used to understand the effects of different rainfall patterns and seasonality on the soil water contents.



**Volumetric water content**

1. The monitoring of volumetric water content showed fluctuations that varied with depth and season. Continuous fluctuations in volumetric water content were recorded at 0.3 m throughout the monitoring period, while conditions at 1.2 m remained fairly constant, except during the monsoon. The changes in volumetric water content at 1.2 m during the monsoon showed that the wetting front advanced further below this depth.
2. During a 40-day continuous rainfall period between 21/06/2019 and 30/07/2019, the degree of saturation increased by 10% or more at all measured depths. This increased the degree of saturation at 1.2 m to ~90%. The advancement of the wetting front beyond 1.2 m could lead to saturation of soil at 1.5 m (chapter 4).
3. During a 65-day long dry period from 09/10/2019 to 12/12/2019, the degree of saturation at 0.3 m decreased by 27%, while that at 1.2 m decreased by 4% only. This showed that the effect of atmospheric drying decreased with depth, which explains the consistently high volumetric water content recorded at 1.2 m. The slower rate of drying due to evapotranspiration compared to wetting during rainfall was also reported by Hawke and McConchie (2011).
4. Compared to 0.3 m and 0.8 m, the percentage increase in average daily volumetric water content at 1.2 m was relatively small (~11%). However, since the volumetric water content of soil at 1.2 m remained consistently high throughout the year, even a small increment in volumetric water content during monsoon increased the degree of saturation to ~90%. This shows that the consecutive wet days during the monsoon could cause saturation of soil at shallow depth. Such a progressive wetting can cause dissipation of matric suction and reduction of shear strength, which can ultimately lead to shallow slope failures.
5. The evaluation of hourly changes in volumetric water content revealed a delayed response of volumetric water content with increasing depth during rainfall events. The time-lag of volumetric water content response at 0.3 m, 0.8 m and 1.2 m after a rainfall event was evaluated using cross-correlation analysis. This showed that the correlations between hourly rainfall and volumetric water content at 0.3 m, 0.8 m and 1.2 m were statistically significant at time-lags of 2 to 5 hours, 7 to 10 hours and 11 to 15 hours respectively. The changes in the time-lag with increasing depth from were found to agree with time-lags evaluated visually from the monitoring data.
6. To evaluate if any relationship exists between the change in volumetric water content during individual rainfall events and the features of the events like total rainfall, duration, average intensity, peak intensity and maximum intensity, a simple correlation analysis was performed. A statistically significant correlation ( $r = 0.72$

- to 0.78,  $p < 0.0001$ ) was found between total rainfall and percentage change in volumetric water content.
7. Considering the significant correlation between total rainfall and percentage change in volumetric water content, their relationship was defined using regression analysis. The logarithmic regression function fitted to the relationship between total rainfall and percentage change in volumetric water content at 0.3 showed that at least 3 mm of rainfall would be necessary to initiate an increase in the volumetric water content at this depth. At higher rainfall totals, however, this association became less clear as greater rainfall totals typically contribute less to infiltration (Tsaparas et al., 2003; Rahardjo et al., 2005), consequently causing smaller changes in the volumetric water content. Similarly, a linear relationship was defined between the rainfall total and percentage change in volumetric water content at 1.2 m. The fitted linear regression showed that at least 4 mm of rainfall would be needed to trigger a change in volumetric water content at this depth. These empirical relationships did not take into account the initial soil water conditions, rainfall characteristics, topography and varying soil properties, which would make transferring this model to different locations difficult. However, they do provide an indication of the scale to which volumetric water content changes can be expected during various rainfall events during the monsoon.
  8. The evaluation of the effects of average rainfall intensity and duration showed that the rainfall events which lasted for a shorter duration (2 to 3 hours) caused minimum changes in the volumetric water content. Moreover, the duration of rainfall events was found to be critical in determining the change in the volumetric water content at the measured depths. The high-intensity rainfall events (>6 mm/hr) that lasted for more than 6 hours (high-intensity, long-duration) caused a significant increase in the volumetric water content at all depths. However, this response could be affected by the duration of sustained high rainfall intensity within a rainfall event.
  9. During the monitoring period, the critical threshold for landsliding developed for Nepal by Dahal and Hasegawa (2008) was not exceeded by any observed rainfall events. Yet, the longer duration rainfall events caused a significant increase in volumetric water content of shallow soils, increasing the degree of saturation to ~90% at 1.2 m. This suggests that slopes can be prone to shallow landsliding even when the regional rainfall-based thresholds for landsliding are not exceeded. Further discussions on the monitored data and their implications on slope stability are presented in chapter 7.

10. The rainfall events during the monsoon triggered changes in the volumetric water content at all depths. However, the intermittent rainfall events that occurred during the dry seasons caused a significant increase in volumetric water content at 0.3 m while causing negligible changes below. This most likely is the result of the prolonged dry period that preceded the intermittent rainfall events during the dry season which reduced the permeability of soil. Hawke and McConchie (2011) reported similar observation and argued that this may be due to higher porosity of soil near the surface. Moreover, following the discussions by Toll (2006), the intermittent rainfall may have created a near-surface zone with high degree of saturation which promoted flow within this zone rather than percolating down to greater depths. Hence, the effect of seasonal changes which controls the initial water content of soil rainfall plays an important role in determining the amount of rainwater that infiltrates into the slope.
11. The above observations suggest that by monitoring the volumetric water content changes at different depths, it is possible to visualise and understand the wetting front advancement in response to the rainwater that infiltrates into the ground during different seasons. The empirical infiltration models that are used to evaluate the wetting front advancement, on the other hand, do not take into account the soil heterogeneity, rainfall characteristics, temperature, initial moisture conditions and most importantly, the portion of rain water that is lost by vegetation interception and depression storage. Continuous monitoring of soil water content in the field implicitly takes these factors into account, thereby eliminating the limitations of the empirical infiltration models.

# Chapter 6

## Numerical modelling in PLAXIS 2D

---

### 6.1 Chapter outline

In chapter 2, the effects of slope cutting for road construction on landsliding was discussed using observational findings from the field reconnaissance surveys. The existing gap in the understanding of the physical process of landsliding due to the interaction of roads and rainfall was also recognised in chapter 2. This chapter focuses on addressing this knowledge gap by conducting a back-analysis of Kanglang landslide using the finite element software PLAXIS 2D.

The first part of this chapter presents a discussion of the existing methods for the analysis of slope stability. This is followed by a review of the studies that have utilised various numerical modelling methods to study the effects of slope cutting and rainfall on the stability of slopes. The second part of this chapter presents the numerical modelling approach utilised in this study and the final section is the summary of the results from the numerical analyses.

### 6.2 Review of numerical slope stability analysis methods

#### 6.2.1 Limit equilibrium method

The limit equilibrium method has been in use for slope stability analysis since the early twentieth century (Krahn, 2003). The performance of a slope in this method is assessed in terms of the factor of safety defined for static equilibrium of forces and/or moments. In the conventional limit equilibrium methods, the effect of negative pore water pressure in the unsaturated zone is usually ignored. However, when the concern is over the possibility of shallow failures above the groundwater table, ignoring suction becomes unrealistic (Rahardjo and Fredlund, 1991).

To incorporate the contribution of matric suction in slope stability analysis, Rahardjo et al. (1995) proposed a semi-infinite method and Rahardjo and Fredlund (1991) proposed the method of slices. Both methods combine the conventional limit equilibrium method with the Extended Mohr-Coulomb failure criterion (Fredlund et al., 1978) discussed in chapter 4

to incorporate the effect of matric suction. The semi-infinite method is applied when the sliding surface is considered parallel to the ground surface. Four formulations of the factor of safety for hydrostatic and non-hydrostatic pore water pressure distributions have been developed allowing the factor of safety to be computed manually. Similarly, the method of slices proposed entails discretisation of the soil mass above the slip surface into a finite number of vertical slices and the static forces per unit width acting on a slice within the sliding body are computed. Using this method, the factor of safety can be obtained satisfying the equilibrium of moments and/or equilibrium of horizontal forces. A detailed summary of these methods has been discussed by Rahardjo et al. (2012).

## 6.2.2 Finite element method

The limit equilibrium method can address the overall stability of the slope but provides little insight into the stresses and deformations within the sliding mass during or before the failure (Krahn, 2003; Chowdhury et al., 2009). However, information on deformation can be as valuable as the factor of safety in cases where it may be necessary to predict the extent of movement (Chowdhury et al., 2009). For this, the finite element method is increasingly used in geotechnical practice. The finite element method can not only evaluate the overall stability but can also be used for the calculation of stresses, deformations and pore water pressures by including non-linear constitutive relationships in homogenous and non-homogenous soil conditions (Duncan, 1996).

Various physical processes like seepage and deformation can be modelled as partial differential equations that combine the constitutive behaviour of a material with the conservation laws such as conservation of mass and energy (Fredlund et al., 2012). The finite element method is one of the most common numerical technique for obtaining approximate solutions to a series of partial differential equations. The fundamental principle behind this method is that the behaviour of a soil system, regarded as a continuum, can be approximately defined by the collective behaviour of the smaller elements that make up the continuum (Schuster and Krizek, 1978).

The finite element method has been in use since the late 1960s after Clough and Woodward (1967) first introduced this into geotechnical engineering. With a suitable definition of initial conditions, constitutive relationship, soil properties and loading sequences, the finite element model can closely replicate the in-situ conditions (Potts and Zdravkovid, 1999). Hence, to model seepage, deformation and stability of saturated and unsaturated soils under rainfall, various numerical modelling programs based on the finite element method have been developed, some of which include PLAXIS (Bentley Systems Inc., 2018), SIGMA/W and

SEEP/W (GeoStudio, 2020), SVFLUX (SoilVision, 2020), RS2 (Rocscience Inc., 2020) and HYDRUS (Šimůnek et al., 1998).

### 6.2.3 Numerical seepage analysis

To evaluate the rate and direction of water flow and the pore water pressure distribution within the flow regime, seepage analysis is performed (Fredlund and Rahardjo, 1993). The governing equation of water flow in unsaturated soils is formulated by combining Darcy's law with the principle of mass conservation or the continuity equation. According to the principle of mass conservation, steady-state flow is a condition when the volume of water flowing in and out of the elemental soil volume is equal and the change in the hydraulic head at any point in time is constant. In two-dimensional differential equation form, the governing equation for steady-state flow (time-independent) is expressed as Equation 6.1.

$$\frac{\partial}{\partial x} \left( k_x \frac{\partial h}{\partial x} \right) + \frac{\partial}{\partial y} \left( k_y \frac{\partial h}{\partial y} \right) = 0 \quad (6.1)$$

Where

$k_x$  and  $k_y$  = coefficients of permeability with respect to matric suction or water content in x- and y- directions respectively.

If an additional flux in the form of precipitation or infiltration is added to the soil domain, the equation that governs steady-state flow is written as Equation 6.2.

$$\frac{\partial}{\partial x} \left( k_x \frac{\partial h}{\partial x} \right) + \frac{\partial}{\partial y} \left( k_y \frac{\partial h}{\partial y} \right) + q_{flow} = 0 \quad (6.2)$$

Where

$q_{flow}$  = applied boundary flux

In transient flow, the hydraulic head varies with respect to time, and hence, water can be either stored or discharged from the soil element. To take this aspect into account, the governing equation for transient flow in the soil incorporates the changes in water storage in an element with time. In two-dimensional differential equation form, the governing equation for transient flow can be expressed as Equation 6.3.

$$\frac{\partial}{\partial x} \left( k_x \frac{\partial h}{\partial x} \right) + \frac{\partial}{\partial y} \left( k_y \frac{\partial h}{\partial y} \right) + q_{flow} = \frac{\partial \theta}{\partial t} \quad (6.3)$$

Where

$\theta$  = volumetric water content

$\frac{\partial \theta}{\partial t}$  = rate at which water is lost or gained during a transient process

The right-hand side of the equation representing the transient change in the soil-water content can also be expressed in terms of matric suction, which is given in Equation 6.4.

$$\frac{\partial \theta}{\partial t} = \frac{\partial \theta}{\partial u_w} \times \frac{\partial u_w}{\partial t} = m_w \frac{\partial u_w}{\partial t} \quad (6.4)$$

Where

$m_w$  = soil-water retention capacity = slope of the soil-water retention curve

Equation 6.3 can hence be written as:

$$\frac{\partial}{\partial x} \left( k_x \frac{\partial h}{\partial x} \right) + \frac{\partial}{\partial y} \left( k_y \frac{\partial h}{\partial y} \right) + q_{flow} = m_w \frac{\partial u_w}{\partial t} \quad (6.5)$$

The above equation, also known as Richard's equation (L. A. Richards, 1931), governs the transient flow of water through unsaturated soil. This equation takes into account the time-dependent changes in the water storage capacity of the soil, environmental conditions and soil permeability to obtain a more realistic distribution of pore water pressure in the unsaturated-saturated soil system.

To solve Richard's equation for water flow, it is necessary to define the soil-water retention curve and the permeability function. As discussed in chapter 4, permeability varies non-linearly depending on the amount of water present in the soil, which in turn, is related to the matric suction. Additionally, the water storage capacity of soil also depends on the matric suction and the soil-water retention characteristics. Since both relationships – permeability function and soil-water retention curve are non-linear, the solution to Equation 6.5 is complex. Hence, solutions for the seepage problem are often obtained using numerical modelling software such as PLAXIS (Bentley Systems Inc., 2018), SEEP/W (GeoStudio, 2020), SVFLUX (SoilVision, 2020), and HYDRUS (Šimůnek et al., 1998).

### 6.2.4 Slope stability analysis with the finite element method

In the finite element analysis, the factor of safety is often determined using the shear strength reduction technique. Assuming a Mohr-Coulomb failure criterion, the shear strength parameters of soil (cohesion and angle of shearing resistance) are reduced incrementally by a strength reduction factor until slope failure occurs (Matsui and San, 1992; Griffiths and Lane, 1999; Cai and Ugai, 2004). The ratio of the shear strength parameters to that at failure is defined as the factor of safety (FOS) (Equation 6.6). The advantages of the strength reduction method are elaborated by Griffiths and Lane (1999). The most important of them is that, in the finite element method, the critical failure surface is allowed to develop naturally from the development of shear strain arising from the reduction of shear strength without any presumptions about the failure plane (Griffiths and Lane, 1999).

$$FOS = \frac{c'}{c'_{failure}} = \frac{\tan \phi'}{\tan \phi'_{failure}} \quad (6.6)$$

Where the subscript '*failure*' denotes the shear strength parameters at failure.

## 6.3 Review of numerical analyses of slope failures

The numerical analyses of rainfall-related slope failures within the framework of unsaturated soil mechanics have been performed using two distinct approaches: uncoupled and coupled approach.

In the uncoupled approach, numerical seepage analysis is conducted assuming the soil skeleton is non-deformable. The resultant pore water pressures are then used as input into stability analysis. The commercial software packages SEEP/W and SLOPE/W are commonly utilised for uncoupled analysis; the pore water pressure distribution obtained from SEEP/W is imported into SLOPE/W for calculation of factor of safety based on limit equilibrium method (Ng and Shi, 1998; Tsaparas et al., 2002; Rahimi et al., 2010; Hughes et al., 2015).

Ng and Shi (1998) used uncoupled transient seepage and stability analysis using SEEP/W and SLOPE/W to understand the distribution of pore water pressure and subsequent changes in the factor of safety due to rainfall in a typical unsaturated hillslope with a steep cut slope in Hong Kong. This study showed that the rainwater ingress into the initially unsaturated soil slope causes an increase of soil water content, reduction of matric suction,



increase in soil permeability and may develop a perched water table above the main groundwater table. The authors also suggested that the rainfall intensity, duration and antecedent rainfall condition have a direct influence on the slope stability. When the soil has a relatively high permeability ( $k_s \geq 10^{-5}$  m/s), slope failures can occur due to the rise in the groundwater table (Rahardjo et al., 2007). Ng and Shi (1998) demonstrated that in anisotropic soils ( $k_x/k_y \sim 4$ ), the groundwater table can rise towards the face of the road cut during high-intensity rainfall. This suggests that the presence of a road cut in the slopes with high and anisotropic permeability could alter the groundwater seepage and may also induce failures during rainfall. However, the influence of the road cut on the hydrological response of the slope during rainfall was not explicitly discussed in this study.

Guadagno et al. (2003) adopted the finite difference code (FLAC 2.0) to compare the equilibrium condition and steady-state seepage in pyroclastic soil slopes with and without road cuts. This study aimed to evaluate the role of natural and man-made cuts on the occurrence of widespread shallow translational slides that evolved into debris flows in Campania, Italy. Their analysis showed that the natural and man-made discontinuities in a natural hillslope could modify the equilibrium condition, form local yield zones and increase displacement in the upslope portions of the cut slope under steady-state saturated flow condition. Cascini et al. (2008) extended this study by conducting uncoupled numerical analysis in SEEP/W and SLOPE/W. This study showed that ponding on the mountain tracks during rainfall could increase the transient pore water pressures below the road and aggravate slope instability, depending on the in-situ soil stratigraphy.

Furthermore, Holcombe et al. (2016) used CHASM (Combined Hydrology and Stability Model) (Anderson and Lloyd, 1991) to evaluate slope stability in response to progressive urbanisation (deforestation, slope cutting, and house construction), for six design storms recorded in Saint Lucia. CHASM is a physically-based numerical model which uses finite-difference method for seepage analysis and integrates the resultant pore water pressures into limit equilibrium analysis that uses Bishop's simplified circular method (Bishop, 1955) or Janbu's non-circular method (Janbu, 1954) (Wilkinson et al., 2002). This study found that slope excavation to create flatter sites for building houses was the dominant driver of instability causing a decrease in the factor of safety; whereas deforestation and housing had minimum impact on the stability of slopes. This study also found that multiple slope cuttings on a hillslope shifted the potential failure surface towards the face of each cut, ultimately leading to localised slip surfaces and low factor of safety.

Bozzolan et al. (2020) used the extended CHASM+ and evaluated the probability of slope failure due to informal urbanisation in the humid tropics. Different aspects of urbanisation were considered including vegetation removal, slope cutting, leakage from pipes and tanks

and absence or presence of roof gutters and their influence on the probability of slope failure were evaluated. This study found that slope cutting was the most detrimental factor causing slope instabilities compared to other urbanisation aspects, which is similar to the conclusion drawn by Holcombe et al. (2016).

Studies have also adopted the uncoupled approach to understand the influence of rainfall patterns and soil properties on the stability of saturated and unsaturated slopes (Ng and Shi, 1998; Gasmo et al., 2000; Tsaparas et al., 2002; Cai and Ugai, 2004; Yoo and Jung, 2006; Rahardjo et al., 2007, 2010; Lee et al., 2009; Rahimi et al., 2010; Harris et al., 2012; Hughes et al., 2015; Oh and Lu, 2015; Qi and Vanapalli, 2015).

Rahardjo et al. (2007) and Tsaparas et al. (2002) conducted parametric studies on a homogenous soil slopes to identify the factors that control slope stability during rainfall. Both studies utilised uncoupled analysis using SEEP/W and SLOPE/W to obtain pore water pressure distributions and factor of safety. From the analysis, the authors indicated that the rainfall intensity, duration and saturated permeability of soils are the primary factors that govern the stability of slopes under rainfall. Rahardjo et al. (2007) showed that slopes with low saturated permeability ( $\leq 10^{-6}$  m/s) are less likely to be affected by short-duration rainfall events ( $\leq 24$  hours), regardless of the rainfall intensity. Rahardjo et al. (2007) found that in slopes with lower permeability ( $\leq 10^{-6}$  m/s), rise in groundwater table did not take place during rainfall events with intensity greater than or equal to the saturated soil permeability. Whereas in the slopes with a higher coefficient of permeability ( $\geq 10^{-5}$  m/s), the short-duration, high-intensity rainfall events affected both the stability and the rise in the groundwater table.

Tsaparas et al. (2002) showed that during rainfall, the depth of wetting front and change in pore water pressure increase with the increase in soil permeability as well as the duration of rainfall. Most importantly, this study highlighted that the change in pore water pressure and factor of safety due to infiltration can be better understood using the ratio between the rainfall intensity and the saturated permeability ( $I_r/k_{sat}$ ) rather than using the rainfall pattern (intensity and duration) alone. Their analysis showed that if the  $I_r/k_{sat}$  ratio is low, more water can infiltrate into the ground and cause greater changes in pore water pressures and lower the factor of safety. On the other hand, if a rainfall event with high intensity occurs on a low permeability soil (high  $I_r/k_{sat}$ ), the increase in pore water pressure can be small during or immediately after a rainfall event, as more rainfall runs off the slope, but may rise eventually in time.

Moreover, in the study by Rahardjo et al. (2007), the authors evaluated the influence of slope geometry including slope angle and slope height on slope stability. The results showed

that the initial and minimum factor of safety decreased with the increase in slope angle. Regarding the slope height, this study found that the higher slopes have a lower initial factor of safety and hence, a smaller safety margin and a higher risk of failure. However, the authors argue that whether a slope of any given height or angle will fail or not is determined by the soil permeability and rainfall intensity and duration. Yubonchit et al. (2017) conducted a coupled analysis and supported the observations by Rahardjo et al. (2007). Yubonchit et al. (2017) added that since the steeper slopes have a smaller initial factor of safety, the failure of such slopes might be triggered easily. Additionally, it was also suggested in this study that the time to failure could be accelerated by the steepness of the slope (Yubonchit et al., 2017).

The uncoupled analyses discussed above provides useful understanding of how anthropogenic activity such as slope cutting, and the hydrologic soil parameters influence the stability of slopes during rainfall. This method of analysis is considered relatively simple and hence attractive (Zhang et al., 2019). However, in a deformable three-phased medium such as unsaturated soil, seepage and stress-deformation mechanisms are inter-related (Song and Borja, 2014). On one hand, infiltration causes changes in pore water pressure and hence, changes the effective stresses and causes soil deformation (flow-induced deformation) and on the other hand, soil deformation (volume changes) modifies the seepage process and hence, changes the pore water pressure distribution (deformation driven flow) (Zhang et al., 2005, 2018, chap. 4; Song and Borja, 2014). The uncoupled analysis cannot capture the interdependence between the two processes, which is an inherent limitation of this method (Yang et al., 2017). To fully understand the hydro-mechanical behaviour of unsaturated soil slopes subjected to rainfall, it is necessary to integrate the two processes taking into account the interdependence between seepage and deformation. This brings us to the coupled hydro-mechanical or flow-deformation approach.

Broadly, in the coupled flow-deformation analysis, the mass-balance equation (continuity equation) and the momentum-balance equation (deformation equation) are solved simultaneously (Galavi et al., 2009). It allows incorporation of both flow-induced deformation and deformation-induced flow in the analysis.

Qi and Vanapalli (2015) compared the hydro-mechanical response of a typical expansive soil slope using uncoupled and coupled analyses using SEEP/W and SIGMA/W respectively and estimated the factor of safety using infinite slope formulation. This study showed that the uncoupled analysis produced a higher critical factor of safety when compared to the coupled analysis. This observation is consistent with the study by Rahim and Toll (2014) and Toll et al. (2019) where the effect of rainfall on an experimental soil slope in Singapore

was evaluated using both coupled and uncoupled methods in PLAXIS and SEEP/W with SLOPE/W respectively. This study also found that the uncoupled analysis predicted a higher factor of safety than that by the coupled analysis. Furthermore, Qi and Vanapalli (2015) found that the coupled and uncoupled analysis predicted different pore water pressure profiles and the former predicted a relatively well-defined wetting front. In contrast, Rahim and Toll (2014) reported a similar trend of changes in pore water pressures during infiltration which was also comparable to that measured in the field. This discrepancy could be because of the expansive nature of soil analysed by Qi and Vanapalli (2015) in which volume changes can be large and non-uniform during rainfall (Fredlund et al., 2012; Xue et al., 2016). In such soils, the coupled analysis would be more effective for predicting hydro-mechanical behaviour (Qi and Vanapalli, 2015).

Furthermore, Oh and Lu (2015) conducted a hydro-mechanical analysis of two unsaturated cut slopes in Korea. This study showed that the coupled hydro-mechanical analysis can not only provide a better physical representation of water flow and stresses but predict the actual failure times. In general, the failure times are predicted by examining the change in the factor of safety over time. Using the stress and pore water pressures generated by the coupled analysis, either the shear strength reduction method (Griffiths and Lu, 2005) or limit equilibrium method (Borja et al., 2012) are used to determine the factor of safety. The ability of coupled hydro-mechanical analysis to predict the failure time has also been stated by Md. Rahim (2016) and Yang et al. (2017, 2019, 2020). The study undertaken by Yang et al. (2017) demonstrated that the coupled flow-deformation analysis can be used to identify the initiation time of failure and to review the effect of rainfall infiltration on the pre-failure mechanism. As for uncoupled analysis, Harris et al. (2012) used SEEP/W and SLOPE/W to back-analyse a rainfall-induced failure of a road embankment in New Zealand and by determining the factor of safety at hourly time steps, this study aimed to predict the timing of the failure. However, the factor of safety obtained from SLOPE/W dropped below 1 (indicating failure) approximately 600 hours after the first movement was detected on the investigated slope. This suggests that the timing of slope failure could be predicted more accurately using the coupled hydro-mechanical approach.

Hamdhan and Schweiger (2013) performed a fully-coupled flow deformation analysis of an instrumented slope in China subjected to rainfall using PLAXIS 2D and compared the predicted pore water pressures with the in-situ measurements. A reasonable agreement was found between the observed and predicted pore water pressures. However, the model was found to under-estimate the pore water pressure, compared to the field, especially near the ground surface. The authors have argued that this difference could be due to the

presence of surficial cracks and fissures that may have influenced the pore water pressures in the field.

Hence, considering the relative advantages of using the finite element method and coupled analysis approach, in this study, fully coupled flow-deformation analyses were undertaken using finite element-based software- PLAXIS 2D.

## **6.4 Uncertainties in numerical modelling of landslides**

While numerical modelling techniques are powerful tools utilised in various geotechnical applications, there are uncertainties and limitations associated with their application, which should be acknowledged. For the numerical model to represent the slope movement, the local site characteristics including slope geometry, stratigraphy, groundwater, internal structures and physical and hydro-mechanical soil properties and the external controlling factors such as rainfall, temperature and soil water content need to be defined (Van Asch et al., 2007). Since these data can be difficult to be defined precisely, approximations and simplifications are made in the input and geometry of the model, which introduces uncertainty in the slope stability assessment. In this context, Anderson and Holcombe (2013) have underlined two specific sources of uncertainty - the uncertainty in soil parameters and uncertainty related to the representation of the physical landsliding mechanism.

According to Zhang et al. (2018), the major sources that introduce uncertainties in soil parameters include the inherent spatial soil heterogeneity, limited information about the subsurface conditions and measurement errors caused by sampling disturbance, imperfect testing, human imperfections, and empirical estimation of soil properties. Besides, Anderson and Holcombe (2013) have added that the interpretation, as well as selection of the soil properties for stability analysis, is subjective, and this adds to the uncertainty in soil properties. The uncertainty related to the representation of the physical landsliding process in numerical modelling can stem from different sources including the boundary and initial conditions, time-steps in transient analyses, 2D representation of a 3D slope instability problem, temporal changes such as land-use modification and limitations within the numerical modelling method (El-Ramly, 2001; Zhang et al., 2011; Anderson and Holcombe, 2013). Furthermore, the reliability of the predictions of physically based slope stability models is generally assessed by comparing or calibrating with the observed behaviour of the systems. However, as the prediction involves several input parameters, there may be a case of equifinality, which results in uncertainty of the model predictability (Beven, 1996).

To incorporate the uncertainties in soil properties in slope stability analyses, various probabilistic techniques are adopted, which are elaborated in detail by El-Ramly (2001) and Uzielli et al. (2006). In contrast to the traditional deterministic methods, where the slope stability analyses are conducted using sets of measured or estimated input parameters, the probabilistic approach predicts the probability of slope failure and the input parameters are treated as random variables within a pre-determined or observed range (Queiroz, 2016; Zhang et al., 2018). The commonly used probabilistic approach is the Monte Carlo method, which generates random samples or a combination of model parameters based on their probability distribution and evaluates the distribution of safety factors using deterministic physically based models (Uzielli et al., 2006; Almeida et al., 2017; Bozzolan et al., 2020). Additionally, sensitivity analyses can be conducted to address the uncertainty in soil parameters using numerical programs like PLAXIS (Bentley Systems Inc., 2018) and SLOPE/W (GeoStudio, 2020). In such analyses, by specifying a definite range of input soil parameters, it is possible to analyse which variable has the greatest influence on the model prediction of the factor of safety, displacements, and stresses. By identifying the factor to which the model prediction is most sensitive to, it is possible to evaluate how the model can be optimised to better represent the observed behaviour of the system (Sandström, 2016).

Although the probabilistic methods and sensitivity analyses account for the uncertainties, they can be computationally demanding and time-consuming (Queiroz, 2016). Further, the probabilistic method requires adequate information to develop probability distribution of the input soil parameters, the absence of which limits the application of this method (El-Ramly, 2001; Chowdhury et al., 2009). In a data-scarce region, where such information are generally limited, with a sound understanding and interpretation of the site conditions, the deterministic method for slope stability analysis can be the useful approach. Using the limited set of input parameters, the deterministic model predictions can be compared or calibrated against the observed responses for more accurate assessments (Chowdhury et al., 2009). Hence, as Chowdhury et al. (2009) and Uzielli et al. (2006) have noted, the two approaches discussed above should be considered as complementary and not that one method is superior to the other; proper understanding and interpretation of the ground conditions and modelling results are necessary for any type of analysis to be useful.

## **6.5 Some limitations in numerical modelling of unsaturated soils**

Unsaturated soils exhibit hysteretic behaviour when subjected to drying and wetting, as discussed in chapter 4 (section 4.2.4). However, numerical modelling software packages like PLAXIS, SEEP/W and SLOPE/W are not programmed to incorporate hysteretic

behaviour during drying and wetting. Incorporating hysteresis into the analysis can be complicated because a slope can experience drying and wetting simultaneously. For instance, after a rainfall event, the upper layers of the slope may experience drying while the lower layers may be wetting due to percolation of rainwater from the upper layers (Tsaparas, 2002; Yang et al., 2012; Kristo et al., 2019; Toll et al., 2019).

Tami et al. (2004) suggested that in the seepage analysis, the drying or wetting SWRC should be selected based on the process that the soil experiences, rather than the flux-boundary condition like rainfall or evaporation at the surface. In the studies undertaken by Toll et al. (2019) and Tsaparas (2002), the SWRC for the surficial layers was switched manually to the drying phase immediately after a rainfall event, while continuing to use the wetting phase of the SWRC for the lower layers. However, according to Yang et al. (2012), sudden changes in the relationship between the soil suction and the water content and permeability by switching to the drying or wetting phase can sometimes cause convergence problems in seepage analysis.

It is still debated in the literature whether the wetting or the drying portion of the SWRC should be implemented for analysing rainfall-induced slope failures. Some studies have utilised the main drying curve for numerical analysis (Harris et al., 2012; Md. Rahim, 2016), while others have implemented the wetting SWRC (Borja et al., 2012; Song et al., 2016; Yang et al., 2019). However, when Li et al. (2005) compared the SWRC determined in the laboratory with that measured in the field, the field SWRC was found to match closely with the wetting portion of the SWRC determined in the laboratory. Furthermore, Kristo et al. (2019) and Kim et al. (2018) have also suggested that the use of wetting SWRC can be a better alternative for modelling rainfall-induced soil slope failures when hysteresis cannot be incorporated. Hence, considering that infiltration corresponds to the wetting phase of the SWRC, it is perhaps more sensible to adopt the wetting path of the SWRC in the numerical analysis if hysteresis cannot be modelled.

Another factor that is known to influence the stability of natural as well as artificial slopes during rainfall is vegetation. The positive and negative effects of vegetation on slope stability have been elaborated by Wu (1984). In areas like abandoned agricultural terraces, the presence of organic matter in soil contributed by decayed plant roots may create non-capillary macropores and surficial cracks, thereby increasing the infiltration capacity of the soils near the ground surface (Collison et al., 1995; Wu et al., 2015). To incorporate such field conditions in the numerical model, Toll et al. (2019) and Gasmo et al. (2000) recommended the incorporation of a surficial soil layer with relatively high vertical permeability compared to that measured in the laboratory. Toll et al. (2014) and Md. Rahim (2016) modelled the desiccated surficial layer with a vertical permeability that is two to

three orders higher in magnitude than the horizontal permeability. By doing so, the authors found that the numerical prediction of pore water pressure in comparison to the field measurement was improved.

Although numerical modelling has proven to be a powerful and advantageous method of simulating slope instabilities, it should be recognised that they have limitations that inhibit an actual replication of the site conditions. Nonetheless, as discussed above, studies have found effective ways to tackle these uncertainties, which were also utilised in this study.

## 6.6 Fully coupled flow-deformation analysis in PLAXIS 2D

The coupled flow-deformation formulation in PLAXIS (Bentley Systems Inc., 2018) is derived based on Biot's three-dimensional consolidation theory (Biot, 1941) which couples the equilibrium equation and the continuity equation of the soil-water matrix (Galavi et al., 2009; Galavi, 2010). This allows simultaneous calculation of deformation and groundwater seepage under transient boundary conditions in both saturated and unsaturated soils (Galavi et al., 2009; Galavi, 2010).

In the coupled formulation in PLAXIS, the mechanical behaviour of unsaturated soil is modelled using Bishop's effective stress concept (Bishop and Blight, 1963) which was discussed in chapter 4. The pore air pressure is assumed to be negligible and the matric suction coefficient ( $\chi$ ) is considered to be equal to the effective degree of saturation. The effective stress formulation used in PLAXIS can be written as Equation 6.7. By combining Bishop's stress with the Mohr-Coulomb failure criterion, the shear strength of the soil is obtained using Equation 6.8.

$$\sigma = \sigma' + (S_e u_w) \quad (6.7)$$

$$\tau = c' + (\sigma - S_e u_w) \tan \phi' \quad (6.8)$$

Where

$\sigma$  = total stress

$\sigma'$  = effective stress

$S_e$  = effective degree of saturation

$u_w$  = pore water pressure

$\tau$  = shear strength of soil



$c'$  = effective cohesion

$\phi'$  = effective angle of shearing resistance

To describe the hydraulic behaviour of unsaturated soil, the van Genuchten hydrological model (van Genuchten, 1980) is used, which can be written as:

$$S_e = \frac{S(\psi) - S_r}{S_s - S_r} = \left[ 1 + (g_a |\psi|)^{g_n} \right]^{g_c} \quad (6.9)$$

Where

$S(\psi)$  = degree of saturation as a function of suction head

$$\psi = \text{matric suction head (m)} = -\frac{u_w}{\gamma_w}$$

$\gamma_w$  = unit weight of water

$S_r$  = residual degree of saturation

$S_s$  = saturated degree of saturation

$g_a$  = fitting parameter related to the air-entry value (unit of pressure head, 1/m), equivalent to  $\alpha$  defined in chapter 4

$g_n$  = fitting parameter related to the slope of the soil water retention curve, equivalent to  $n$  defined in chapter 4

$g_c$  = fitting parameter equivalent to the  $m$  value defined in chapter 4 =  $\frac{1 - g_n}{g_n}$

According to van Genuchten (1980), the permeability of unsaturated soil is obtained by multiplying the saturated coefficient of permeability by the relative permeability which is related to the effective degree of saturation. The relative permeability is obtained using the following equation:

$$k_r = (S_e)^{g_r} \left[ 1 - \left\{ 1 - S_e^{\left( \frac{g_n}{g_n - 1} \right)} \right\}^{\left( \frac{g_n - 1}{g_n} \right)} \right]^2 \quad (6.10)$$

Where

$k_r$  = relative coefficient of permeability

$g_j$  = fitting parameter related to pore tortuosity and pore connectivity (Schaap and Leij, 2000).

## 6.7 Numerical modelling approach

The numerical modelling approach utilised in this study is shown schematically in Figure 6.1. This figure shows the four main parts: model calibration, stability analysis before Kanglang landslide (December 2017 to June 2018), back-analysis of Kanglang landslide and stability analysis without road cut. As shown in this figure, the first part is the calibration of the numerical model against the field-measured volumetric water contents. The calibrated model was then used for analysis in parts 2, 3 and 4. The main difference to note between parts 2, 3 and 4 is the input flux applied to the model. Further descriptions of each part are presented below.

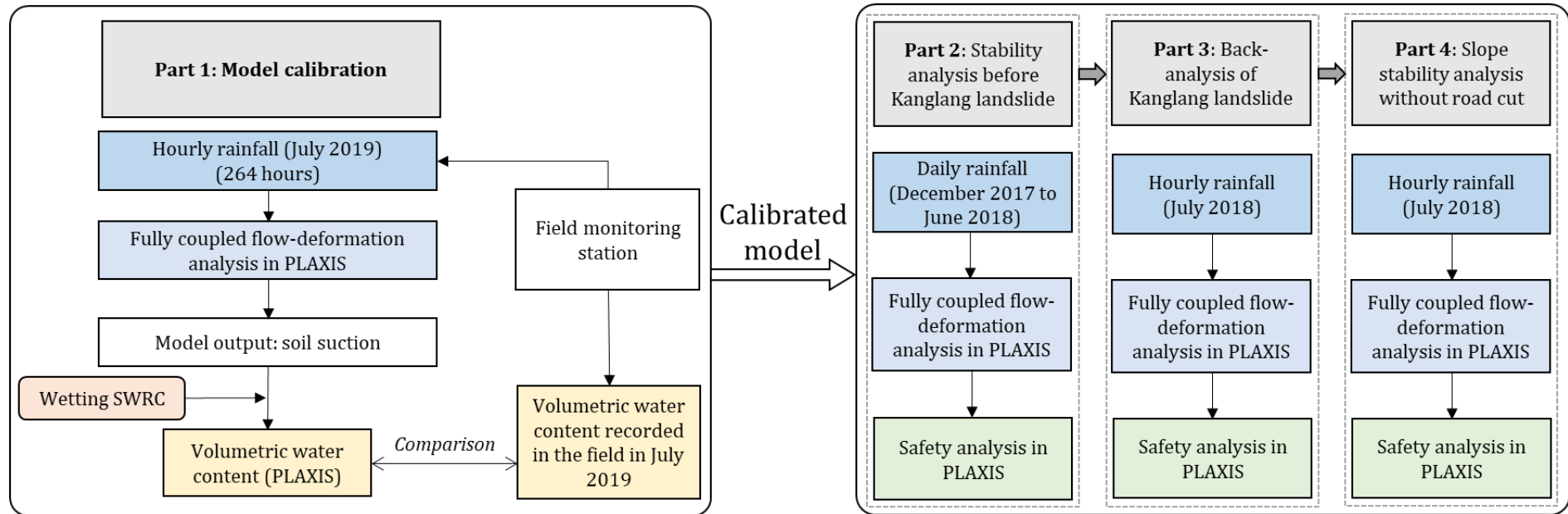


Figure 6.1 Numerical modelling approach utilised in this study.

### 6.7.1 Part 1: Model calibration

As the field monitoring station was not in place when Kanglang landslide occurred in July 2018, before conducting a back-analysis, it was necessary to calibrate the numerical model to ensure reliable predictions of slope behaviour can be made under different rainfall scenarios. Calibration of numerical models is generally performed by comparing the model output with the known or measured field data, adjusting certain material properties if necessary. In this study, calibration was performed by comparing the model output with the volumetric water content recorded by the 10HS soil moisture sensors installed in the field (chapter 5).

For calibration, a two-dimensional finite element model was constructed in PLAXIS representing a simplified cross-section of Kanglang landslide (section 6.8.1) and a fully coupled flow-deformation analysis was performed (Figure 6.1). In the analysis, to model infiltration, the hourly rainfall recorded in July 2019 at the field monitoring station installed near Kanglang landslide (chapter 5) was used as the influx on the upper surface boundaries. Since PLAXIS does not produce direct output as volumetric water content, the soil suction predicted by PLAXIS after the fully coupled analysis was converted to volumetric water content using the wetting SWRC. The predicted volumetric water content was then compared to that measured by the 10HS soil moisture sensors in the field during this period.

A good agreement between the volumetric water content measured during the monitoring period in July 2019 and the simulated volumetric water content obtained from PLAXIS under July 2019 rainfall would imply that the calibrated model is capable of replicating the field conditions during this time of the year. With this understanding, it was assumed that the calibrated model can reliably be used to model the actual failure mechanism of Kanglang landslide that occurred in July 2018.

### 6.7.2 Part 2: Stability analysis before Kanglang landslide (Dec 2017 - Jun 2018)

Before conducting the back-analysis of Kanglang landslide that occurred in July 2018, it was important to assess the stability of the slope before this event. Hence, the calibrated finite element model and soil parameters (from part 1) were used to predict the stability of the slope between December 2017 and June 2018. Since the slope at Kanglang landslide was recently cut for road widening when the reconnaissance survey was conducted in December 2017, the period before December 2017 was not incorporated in the analysis.

As shown in Figure 6.1, a fully coupled flow-deformation analysis followed by safety analysis was undertaken in this part. Due to the unavailability of hourly rainfall data, this analysis was performed using the daily rainfall totals. Daily rainfall data was from obtained from DHM (2018) for the four nearest rainfall stations (Figure 6.2) and a weighted average of daily rainfall at the study site was estimated based on the horizontal distance between the stations and the investigated slope. This rainfall was applied as daily flux into the model to evaluate the factor of safety between December 2017 and June 2018. It is worth noting here that the safety analysis performed using daily rainfall can give a conservative estimate of the factor of safety because the intermittent dry hours between rainfall events are not taken into account. Nonetheless, the goal here was to assess if the slope was predicted by the model to remain stable before the main landslide occurred in July 2018. If the factor of safety is greater than 1 before July 2018 using this approach, it can be assumed that the slope was stable before the occurrence Kanglang landslide.

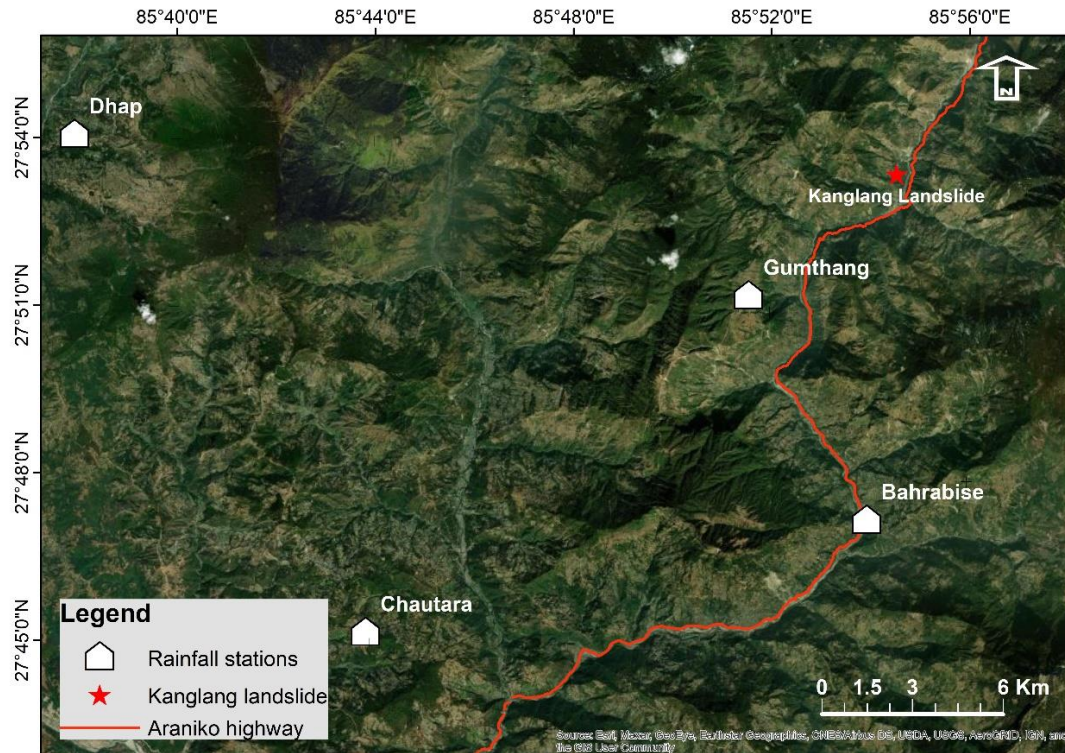


Figure 6.2 Rainfall stations located near Kanglang landslide – i) Gumthang (27°51'19.12"N 85°51'34.75"E, 1846 m a.s.l.), ii) Bahrabise (27°47'19.25"N 85°53'59.95"E, 884 m a.s.l.), iii) Chautara (27°45'13.62"N 85°43'55.48"E, 1552 m a.s.l.) and iv) Dhap (27°54'5.13"N 85°37'57.00"E, 1347 m a.s.l.).

### 6.7.3 Part 3: Back-analysis of Kanglang landslide (July 2018)

After successfully completing parts 1 and 2, the back-analysis of Kanglang landslide was conducted. As discussed in chapters 1 and 2, the back-analysis of Kanglang landslide to understand the mechanism of failure and to understand the role of the road cut and rainfall on slope instability is one of the key objectives of this study.

For the back-analysis, hourly rainfall data of July 2018 was obtained from Bahrabise rainfall station, which is ~12 km from the study site (Figure 6.2). Under this rainfall as influx boundaries, a fully coupled flow deformation analysis combined with safety analysis was conducted using the calibrated model (part 1), as shown in Figure 6.1. Although it would be more desirable to use the rainfall data from the nearest rainfall station (Gumthang, Figure 6.2), due to the unavailability of hourly rainfall data, this analysis was conducted using the rainfall from Bahrabise rainfall station. During the analysis, it was presumed that the factor of safety will drop to 1 or less during simulation indicating the occurrence of Kanglang landslide. It was also anticipated that this will occur before 16 July 2018, before which the Kanglang landslide was said to have occurred by the owner of this site.

#### 6.7.4 Part 4: Stability analysis without road cut

The numerical simulation described in part 3 (back-analysis of Kanglang landslide) was replicated in part 4 using a new geometry without the road cut. This analysis aimed to evaluate the slope stability in an idealised setting where the slope had not been cut for road construction, under the same flux boundary condition (July 2018 rainfall) which triggered Kanglang landslide. The comparison of the factor of safety obtained from this analysis with that from part 3 (back-analysis of Kanglang landslide) could provide a useful understanding of the contribution of the road cut on the occurrence of Kanglang landslide.

### 6.8 Setting up the model for numerical modelling in PLAXIS

#### 6.8.1 Model geometry and finite element mesh

A simplified two-dimensional plane strain model of the investigated slope – Kanglang landslide before failure was created in PLAXIS for part 1 (model calibration), 2 (stability analysis (December 2017 – June 2018)) and 3 (back-analysis of Kanglang landslide) (Figure 6.3). The slope geometry was constructed based on the measurements in the field and the digital elevation map of the study area. The finite element mesh of the model created by PLAXIS is shown in Figure 6.4, which consists of 3399 15-noded triangular elements and 27515 nodes. A finer mesh was defined for the upper layers because higher deformation was expected in this part of the model and the focus was also to obtain volumetric water content changes at 0.3 m, 0.8 m and 1.2 m for model calibration (part 1). Since the vertical distance between these points is small, a coarse mesh could give an inaccurate prediction. In the lower layers, however, the mesh coarseness was increased to reduce computational time.

Figure 6.5 and Figure 6.6 illustrate the simplified two-dimensional plane strain model and finite element mesh created for part 4 (stability analysis without road cut). The finite element model used for part 1, 2 and 3 (Figure 6.3) was modified to represent the natural hillslope at Kanglang landslide without the road cut. The finite element mesh used for this analysis consisted of 3623 triangular elements and 29303 nodes. The coarseness of the mesh was kept the same as that in Figure 6.4 for the back-analysis so that the resulting factor of safety are comparable.

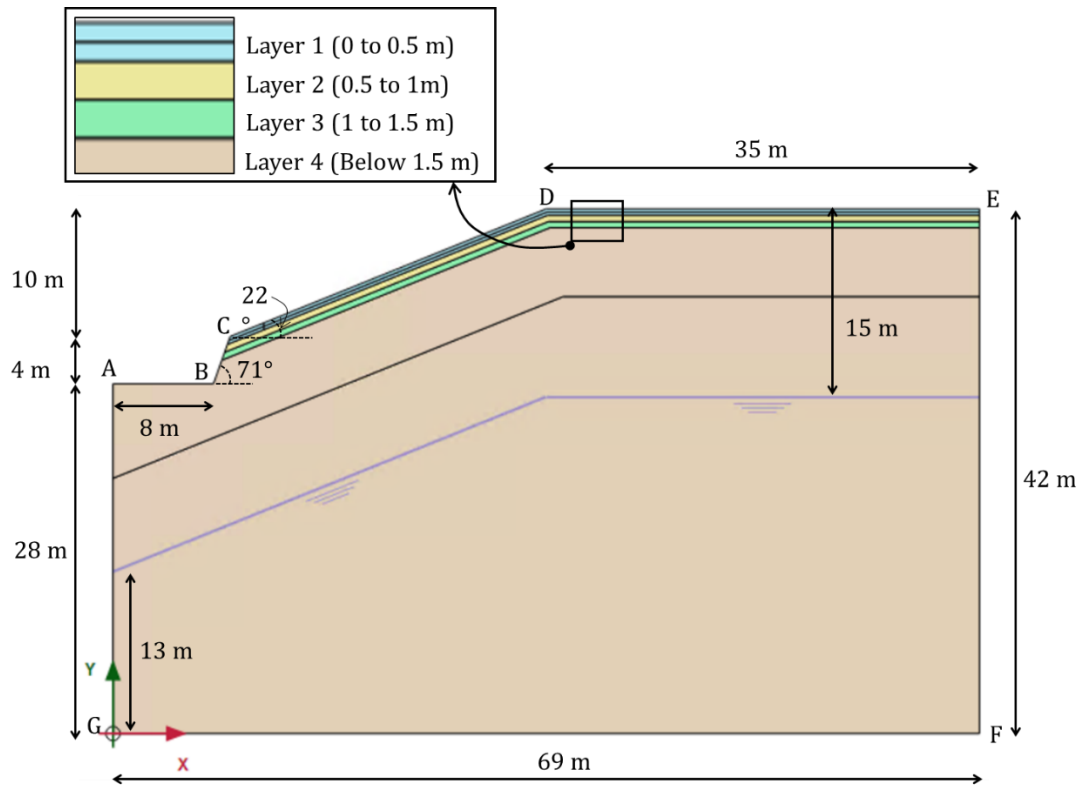


Figure 6.3 Geometry of the model for part 1 (model calibration), part 2 (stability analysis before Kanglang landslide (Dec 2017 - Jun 2018)) and part 3 (back-analysis of Kanglang landslide).

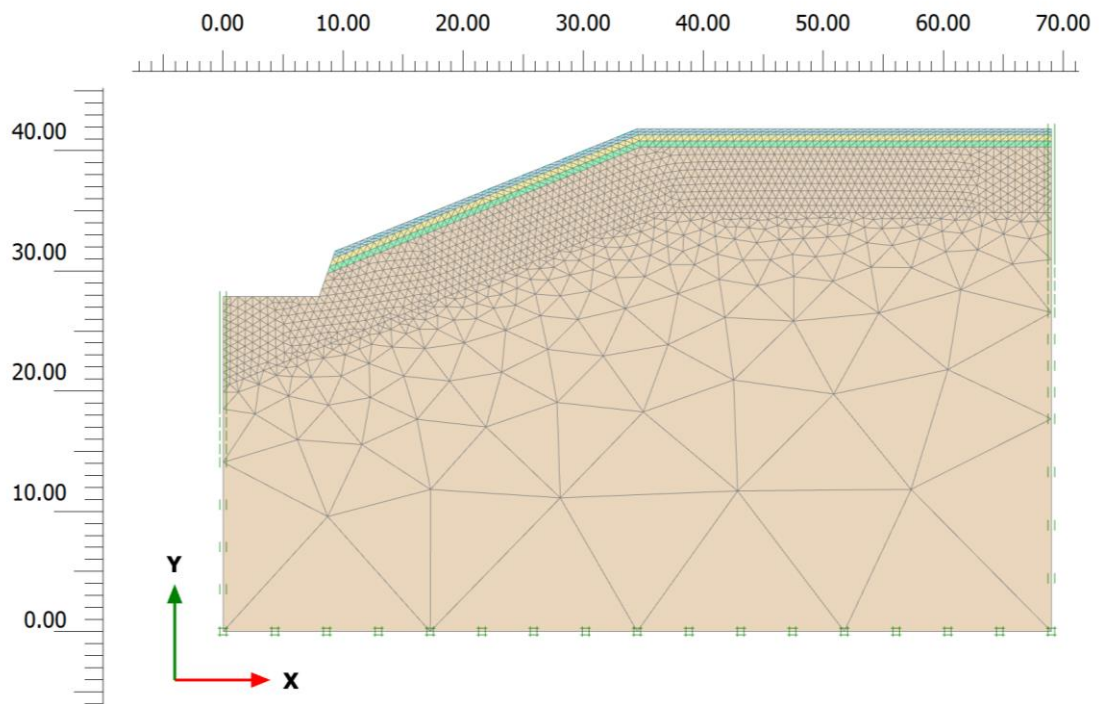


Figure 6.4 Finite element mesh for part 1 (model calibration), part 2 (stability analysis before Kanglang landslide (Dec 2017 - Jun 2018)) and part 3 (back-analysis of Kanglang landslide) (the vertical and horizontal axes show model dimensions in meters).



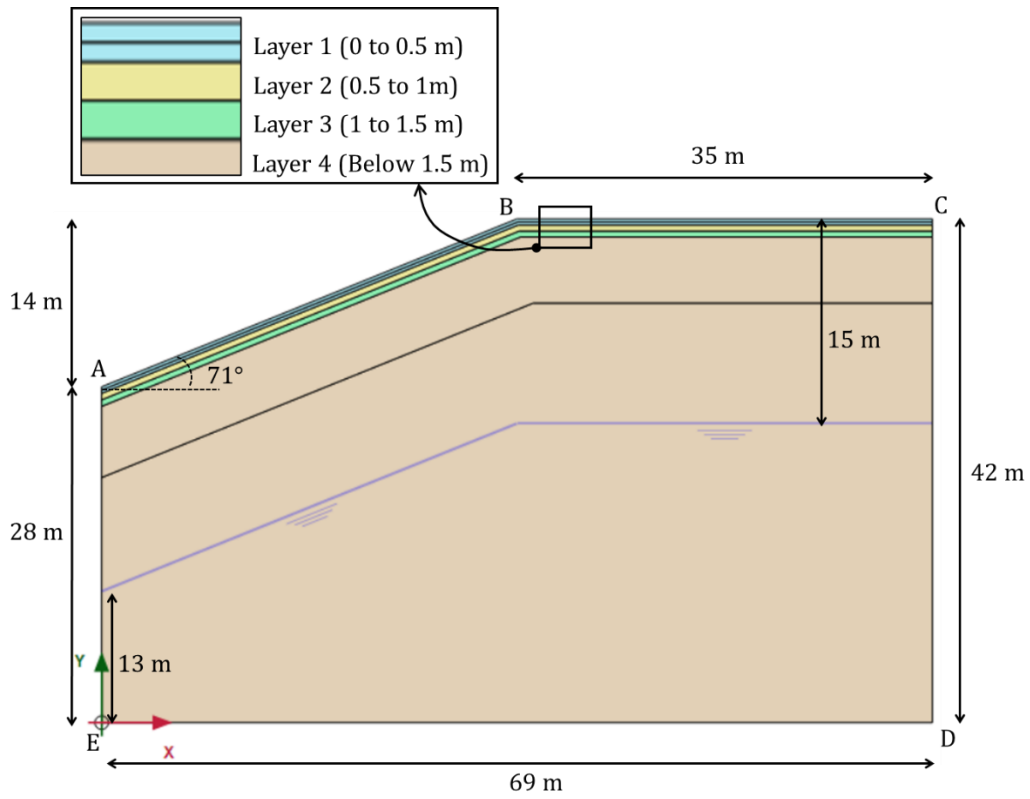


Figure 6.5 Geometry of the model for part 4 (stability analysis without road cut).

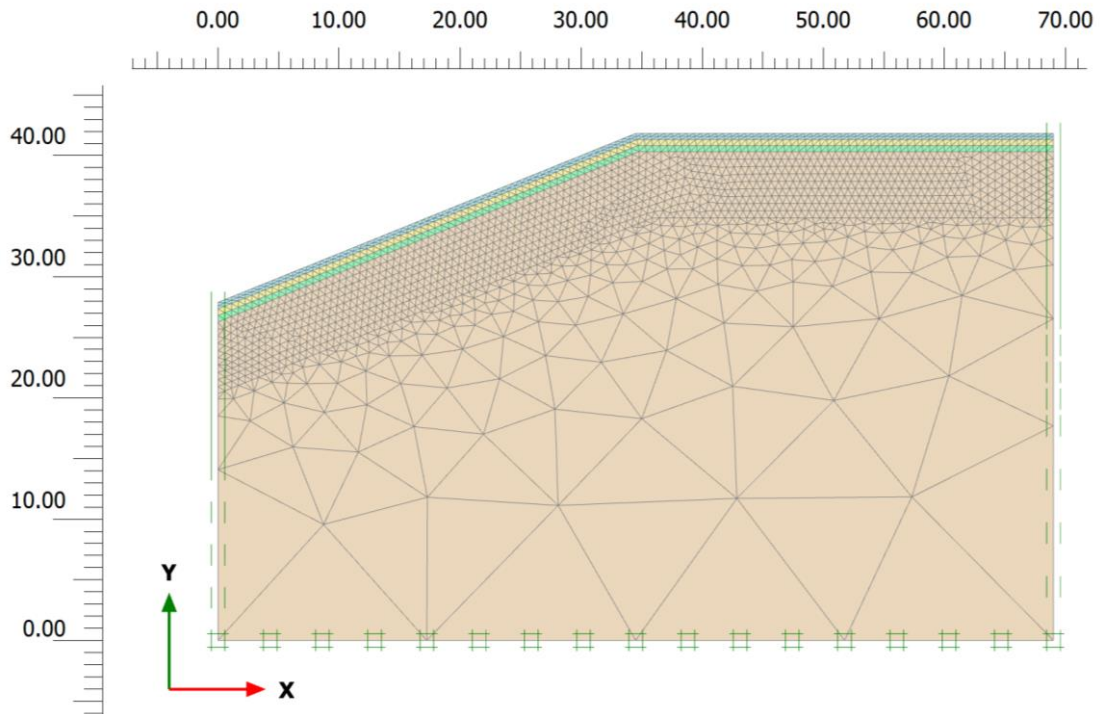


Figure 6.6 Finite element mesh of the model for part 4 (stability analysis without road cut) (the vertical and horizontal axes show model dimensions in meters).

## 6.8.2 Material properties

The conventional Mohr-Coulomb model was used to represent the constitutive relationship of the soils. As discussed in chapter 4, it is known that at larger strains, as will exist in such a failure, the strength of the soil eventually reaches a critical state condition. Since the silt-sized particles dominate the particle size distribution of soils from the site (chapter 4), it would not be expected that a residual state would be created due to clay particles aligning within the shear zone. Most importantly, during the triaxial test, the saturated samples did not exhibit a distinctive peak, rather contractive behaviour typical for relatively loose or normally consolidated soils was observed at lower confining pressures ( $\leq 75$  kPa) (Figure 4.16, chapter 4). Hence, the angle of shearing resistance ( $\phi$ ) at the critical state ( $36^\circ$ ) was adopted based on the saturated triaxial test results (Figure 4.16, chapter 4). Although the effective cohesion is negligible at the critical state, a small value of cohesion is usually assigned in the stability analyses to prevent numerical instability near the surface, under low effective stresses. In this study, a cohesion of 3 kPa was assigned to the materials because the use of a lesser value of cohesion predicted a localised failure at the steep face of the cut slope (essentially modelling surface raveling), which prevented the analysis of a deeper failure from proceeding further. The elastic modulus of soil was estimated empirically using the SPT  $(N_1)_{60}$  values based on Bowles (1996) (Table 6.1).

The SPT tests conducted in BH-1 (Figure 3.7, chapter 3) showed that the subsurface near the crown of Kanglang landslide is underlain by a fairly uniform soil as indicated by the SPT  $(N_1)_{60}$  values. The trial pit excavated near the crown of Kanglang landslide also showed similar subsoil condition down to a depth of 1.5 m with only a noticeable change in wetness (Figure 3.9, chapter 3). Moreover, the laboratory test results indicated that the samples obtained from various depths within the trial pit contained similar particle size distribution, Atterberg limits and particle density (chapter 4). Hence, the angle of shearing resistance and cohesion were considered to be uniform throughout the model (Table 6.1).

In the simplified four-layer model shown in Figure 6.3 and Figure 6.5, the four soil layers were defined based on their hydraulic properties (saturated permeability and SWRC parameters). The van Genuchten hydraulic model (van Genuchten, 1980) was used to fit the SWRC and the permeability function which were discussed in chapter 4. The saturated permeability of soil was determined by extrapolation based on effective confining pressures (Figure 6.7). For the first layer (0 to 0.5 m), two times higher saturated permeability than the calculated value was assigned to account for the increased conductivity due to the presence of surficial cracks and organic matter (Dixon et al., 2019; Toll et al., 2019).

For the numerical analyses in part 1 (model calibration), the wetting SWRC parameters were used to model both drying and wetting phases to avoid over-estimation of suction. Since the SWRC was obtained from the laboratory for the upper two layers (Layer 1 and 2), the  $g_a$  values for layers 3 and 4 were adjusted to match the initial volumetric water content in the model to that measured in the field at 1.2 m. As the air-entry value tends to increase with the increase in normal stress and decrease in void ratio (Miller et al., 2008), a lower value of  $g_a$  than the upper layers was considered to be a reasonable assumption.

In part 3 (back-analysis of Kanglang landslide) and part 4 (stability analysis without road cut), the hydraulic properties of soil adopted for part 1 (model calibration) were used. However, in part 2 (stability analysis before Kanglang landslide (Dec 2017 - Jun 2018)) because the period from 01/12/2017 until 28/02/2018 was dry with only a few days of rainfall, the unsaturated soil behaviour was modelled using the drying SWRC. After the end of the dry period, from 01/03/2018 to 30/06/2018, the wetting SWRC was used to represent the unsaturated soil behaviour. The soil properties used in the numerical analyses are summarised in Table 6.1.

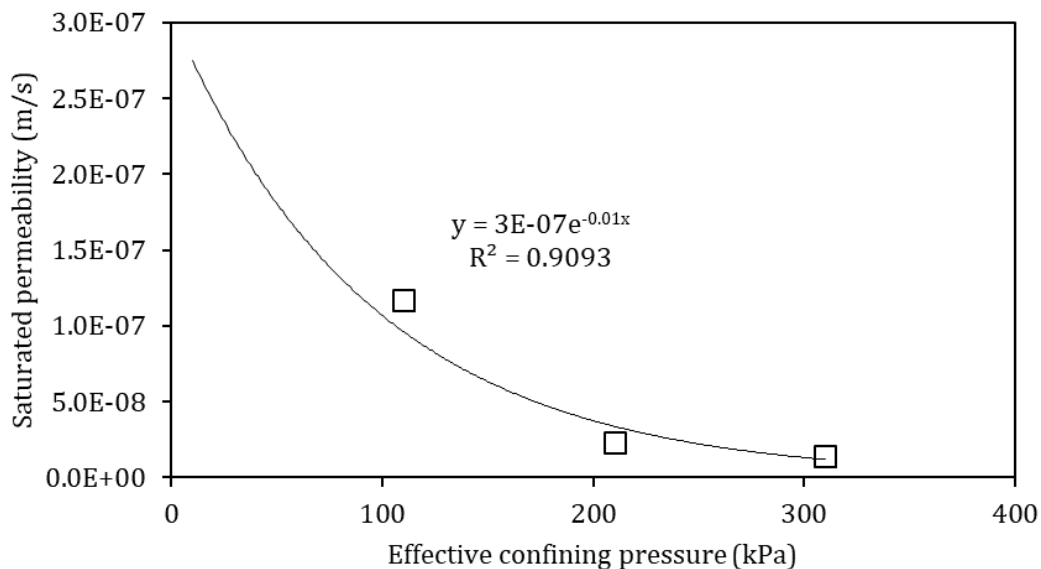


Figure 6.7 Relationship between effective confining pressure and saturated permeability extrapolated from the laboratory results (chapter 4, Figure 4.27).

Table 6.1 Summary of soil properties used for each layer for numerical modelling.

Layers	Depth (m)	Material type	Unit weight (kN/m <sup>3</sup> )		Mohr-Coulomb model parameters			Permeability ( $k_x$ and $k_y$ ) (m/s)	van Genuchten parameters						
			$\gamma_{unsat}$	$\gamma_{sat}$	$E$ (MPa)	$\nu$	$c'$ (kPa)		$\phi'$ (°)	Wetting SWRC			Drying SWRC		
										$g_a$	$g_n$	$g_c$	$g_a$	$g_n$	$g_c$
1	0 - 0.5	SILT to Sandy SILT	17.4	18.4	6	0.35	3	36°	5.8E-07	0.272	1.315	-0.239	0.121	1.372	-0.240
2	0.5 - 1	SILT	17.4	18.4	7	0.35	3	36°	2.7E-07	0.226	1.405	-0.288	0.063	1.65	-0.394
3	1 - 1.5	SILT	19.1	20.1	7	0.35	3	36°	2.6E-07	0.14	1.405	-0.288	0.063	1.65	-0.394
4	Below 1.5	Sandy SILT	20.2	21.2	7	0.35	3	36°	2.4E-07	0.14	1.405	-0.288	0.063	1.65	-0.394

### 6.8.3 Boundary and initial conditions

#### 6.8.3.1 Part 1: Model calibration

In part 1 of the analysis, the standard fixities were applied at the external boundaries of the model which allows vertical movement for the two lateral boundaries, free movement of the upper boundary and restrains movement at the bottom boundary. The initial stresses were generated using the gravity loading function in PLAXIS which is recommended for non-horizontal sloping ground. With the gravity loading function, initial stresses are generated by the application of self-weight.

The hydraulic boundary at the two lateral sides were closed and the bottom boundary was assigned as an open boundary. The groundwater table was assumed to be located 15 m below the top boundary DE in Figure 6.3 and BC in Figure 6.5. The initial pore water pressure was generated by applying a small constant flux of  $3.3\text{E-}08$  m/s at the ground surface for five years until a steady-state condition was attained where no further change in the pore water pressure with time was observed. The groundwater table in conjunction with the applied initial hydraulic condition was varied until the starting volumetric water contents were close to the field measurements at the start of July 2019.

After a steady-state condition was reached, the hourly rainfall was applied as an influx on the upper surface boundaries of the model. For calibrating the model, the rainfall obtained from the field monitoring station between 01/07/2019 and 11/07/2019 was used. During the dry hours, a negative flux of  $0.167\text{E-}03$  m/hr equivalent to 4 mm daily evapotranspiration was applied. The daily evapotranspiration was estimated from Lambert and Chitrakar (1989) based on the elevation of the study site.

It was assumed that ponding does not occur at the surface; hence, a small value of maximum pore water pressure head of 0.1 mm was assigned on the upper surface boundaries. A minimum pressure head of -30 m corresponding to the minimum volumetric water content of  $0.23 \text{ m}^3/\text{m}^3$  recorded during the monitoring period was prescribed at all upper surface boundaries to prevent unrealistic suction development due to evapotranspiration.

#### 6.8.3.2 Part 2: Stability analysis before Kanglang landslide (Dec 2017 - Jun 2018)

In this part of the analysis, the boundary conditions and the initial conditions used for calibrating the numerical model (part 1) was adopted (section 6.8.3.1). After a steady-state condition was reached, the weighted average daily rainfall from 01/12/2017 to 30/06/2018 computed from the daily rainfall measured at the four nearby rainfall stations

(Figure 6.2) was applied as influx on the upper surface boundaries as described in section 6.7.2. For the days with no rainfall, a negative flux of 4 mm/day was applied at the surface to model evapotranspiration.

#### 6.8.3.3 Part 3: Back-analysis of Kanglang landslide (July 2018)

The boundary conditions and initial conditions adopted for part 1 was used for the back-analysis of Kanglang landslide. The July 2018 hourly rainfall data obtained from the Bahrabise meteorological station (DHM, 2018) was applied as the influx on the upper surface boundaries after a steady-state condition was reached. Similar to parts 1 and 2, a negative flux of 0.167E-03 m/hr was applied on the upper surface boundaries to model evapotranspiration.

#### 6.8.3.4 Part 4: Stability analysis without road cut

The initial conditions, boundary conditions and flux at the upper surface boundaries (rainfall and evapotranspiration) utilised in part 3 (back-analysis of Kanglang landslide) (section 6.7.3.3) was used in this analysis.

## 6.9 Results of the numerical analyses

### 6.9.1 Part 1: Model calibration

After the end of the numerical simulation, the soil suctions computed by the model at 0.3 m, 0.8 m and 1.2 m below the ground surface (DE) were converted to volumetric water content using the wetting SWRC (Table 6.1). The resulting volumetric water contents were then compared to those recorded by the 10HS sensors installed in the field (chapter 5), which are shown in Figure 6.8, Figure 6.9 and Figure 6.10. From the figures, it is evident that the model captured the trend and the timing of volumetric water content change at the three measured depths. However, the model predicted greater changes in volumetric water content during rainfall than was recorded in the field and this is apparent mainly at 0.3 m and 0.8 m (Figure 6.8 and Figure 6.9). This discrepancy may have resulted from i) soil heterogeneity, ii) use of single wetting SWRC to convert computed suction into volumetric water content and iii) hydraulic hysteresis that was not incorporated in PLAXIS. However, the volumetric water content predicted by PLAXIS at 1.2 m was found to be in close agreement with the field-measured volumetric water content. Moreover, the timing and the trend of the increase and decrease of volumetric water content during and after rainfall predicted by the model was found to be in good agreement with that recorded in the field

for all measured depths. Given the reliability of the model to predict this, it was decided to adopt the model for the back-analysis described in the following sections.

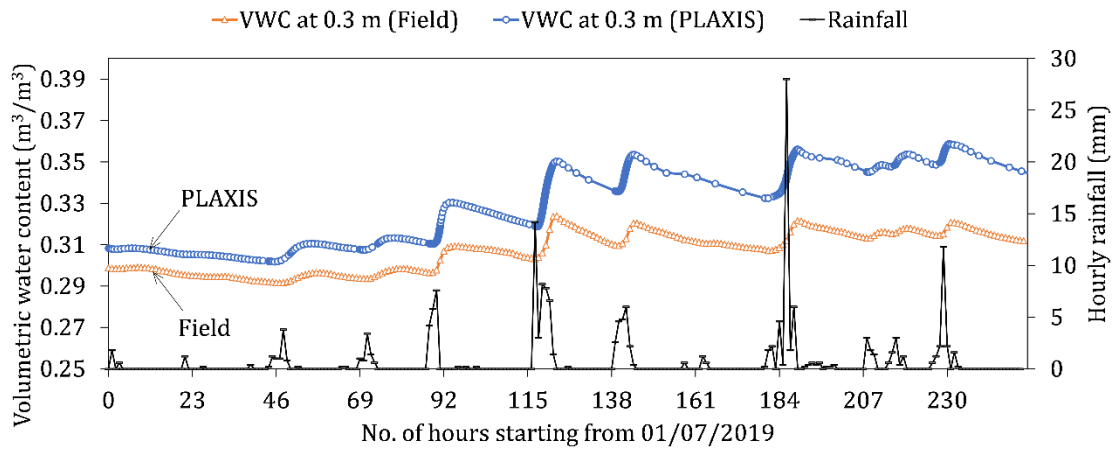


Figure 6.8 Comparison between hourly volumetric water content measured in the field and simulated in PLAXIS at 0.3 m depth from the surface from 01/07/2019 00:00 to 11/07/2019 11:00.

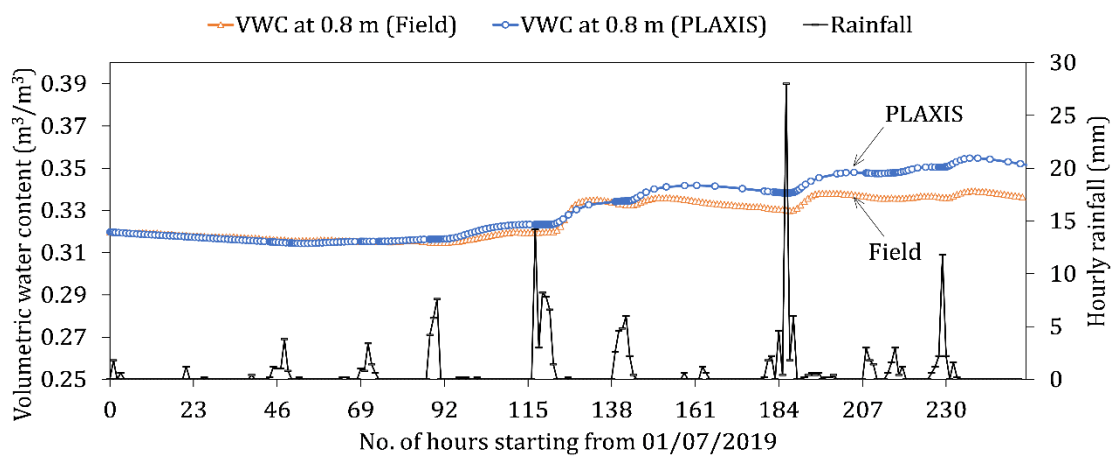


Figure 6.9 Comparison between hourly volumetric water content measured in the field and simulated in PLAXIS at 0.8 m depth from the surface from 01/07/2019 00:00 to 11/07/2019 11:00.

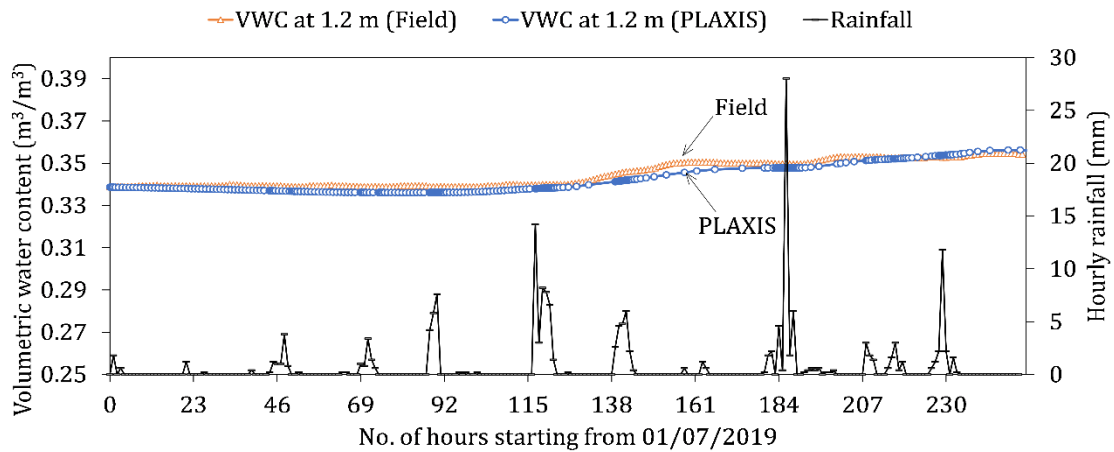


Figure 6.10 Comparison between hourly volumetric water content measured in the field and simulated in PLAXIS at 1.2 m depth from the surface from 01/07/2019 00:00 to 11/07/2019 11:00.

### 6.9.2 Part 2: Stability analysis before Kanglang landslide (Dec 2017 - Jun 2018)

The fluctuations in the factor of safety in response to daily rainfall from 01/12/2017 to 30/06/2018 is plotted in Figure 6.11. An increase in the factor of safety can be seen during the relatively dry period until the end of February 2018 which is expected due to the increase in suction as a result of drying. After the introduction of the wetting curve on 01/03/2018, a slight decrease in the factor of safety can be seen, but this remained fairly constant until 18/05/2018 (163<sup>rd</sup> day from 01/12/2017) during which the rainfall was close to 12 mm/day or less. The smaller changes in the factor of safety during this period can be explained in terms of the effective degree of saturation and relative permeability. As shown in Figure 6.12 during the dry days, the effective degree of saturation and relative permeability are low. Consequently, limited infiltration occurs in the soil, which explains the consistently high factor of safety during this period. As the number of wet days increased, the effective saturation and relative permeability of the soil can be seen to increase (Figure 6.12) and with this increase, a greater amount of rainwater could infiltrate into the soil which led to a drop in the factor of safety (Figure 6.13). In Figure 6.11 it can be seen that the factor of safety dropped slightly below 1 on a few days in June 2018, but can be seen to recover with a decrease in the total daily rainfall. Although this indicates failure, it is worth noting that this analysis was conducted under daily rainfall totals. In such analysis, the degree of saturation of soil is expected to rise continuously during consecutive wet days (Figure 6.12) because the intermittent dry hours between the rainfall events are not taken into account. Considering this limitation in the analysis, it can be assumed that the slope was in a stable condition between December 2017 and June 2018.



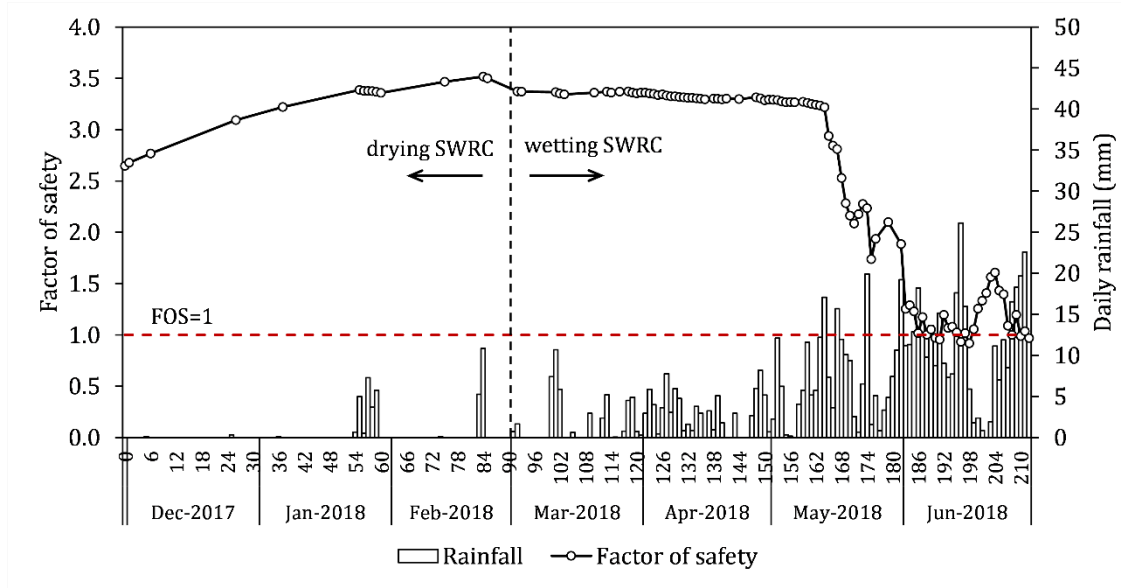


Figure 6.11 Variation of factor of safety from 01/12/2017 to 30/06/2018

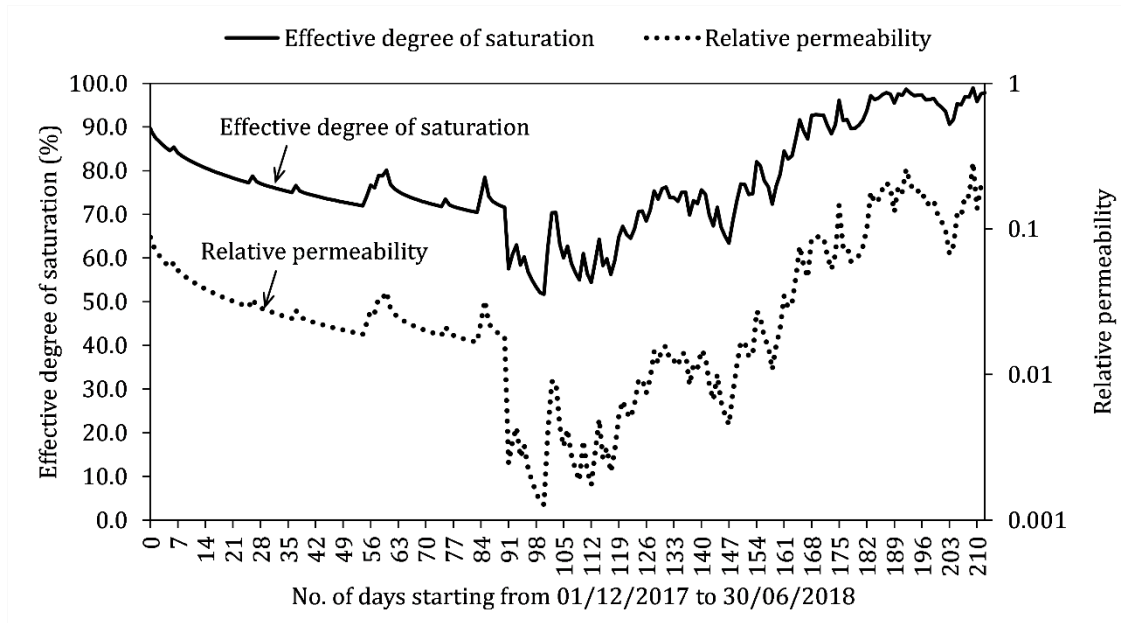


Figure 6.12 Daily variation in effective degree of saturation and relative permeability starting from 01/12/2017 to 30/06/2018.

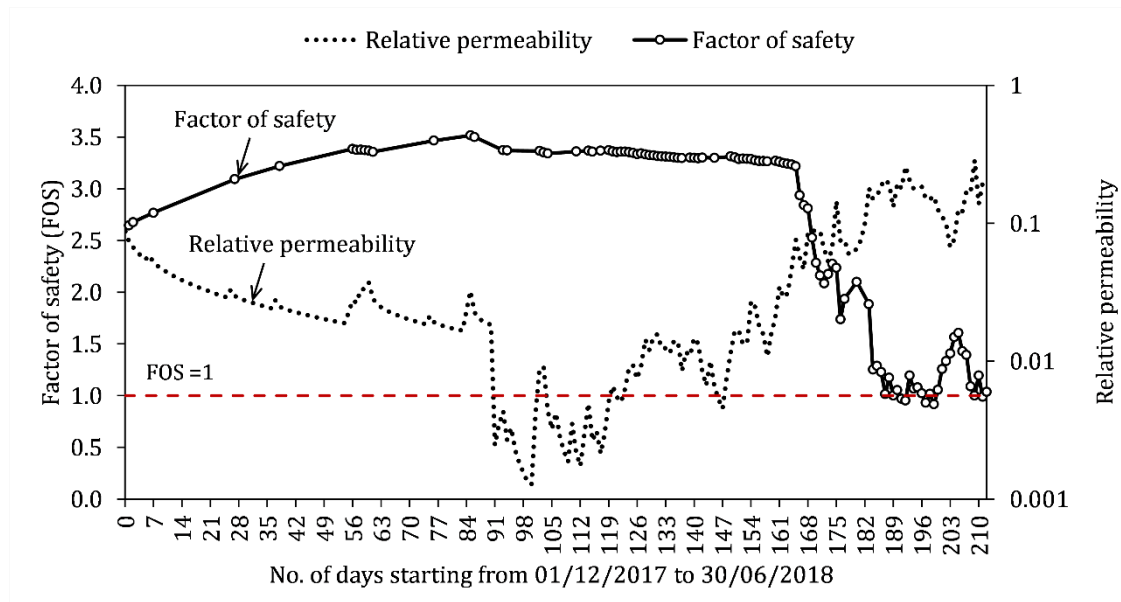


Figure 6.13 Daily variation in the factor of safety and relative permeability starting from 01/12/2017 to 30/06/2018.

### 6.9.3 Part 3: Back-analysis of Kanglang landslide (July 2018)

#### 6.9.3.1 Factor of safety

The variation of factor of safety with time from 01/07/2018 is shown in Figure 6.14 where the significant rainfall events are labelled from 1 to 6 in the figure. It should be noted that the starting factor of safety on 01/07/2018 in Figure 6.14 does not match the final factor of safety on 30/06/2018 from the previous analysis (Figure 6.11). This is because the back-analysis of Kanglang landslide was performed using hourly rainfall data and hourly time steps, whereas the previous analysis (part 3) was conducted using daily rainfall data and daily time steps.

In the back-analysis, as can be seen in Figure 6.14, the factor of safety reduced during rainfall and increased during dry periods and eventually dropped below 1 during a relatively low-intensity (4.4 mm/hr), long-duration (10 hours) rainfall event no. 6. The factor of safety reached 0.96 on 12/07/2018, after five hours of continuous rainfall (267<sup>th</sup> hour in Figure 6.14). This indicates that Kanglang landslide may have occurred during this time. This time frame is in line with the landowner’s statement according to which the Kanglang landslide occurred before 16/07/2018.

An interesting observation to note from Figure 6.14 is that the decrease in the factor of safety during high-intensity ( $\geq 6$  mm/hr)-short-duration (<6 hours) rainfall was relatively small. On the other hand, relatively low intensity but longer duration rainfall events caused

a notable decrease in the factor of safety. Based on this understanding, the relationship between the rainfall duration and the percentage decrease in the factor of safety was explored (Figure 6.15). A statistically significant relationship ( $R^2=0.9661$ ,  $p<0.001$ ) was found to exist between these two factors, suggesting that a greater decline in the factor of safety can be expected during long-duration rainfall events. This trend can be explained in terms of  $I_r/k_{sat}$  ratio. When this ratio is higher (rainfall event no. 1, 2, 3 and 5), as would be the case for high-intensity, short-duration rainfall events, less water can infiltrate into the ground to influence its stability. However, when this ratio is smaller (rainfall event no. 4 and 6) for low-intensity, longer duration rainfall events, a greater amount of water can infiltrate into the slope and influence slope stability. This agrees with the field observation discussed in chapter 5 where it was noted that greater changes in in-situ volumetric water content were recorded during longer duration rainfall events than during shorter duration rainfall events.

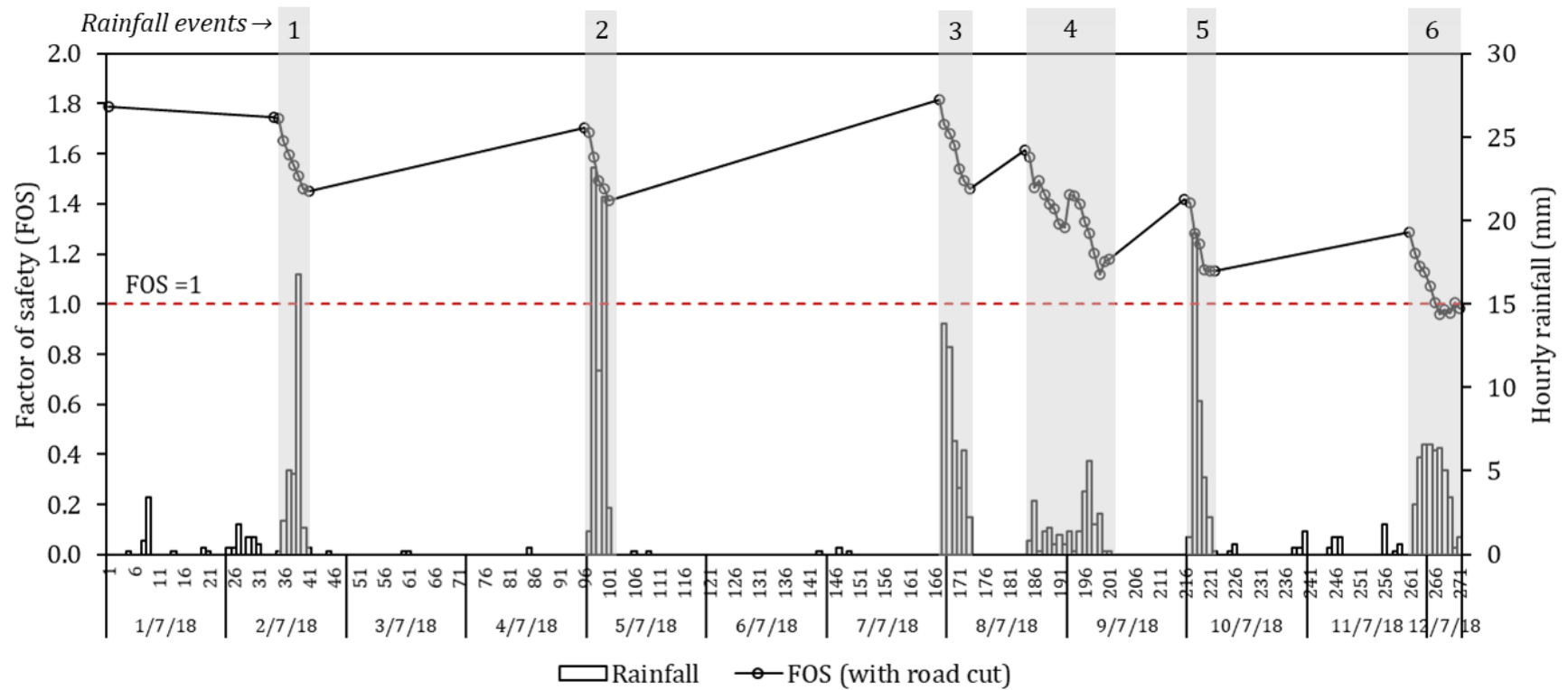


Figure 6.14 Variation in factor of safety with time from 01/07/2018 00:00 to 12/07/18 06:00. The numbers in the figure denote rainfall events\* (\*only the continuous rainfall events with more than 5 mm total rainfall are highlighted).

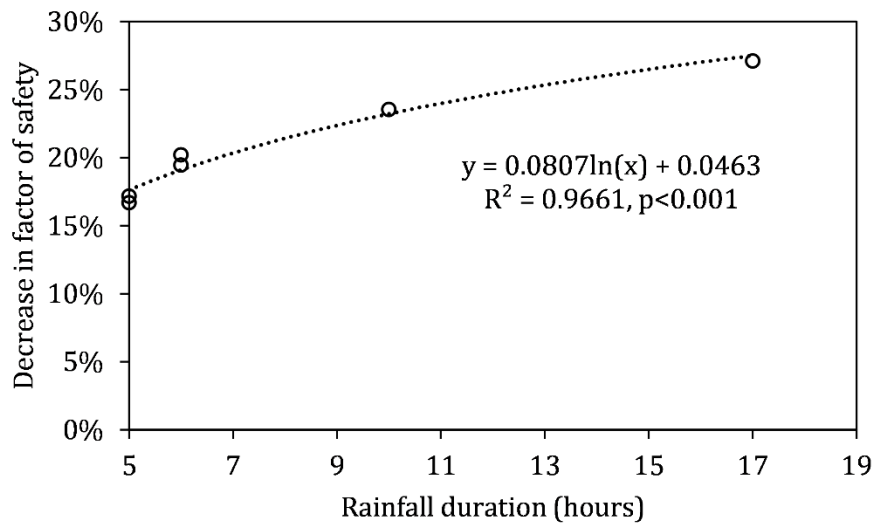


Figure 6.15 Relationship between rainfall duration and percentage decrease in the factor of safety.

#### 6.9.3.2 Suction

The contours of suction at the time of failure (267th hour in Figure 6.14) during rainfall event no. 6 is shown in Figure 6.16. A uniform reduction of suction near the ground surface can be seen in this figure. To closely examine the changes in soil suction during rainfall event no. 6, two sections - near the face of the cut slope (A-A\*) and at the upper hillslope (mid-slope) above the road cut (B-B\*) were selected (Figure 6.16). The fluctuations in soil suction with depth at the two sections A-A\* and B-B\* are plotted in Figure 6.17 and Figure 6.18 respectively. From the figures, the following observations can be made:

- i. The cumulative rainfall plotted in Figure 6.17 and Figure 6.18 show that rainfall event no. 6 that triggered Kanglang landslide was uniformly distributed with an average hourly intensity of 4.4 mm/hr except during the last two hours.
- ii. Figure 6.17 and Figure 6.18 clearly capture the advancement of the wetting front with progressive infiltration from the surface.
- iii. At both sections (A-A\* and B-B\*), suction at the ground surface dropped to zero within the first two hours of rainfall and remained so until the rainfall subsided during the last two hours.
- iv. In the both figures, it can be seen that the surficial soil layers (above 0.3 m depth) responded rapidly after the start of the rainfall event, similar to the volumetric water content response observed in the field at 0.3 m (chapter 5) and caused notable decrease in soil suction.

- v. After 5 hours of continuous rain, at the time of failure (267th hour), the infiltrating water had advanced down to 1.3 m and 1.1 m at sections A-A\* and B-B\* respectively, as indicated by the decrease in suction at these depths.
- vi. Compared to section B-B\*, suction near the ground surface at section A-A\* recovered more quickly as the rainfall subsided in the last two hours (270 and 271 hours). Likewise, at section A-A\*, the infiltrating water caused a decrease in suction down to 1.7 m at the end of the rainfall event. On the other hand, at section B-B\* the change in suction at 1.7 m depth was almost negligible. Greater changes in suction down to 1.7 m at section A-A\* is most likely due to infiltration from two parts of the slope: the upper hill slope above the road cut and the lower face of the cut slope adjacent to the road.
- vii. Overall, both figures suggest that only a small amount of rainwater infiltrated to 1.7 m and suction is not completely lost due to infiltration.
- viii. Although slight groundwater rise can be seen in Figure 6.16 there was no evidence of failure due to the rise in the groundwater table. The changes in suction local to the face of the slope are more significant.

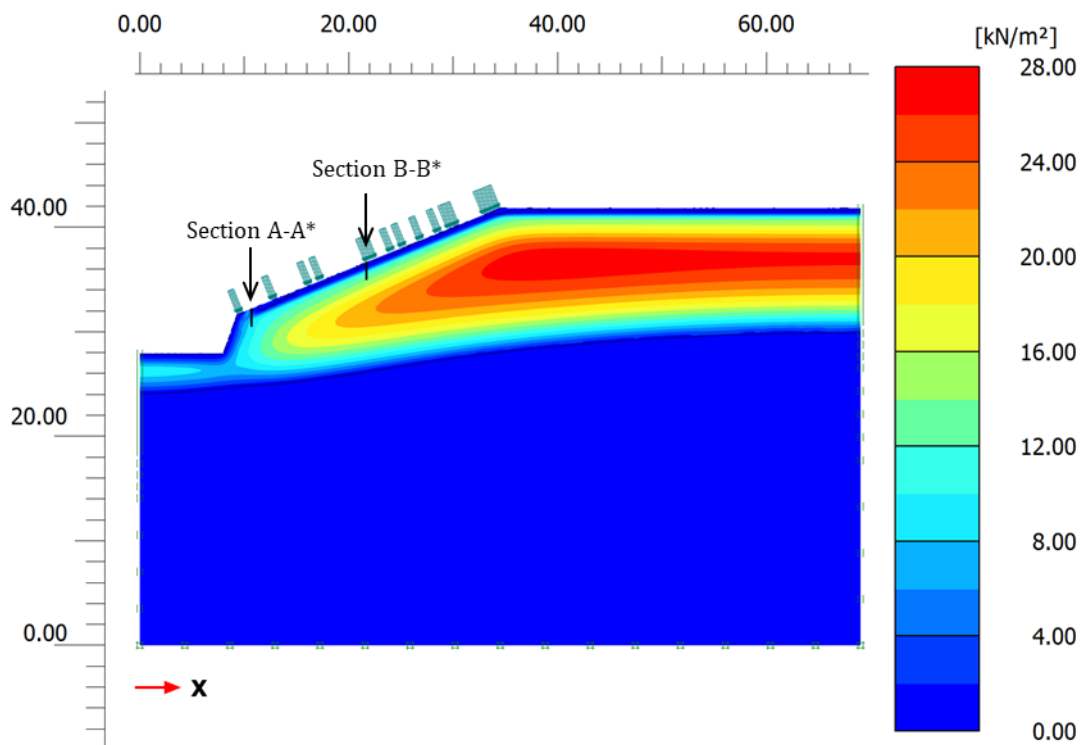


Figure 6.16 Suction contours at 267<sup>th</sup> hour (Figure 6.14) on 12/07/2018; suction profiles at sections A-A\* and B-B\* are shown in Figure 6.17 and Figure 6.18 (the vertical and horizontal axes show model dimensions in meters).

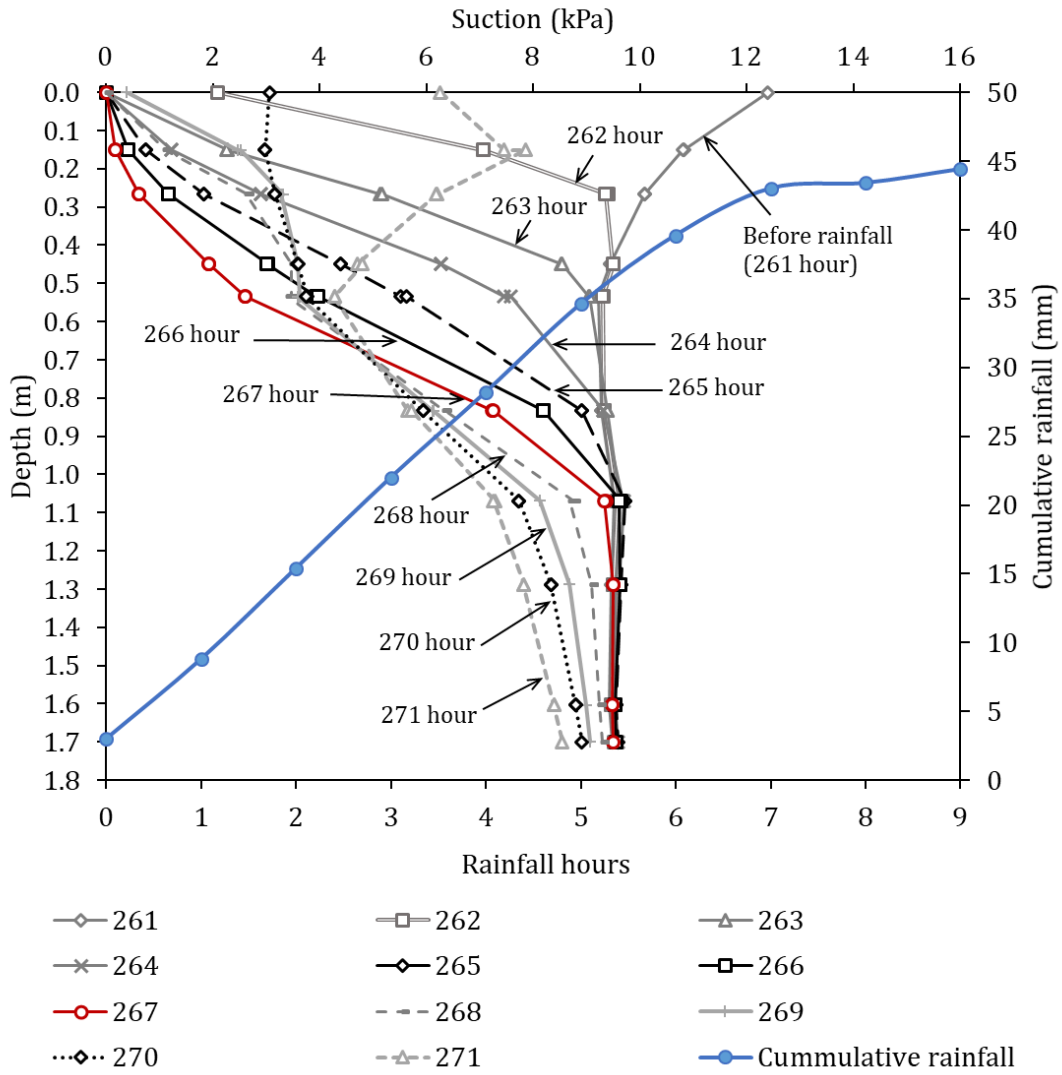


Figure 6.17 Variation of suction with depth during rainfall event no. 6 at section A-A\* (hours in the legend are shown with reference to Figure 6.14).

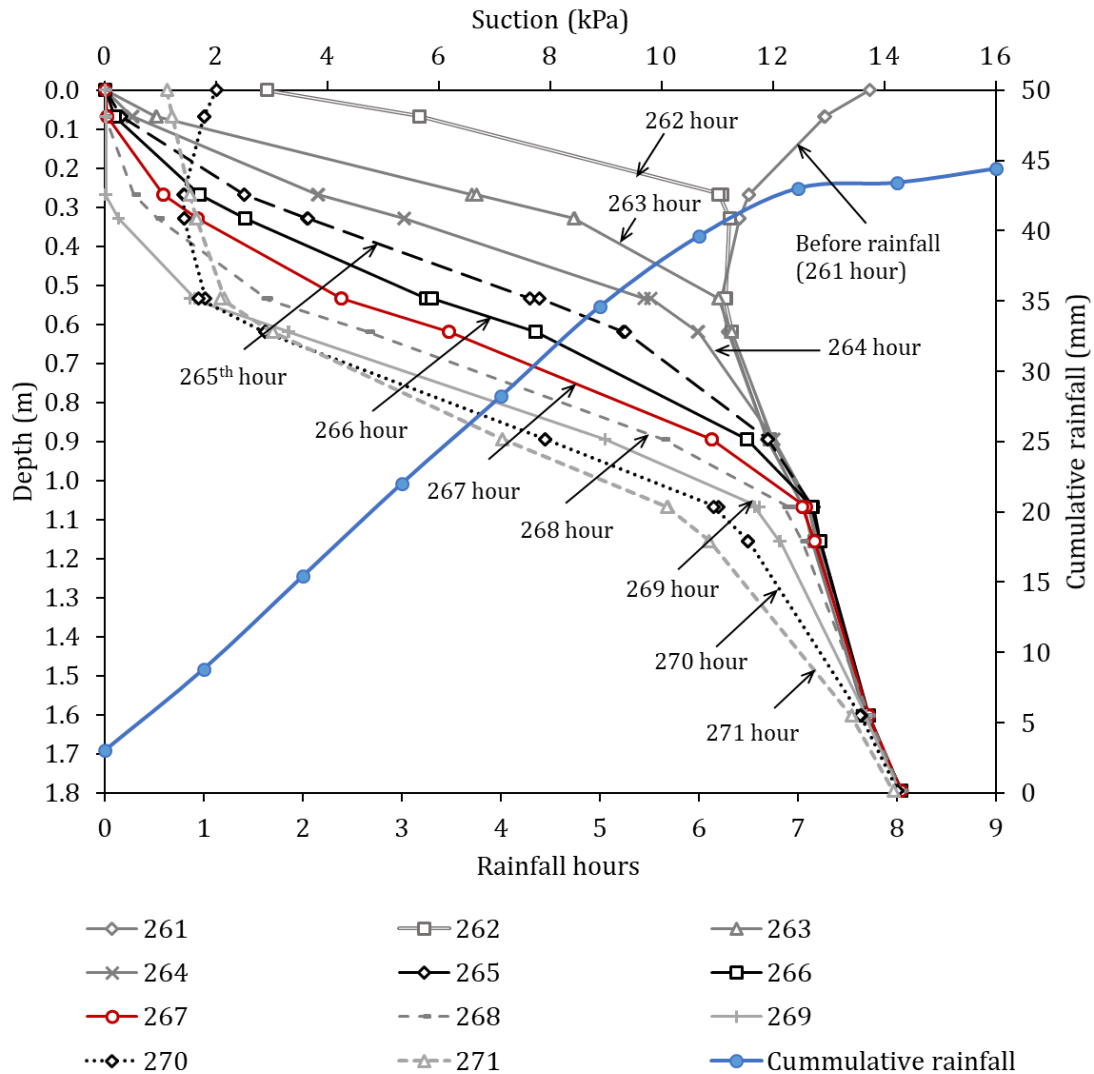


Figure 6.18 Variation of suction with depth during rainfall event no. 6 at section B-B\* (hours in the legend are shown with reference to Figure 6.14).

### 6.9.3.3 Total displacement

To evaluate displacement in the slope in response to rainfall, total displacement contours at the time of failure (267<sup>th</sup> hour in Figure 6.14) was obtained from PLAXIS (Figure 6.19). It can be seen in the figure that at the time of failure, the model predicted a maximum displacement of ~21 mm near the face of the cut slope. An increasing total displacement with the increase in distance to the cut slope can be seen in this figure. A smaller displacement of ~8 mm was also predicted near the mid-and crest of the slope, indicating movement at these locations during the time of failure.

The displacement predicted at the time of failure such as ~21 mm near the face of the cut slope (Figure 6.19) is rather small for a slope failure. However, it should be noted that these



displacements represent the elastic deformation predicted up to the point of failure. At the point of failure, plasticity is invoked which involves irreversible strain development with the Mohr-Coulomb constitutive model (Brinkgreve et al., 2018). However, with the conventional finite element analysis in PLAXIS, the post-failure movements cannot be predicted unless specialist large deformation analyses are used. According to Brinkgreve et al. (2015), finite element analyses are not suitable for problems involving large deformation due to the issue associated with the mesh tangling when the mesh deformations become large. Hence, the analysis presented here provides an assessment of slope behaviour only up to the point of failure.

To further evaluate the process of movement, total displacements predicted at the three selected sections in the slope: near the face of the road cut (section C-C\*), at the mid-slope (section D-D\*) and at the crest of the slope (section E-E\*) (Figure 6.19) were obtained from PLAXIS which are shown in Figure 6.20 to Figure 6.23. From the figures, the following observations can be made:

- i. Figure 6.20 to Figure 6.23 show that the slope displacements are linked directly to the rainfall. Generally, larger slope displacements occurred at all three selected sections of the slope during low-intensity and long-duration rainfall events (event no. 4 and 6), which were the events that caused the greater decline in the factor of safety.
- ii. Figure 6.20 shows that at the road cut (section C-C\*), larger displacements occurred at shallow depths ( $\leq 1.3$  m) than that at 3.6 m. During rainfall event no. 6, when the factor of safety dropped below 1 (267th hour), the displacement at the ground surface (section C-C\*) was  $\sim 17$  mm and that at 0.8 m and 1.3 m were  $\sim 13$  mm and  $\sim 10$  mm respectively. In contrast, the total displacement at 3.6 m was relatively small ( $\sim 6$  mm)
- iii. The larger displacements above 1.3 m depth at the road cut (section C-C\*) and relatively smaller displacements below this depth could be because the wetting front had not advanced beyond 1.3 m to cause a decrease in suction below this depth when the failure occurred (Figure 6.17).
- iv. With further infiltration after 267 hours, as the rainwater infiltrated down to 1.7 m, the displacements at section C-C\* accelerated, increasing the total displacement to 221 mm, 217 mm and 193 mm at the ground surface, 0.3 m and 0.8 m respectively (Figure 6.21).
- v. At the time of failure, a gradual increase in total displacements was predicted at both sections D-D\* and E-E\* due to progressive infiltration even though the magnitude of

displacements was relatively small compared to that at C-C\* (Figure 6.22 and Figure 6.23).

- vi. Similar to section C-C\*, relatively larger displacement was predicted at shallow depths near the mid-slope (section D-D\*) and the slope crest (section E-E\*). This could also be because during rainfall event no. 6, the rainwater did not percolate below 1.6 m. This is shown by the negligible change in suction at this depth (Figure 6.18).

Hence, the factor of safety dropped below 1 for the first time during rainfall event no. 6 when the wetting front reached 1.3 m and 1.1 m below the ground surface at the face of the cut slope and at the upper hillslope (mid-slope) above the road cut. The depth of infiltration predicted by the model during failure is close to the sliding depth (~1.5 m) at the landslide crown which was noted during the reconnaissance survey (chapter 2). The infiltration of rainwater to these depths could be the reason why the total displacements were larger at shallow depths ( $\leq 1.3$  m). With further infiltration after the failure, the wetting front advanced to 1.7 m near the road cut causing a reduction of suction. Similarly, at the mid-slope and slope crest above the road cut, the wetting front reached ~1.6 m at the end of the rainfall event reducing the suction down to this depth. It is important to note that although the wetting front advanced by 1.6-1.7 m depths at the end of the rainfall event, suction was not completely lost. Nonetheless, accelerated displacements exceeding 200 mm at shallow depths ( $\leq 1.3$  m) were predicted at the cut slope adjacent to the road. This indicates that the presence of the steep (~71°) road cut in the hillslope may have promoted the landslide during rainfall.

It should also be noted that the rainfall applied on the model was obtained from the rainfall station located ~12 km from Kanglang landslide and may not represent the actual rainfall condition that occurred at the time of failure. However, this analysis provides an indication of the timing of the failure which is close to the anticipated period based on the statement given by the landowner. Moreover, this analysis also provides an understanding of the mechanism of failure and the type of rainfall which can be detrimental to the stability of the slope.

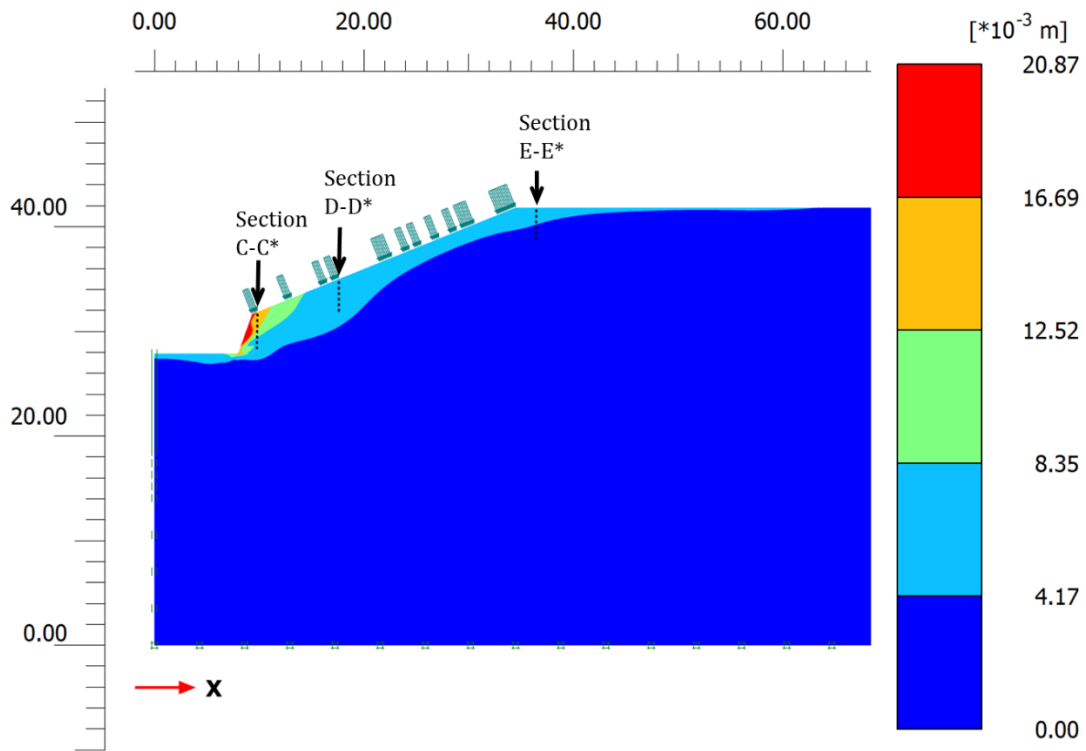


Figure 6.19 Total displacement contours at failure (FOS = 0.96) on 12/07/2018 (267<sup>th</sup> hour in Figure 6.14) (the vertical and horizontal axes show model dimensions in meters).

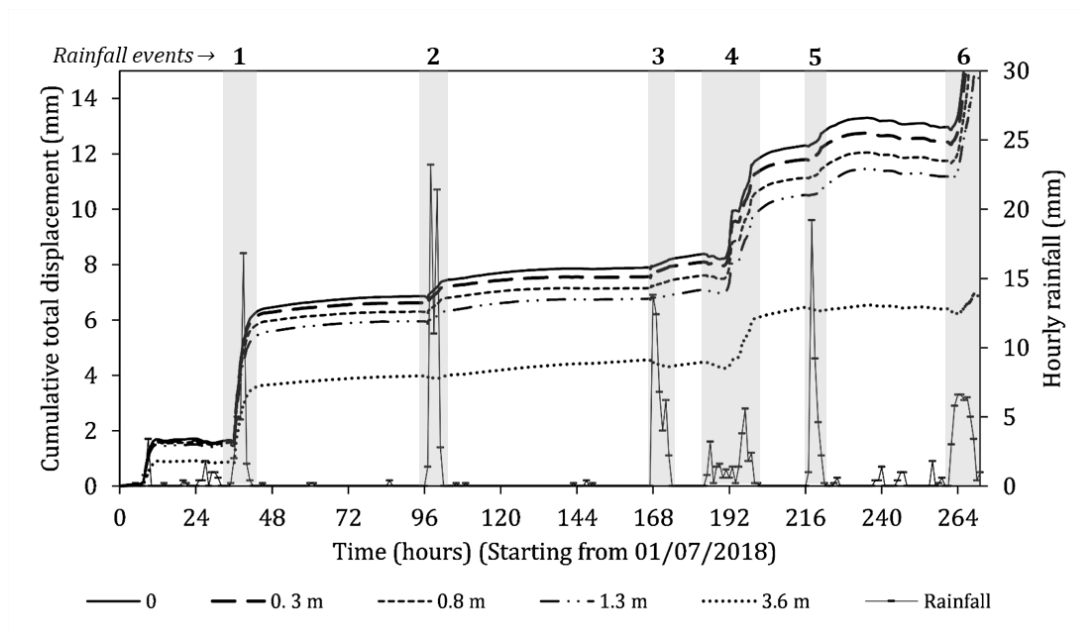


Figure 6.20 Cumulative total displacement measured near the cut slope (section C-C\*) from 01/07/2018 00:00 to 12/07/2018 06:00.

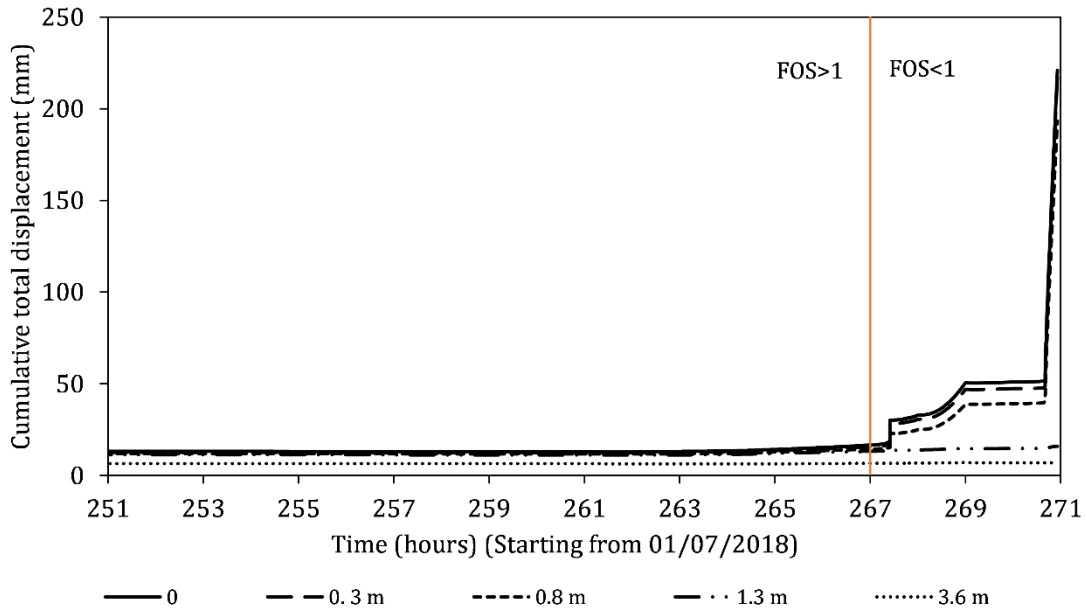


Figure 6.21 Cumulative total displacement measured at the face of the cut slope (section C-C\*) from 11/07/2018 10:00 to 12/07/2018 06:00 highlighting the accelerated displacement during rainfall event no. 6.

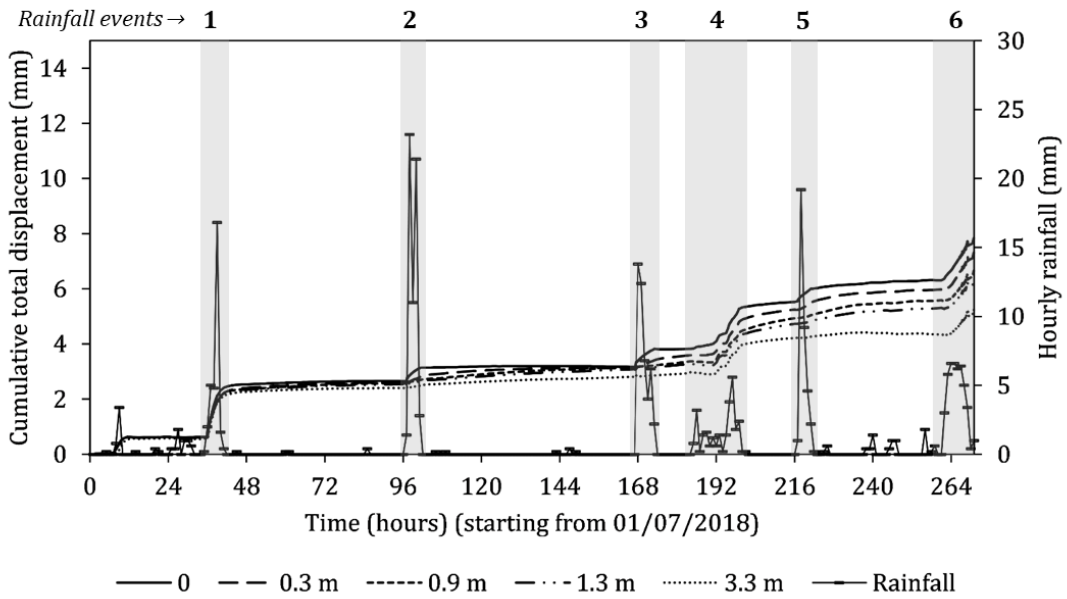


Figure 6.22 Cumulative total displacement measured near the mid-slope (section D-D\*) from 01/07/2018 00:00 to 12/07/2018 06:00.

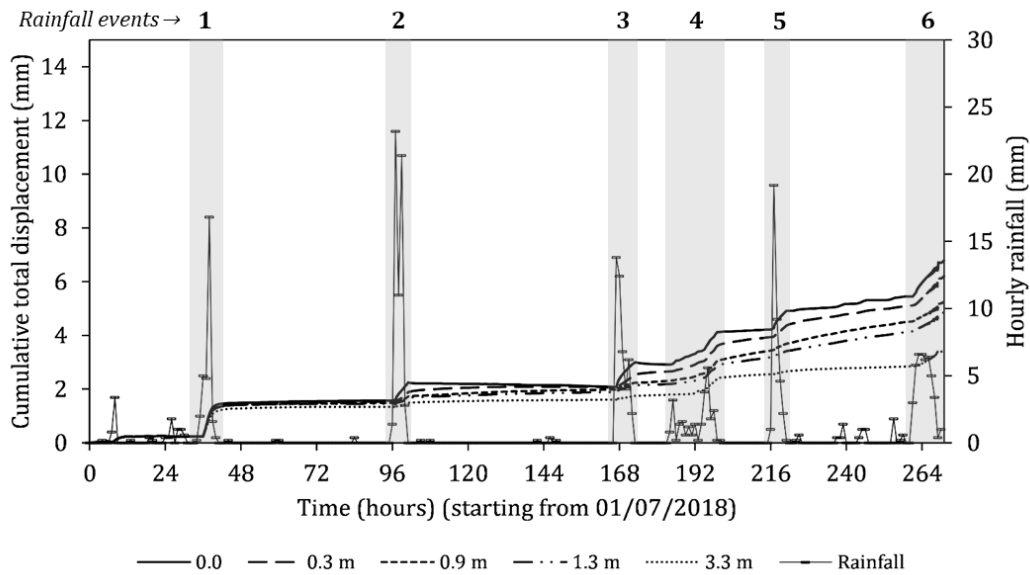


Figure 6.23 Cumulative total displacement measured near the slope crest (Section E-E\*) from 01/07/2018 00:00 to 12/07/2018 06:00.

#### 6.9.4 Part 4: Stability analysis without road cut

In the previous analysis- the back-analysis of Kanglang landslide (part 3), accelerated displacements were predicted near the road cut indicating that the slope failure may have been promoted due to the presence of the steeply cut roadside slope. To reinforce this observation, the coupled analysis presented in part 3 (back-analysis of Kanglang landslide) was repeated on the new geometry without the road cut (Figure 6.5) as discussed in section 6.7.4.

The first observation from this analysis was that the initial factor of safety was greater when there is no road cut (Figure 6.24). In other words, the slope which was modified by a road cut had a lower initial factor of safety, which ultimately increased the possibility of failure during rainfall. Furthermore, under the same rainfall condition, the temporal changes in factor of safety in the two models: with and without road cut were found to be notably different. While the slope without the road cut remained stable with a factor of safety close to 2.5 during the simulation, the factor of safety of the slope with road cut declined in response to every rainfall event before eventually dropping below 1 during rainfall event no. 6.

This finding suggests two main points- first, the presence of a road cut in the slope reduces the initial factor of safety which increases the likelihood of failure during rainfall. Second, the rainfall which triggered the Kanglang landslide and the rainfall events preceding this

were not sufficient to initiate slope failure in its natural undisturbed state. This gives an implicit indication that the modification of slope geometry for road construction can increase the susceptibility of the slope to fail, while the rainfall acts as an external triggering factor leading to the failure.

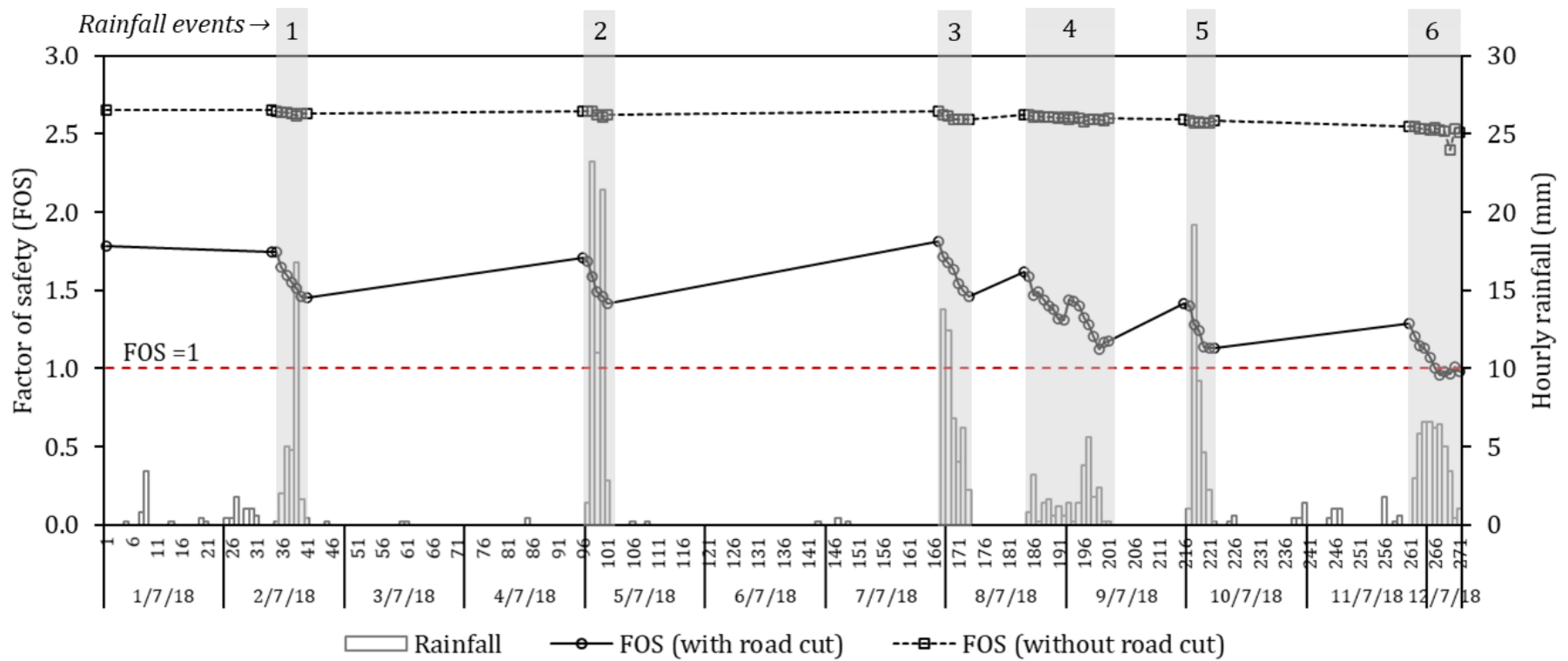


Figure 6.24 Variation of factor of safety with time in the models with a road cut and without a road cut from 01/07/18 00:00 to 12/07/18 06:00. The numbers in the figure denote rainfall events\* (\*only the continuous rainfall events with more than 5 mm total rainfall are highlighted).

## 6.10 Chapter summary

This chapter presented an integrated approach of combining the field-monitored hydrological data with fully coupled flow-deformation analysis to better understand the failure mechanism of the Kanglang landslide. Numerical simulations were conducted in four parts, findings from which are summarised below:

### **Part 1- Model calibration**

1. A fully coupled flow-deformation analysis was conducted in PLAXIS 2D to calibrate the numerical model to ensure that the model can replicate the volumetric water content changes in the field. For calibration, the volumetric water contents predicted by the model were compared to those measured in the field between 01/07/2019 and 11/07/2019.
2. A reasonable agreement was found between the volumetric water contents predicted by PLAXIS and those measured by the 10HS soil moisture sensors in the field. The model effectively captured the general trend and timing of the increase and decrease in volumetric water content during and after the rainfall. Considering the reliability of the model to predict this, the calibrated model was used for further analyses in this chapter.
3. It is worth noting again that hydraulic hysteresis was not taken into account in the numerical analysis. The predictability of the model could potentially be enhanced if the analysis could incorporate this soil behaviour. Nonetheless, the simplified approach of using a single wetting soil-water retention curve did produce a comparable prediction of the volumetric water content response.

### **Part 2 - Stability analysis before Kanglang landslide (Dec 2017 - Jun 2018)**

1. Before undertaking a detailed back-analysis of the failure mechanism of Kanglang landslide which occurred in July 2018, a fully coupled flow-deformation analysis combined with safety analysis was undertaken over a longer time frame to assess the stability of the slope before the occurrence of Kanglang landslide.
2. During the reconnaissance survey conducted in December 2017, the slope at Kanglang landslide was in a stable condition (chapter 3). Hence, this analysis was conducted for the duration between December 2017 and June 2018.
3. The results from this analysis showed that on a few days in June 2018, the factor of safety dropped slightly below 1. Nonetheless, it was noted that this analysis was conducted using daily rainfall totals due to unavailability of hourly rainfall data. Consequently, the intermittent dry hours that help in the recovery of soil suction (and hence, stability) could not be taken into account. Thus, the factor of safety



obtained from this analysis is on the conservative side and it would be reasonable to assume that the model was predicting that the slope had remained stable before the occurrence of Kanglang landslide.

### **Part 3 - Back-analysis of Kanglang landslide**

1. The back-analysis of Kanglang landslide was undertaken using the fully coupled flow-deformation analysis involving a more detailed analysis using hourly rainfall data followed by the safety analysis.
2. The variation of the factor of safety over the simulated period showed that the changes in the factor of safety were directly related to rainfall. A statistically significant correlation was found between the rainfall duration and the percentage decrease in the factor of safety, suggesting that a greater reduction of factor of safety can be expected during longer duration rainfall events.
3. The factor of safety in the back-analysis dropped below 1 on 12/07/18 indicating failure during a low-intensity, long-duration rainfall event. This is close to when this landslide was said to have occurred by the owner of this site.
4. The evaluation of suction predicted by PLAXIS showed that at the time of failure, the rainwater had infiltrated to 1.3 and 1.1 m at the road cut and at the upper hillslope (mid-slope) above the road cut, causing a reduction of soil suction at the time of failure. The advancement of wetting front was quicker at the road cut as the rainwater could infiltrate from two sides - the upper hill slope above the road cut and the lower face of the cut slope adjacent to the road. The advancing wetting front and the consequent reduction of soil suction could be the reason for greater displacements at shallow depths (<1.3 m) at the time of failure. The depth of infiltration predicted by the model is close to the sliding depth (~1.5 m) at the landslide crown which was noted during the reconnaissance survey (chapter 2).
5. With further infiltration after the failure, the wetting front advanced to 1.7 m and 1.6 m at the two selected sections causing a reduction but not a complete loss of suction. Nonetheless, accelerated displacements exceeding 200 mm were predicted at shallow depths (<1.3 m) at the cut slope adjacent to the road. This indicated that the presence of the road cut may have promoted the slope failure as the suction reduced gradually due to advancing wetting front, ultimately leading to the occurrence of the Kanglang landslide.
6. The rainfall data used in the analysis may not mirror the actual rainfall event that triggered Kanglang landslide since this was obtained from a station located ~12 km from the study site. Nonetheless, with this analysis, the plausible cause and the timing of Kanglang landslide was predicted. The prediction of the numerical model can further be improved with actual hourly rainfall data.

#### **Part 4 - Stability analysis of the slope without road cut**

1. A comparison of the factor of safety was made between two models - with and without road cut under the same rainfall condition. The two models that were compared had identical phases, mesh size, material properties, initial condition and boundary conditions.
2. The comparison showed that the presence of road cut decreased the initial factor of safety, which increased the possibility of failure during rainfall.
3. This comparison also showed that the slope remained stable in its natural state (FOS~2.5) during rainfall that triggered Kanglang landslide, which shows that the modification of geometry for constructing the road played an important role in the incidence of Kanglang landslide.

Hence, the modification of natural slope geometry without preventative or protection measures can cause slopes to fail during heavy and continuous rainfall. This highlights the need for careful consideration before cutting the hillslopes to construct roads. Further discussions about the findings are presented in chapter 7.

# Chapter 7

## Discussions and conclusions

---

### 7.1 Chapter outline

In this concluding chapter, the findings of this study are discussed within the framework of the research objectives that were set out at the beginning of this study. The conclusions drawn from the discussions are then presented, followed by the limitations of this study and recommendations for future research.

### 7.2 Discussions

Located in the central section of the Himalayan arc, the mountainous terrain of Nepal is active and evolving. In such a setting, landslides are inevitable natural processes that provide a mechanism to attain a mass balance between tectonic uplift and erosion (Petley et al., 2007). Additionally, landslides occur extensively across the country during the summer monsoon which brings heavy, concentrated rainfall. Although Nepal is a relatively small country with ~0.4% of the global population, 10% of all fatal rainfall triggered landslides between 2004 and 2016, in the category of the global fatal non-seismic landslides, was recorded in Nepal, 93% of which occurred during the summer monsoon (Froude and Petley, 2018). While the evolving mountainous terrain and the climatic conditions favour natural landsliding, growing evidence suggests that the expansion of local roads in Nepal has further increased the number of landslides and landslide fatalities during the monsoon (Petley et al., 2007; Dahal et al., 2010; Leibundgut et al., 2016; Mcadoo et al., 2018; Sudmeier-Rieux et al., 2018; Vuillez et al., 2018). Kincey et al. (2020) have also noted that the landslide activity that started after the 2015 Gorkha earthquake sequence may never completely return to the pre-earthquake levels due to on-going anthropogenic activities like road building.

The Government of Nepal plans to extend the road density to 1.3 km/km<sup>2</sup> by 2030 from 0.55 km/km<sup>2</sup> in 2015 under the sustainable development goals (SDG 9) (Government of Nepal: National Planning Commission, 2017). To fulfil this commitment, local roads continue to be built across the country despite the rising number of suggestions pointing towards the increased risk of landsliding due to non-engineered local road construction. This underlines

the urgency to understand the interaction between two controls on landsliding, rainfall and roads, in Nepal. This study attempts to address this need through an integrated approach. The integrated approach combines reconnaissance field surveys (objective 1), geotechnical investigation and laboratory testing (objective 2), field monitoring (objective 3) and numerical modelling (objective 4) to understand the effects of slope cutting for road construction on the occurrence of landslides during rainfall.

Although most of the road cut soil slopes that fail during the monsoon are initially unsaturated, far too little attention has been given to understanding the unsaturated behaviour of soils in Nepal. Globally, there has been extensive research focusing on rainfall-induced landsliding using the concepts of unsaturated soils. However, it comes as a surprise that there has been no detailed study that incorporates the behaviour of unsaturated soils to decode the process by which slope cutting for road building leads to a greater risk of rainfall-induced landsliding in Nepal. This can be attributed to the cost- and time-intensive processes including field and laboratory studies that are necessary to generate high-quality geotechnical and meteorological data for the low- and middle-income countries like Nepal. In this regard, this research, perhaps for the first time in Nepal, analysed the effect of road-rainfall interaction on landsliding using numerical modelling under the framework of unsaturated soil mechanics. For the numerical analysis, primary geotechnical data was produced through comprehensive laboratory and field investigation, providing fresh insights into the properties of both saturated and unsaturated soils in a geotechnical data-scarce context. Further, a long-term dataset of rainfall and volumetric water content was generated by installing field monitoring station at the study site, which aimed to understand the interaction of surficial soil with transient atmospheric processes and its implications on the stability/instability of the roadside slope.

In the following sub-sections, discussions are presented in the context of the research objectives that were defined at the beginning of this study (chapter 1). The discussion begins with the findings from the case study of a newly widened district road (Daklang-Listi), located in Sindhupalchok district of Nepal. The case study was aimed at identifying broader road-construction related issues that are conducive to landsliding. The focus of the discussion is then narrowed down to understanding the effects of slope cutting for road construction on landsliding by using a site-specific study of Kanglang landslide located along the Daklang-Listi road. The methods utilised to approach each objective are summarised and the research findings and their implications are also discussed in the following sub-sections.

### **7.2.1 Key issues related to local road construction in Nepal that can be conducive to landsliding during rainfall (Objective 1)**

To fulfil the first objective, three reconnaissance surveys were conducted between 2017 and 2018 along a newly widened 13.7 km long stretch of a district road (Daklang-Listi) located in Sindhupalchok district of Nepal. The reconnaissance surveys included the periods before and after the monsoon of 2018, which allowed visual assessment of the roadside slope condition during road widening, after road widening and after the monsoon. This approach constituting a series of reconnaissance surveys conducted over the life cycle of a local road is unique and crucial for a deeper understanding of the underlying problems associated with roadside slope stability.

The first reconnaissance survey was undertaken along the Daklang-Listi road in October 2017 when this road was being widened by cutting into the hillslopes using excavators. The observation from this survey presented first-hand insight into how local roads are built in Nepal using the equipment-based technique. Such a method of constructing roads has become popular in Nepal mainly because of the lower cost and time associated with this technique (World Bank, 2012; Robson et al., 2021). However, the roads built using the equipment-based method in Nepal are often non-engineered and lack adequate planning, design and equipment usage control, which consequently increases the risk of landsliding (World Bank, 2012; Hearn and Shakya, 2017). Slope failures along the road during road construction were not assessed individually during this survey as the focus was to observe the method of local road construction.

To evaluate the immediate or post-construction impacts of slope cutting for road construction on landsliding, the second reconnaissance survey was carried out in December 2017, before the summer monsoon period. The findings of this survey suggested that the immediate impacts on landsliding can be sporadic and perhaps, less serious as 16 landslides were recorded along this road, some of which existed before the Daklang-Listi road was widened. The critical issues related to local road construction that could potentially contribute to landsliding were identified during this survey. The first issue was the steepness of the road cut slopes along the Daklang-Listi road. At several locations along the road, the cut slope angles were found to be much greater than the recommended values given by DoR (2003) for cut slope gradient ( $\leq 51^\circ$  or 1:0.8 V:H). The stability of steeply cut roadside soil slopes during this period (dry season) showed that the unsaturated soil slopes can remain stable at angles greater than their typical friction angle ( $25^\circ$  to  $45^\circ$  (ICIMOD, 1991, p. 883)). While the additional strength of the unsaturated soil slopes imparted by soil suction allows unsaturated soil slopes to remain stable at steep cut angles, the dissipation

or loss of suction during rainfall is known to be the primary cause of the shallow slope failures (Fredlund and Rahardjo, 1993).

DoR (2003) recommends slope protection measures for cut slopes with steep gradients and greater cut heights. However, the lack of adequate and effective slope protection measures was another problematic issue identified along the Daklang-Listi road during the reconnaissance survey in December 2017. Although gabion walls are a preferred method for slope protection for local roads in Nepal, their effectiveness was found to be undermined by inadequate consideration of the cut slope geometry (height and gradient) and seepage conditions.

Since roads modify natural hydrological pathways, water management on roads is crucial to control and divert surface and intercepted subsurface flows to prevent slope failures (Megahan, 1983; DoR, 2003; Sidle and Ochiai, 2006; Fannin and Lorbach, 2007). However, another major problematic issue identified during the reconnaissance survey along the investigated road was the lack of surface and subsurface water management. The absence of drainage systems such as simple roadside drain ditches allowed surface water and intercepted subsurface water to flow along the roadway before eventually discharging downslope from the topographic lows. During heavy rainfall when the surface and subsurface discharge are high, the topographic low points could potentially become preferential sites for gully erosion and landslide initiation.

The loose excavated spoil side-cast downslope from the road without incorporating into the road prism can result in unstable deposits and pose threat to lives and properties especially during rainfall (Sidle and Ochiai, 2006). This was another key problematic factor that was noted during the reconnaissance survey. Not only did the side-cast spoil result in unstable deposits, but also led to the stripping of natural vegetation from the slopes, thereby eliminating their potential contributions to slope stability.

The second reconnaissance survey conducted in December 2017 allowed the identification of the five key issues related to road construction that are potentially conducive to landsliding. These include i) steepness of the road cut slopes, ii) inadequate and ineffective slope protection measures, iii) lack of surface/sub-surface drainage measures, iv) side-casting of loose excavated spoil below the road and v) removal of vegetation due to excavation and side-casting of spoil.

After identifying the key problematic issues, the third reconnaissance survey was carried out during the monsoon in August 2018 to evaluate their actual impacts on landsliding during rainfall. During this survey, 117 landslides (almost 9 landslides per kilometre) were

recorded along the Daklang-Listi road, which is about an order of magnitude increase compared to the slope failures in December 2017. This showed that the number of slope failures can increase dramatically along the non-engineered local roads during the monsoon. Studies have also reported similar or higher rates of landsliding along the mountain roads in China and India (Bansal and Mathur, 1976; Sidle et al., 2014).

Among the 117 landslides along the Daklang-Listi road in August 2018, the majority of the slope failures (93%) was found to have occurred on the cut slopes. This observation was not surprising because the road was widened solely by cutting into the hillslopes. The slope failures encountered along the road were further classified into six categories based on the typical landslide shear surface configurations defined by Hearn (2011) for mountain roads. The most common configuration was found to be *'failure in cut slope extending to hillslope'* which entailed road cut slope failure that extended to the hillslope above the road cut. It was interesting to note that 95% of the slope failures along this road occurred where the cut slope gradients were greater than 51°. Arguably, an indirect implication of this is that the steep cut slope gradients could be detrimental to slope stability. However, without studying all the roadside slopes angles including those that did not fail, the likelihood of landsliding based on the cut slope angles cannot be commented on. Nonetheless, this opens up a new angle for research that could be pursued in the future. The other configuration of slope failure - *'failure in original valley slope'* which included slope failures below the road caused most damage due to partial or complete loss of the carriageway although they were not as frequent as the cut slope failures. The debris-carrying surface runoff was found to be the main reason for such failures, and this demonstrates how the lack of suitable drainage measures to safely divert water away from the roadway is important to prevent such failures below the road. Similar observations were also reported by Leibundgut et al. (2016) where the authors attributed the lack of suitable drainage systems along the roads to be the cause for gully and roadside slope failures in Phewa watershed, Pokhara, Nepal.

Additionally, 9 cut slopes along Daklang-Listi road were found to have failed despite the presence of gabion wall or masonry wall for toe support, whereas 102 slopes that failed had no slope protection. This observation suggests that the slope protection measures are important to prevent failures during rainfall but may not be fully effective unless engineered carefully considering the site-specific conditions such as the cut slope geometry, slope materials and seepage condition.

Thus, the field observations from the third reconnaissance survey showed how the road-construction related issues identified earlier during the first and second reconnaissance surveys can promote landsliding during the monsoon. Referring back to the 'chain of events' (Petley, 2010), the modification of natural hillslope geometry, alteration of hydrological

pathways, removal of vegetation, side-casting of spoil and absence of slope protection measures are perhaps the important causal factors that may not cause immediate slope failures during the dry season, but prepare the suitable setting for the slopes to fail on the onset of the monsoonal rain which acts as the triggering factor.

The major impact of the extensive slope failures along the Daklang-Listi road was on the serviceability of the road. Due to landslide deposits and damaged carriageway, this road became unserviceable throughout the monsoon. This provides an example of the several (~42,805 km) local roads in Nepal that are not serviceable during the monsoon because of poor road conditions and frequent slope failures (Devkota et al., 2014). Additionally, the landslides along the Daklang-Listi road also caused major damage to agricultural lands. Such damage due to seasonal landsliding after road construction is one of the main reasons behind farmland abandonment in Nepal (Oven, 2009; Chaudhary et al., 2020). The risk of landsliding is aggravated further by the temporary or permanent abandonment of farmlands (Khanal and Watanabe, 2006; Chaudhary et al., 2020). Hence, the roadside slope failures during monsoon cause socio-economic damage to the local communities, which contradicts the primary purpose of local road construction which is to enhance the socio-economic status of the rural communities in Nepal.

To conduct a detailed investigation of the slope failures caused by the interaction between road and rainfall, the scope of this study was narrowed down to a site-specific scale. For this, a representative landslide along the Daklang-Listi road was selected. For the selection, the common failure type along this road was identified and then a set of criteria was developed for site-selection. The criteria for selection included representativeness, accessibility, network reception and landowner's permission for access. Additionally, it was important to select a site that had remained stable after widening of the Daklang-Listi road but failed during the subsequent monsoon so that further analyses would provide a better insight into how the rainfall and road cuts interact to cause slope failures. Considering these criteria, Kanglang landslide (27°53'32.0"N, 85°54'28.5"E) located at km 02+420 of the Daklang-Listi road was selected.

At the location of the Kanglang landslide, a steep (~70°) road cut slope was formed to widen the Daklang-Listi road in December 2017. In less than seven months, Kanglang landslide occurred during the monsoon in July 2018, affecting not only the road cut, but also the hillslope above the road. To evaluate the causes and mechanism of this landslide triggered by the road-rainfall interaction, site-specific field investigations, laboratory testing of soil samples and numerical modelling were conducted, which are discussed in the following sections.



### 7.2.2 Primary site-specific geotechnical data from field and laboratory testing generated for numerical modelling (Objective 2)

To fulfil the second objective, a site-specific geotechnical investigation was conducted at Kanglang landslide in March 2019. The investigation program constituted borehole drilling, standard penetration tests and trial pit excavation through which the subsoil condition and groundwater level were explored, and samples were collected for laboratory testing.

Two boreholes were drilled near the crown (BH-1) and the toe (BH-2) of the landslide where standard penetration tests (SPT or SPT (cone)) were conducted. A uniform deposit of medium dense soil with SPT values ( $(N_1)_{60}$ ) ranging from 11 to 19 (with a mean of 14) was encountered in BH-1 from 0 to 7 m depth. The samples extracted from the upper 2 m depth exhibited reddish-brown colour and sandy to silty soil texture. The soil samples extracted from 4 m and 5 m depths also exhibited similar colour and texture. Below 6 m, soil samples could not be extracted as the SPT sampler was replaced by a solid 60° cone to prevent damage to the sampler by coarser materials. Within BH-1 isolated boulder- and cobble-sized materials were encountered frequently which can be considered typical for colluvial deposits. Similarly, during the course of drilling in BH-2, the SPT sampler was replaced by the solid 60° cone as several boulder-, cobble- and gravel-sized materials were encountered during drilling. The upper 1 m consisted of gravelly soil, which included the earthen materials that had been deposited in-place to form the carriageway. At 1.9 m, 3.2 m and 4.2 m below the ground surface, the SPT values ( $(N_1)_{60}$ ) ranged from 13 to 34 (with a mean of 21). In both BH-1 and BH-2, the groundwater table was not encountered during drilling.

Based on the empirical correlation between SPT value ( $(N_1)_{60}$ ) and angle of shearing resistance given by Hatanaka and Uchida (1996), the angle of shearing resistance of soil in BH-1 and BH-2 was estimated to be between 35° to 40° and 36 to 46° respectively. The correlation given by Hatanaka and Uchida (1996) was selected because this relationship takes into account the effect of overburden pressure on the SPT N-values. The elastic modulus of soil in BH-1 and BH-2 was estimated to be between 6 to 8 MPa and 6 to 13 MPa respectively, based on the correlation given by Bowles (1996).

A trial pit (1.5 m × 1 m) was excavated manually to 1.5 m depth at ~10 m distance from the crown of Kanglang landslide. The samples collected from the trial pit were predominantly fine and exhibited slight dilatancy, grittiness and lustre indicating the presence of silty and sandy particles. The upper 0.25 m of soil was relatively loose and appeared greyish brown in colour perhaps due to the presence of organic matter and weathering. Below this layer, a

slightly darker reddish-brown sandy-silty soil was encountered. The soil below 0.5 m depth from the surface was slightly wet and hence, appeared darker than the layers above. The apparent difference in soil moisture within the trial pit suggested that the effect of atmospheric drying was less pronounced below 0.5 m depth.

Soil samples collected from the borehole (BH-1) and the trial pit were brought to Durham University laboratory for testing. Soil samples were not extracted from BH-2 as the split-spoon sampler for SPT was replaced by the solid cone during the test. The samples brought to the laboratory included disturbed bag samples and core samples. The core samples were obtained from the bottom of the trial pit using open-ended steel sampling tubes ( $\phi$  37-38 mm), which were sealed at the site with paraffin wax and wrapped in plastic film to prevent any loss of moisture.

Laboratory tests were performed on the samples collected from the field to determine the geotechnical soil parameters for input into the numerical model (objective 4). The laboratory testing program included a series of index and classification tests, saturated triaxial tests, soil-water retention curve measurements and saturated permeability tests. The particle size distribution tests showed that the samples contained less than 12% clay-sized particles, while silt- and sand-sized particles dominated the distribution. Based on the particle size distribution, the samples obtained from the trial pit and the borehole (BH-1) to a depth of 5.45 m were classified as silt or sandy silt. Within BH-1, below 5.45 m, the samples contained a relatively higher sand fraction and were classified as very silty sand based on their particle size distribution.

In the Atterberg limit tests, the finer fraction ( $<0.425$  mm) of the samples exhibited intermediate plasticity with plasticity index from 14 to 17% and liquid limit from 37 to 40%. The lower plasticity and smaller clay content in the samples suggest a lower potential for swelling and shrinking due to change in the water contents. Furthermore, the particle density of the samples was found to range from 2.72 to 2.78 Mg/m<sup>3</sup>. The XRF analyser showed that soil samples contained a higher iron content which contributed to their reddish-brown to brown colour and a relatively high particle density.

The in-situ soil properties were determined in the laboratory from the sealed core samples. The samples obtained from shallow depth (0.5 m) was found to be relatively loose with a higher void ratio ( $\sim 1.04$ ), which decreased with the increasing depth from the surface. As expected, the degree of saturation of the soil was found to be lower ( $\sim 47\%$ ) near the surface (0.5 m) which increased with increasing depth from the ground. This confirms the observation from the trial pit that the soil below 0.5 m appeared wetter than the layers above.

To understand the mechanical behaviour of the soil, saturated triaxial tests were performed on three samples obtained from 0.5 to 0.75 m depth. The samples were consolidated to effective confining pressures of 25 kPa, 75 kPa and 100 kPa and then sheared under an undrained condition with continuous measurement of pore water pressure (CU test). Towards the end of the triaxial tests, the changes in the pore water pressures became negligible indicating that the critical state was being approached. In the  $p'-q$  space, the stress path of the sample consolidated at lower effective confining pressure (25 kPa) climbed almost vertically towards the critical state line, while those consolidated at greater confining pressure (75 kPa and 100 kPa) exhibited a greater tendency for contraction leading to an increase in positive pore water pressures. For the sample consolidated at 100 kPa, a change in the direction of stress path after reaching the critical state line was observed, which indicated a tendency for dilation of the sample with a further increase of the shear strain after the critical state. Within the  $p'-q$  space, the critical state line with a stress ratio ( $M$ ) of 1.47 was obtained, which corresponds to a critical state angle of shearing resistance of  $36^\circ$ . This is comparable to the angle of shearing resistance corresponding to the SPT values  $((N_1)_{60})$  recorded in BH-1 ( $35^\circ$  to  $40^\circ$ ) as per the correlation given by Hatanaka and Uchida (1996).

To evaluate the hydraulic behaviour of the soils, the saturated coefficient of permeability and the soil-water retention curves were obtained in the laboratory. The saturated coefficient of permeability was measured using the standard triaxial constant head permeability test. The coefficient of permeability was measured at effective confining pressures of 100 kPa, 200 kPa and 300 kPa under a constant pressure head of 20 kPa. Although the sample used for this test was obtained from a shallow depth (0.5 to 0.75 m), the tests were performed on higher confining pressures due to difficulty in maintaining a constant pressure head of 20 kPa at lower confining pressures. At the three confining pressure levels, the saturated coefficient of permeability ranged between  $1.17 \times 10^{-7}$  m/s and  $1.43 \times 10^{-8}$  m/s, which is within the typical range of saturated permeability for silts and silty sands (Lu and Likos, 2004). It was also observed that the coefficient of permeability decreased non-linearly with the increase in effective confining pressure or decrease in void ratio.

The soil-water retention curves describing the relationship between matric suction and water content (gravimetric and volumetric) were obtained using the discrete(staged) wetting and drying method where the soil suction was measured using the high-capacity tensiometer developed at Durham University (Toll et al., 2013). Four samples were prepared from the soils obtained from 0.3 to 0.5 m (K3) and 0.75 to 1 m (K4) depths. As the samples undergo a change in total volume due to drying and wetting during the test, the

changes in void ratio during the tests were evaluated against the gravimetric water content changes. It was observed that the void ratio decreased significantly during drying in both samples obtained from 0.3 to 0.5 m and 0.75 to 1 m depths. The decrease was found to be more prominent during the initial stages when the gravimetric water content was more than 20% after which the reduction in void ratio became less pronounced. A greater reduction in the void ratio was found in the sample with a greater void ratio obtained from the shallow depth (0.3 to 0.5 m) when compared to that obtained from a greater depth (0.75 to 1 m). In contrast, less significant changes in the void ratio were observed when the samples were wetted. This observation is similar to a previous study undertaken by Md. Rahim (2016) who reported similar behaviour of soil during the wetting process, which the author associated with a stiffer elastic response of the soil.

It is common to express the soil-water retention curve in terms of volumetric measurements instead of gravimetric water content in situations where the soils undergo volume changes (Fredlund and Rahardjo, 1993). Hence, the soil-water retention curves were plotted in terms of volumetric water content and matric suction. Although there are several empirical models developed for the soil water retention curve, the van Genuchten model (van Genuchten, 1980) is commonly used in practice. The experimental data was fitted to this model and the curve fitting parameters ( $\alpha$ ,  $n$  and  $m$ ) were determined. The fitted curves clearly exhibited the hysteretic soil behaviour of soil during drying and wetting and as would be expected, the wetting-scanning curve obtained by wetting the sample immediately after the end of the drying stage reached the primary wetting curve. Furthermore, the air-entry value of the soil during drying was found to be affected by the depth from which the samples were obtained. The K3 soil samples representing soil near the ground surface (0.3 to 0.5 m) had a smaller air-entry value (83 kPa) compared to the K4 samples that were obtained from (0.75 to 1 m) where the air-entry value was 158 kPa. This can be related to the void ratio of the soil samples. As the initial void ratio of the sample from 0.3 to 0.5 m was higher than that of the sample from 0.75 to 1 m, smaller suction would be needed to desaturate the larger pores present.

Collectively from the field and laboratory testing, the shallow subsoil profile and geotechnical properties of the soil (physical, mechanical and hydraulic properties) were determined. These parameters were used as input into the numerical modelling to fulfil the fourth objective of this study.

### 7.2.3 Effects of atmospheric wetting and drying processes on the hydrologic response of surficial soils and their implications on slope stability (Objective 3)

A field monitoring station was installed near the crown of Kanglang landslide in March 2019 and was equipped with a rain gauge, three 10HS soil moisture sensors and a data logger. The purpose of installing the field-monitoring station was to evaluate the rainfall distribution in the study area, to assess the temporal changes in volumetric water content at different depths in response to infiltration and drying and to assess the effects of seasonality and rainfall characteristics on the volumetric water content response. Additionally, the field-monitored volumetric water content and rainfall were used to calibrate the numerical model to fulfil the final objective of this study.

The rainfall measured during the monitoring period reflected a clear monsoon-dominated rainfall pattern that is prevalent in Nepal; a total of 2690 mm rainfall was recorded, ~81% of which occurred during the monsoon (June – September). During the monsoon, rainfall occurred almost every day with a maximum of 90 mm total daily rainfall and only 6 individual dry days. Compared to the 64-year average rainfall from 1955 to 2018 (3599 mm) recorded at the nearest rainfall station in Gumthang, the rainfall recorded during the monitoring period was found to be ~25% less, indicating that the monitoring period was relatively dry. When a comparison was made between the monthly rainfall totals measured at the two locations, it was observed that the monthly totals were generally greater at the field-monitoring station in 2019 (March – October). This discrepancy can be expected because of the distance between the two stations (~6 km), the elevation difference (~390 m), the topography and localised rainfall events. Furthermore, from the rainfall data obtained from the monitoring station, 182 individual rainfall events that accumulated more than 2 mm rainfall in one hour or more were identified. The distribution of these rainfall events showed that the occurrence of relatively extreme events such as those with high rainfall totals (>40 mm), longer duration (>10 hours), high average hourly rainfall intensity (>12 mm/hr) and high peak hourly intensity (>25 mm/hr) was less frequent during the monitoring period.

The average daily volumetric water content of soils measured over the year-long monitoring period showed that the fluctuations in volumetric water content were directly associated with the rainfall, atmospheric drying, seasons and depth from the ground surface. The sensor located closest to the ground (0.3 m) recorded a quick response to both drying and infiltration throughout the monitoring period, which can be associated with the presence of surficial cracks that dominate the hydraulic conductivity of soil at the surface (Dixon et al., 2019; Toll et al., 2019). During the pre-and post-monsoon periods, the

volumetric water content response at 0.8 m was found to be less pronounced than that at 0.3 m and that at 1.2 m was found to be relatively stable and consistently higher than the upper layers. This observation is similar to that reported by Tu et al. (2009) where the active zone of infiltration and evaporation was reported to be within 0.7 m from the ground surface when the rainfall intensity was less than 40 mm/day. In contrast, during the monsoon, continuous changes in volumetric water content were recorded at all three measured depths.

The average daily volumetric water contents were then used to evaluate the effects of prolonged drying and wetting periods. It was observed that during the 65-day long drying period between 09/10/2019 to 12/12/2019, the degree of saturation of soil decreased by ~27%, ~14% and ~4% at 0.3 m, 0.8 m and 1.2 m respectively. The smaller percentage decrease in volumetric water content at 0.8 m and 1.2 m showed that the effect of atmospheric drying becomes less pronounced with increasing depth from the ground surface. This explains why the volumetric water content response at 1.2 m was found to be consistently high during the pre-and post-monsoon periods. This also explains the observation of wetter soil below 0.5 m encountered within the trial pit during field investigation (chapter 3). On the other hand, during a 40-day long continuous rainfall period between 21/06/2019 to 30/07/2019, the degree of saturation at 0.3 m, 0.8 m and 1.2 m increased by ~21%, ~27% and ~10% respectively. This suggests that the wetting of soil is much quicker and perhaps easier than drying of the soil, similar to the observations reported by Hawke and McConchie (2011) and Md. Rahim and Toll (2014). Moreover, since the volumetric water content (and degree of saturation) of soil at 1.2 m was already greater than the upper layers during the pre-and post-monsoon periods, with a relatively smaller (~10%) increase during the monsoon, the degree of saturation of soil at 1.2 m reached ~90% (VWC = 0.36 m<sup>3</sup>/m<sup>3</sup>). The changes in volumetric water content observed at 1.2 m during the monsoon suggested that the rainwater may have percolated below this depth. Since the porosity of soil at 1.5 m was estimated to be 0.364, if the infiltration pattern observed down to 1.2 m continued down to 1.5 m, the soil at this depth could be fully saturated.

These observations imply that during prolonged dry periods (pre-and post-monsoon), the soil at 1.2 m depth or below is not subject to the same degree of drying and the soil remains wetter than the upper layers. However, rainwater can easily infiltrate to this depth during a prolonged wet period, the monsoon, as was observed in the field. This mechanism can quickly lead to the saturation of soils at shallow depths ( $\leq 1.2$  m). Such a progressive wetting of soil could lead to dissipation or loss of matric suction, reduction of shear strength and eventually cause shallow slope failures. This implicitly supports the suggestion by Dahal et

al. (2009) that continuous rainfall lasting for 1 to 2 days can be considered responsible for shallow slope failures in the Lesser Himalayan region in Nepal. It is worth noting that the monitoring period was considered to be relatively dry as compared to the 64-year average rainfall in this area and as would be expected, the landslide-triggering rainfall threshold for Nepal suggested by Dahal and Hasegawa (2008) was not exceeded during the monitoring period. Yet, the monitored data showed that the non-extreme rainfall during this period was capable of nearly saturating the soil at ~1.5 m depth. This suggests that the rainfall thresholds for shallow landsliding could be lower than that for deep-seated failures, as noted by Toll (2001). This also highlights that the occurrence of landslides in a larger area is less likely to be predicted successfully by the regional rainfall total- or intensity-based landslide thresholds.

To understand the infiltration mechanism in the field, the hourly changes in volumetric water content in response to rainfall during mid-monsoon (30/07/2019 and 07/08/2019) were presented in this study. Predictably, the sensor at 0.3 m responded first during a rainfall event followed by the sensors located at 0.8 m and 1.2 m. A lag in volumetric water content response during/after a rainfall event was noted visually from the hourly time-series for the sensors located at 0.3 m, 0.8 m and 1.2 m and this was found to be influenced by the rainfall intensity and duration. To evaluate the response time-lags throughout the monsoon, a cross-correlation analysis was undertaken. This analysis showed that the sensor located at 0.3 m responded first within 2 to 5 hours of the rainfall and those located at 0.8 m and 1.2 m responded after 7 to 10 hours and 11 to 15 hours respectively. This was found to be in good agreement with the visually noted time-lags from the hourly time-series of volumetric water content response. Smith et al. (2013) also noted similar field observation where the time-lag in response to rainfall and drying was found to be proportional to the depth of the sensor. Hence, it can be said that the volumetric water content sensors installed at increasing depths from the ground surface can effectively capture the advancement of the wetting front during rainfall. The local site-conditions that the empirical infiltration models cannot take into account are intrinsically incorporated by continuous monitoring of the volumetric water content in the field.

The hourly changes in volumetric water content during the monsoon suggested that the magnitude of change was influenced by the rainfall features. Among the other rainfall features - peak hourly rainfall intensity, minimum hourly rainfall intensity, average intensity and rainfall duration, the highest statistically significant positive correlation ( $r = 0.72$  to  $0.78$ ,  $p < 0.0001$ ) was found between the total rainfall amount and the percentage change in volumetric water content at all measured depths. This indicated that the total rainfall amount during a rainfall event had a greater influence on the magnitude of

volumetric water content increase. To estimate the dependency of volumetric water content change on the rainfall totals, simple regression functions were fitted to the monitored data points and fairly significant positive correlations ( $R^2 = 0.52$  to  $0.64$  with  $p < 0.0001$ ) were obtained. These relationships could be used to predict the percentage change in volumetric water content that can be expected during a particular rainfall event. However, the empirically obtained relationships do not take into account the effects of individual rainfall patterns, soil properties and topographic variations, which could make transferring this model to a different location difficult. This could potentially be addressed in a more complex model, but this is beyond the scope of this study.

The changes in volumetric water content recorded during the monitoring period were also evaluated to understand the influence of rainfall intensity and duration. The evaluation showed that the duration of rainfall played a critical role in determining the magnitude of change in volumetric water content and also the depth of infiltration; longer duration rainfall events were found to trigger greater increments in volumetric water content, irrespective of the average rainfall intensity. A maximum increase in volumetric water content was recorded during high-intensity, long-duration rainfall events. It was also observed from the evaluation that the sustainment of the high rainfall intensity is an important factor determining the change in volumetric water content. The high-intensity rainfall events with the same average rainfall intensity and duration were found to have different effects - the rainfall event with a sustained high intensity was found to cause a relatively significant increase in volumetric water content at the measured depths. This shows that the rainfall duration and the high rainfall intensity sustainment are the important determinants of the volumetric water content response in soil.

Besides the rainfall features, it was recognised in this study that the volumetric water content response of soil is season dependent. During the monsoon, the maximum volumetric water content increments due to a rainfall event were  $\sim 9\%$ ,  $\sim 8\%$  and  $\sim 4\%$  at 0.3 m, 0.8 m and 1.2 m respectively. In contrast, during the post-monsoon season, an intermittent rainfall event following a prolonged dry period led to  $\sim 17\%$ ,  $\sim 3\%$  and negligible increase in volumetric water contents at 0.3 m, 0.8 m and 1.2 m respectively. It was also observed that the response time of the sensors was much slower during the pre- and post-monsoon periods than during the monsoon. The higher increase in the volumetric water content at 0.3 m during the pre- and post-monsoon season as compared to the monsoon shows that the volumetric water content response during rainfall can be influenced by the number of dry days that precede the rainfall event, which supports the suggestion by Tsaparas et al. (2003) and Rahardjo et al. (2005). Moreover, these observations suggest that the intermittent rainfall events during the pre-and post-monsoon



periods cannot effectively infiltrate to greater depths. Hawke and McConchie (2011) have argued that because of the higher porosity of soil near the surface, the voids capture most of the available water impeding flow to the lower layers. Toll (2006) noted that infiltration creates a zone near the ground surface with a high degree of saturation and permeability. As the degree of saturation and permeability in the lower layers are comparatively low, the infiltrated water is encouraged to flow down the slope within the near-surface zone with higher permeability, rather than flowing to greater depths. Collectively, these studies suggest that during the intermittent rainfall events in the pre-and post-monsoon periods, the drier and more porous layer closest to the ground captures the rainfall and creates a zone with a high degree of saturation (and hence high permeability) within which water flows instead of percolating to greater depths. This may have resulted in little to no increase in volumetric water content at 0.8 m and 1.2 m during the rainfall events during pre-and post-monsoon periods. Based on this observation, it can be said that the possibility of shallow landsliding due to rainfall during pre-and post-monsoon is less as the rainwater cannot infiltrate to greater depths. This provides an explanation for why only a few roadside slope failures were encountered along the Daklang-Listi road when the reconnaissance survey was undertaken during the post-monsoon season (December 2017).

#### **7.2.4 The influence of the road cut, rainfall, and their interaction on landsliding (Objective 4)**

The physical mechanism of landsliding caused by the interaction between roads and rainfall is still not well-understood in Nepal even though several studies have recognised slope cutting for road construction as an important causal factor for increased risk of rainfall-induced landsliding. To address this issue, numerical modelling was undertaken to simulate the mechanism of Kanglang landslide that occurred in July 2018 as a result of this interaction and this is the final objective of this study.

For numerical modelling, a fully coupled flow-deformation analysis was undertaken using the finite element software PLAXIS 2D. One of the limitations within PLAXIS is that this program cannot take into account hydraulic hysteresis during drying and wetting. In this study, the wetting soil-water retention curve obtained from the laboratory was used to model the unsaturated soil behaviour during rainfall. Additionally, in PLAXIS the mechanical behaviour of unsaturated soil is modelled using Bishop's effective stress concept (Bishop and Blight, 1963) where the suction coefficient ( $\chi$ ) is considered to be equal to the effective degree of saturation. While it may be argued that Bishop's effective stress concept is a simplification for defining the stress state of unsaturated soils, it has been demonstrated that in soils where the degree of saturation is high ( $\geq 75\%$ ), as would be the

case for rainfall-induced landslides, the Bishop stress concept is still valid and can provide a realistic prediction of the unsaturated soil behaviour (Toll et al., 2019; Toll, 2020).

Within PLAXIS, a simplified two-dimensional finite element model was constructed based on the SPT value ( $(N_1)_{60}$ ) and the trial pit observations (chapter 3). The input parameters for the model were obtained from the laboratory tests (chapter 4). The numerical analyses were conducted in four parts which are described below.

In part 1, calibration of the numerical model was conducted by performing a fully coupled flow-deformation analysis under transient hourly rainfall recorded at the field monitoring station in July 2019 (01/07/2019 - 11/07/2019). The results showed that the model captured the trend and timing of the volumetric water content changes at all three measured depths (0.3 m, 0.8 m and 1.2 m). At 1.2 m, the model prediction matched very closely with the field measurements. However, at 0.3 m and 0.8 m, the model slightly over-estimated the volumetric water content during rainfall compared to the field monitored values. This discrepancy could be due to the inability to incorporate hysteretic behaviour, the use of wetting soil-water retention curve to convert suction to volumetric water content and other local site conditions. Nonetheless, considering the reliability of the model to predict the overall trend and timing of the increase and decrease of volumetric water contents during and after rainfall at all three depths, the calibrated model was adopted for the back-analysis of Kanglang landslide.

Before the back-analysis of Kanglang landslide that occurred in July 2018, in the second part of the numerical analyses, an assessment of slope stability before July 2018 was conducted to evaluate if the slope was stable before this landsliding event took place. The stability of the slope from December 2017 to June 2018 was evaluated by performing a fully coupled flow-deformation analysis followed by safety analysis using the calibrated numerical model (part 1). The field evidence showed that the slope at Kanglang landslide was stable in December 2017 after being cut for the road widening. Hence, the period before December 2017 was not considered in the analysis. Due to the unavailability of hourly rainfall data, this analysis was performed using daily rainfall data estimated by taking a weighted average of rainfall from the four nearby rainfall stations based on their distance from the site.

The results showed that the factor of safety remained consistently high during the dry periods when the daily rainfall was  $\leq 12$  mm/day. This was expected as during the dry periods, the effective degree of saturation and unsaturated soil permeability are naturally low, resulting in a higher suction and lower infiltration. However, during consecutive wet days, on the onset of the monsoon, the factor of safety dropped continuously. The drop in the factor of safety was found to be linked to the gradual increase in the effective degree of

saturation and relative permeability due to rainfall. Because of the prolonged consecutive wet days, the factor of safety dropped to 1 on a few days in June 2018. Although this indicates slope failure, it should be noted that this analysis was conducted using daily rainfall totals which does not consider the intermittent dry hours between two rainfall events. Hence, the factor of safety computed from this analysis presents a rather conservative estimate of the factor of safety. With this limitation in the analysis, it can be assumed that the slope was in a stable condition between December 2017 and June 2018.

In the third and the most important part of the numerical analyses, the calibrated numerical model (part 1) was used to back-analyse the failure mechanism of Kanglang landslide. As the field monitoring station was not in place when Kanglang landslide occurred in July 2018, hourly rainfall recorded at the nearby rainfall station in Bahrabise (27°47'19.25"N, 85°53'59.95"E, 884 m a.s.l.) in July 2018 was applied as a flux on the surface boundaries of the calibrated model and a fully coupled flow-deformation analysis combined with safety analysis was performed. Although it is desirable to use the rainfall data from the nearest station, due to the unavailability of hourly rainfall records, this analysis was conducted using the data from Bahrabise meteorological station that is located ~12 km from the site.

The back-analysis showed that the factor of safety dropped below 1 on 12/07/2018 after 5 hours of continuous rainfall indicating that Kanglang landslide may have occurred during this time. The predicted time frame agrees with the statement from the landowner that the landslide had occurred before 16/07/2018. This shows that the coupled analysis in PLAXIS combined with safety analysis can reliably predict the failure times as was suggested by the previous studies by Oh and Lu (2015), Md. Rahim (2016) and Yang et al. (2017, 2019, 2020).

The variation of factor of safety during the analysis from 01/07/2018 illustrated the decrease in the factor of safety during rainfall and also the gradual increase during the dry hours between the rainfall events. An interesting point to note from the back-analysis results was that the decrease in the factor of safety during high-intensity, short-duration rainfall events was smaller compared to that during low-intensity, longer-duration rainfall events. The rainfall event which triggered the Kanglang landslide was also a relatively low-intensity (4.4 mm/hr) rainfall that lasted for 10 hours. This trend can be explained in terms of the  $I_r/k_{sat}$  ratio (rainfall intensity/saturated permeability) as discussed by Tsaparas et al. (2002). According to Tsaparas et al. (2002), when the  $I_r/k_{sat}$  ratio is low, as would be true for low-intensity, long-duration rainfall events, more rainwater can infiltrate into the ground resulting in a greater reduction in the factor of safety. This prediction from PLAXIS also agrees with the behaviour observed in the field where a greater increase in volumetric water content was found in response to longer duration rainfall events. In addition, the evaluation of average hourly volumetric water content changes in the field had also shown

that the duration of rainfall played a critical role in determining the magnitude of increase in volumetric water content. Based on these understandings, the relationship between the rainfall duration and the percentage decrease in the factor of safety was assessed. A statistically significant relationship ( $R^2=0.9661$ ,  $p<0.001$ ) was obtained between these two factors suggesting that a greater reduction in the factor of safety can be expected during longer duration rainfall events. These observations are in line with the study by Rahardjo et al. (2007) in which it was shown that the slopes with low saturated permeability ( $\leq 10^{-6}$  m/s) are less affected by short-duration rainfall events, regardless of the rainfall intensity.

To understand the mechanism of the Kanglang landslide, the changes in soil suction and total displacements during the time of failure were evaluated. When the factor of safety first dropped below 1, the infiltrating water had advanced down to 1.3 m and 1.1 m depths at the face of the cut slope and the upper hillslope (mid-slope) above the road cut respectively, as indicated by the reduction in soil suction. At the time of the slope failure, the total slope displacement was also found to be greater at shallow depths ( $<1.3$  m), which may be because the wetting front had not advanced beyond this depth to cause a reduction of soil suction. The depth of infiltration, as well as the depth where maximum total displacement was predicted by PLAXIS, were found to be close to the sliding depth ( $\sim 1.5$  m) at the crown of Kanglang landslide which was observed in the field in August 2018. With further infiltration after the failure, the wetting front advanced to 1.7 m and 1.6 m depths near the road cut and the upper hillslope section respectively. However, this did not cause complete loss of the soil suction. Yet, accelerated displacements exceeding 200 mm was predicted at shallow depths ( $<1.3$  m) near the road cut slope and increased displacements were predicted at the mid-and crest- of the hillslope above the road cut. These observations together suggest that the occurrence of Kanglang landslide may have been promoted by the presence of the steep ( $\sim 71^\circ$ ) road cut in the hillslope. This analysis result agrees with the study undertaken by Holcombe et al. (2016), where the authors found that the slope cuttings on the hillslope shift the failure surface towards the face of the cut, ultimately lowering the factor of safety and causing instabilities.

To further reinforce the above observation that the presence of the road cut may have played a role in promoting the landslide, the back-analysis of the Kanglang landslide was repeated on a new finite element model without the road cut. This model represented an idealised undisturbed hillslope at this location which had not been modified by road construction. In this fourth and final part of the analysis, a fully coupled flow-deformation analysis followed by safety analysis was conducted under July 2018 rainfall that triggered the Kanglang landslide. This analysis showed that the presence of a road cut decreased the initial factor of safety of the slope, which ultimately increased the possibility of failure

during rainfall. Additionally, the safety factor of this model (without road cut), fluctuated at 2.5 even during the rainfall event which was predicted to have triggered the Kanglang landslide. This suggests that the rainfall events that caused a significant reduction of the factor of safety during rainfall events before, during and after Kanglang landslide, were not sufficient to initiate slope failure in the natural, undisturbed state of the hillslope. Hence, it can be said that the modification of natural hillslope geometry for road construction increases the susceptibility to landsliding, while the rainfall acts as the triggering factor.

## 7.3 Conclusions

The key conclusions drawn from this study are summarised below:

### **1. Road construction-related factors that are conducive to landsliding**

The field evidence gathered from the reconnaissance surveys along the Daklang-Listi road showed that the key road-related factors that are conducive to landsliding include i) steepness of the road cut slope, ii) inadequate surface/sub-surface drainage measures, iii) ineffective and inadequate slope protection measures, iv) side-casting of excavated spoil below the road and v) removal of vegetation due to excavation and side-casting of spoil.

### **2. Impacts of non-engineered road construction on landsliding**

This study showed that the non-engineered construction of a local road can cause about an order of magnitude increase in the number of landsliding during the monsoon. The occurrence of extensive slope failures along mountain roads during the monsoon has adverse impacts on the environment as well as on the socio-economic development, which negates the Government's goal of constructing sustainable local roads for development.

### **3. Factors influencing the volumetric water content response of unsaturated soils**

The study site (Kanglang landslide) was monitored for a year and the changes in volumetric water content and rainfall were measured. The monitored data showed how the volumetric water contents at shallow depths can be influenced by depth from the ground surface, atmospheric processes (drying and wetting), rainfall features (total rainfall, rainfall intensity and rainfall duration) and seasonal changes. The installation of soil moisture sensors was demonstrated to be an effective way of visualising and understanding the infiltration mechanism by implicitly taking into account the local site conditions, thereby eliminating the need for making certain

assumptions as in empirical infiltration models. The monitored data further showed that the progressive wetting during consecutive wet days such as the monsoon can saturate the soil at shallow depths (~1.5 m), which can cause a reduction of soil suction and ultimately lead to shallow slope failures.

#### **4. Prediction of volumetric water content response using PLAXIS 2D**

The in-situ changes in volumetric water content during both drying and wetting can be predicted reliably using the fully coupled flow-deformation analysis in PLAXIS by incorporating only the wetting soil-water retention curve. Nonetheless, the accuracy of prediction could be enhanced further if hydraulic hysteresis was taken into account.

#### **5. The role of the road cut on landsliding during rainfall**

The numerical modelling approach combining the fully coupled flow-deformation analysis and safety analysis was used to predict the timing and mechanism of Kanglang landslide. The evaluation of the factor of safety showed that the landslide may have been triggered by a low-intensity (4.4 mm/hr), long-duration (10 hours) rainfall event on 12/07/2018. The analysis results showed that the rainfall event did not cause a complete loss of suction but predicted accelerated displacements at the road cut slope. This suggested that the steeply cut roadside slope may have promoted the slope failure during rainfall. This observation was validated by the stability analysis of this slope without the road cut. The slope in its natural state (without road cut) was found to be stable even during the rainfall event that triggered the Kanglang landslide. This analysis also showed that the presence of the road cut reduces the initial factor of safety of the slopes, ultimately increasing the possibility of failure during rainfall. Together, the numerical analyses demonstrated that slope cutting for road construction increases the risk of landsliding during rainfall. This underlines the need for careful consideration before constructing local roads to prevent and mitigate landslides during rainfall.

#### **6. Effect of rainfall duration on slope stability**

The field-monitored data showed that the rainfall duration was a critical factor determining the amount and extent of volumetric water content changes in the soil. The variation of the factor of safety obtained from the back-analysis of the Kanglang landslide also showed that a greater reduction in the factor of safety occurred during longer duration rainfall events. Based on these findings, an empirical relationship

between the rainfall duration and the percentage change in the factor of safety was proposed.

## 7.4 Limitations of the study

1. Soil-specific calibration of the soil moisture sensors was not conducted. However, the measured volumetric water contents were comparable to those measured in the laboratory, giving confidence in the results obtained.
2. A simplified two-dimensional model was adopted for numerical analysis that may not fully represent the site-conditions. However, 3D analyses can show a more conservative result than 2D analyses. Since the 2D model seems to predict the time of failure well, it seems the model was appropriate for this landslide.
3. Due to limited data availability, for all fully coupled analyses (except model calibration), simulations were undertaken using rainfall recorded at the nearby rainfall stations that are located  $\geq 6$  km from the study site.
4. In the numerical analysis, ponding at the surface was not taken into consideration. Ponding could not happen on the sloping ground but could occur on flat surfaces.
5. The soil suction predicted by PLAXIS was converted to volumetric water content using a single wetting soil-water retention curve to calibrate the numerical model and hydraulic hysteresis was not taken into account in the analyses.

## 7.5 Recommendations for future work

1. During the reconnaissance survey conducted in December 2017 (pre-monsoon), roadside slopes were not assessed individually using specific slope assessment forms because this was outside the scope of this survey. In future studies, field survey forms (similar to the landslide information sheet prepared in this study) could be used for the assessment of existing roadside slopes (before landsliding). This approach can be more systematic when conducting such a study over a larger spatial scale. The documents prepared by DHV Consultants (2007) and DoR (2003) for Nepal or by GEO (2018) for Hong Kong provide useful examples of the documents that could be used for the inspection of both natural and man-made slopes in the field.
2. By calibrating the numerical model against the field-measured volumetric water contents, this study has provided a starting point for parametric studies. Future studies can adopt this calibrated model to conduct parametric analysis by varying the input soil parameters, slope geometry and groundwater condition to develop design charts for roadside slopes construction.

3. It was highlighted in chapter 2 and 6 that the presence of a steeply cut roadside slope played an adverse role in the stability of slopes during rainfall. By varying the cut slope gradients, parametric studies can be conducted in the future to examine if there is an optimised slope angle that could be adopted to minimise roadside slope failures during rainfall.
4. The hydro-mechanical soil properties were determined for the investigated site through comprehensive field and laboratory testing in this study. Using these as a reference, probabilistic and sensitivity analyses can be pursued in the future to address the influence of uncertainties in soil parameters and model representation on the stability or response of the model.
5. A significant gap in the understanding unsaturated properties of soils in Nepal was found during this study. Further research focusing on enhancing this aspect could be valuable in the study of rainfall-induced landsliding.
6. The volumetric water content response to rainfall and drying were evaluated based on daily and hourly average values. Further studies at a smaller timescale could provide better visualisation and understanding of the soil response.
7. Hydraulic hysteresis was not taken into account in the numerical analysis. Further studies using sophisticated numerical modelling techniques that incorporate hysteresis could improve the prediction of volumetric water content that is close to the field-monitored data.



# References

---

Abd Elbasit, M., Ojha, C., Abu-Zerig, M., Yasuda, H., Gang, L., and Ahmed, F. (2019) 'Estimation of surface depression storage capacity from surface roughness', *Hydrology and Earth System Sciences Discussions*, (March), pp. 1–18. doi: 10.5194/hess-2019-74.

Adhikari, T. L. (2001) 'Landslide control and stabilisation measures for mountain roads: A case study of Araniko highway, Central Nepal', *Landslide Hazard Mitigation In the Hindu Kush-Himalayas*. Edited by G. Rana et al. Kathmandu: International Centre for Integrated Mountain Development (ICIMOD). Available at: <http://lib.icimod.org/record/7477>.

Almeida, S., Ann Holcombe, E., Pianosi, F., and Wagener, T. (2017) 'Dealing with deep uncertainties in landslide modelling for disaster risk reduction under climate change', *Natural Hazards and Earth System Sciences*, 17(2), pp. 225–241. doi: 10.5194/nhess-17-225-2017.

Alonso, E. E., Pereira, J. M., Vaunat, J., and Olivella, S. (2010) 'A microstructurally based effective stress for unsaturated soils', *Geotechnique*, 60(12), pp. 913–925. doi: 10.1680/geot.8.P.002.

Anderson, M. G., and Lloyd, D. M. (1991) 'Using a combined slope hydrology stability model to develop cut slope design charts', *Proceedings of the Institution of Civil Engineers Part 2-Research and Theory*, 91, pp. 705–718. doi: 10.1680/iicep.1991.17486.

Anderson, M., and Holcombe, E. (2013) *Community-based landslide risk reduction*. doi: 10.1596/978-0-8213-9456-4.

Van Asch, T. W. J., Malet, J.-P., van Beek, L. P. H., and Amitrano, D. (2007) 'Techniques, advances ,problems and issues in numerical modelling of landslide hazard', *Bulletin de la Société Géologique de France*, 2(0), pp. 65–88. doi: 10.2113/gssgfbull.178.2.65.

Assouline, S. (2013) 'Infiltration into soils: Conceptual approaches and solutions', *Water Resources Research*, 49(4), pp. 1755–1772. doi: 10.1002/wrcr.20155.

Balzano, B., Tarantino, A., and Ridley, A. (2019) 'Preliminary analysis on the impacts of the rhizosphere on occurrence of rainfall-induced shallow landslides', *Landslides*. *Landslides*, 16(10), pp. 1885–1901. doi: 10.1007/s10346-019-01197-5.

Bansal, R. C., and Mathur, H. N. (1976) 'Landslides - the nightmares of hill roads', *Soil*

*Conservation Digest.*

Barbour, S. L., and Fredlund, D. G. (1989) 'Mechanisms of osmotic flow and volume change in clay soils', *Canadian Geotechnical Journal*, 26(4), pp. 551–562. doi: 10.1139/t89-068.

Beazley, R. E., and Lassoie, J. P. (2017) *Himalayan mobilities an exploration of the impacts of expanding rural road networks on social and ecological systems in the Nepalese himalaya*. doi: 10.1007/978-3-319-55757-1.

Bentley Systems Inc. (2018) <https://www.bentley.com/en/products/brands/plaxis>.

Beven, K. (1996) 'Equifinality and uncertainty in geomorphological modelling', *The scientific nature of geomorphology. Proceeding of the 27th Binghamton Symposium in Geomorphology*, (September 1996), pp. 289–314.

Bhandary, N. P., Yatabe, R., Dahal, R. K., Hasegawa, S., and Inagaki, H. (2013) 'Areal distribution of large-scale landslides along highway corridors in central Nepal', *Georisk*, 7(1), pp. 1–20. doi: 10.1080/17499518.2012.743377.

Bishop, A. W. (1955) 'The use of the slip circle in the stability analysis of slopes', *Géotechnique*, 5(1), pp. 7–17. doi: 10.1680/geot.1955.5.1.7.

Bishop, A. W., and Blight, G. E. (1963) 'Some aspects of effective stress in saturated and partly saturated soils', *Geotechnique*, 13(3), pp. 177–197. doi: 10.1680/geot.1963.13.3.177.

Blight, G. E. (1967) 'Effective stress evaluation for unsaturated soils', *Journal of the soil mechanics and foundations division*. ASCE, 93(2), pp. 125–148.

Blott, S. J., Croft, D. J., Pye, K., Saye, S. E., and Wilson, H. E. (2004) 'Particle size analysis by laser diffraction', *Geological Society, London, Special Publications*, 232(1), pp. 63–73. doi: 10.1144/GSL.SP.2004.232.01.08.

Borja, R. I., White, J. A., Liu, X., and Wu, W. (2012) 'Factor of safety in a partially saturated slope inferred from hydro-mechanical continuum modeling', *International Journal for Numerical and Analytical Methods in Geomechanics*, 36, pp. 236–248. doi: 10.1002/nag.

Boso, M., Romero, E., and Tarantino, A. (2006) 'The use of different suction measurement techniques to determine water retention curves', *Unsaturated Soils: Experimental Studies*, pp. 169–181. doi: 10.1007/3-540-26736-0\_14.

Bozzolan, E., Holcombe, E., Pianosi, F., and Wagener, T. (2020) 'Including informal housing in slope stability analysis – an application to a data-scarce location in the humid tropics', *Natural Hazards and Earth System Sciences*, 20(11), pp. 3161–3177. doi: 10.5194/nhess-20-3161-2020.

Brinkgreve, R. B. J., Bürg, M., Andreykiv, A., and Lim, L. J. (2015) 'Beyond the finite element method in geotechnical analysis', *BAWMitteilungen*, 98, pp. 91–102. Available at: <https://hdl.handle.net/20.500.11970/102525>.

Brinkgreve, R. B. J., Kumarswamy, S., Swolfs, W. M., and Foria, F. (2018) 'PLAXIS 2D reference manual 2018'. Delft: PLAXIS BV, pp. 1–168. Available at: <https://www.plaxis.com/support/manuals/plaxis-2d-manuals/>.

Brooks, R. H., and Corey, A. T. (1964) 'Hydraulic properties of porous media', *Hydrology papers*, 3.

BSI (1990) 'Methods of test for soils for civil engineering purposes - Part 6: Consolidation and permeability tests in hydraulic cells and with pore pressure measurement (BS 1377-6:1990)'. British Standards Institution.

BSI (2005) 'Geotechnical investigation and testing - Field testing - Part 3: Standard penetration test (BS EN ISO 22476-3:2005+A1:2011)'. British Standards Institution.

BSI (2012a) 'Geotechnical investigation and testing - Geohydraulic testing - Part 5: Infiltration tests (BS EN ISO 22282-5:2012)'. British Standards Institution.

BSI (2012b) 'Geotechnical investigation and testing — Geohydraulic testing - Part 2: Water permeability tests in a borehole using open systems (BS EN ISO 22282-2:2012)'. British Standards Institution.

BSI (2015) 'Code of practice for ground investigations (BS 5930:2015)'. British Standards Institution.

BSI (2017a) 'Soil quality - Sampling - Part 102: Selection and application of sampling techniques (BS ISO 18400-102:2017)'. British Standards Institution.

BSI (2017b) 'Soil quality - Sampling - Part 105: Packaging, transport, storage and preservation of samples (BS ISO 18400-105:2017)'. British Standards Institution.

BSI (2018a) 'Geotechnical investigation and testing - Identification and classification of soil - Part 1: Identification and description (BS EN ISO 14688-1:2018)'. British Standards Institution.

BSI (2018b) 'Geotechnical investigation and testing - Laboratory testing of soil - Part 12: Determination of liquid and plastic limits (BS EN ISO 17892-12:2018)'. British Standards Institution.

BSI (2018c) 'Geotechnical investigation and testing - Laboratory testing of soil - Part 9: Consolidated triaxial compression tests on water saturated soils (BS EN ISO 17892-9:2018)'. British Standards Institution.

BSI (2019) 'Geotechnical investigation and testing - Laboratory testing of soil - Part 11: Permeability tests (BS EN ISO 17892-11:2019)'. British Standards Institution.

Buckingham, E. (1907) 'Studies on the movement of soil moisture', *US Dept. Agric. Bur. Soils Bull.*, 38.

Cai, F., and Ugai, K. (2004) 'Numerical analysis of rainfall effects on slope stability', *International Journal of Geomechanics*, 4(2), pp. 69–78. doi: 10.1061/(ASCE)1532-3641(2004)4:2(69).

Cai, Z., and Ofterdinger, U. (2016) 'Analysis of groundwater-level response to rainfall and estimation of annual recharge in fractured hard rock aquifers, NW Ireland', *Journal of Hydrology*. Elsevier B.V., 535(February), pp. 71–84. doi: 10.1016/j.jhydrol.2016.01.066.

Caine, N. (1980) 'The Rainfall intensity - duration control of shallow landslides and debris flows', *Geografiska Annaler. Series A, Physical Geography*, 62(1/2), p. 23. doi: 10.2307/520449.

Caine, N., and Mool, P. K. (1982) 'Landslides in the Kolpu Khola drainage, Middle Mountains, Nepal', *Mountain Research and Development*, 2(2), pp. 157–173. Available at: <https://www.jstor.org/stable/3672961>.

Cascini, L., Cuomo, S., and Pastor, M. (2008) 'The role played by mountain tracks on rainfall-induced shallow landslides: A case study', in *Proc. iEMSs 4th Biennial Meeting - Int. Congress on Environmental Modelling and Software: Integrating Sciences and Information Technology for Environmental Assessment and Decision Making, iEMSs 2008*, pp. 1484–1491.

Casini, F., Minder, P., and Springman, S. M. (2011) 'Shear strength of an unsaturated silty sand', *Unsaturated Soils - Proceedings of the 5th International Conference on Unsaturated Soils*, 1(Colombo 2009), pp. 211–216. doi: 10.1201/b10526-24.

Chae, B.-G., and Kim, M.-I. (2012) 'Suggestion of a method for landslide early warning using the change in the volumetric water content gradient due to rainfall infiltration',

*Environmental Earth Sciences*, 66(7), pp. 1973–1986. doi: 10.1007/s12665-011-1423-z.

Chae, G. T., Yun, S. T., Kim, D. S., Kim, K. H., and Joo, Y. (2010) 'Time-series analysis of three years of groundwater level data (Seoul, South Korea) to characterize urban groundwater recharge', *Quarterly Journal of Engineering Geology and Hydrogeology*, 43(1), pp. 117–127. doi: 10.1144/1470-9236/07-056.

Chapuis, R. P. (2004) 'Predicting the saturated hydraulic conductivity of sand and gravel using effective diameter and void ratio', *Canadian Geotechnical Journal*. NRC Research Press, 41(5), pp. 787–795. doi: 10.1139/t04-022.

Chaudhary, S., Wang, Y., Dixit, A. M., Khanal, N. R., Xu, P., Fu, B., Yan, K., Liu, Q., Lu, Y., and Li, M. (2020) 'Spatiotemporal degradation of abandoned farmland and associated eco-environmental risks in the high mountains of the Nepalese Himalayas', *Land*, 9(1), pp. 1–19. doi: 10.3390/land9010001.

Chen, L., and Young, M. H. (2006) 'Green-Ampt infiltration model for sloping surfaces', *Water Resources Research*, 42(7), pp. 1–9. doi: 10.1029/2005WR004468.

Childs, E. C. (1969) *An introduction to the physical basis of soil water phenomena*. London: Wiley-Interscienc.

Childs, E. C., and Collis-George, N. (1950) 'The permeability of porous materials', *Proceedings of the Royal Society of London. Series A. Mathematical and Physical Sciences*. The Royal Society London, 201(1066), pp. 392–405.

Chowdhury, R., Flentje, P., and Bhattacharya, G. (2009) *Geotechnical slope analysis*. London, UK: CRC Press Taylor & Francis Group. doi: 10.1201/9780203864203.

Clayton, C. R. I., Matthews, M. C., and Simons, N. E. (1995) *Site investigation: a handbook for engineers*, Blackwell Science.

Clough, R. W., and Woodward, R. J. (1967) 'Analysis of embankment stresses and deformations', *Journal of Soil Mechanics & Foundations Div.*

Collison, A. J. C., Anderson, M. G., and Lloyd, D. M. (1995) 'Impact of vegetation on slope stability in a humid tropical environment: A modelling approach', *Proceedings of the Institution of Civil Engineers: Water, Maritime and Energy*, 112(2), pp. 168–175. doi: 10.1680/iwtme.1995.27662.

Comegna, L., Damiano, E., Greco, R., Guida, A., Olivares, L., and Picarelli, L. (2016) 'Field hydrological monitoring of a sloping shallow pyroclastic deposit', *Canadian Geotechnical*

*Journal*, 53(7), pp. 1125–1137. doi: 10.1139/cgj-2015-0344.

Craig, R. F. (2004) *Craig's soil mechanics*. 7th edn. London: Taylor & Francis Group, London and New York.

Czarnomski, N. M., Moore, G. W., Pypker, T. G., Licata, J., and Bond, B. J. (2005) 'Precision and accuracy of three alternative instruments for measuring soil water content in two forest soils of the Pacific Northwest', *Canadian Journal of Forest Research*, 35(8), pp. 1867–1876. doi: 10.1139/x05-121.

Dahal, R. K., Hasegawa, S., Masuda, T., and Yamanaka, M. (2006) 'Roadside slope failures in Nepal during torrential rainfall and their mitigation', in *Disaster mitigation of debris flows, slope failures, and landslides: proceedings of the INTERPRAEVENT international symposium*, pp. 503–514.

Dahal, R. K., Hasegawa, S., Yamanaka, M., Dhakal, S., Bhandary, N. P., and Yatabe, R. (2009) 'Comparative analysis of contributing parameters for rainfall-triggered landslides in the Lesser Himalaya of Nepal', *Environmental Geology*, 58(3), pp. 567–586. doi: 10.1007/s00254-008-1531-6.

Dahal, R. K. (2012) 'Rainfall-induced landslides in Nepal', *International Journal of Japan Erosion Control Engineering*, 5(1), pp. 1–8. doi: 10.13101/ijece.5.1.

Dahal, R. K., and Bhandary, N. P. (2013) 'Geo-disaster and its mitigation in Nepal', in Wang, F. et al. (eds) *Progress of Geo-Disaster Mitigation Technology in Asia*. Berlin, Heidelberg: Springer Berlin Heidelberg (Environmental Science and Engineering), pp. 263–275. doi: 10.1007/978-3-642-29107-4.

Dahal, R. K., and Hasegawa, S. (2008) 'Representative rainfall thresholds for landslides in the Nepal Himalaya', *Geomorphology*, 100(3), pp. 429–443. doi: <https://doi.org/10.1016/j.geomorph.2008.01.014>.

Dahal, R. K. R., Hasegawa, S., Bhandary, N. P., and Yatabe, R. (2010) 'Low cost road for the development of Nepal and its engineering geological consequences', in Williams, A. L. et al. (eds) *Proceedings of the 11th IAEG Congress*. Auckland: Taylor & Francis Group, London, pp. 4085–4094.

Das, B. M. (2008) *Advanced soil mechanics*. 3rd edn. Taylor & Francis Group, London and New York. Available at: <http://doi.wiley.com/10.1029/E0066i042p00714-02>.

Datta, A., Sigdel, S., Oves, K., Rosser, N., Densmore, A., and Rijal, S. (2018) *The role of*

*scientific evidence during the 2015 Nepal earthquake relief efforts, Overseas Development Institute.* London, UK.

Decagon Devices (2010) *10 HS Soil Moisture Sensor Operator's Manual Version 3.* USA. Available at: [www.decagon.com](http://www.decagon.com).

Devkota, S., Sudmeier-Rieux, K., Penna, I., Erble, S., Jaboyedoff, M., Andhikari, A., and Khanal, R. (2014) *Community-based bio-engineering for eco-safe roadsides in Nepal.* Lausanne.

DHM (2018) 'Precipitation data'. Kathmandu, Nepal: Meterological Data Management Section. Available at: <https://www.dhm.gov.np/> (Accessed: 7 April 2019).

DHV Consultants (2007) *Roadside Geotechnical Problems: A Practical Guide to their Solution.* Nepal. Available at: [https://dor.gov.np/uploads/publication/publication\\_1472792371.pdf](https://dor.gov.np/uploads/publication/publication_1472792371.pdf).

Dixon, N., Crosby, C. J., Stirling, R., Hughes, P. N., Smethurst, J., Briggs, K., Hughes, D., Gunn, D., Hobbs, P., Loveridge, F., Glendinning, S., Dijkstra, T., and Hudson, A. (2019) 'In situ measurements of near-surface hydraulic conductivity in engineered clay slopes', *Quarterly Journal of Engineering Geology and Hydrogeology*, 52(1), pp. 123–135. doi: 10.1144/qjegh2017-059.

DMG (1994) *Geology of Nepal.* Nepal: Department of Mines and Geology, ICIMOD. Available at: <https://rds.icimod.org/Home/DataDetail?metadataId=2521&searchlist=True> (Accessed: 7 December 2020).

DoLIDAR (2009) *Rural road maintenance technical handbook.* Nepal: Government of Nepal; Ministry of Local Development; Department of Local Infrastructure Development and Agricultural Roads (DoLIDAR). Available at: <http://archive.rapnepal.com/report-publication/rural-road-maintenance-technical-handbook>.

DoLIDAR (2016) *Statistics of Local Road Network (SLRN) 2016.* Kathmandu: Government of Nepal, Ministry of Federal Affairs and Local Development, Department of Local Infrastructure Development and Agricultural Roads (DoLIDAR). Available at: [http://www.dolidar.gov.np/wp-content/uploads/2017/02/DoLIDAR\\_Book\\_layout\\_RAM\\_webpage.pdf](http://www.dolidar.gov.np/wp-content/uploads/2017/02/DoLIDAR_Book_layout_RAM_webpage.pdf).

DoR (2003) *Guide to road slope protection works.* Kathmandu, Nepal: Government of Nepal; Ministry of Physical Planning and Works; Department of Roads (DoR). Available at: <https://dor.gov.np/home/publication/gesu-publication/guide-to-road-slope-protection->

works.

DSCWM (2016) *Guideline on landslide treatment and mitigation*. Kathmandu, Nepal: Department of Soil Conservation and Watershed Management (DSCWM), Ministry of Forests and Soil Conservation.

Duncan, J. M. (1996) 'State of the art: Limit equilibrium and finite-element analysis of slopes', *Journal of Geotechnical Engineering*, 122(7), pp. 577–596. doi: 10.1061/(asce)0733-9410(1996)122:7(577).

Eichenberger, J., Nuth, M., and Laloui, L. (2011) 'Hydromechanically coupled analysis of transient phenomena in a rainfall-induced landslide', *2nd International Symposium on Computational Geomechanics*, (EPFL-CONF-165427), pp. 547–556.

El-Ramly, H. (2001) *Probabilistic analyses of landslide hazards and risks: Bridging theory and practice*. University of Alberta. doi: <https://doi.org/10.7939/R3GH9BK6F>.

Fannin, R. J., and Lorbach, J. (2007) *Guide to forest road engineering in mountainous terrain*. Rome, Italy.

Fisher, P., Aumann, C., Chia, K., O'Halloran, N., and Chandra, S. (2017) 'Adequacy of laser diffraction for soil particle size analysis', *PLoS ONE*, 12(5), pp. 1–20. doi: 10.1371/journal.pone.0176510.

Fookes, P. G., Sweeney, M., Manby, C. N. D., and Martin, R. P. (1985) 'Geological and geotechnical engineering aspects of low-cost roads in mountainous terrain', *Engineering Geology*, 21(1–2), pp. 1–152. doi: 10.1016/0013-7952(85)90002-X.

Fredlund, D. G. (1987) 'Slope stability analysis incorporating the effect of soil suction', in Anderson, M. G. and Richards, K. S. (eds) *Slope Stability*. John Wiley & Sons, Ltd, pp. 113–144.

Fredlund, D. G., Anqing Xing, and Shangyan Huang (1994) 'Predicting the permeability function for unsaturated soils using the soil-water characteristic curve', *Canadian Geotechnical Journal*, 31(4), pp. 533–546. doi: 10.1139/t94-062.

Fredlund, D. G., Morgenstern, N. R., and Widger, R. A. (1978) 'The shear strength of unsaturated soils', *Canadian Geotechnical Journal*, 15, pp. 313–321.

Fredlund, D. G., and Rahardjo, H. (1993) *Soil mechanics for unsaturated soils*. John Wiley & Sons, Inc. doi: 10.1002/9780470172759.ch13.



Fredlund, D. G., Rahardjo, H., and Fredlund, M. D. (2012) *Unsaturated Soil Mechanics in Engineering Practice*. John Wiley & Sons, Inc.

Fredlund, D. G., Sheng, D., and Zhao, J. (2011) 'Estimation of soil suction from the soil-water characteristic curve', *Canadian Geotechnical Journal*, 48(2), pp. 186–198. doi: 10.1139/T10-060.

Fredlund, D. G., and Xing, A. (1994) 'Equations for the soil-water characteristic curve', *Canadian Geotechnical Journal*. NRC Research Press, 31(4), pp. 521–532. doi: 10.1139/t94-061.

Froude, M. J., and Petley, D. N. (2018) 'Global fatal landslide occurrence from 2004 to 2016', *Natural Hazards and Earth System Sciences*, 18(8), pp. 2161–2181. doi: 10.5194/nhess-18-2161-2018.

Galavi, V., Brinkgreve, R. B. J., Bonnier, P. G., and Gonzalez, N. A. (2009) 'Fully coupled hydro-mechanical analysis of unsaturated soils', in Pietruszczak, S. et al. (eds) *Proceedings of the 1st International Symposium on Computational Geomechanics (COMGEO I)*. Paris, France, pp. 486–495.

Galavi, V. (2010) *Groundwater flow, fully coupled flow deformation and undrained analyses in PLAXIS 2D and 3D*. doi: 10.13140/RG.2.1.1940.7763.

Gasmo, J. M., Rahardjo, H., and Leong, E. C. (2000) 'Infiltration effects on stability of a residual soil slope', *Computers and Geotechnics*, 26(2), pp. 145–165. doi: 10.1016/S0266-352X(99)00035-X.

van Genuchten, M. T. (1980) 'A closed-form equation for predicting the hydraulic conductivity of unsaturated soils', *Soil Science Society of America Journal*, 44(5), pp. 892–898.

GEO (2018) *Guide to Slope Maintenance (Geoguide 5)*. 3rd edn. Hong Kong: Geotechnical Engineering Office, Civil Engineering and Development Department, HKSAR Government.

GeoStudio (2020) <https://www.geoslope.com/products/geostudio>.

Gerrard, J. (1994) 'The landslide hazard in the Himalayas: geological control and human action', *Geomorphology*, 10(1–4), pp. 221–230. doi: 10.1016/0169-555X(94)90018-3.

Gerrard, J., and Gardner, R. A. M. (2000) 'Relationships between rainfall and landsliding in the Middle Hills, Nepal', *Norsk Geografisk Tidsskrift*, 54(2), pp. 74–81. doi:

10.1080/002919500423807.

Godt, J. W., Şener-Kaya, B., Lu, N., and Baum, R. L. (2012) 'Stability of infinite slopes under transient partially saturated seepage conditions', *Water Resources Research*, 48(5), pp. 1–14. doi: 10.1029/2011WR011408.

Godt, J. W., Baum, R. L., and Lu, N. (2009) 'Landsliding in partially saturated materials', *Geophysical Research Letters*, 36(2), pp. 1–5. doi: 10.1029/2008GL035996.

Gonzalez-Ollauri, A., and Mickovski, S. B. (2017) 'Hydrological effect of vegetation against rainfall-induced landslides', *Journal of Hydrology*. Elsevier B.V., 549, pp. 374–387. doi: 10.1016/j.jhydrol.2017.04.014.

Government of Nepal: National Planning Commission (2017) *Sustainable development goals. Status and roadmap: 2016-2030*. Kathmandu, Nepal. Available at: [https://www.npc.gov.np/images/category/SDG\\_Status\\_and\\_Roadmap\\_\(2016-2030\).pdf](https://www.npc.gov.np/images/category/SDG_Status_and_Roadmap_(2016-2030).pdf) (Accessed: 28 January 2021).

Government of Nepal: National Planning Commission (2020) *Sustainable development goals. Progress assessment report 2016-2019*. Kathmandu, Nepal. Available at: [https://npc.gov.np/images/category/SDG\\_Progress\\_Report\\_2016-2019\\_final.pdf](https://npc.gov.np/images/category/SDG_Progress_Report_2016-2019_final.pdf) (Accessed: 28 January 2021).

Green, W. H., and Ampt, G. A. (1911) 'Studies on soil physics. Part I - The flow of air and water through soils', *Journal of Water Resource and Protection*, IV(1).

Griffiths, D. V., and Lane, P. A. (1999) 'Slope stability analysis by finite elements', *Geotechnique*, pp. 387–403.

Griffiths, D. V., and Lu, N. (2005) 'Unsaturated slope stability analysis with steady infiltration or evaporation using elasto-plastic finite elements', *International Journal for Numerical and Analytical Methods in Geomechanics*, 29(3), pp. 249–267. doi: 10.1002/nag.413.

Guadagno, F. M., Forte, R., Revellino, P., Fiorillo, F., and Focareta, M. (2005) 'Some aspects of the initiation of debris avalanches in the Campania Region: The role of morphological slope discontinuities and the development of failure', *Geomorphology*, 66(1-4 SPEC. ISS.), pp. 237–254. doi: 10.1016/j.geomorph.2004.09.024.

Guadagno, F. M., Martino, S., and Mugnozza, G. S. (2003) 'Influence of man-made cuts on the stability of pyroclastic covers (Campania, southern Italy): a numerical modelling

approach', *Environmental Geology*, 43(4), pp. 371–384. doi: 10.1007/s00254-002-0658-0.

Haigh, M., and Rawat, J. (2012) 'Landslide disasters: seeking causes – A case study from Uttarakhand, India', in Křeček, J. et al. (eds) *Management of mountain watersheds*. Capital Publishing Company, pp. 218–253. doi: 10.1007/978-94-007-2476-1\_18.

Haigh, M., and Rawat, J. S. (2011) 'Landslide causes: Human impacts on a Himalayan landslide swarm', *Belgeo*, (3–4), pp. 201–220. doi: 10.4000/belgeo.6311.

Hamdhan, I. N., and Schweiger, H. F. (2013) 'Finite element method-based analysis of an unsaturated soil slope subjected to rainfall infiltration', *International Journal of Geomechanics*, 13(5), pp. 653–658. doi: 10.1061/(ASCE)GM.1943-5622.0000239.

Harris, S. J., Orense, R. P., and Itoh, K. (2012) 'Back analyses of rainfall-induced slope failure in Northland Allochthon formation', *Landslides*, 9(3), pp. 349–356. doi: 10.1007/s10346-011-0309-1.

Hatanaka, M., and Uchida, A. (1996) 'Empirical correlation between penetration resistance and internal friction angle of sandy soils', *Soils and Foundations*, 36(4), pp. 1–9. doi: 10.3208/sandf.36.4\_1.

Hawke, R., and McConchie, J. (2011) 'In situ measurement of soil moisture and pore-water pressures in an "incipient" landslide: Lake Tutira, New Zealand', *Journal of Environmental Management*. Elsevier Ltd, 92(2), pp. 266–274. doi: 10.1016/j.jenvman.2009.05.035.

Hazen, A. (1892) 'Some physical properties of sands and gravels: with special reference to their use in filtration', *State Sanitation: A Review of the Work of the Massachusetts State Board of Health*. Harvard University Press, II, pp. 232–248.

Hearn, G., Petley, D., Hart, A., Massey, C., and Chant, C. (2003) *Landslide risk assessment in the rural sector: Guidelines on best practice*. Available at: <https://www.gov.uk/dfid-research-outputs/landslide-risk-assessment-in-the-rural-sector-guidelines-on-best-practice-add017>.

Hearn, G. J. (2011) *Slope engineering for mountain roads*. London: Geological Society of London (Engineering geology special publication). doi: <https://doi.org/10.1144/EGSP24>.

Hearn, G. J., and Hunt, T. (2011) 'C2 Earthworks', *Geological Society, London, Engineering Geology Special Publications*. London: Geological Society, London, Engineering Geology Special Publications, 24(1), pp. 145–163. doi: 10.1144/EGSP24.11.

Hearn, G. J., and Massey, C. I. (2009) 'Engineering geology in the management of roadside slope failures: contributions to best practice from Bhutan and Ethiopia', *Quarterly Journal of Engineering Geology and Hydrogeology*, 42(Fookes 1997), pp. 511–528. doi: 10.1144/1470-9236/08-004.

Hearn, G. J., and Shakya, N. M. (2017) 'Engineering challenges for sustainable road access in the Himalayas', *Quarterly Journal of Engineering Geology and Hydrogeology*, p. 2017. doi: 10.1144/qjegh2016-109.

Hillel, D. (1998) *Environmental Soil Physics*. Elsevier.

Holcombe, E. A., Beesley, M. E. W., Vardanega, P. J., and Sorbie, R. (2016) 'Urbanisation and landslides: hazard drivers and better practices', *Proceedings of the Institution of Civil Engineers - Civil Engineering*, 169(3), pp. 137–144. doi: 10.1680/jcien.15.00044.

Hughes, D., Karim, M. R., Briggs, K., Glendinning, S., Toll, D., Dijkstra, T., Powrie, W., and Dixon, N. (2015) 'A comparison of numerical modelling techniques to predict the effect of climate on infrastructure slopes', *Geotechnical Engineering for Infrastructure and Development - Proceedings of the XVI European Conference on Soil Mechanics and Geotechnical Engineering, ECSMGE 2015*, 7(January), pp. 3663–3668.

ICIMOD (1991) *Mountain risk engineering handbook: Part 2*. Edited by B. Deoja et al. Kathmandu: International Centre for Integrated Mountain Development (ICIMOD).

Jackson, N., and Dhir, R. K. (1996) *Compressibility of Soil*. 5th edn, *Civil Engineering Materials*. 5th edn. The McGraw-Hill Companies, Inc. doi: 10.1007/978-1-349-13729-9\_26.

Janbu, N. (1954) 'Application of composite slip surface for stability analysis', in *Proceedings of European Conference on Stability of Earth Slopes, Sweden, 1954*, pp. 43–49.

Jankauskas, B., Jankauskiene, G., Fullen, M. a, and Booth, C. a (2008) 'Utilizing palm-leaf geotextiles to control soil erosion on roadside slopes in Lithuania', *Žemes Ukio Mokslai*, 15(3), pp. 22–28.

Jennings, J. E. B., and Burland, J. B. (1962) 'Limitations to the use of effective stresses in partly saturated soils', *Geotechnique*, 12(2), pp. 125–144. doi: 10.1680/geot.1962.12.2.125.

Kargas, G., and Soulis, K. X. (2012) 'Performance analysis and calibration of a new low-cost capacitance soil moisture sensor', *Journal of Irrigation and Drainage Engineering*, 138(7), pp. 632–641. doi: 10.1061/(ASCE)IR.1943-4774.0000449.

Karki, R., Talchabhadel, R., Aalto, J., and Baidya, S. K. (2016) 'New climatic classification

of Nepal', *Theoretical and Applied Climatology*. Theoretical and Applied Climatology, 125(3–4), pp. 799–808. doi: 10.1007/s00704-015-1549-0.

Khalili, N., and Khabbaz, M. H. (1998) 'A unique relationship for  $\chi$  for the determination of the shear strength of unsaturated soils', *Geotechnique*, 48(5), pp. 681–687. doi: 10.1680/geot.1998.48.5.681.

Khanal, N. R., and Watanabe, T. (2006) 'Abandonment of agricultural land and its consequences', *Mountain Research and Development*, 26(1), pp. 32–40. doi: 10.1659/0276-4741(2006)026[0032:aoalai]2.0.co;2.

Kim, J., Hwang, W., and Kim, Y. (2018) 'Effects of hysteresis on hydro-mechanical behavior of unsaturated soil', *Engineering Geology*. Elsevier, 245(July), pp. 1–9. doi: 10.1016/j.enggeo.2018.08.004.

Kincey, M., Rosser, N., Robinson, T. R., Densmore, A., Shrestha, R., Pujara, D. S., Oven, K. J., Williams, J. G., and Swirad, Z. M. (2020) 'Evolution of coseismic and post-seismic landsliding after the 2015 Mw 7.8 Gorkha earthquake, Nepal', *Earth and Space Science Open Archive ESSOAr*. Available at: <https://doi.org/10.1002/essoar.10505237.1>.

Konert, M., and Vandenberghe, J. (1997) 'Comparison of laser grain size analysis with pipette and sieve analysis: a solution for the underestimation of the clay fraction', *Sedimentology*, (44), pp. 523–535.

Krahn, J. (2003) 'The 2001 R.M. Hardy Lecture: The limits of limit equilibrium analyses', *Canadian Geotechnical Journal*, 40(3), pp. 643–660. doi: 10.1139/t03-024.

Krahn, J., and Fredlund, D. G. (1971) 'On total, matric and osmotic suction.pdf', *Soil Science*, pp. 339–348.

Kristo, C., Rahardjo, H., and Satyanaga, A. (2019) 'Effect of hysteresis on the stability of residual soil slope', *International Soil and Water Conservation Research*. Elsevier Ltd, 7(3), pp. 226–238. doi: 10.1016/j.iswcr.2019.05.003.

Kwok, S. Y. F., and Tung, Y.-K. (2003) 'Uncertainty and sensitivity analysis of coupled surface and subsurface flows', in *Groundwater Quality Modeling and Management Under Uncertainty*. Reston, VA: American Society of Civil Engineers (Proceedings), pp. 58–71. doi: 10.1061/40696(2003)6.

Lam, L., Fredlund, D. G., and Barbour, S. L. (1987) 'Transient seepage model for saturated-unsaturated soil systems: a geotechnical engineering approach', *Canadian*

*Geotechnical Journal*, 24(4), pp. 565–580. doi: 10.1139/t87-071.

Lambe, T. W., and Whitman, R. V. (1969) *Soil Mechanics*. John Wiley & Sons, Inc.

Lambert, L., and Chitrakar, B. D. (1989) 'Variation of potential evapotranspiration with elevation in Nepal', *Mountain Research and Development*, 9(2), pp. 145–152. Available at: <https://www.jstor.org/stable/3673477>.

Larsen, M. C., and Parks, J. E. (1997) 'How wide is a road? The association of roads and mass-wasting in a forested montane environment', *Earth Surface Processes and Landforms*, 22(9), pp. 835–848. doi: 10.1002/(SICI)1096-9837(199709)22:9<835::AID-ESP782>3.0.CO;2-C.

Lee, L. M., Gofar, N., and Rahardjo, H. (2009) 'A simple model for preliminary evaluation of rainfall-induced slope instability', *Engineering Geology*. Elsevier B.V., 108(3–4), pp. 272–285. doi: 10.1016/j.enggeo.2009.06.011.

Leibundgut, G., Sudmeier-Rieux, K., Devkota, S., Jaboyedoff, M., Derron, M.-H., Penna, I., and Nguyen, L. (2016) 'Rural earthen roads impact assessment in Phewa watershed, Western region, Nepal', *Geoenvironmental Disasters*, 3(1), p. 13. doi: 10.1186/s40677-016-0047-8.

Leij, F. J., Alves, W. J., van Genuchten, M. T., and Williams, J. R. (1996) *The UNSODA unsaturated hydraulic database (EPA/600/R-96/095)*. Cincinnati, OH, USA.

Lennartz, T. (2013) 'Constructing roads - constructing risks? Settlement decisions in view of landslide risk and economic opportunities in western Nepal', *Mountain Research and Development*, 33(4), pp. 364–371. doi: 10.1659/MRD-JOURNAL-D-13-00048.1.

Leong, E. C. (2019) 'Stress state variables for unsaturated soils - Consensus and controversy', in Ilamparuthi, K. and Robinson, R. G. (eds) *Geotechnical Design and Practice: Selected Topics*. Singapore: Springer Singapore, pp. 79–89. doi: 10.1007/978-981-13-0505-4\_7.

Leong, E. C., and Rahardjo, H. (1997) 'Permeability functions for unsaturated soils', *Geotechnical and Geoenvironmental Engineering*, 123(12), pp. 1118–1126.

Li, A. G., Tham, L. G., Yue, Z. Q., Lee, C. F., and Law, K. T. (2005) 'Comparison of field and laboratory soil–water characteristic curves', *Journal of Geotechnical and Geoenvironmental Engineering*, 131(9), pp. 1176–1180. doi: 10.1061/(asce)1090-0241(2005)131:9(1176).

Li, A. G., Tham, L. G., Law, K. T., Yue, Z. Q., and Lee, C. F. (2005) 'Field-monitored

variations of soil moisture and matric suction in a saprolite slope', *Canadian Geotechnical Journal*, 42(1), pp. 13–26. doi: 10.1139/t04-069.

Liao, S. S. C., and Whitman, R. V. (1986) 'Overburden correction factors for SPT in sand', *Journal of Geotechnical Engineering*, 112(3), pp. 373–377.

Liu, H. W., Feng, S., and Ng, C. W. W. (2016) 'Analytical analysis of hydraulic effect of vegetation on shallow slope stability with different root architectures', *Computers and Geotechnics*, 80, pp. 115–120. doi: 10.1016/j.compgeo.2016.06.006.

Loizeau, J. L., Arbouille, D., Santiago, S., and Vernet, J. P. (1994) 'Evaluation of a wide range laser diffraction grain size analyser for use with sediments', *Sedimentology*. doi: 10.1111/j.1365-3091.1994.tb01410.x.

Lourenço, S., Gallipoli, D., Toll, D., Evans, F., and Medero, G. (2007) 'Determination of the Soil Water Retention Curve with Tensiometers', *Experimental Unsaturated Soil Mechanics*, (2000), pp. 95–102. doi: 10.1007/3-540-69873-6\_9.

Lourenço, S. D. N., Gallipoli, D., Toll, D. G., and Evans, F. D. (2006) 'Development of a commercial tensiometer for triaxial testing of unsaturated soils', *Geotechnical Special Publication*, 40802(147), pp. 1875–1886. doi: 10.1061/40802(189)158.

Lourenço, S. D. N., Gallipoli, D., Toll, D. G., Augarde, C. E., Evans, F. D., and Medero, G. M. (2008) 'Calibrations of a high-suction tensiometer', *Geotechnique*, 58(8), pp. 659–668. doi: 10.1680/geot.2008.58.8.659.

Lu, N., and Likos, W. J. (2004) *Unsaturated soil mechanics*. New Jersey, United States of America: John Wiley & Sons, Inc. doi: 10.1051/lait.

Lumb, P. (1962) 'Effect of rain storms on slope stability', in *Proceedings of Symposium on Hong Kong Soils*. Hong Kong: Local Property & Printing Company, Limited, pp. 73–87. Available at: <https://books.google.co.uk/books?id=Sse9ZwEACAAJ>.

Lumb, P. (1975) 'Slope failures in Hong Kong', *Quarterly Journal of Engineering Geology*, 8(1), pp. 31–65. doi: 10.1144/GSL.QJEG.1975.008.01.02.

Mahmood, R., Littell, A., Hubbard, K. G., and You, J. (2012) 'Observed data-based assessment of relationships among soil moisture at various depths, precipitation, and temperature', *Applied Geography*. Elsevier Ltd, 34, pp. 255–264. doi: 10.1016/j.apgeog.2011.11.009.

Matsui, T., and San, K.-C. (1992) 'Finite element slope stability analysis by shear

strength reduction technique', *Soils and Foundations*, 32(1), pp. 59–70. Available at: <http://www.mendeley.com/research/geology-volcanic-history-eruptive-style-yakedake-volcano-group-central-japan/>.

Mcadoo, B. G., Quak, M., Gnyawali, K., Adhikari, B. R., Devkota, S., Rajbhandari, P., and Sudmeier, K. (2018) 'Brief communication: Roads and landslides in Nepal: How development affects risk', *Natural Hazards and Earth System Sciences Discussions*, (1979), pp. 1–6. doi: 10.5194/nhess-2017-461.

McGuffey, V. C., Modeer, V. A., and Turner, A. K. (2014) 'Subsurface exploration', in *Landslides-Investigation and mitigation. Transportation: Research Board Special Report 247*. Transportation Research Board. Available at: <http://onlinepubs.trb.org/Onlinepubs/sr/sr247/sr247-010.pdf>.

Md. Rahim, M. S. (2016) *Hydro-mechanical behaviour of a residual soil slope in Malaysia*, PhD Thesis. Durham University. Available at: <http://etheses.dur.ac.uk/11689/>.

Md. Rahim, M. S., and Toll, D. (2014) 'Fully coupled flow-deformation analyses of infiltration and matric suctions within a tropical soil slope', *Unsaturated Soils: Research and Applications*, pp. 1453–1458.

Megahan, W. F. (1983) 'Hydrologic effects of clearcutting and wildfire on steep granitic slopes in Idaho', *Water Resources Research*, 19(3), pp. 811–819. doi: 10.1029/WR019i003p00811.

Mein, R. G., and Larson, C. L. (1973) 'Modeling infiltration during a steady rain', *Water Resources Research*, 9(2), pp. 384–394.

Melgarejo Corredor, M. L. (2004) *Laboratory and numerical investigations of soil retention curves*, PhD Thesis. Imperial College of Science, Technology & Medicine. Available at: <https://spiral.imperial.ac.uk/handle/10044/1/11282>.

Mendes, J. (2011) *Assessment of the impact of climate change on an instrumented embankment: an unsaturated soil mechanics approach*, PhD Thesis. Durham University. Available at: <http://etheses.dur.ac.uk/612/>.

Merz, J., Dangol, P. M., Dhakal, M. P., Dongol, B. S., Nakarmi, G., and Weingartner, R. (2006) 'Road construction impacts on stream suspended sediment loads in a nested catchment system in Nepal', *Land Degradation and Development*, 17(3), pp. 343–351. doi: 10.1002/ldr.717.



METER Environment (2017) *Soil moisture sensors—How they work. Why some are not research-grade, Knowledge base articles.* Available at: <https://www.metergroup.com/environment/articles/tdr-fdr-capacitance-compared/> (Accessed: 16 June 2020).

Meyerhof, G. G. (1957) 'Discussion on soil properties and their measurement, Discussion 2', in *Proc. of the IVth International, Conference of Soil Mechanics and Foundation Engineering*, p. 110.

Miller, G. A., Houry, C. N., Muraleetharan, K. K., Liu, C., and Kibbey, T. C. G. (2008) 'Effects of soil skeleton deformations on hysteretic soil water characteristic curves: Experiments and simulations', *Water Resources Research*, 44(5), pp. 1–10. doi: 10.1029/2007WR006492.

Mittelbach, H., Lehner, I., and Seneviratne, S. I. (2012) 'Comparison of four soil moisture sensor types under field conditions in Switzerland', *Journal of Hydrology*. Elsevier B.V., 430–431, pp. 39–49. doi: 10.1016/j.jhydrol.2012.01.041.

Mohan, D., Aggarwal, V. S., and Tolia, D. S. (1970) 'Discussion: The correlation of cone size in the dynamic cone penetration test with the standard penetration test', *Géotechnique*, 20(3), pp. 315–319. doi: 10.1680/geot.1971.21.4.423.

Morgan, R. P. C. (2007) 'Vegetative-based technologies for erosion control', in *Eco-and ground bio-engineering: the use of vegetation to improve slope stability*. Springer, pp. 265–272.

Mualem, Y. (1976) 'A new model for predicting the hydraulic conductivity of unsaturated porous media', *Water Resources Research*, 12(3), pp. 513–522.

Mualem, Y. (1986) 'Hydraulic conductivity of unsaturated soils: prediction and formulas', *Methods of Soil Analysis: Part 1 Physical and Mineralogical Methods*. Wiley Online Library, 5, pp. 799–823.

Nawawitphisit, S. (2014) *Groundwater and geotechnical controls on landslide mechanisms of coastal cliffs formed in glacial tills*, PhD Thesis. Durham University. Available at: <http://etheses.dur.ac.uk/10614/>.

Ng, C. W. W., and Shi, Q. (1998) 'A numerical investigation of the stability of unsaturated soil slopes subjected to transient seepage', *Computers and Geotechnics*, 22(1), pp. 1–28. doi: 10.1016/S0266-352X(97)00036-0.

Öberg, A., and Sällfors, G. (1997) 'Determination of shear strength parameters of unsaturated silts and sands based on the water retention curve', *Geotechnical Testing Journal*, 20(1), pp. 40–48. doi: 10.1520/gtj11419j.

Oh, S., and Lu, N. (2015) 'Slope stability analysis under unsaturated conditions: Case studies of rainfall-induced failure of cut slopes', *Engineering Geology*. Elsevier B.V., 184, pp. 96–103. doi: 10.1016/j.enggeo.2014.11.007.

ONSET (2018a) *Rain gauge smart sensor (S-RGx-M002) manual*. 16 June 2020. Available at: [https://www.onsetcomp.com/files/manual\\_pdfs/14091-H\\_S-RGAB\\_Manual.pdf](https://www.onsetcomp.com/files/manual_pdfs/14091-H_S-RGAB_Manual.pdf) (Accessed: 16 June 2020).

ONSET (2018b) *Soil moisture smart sensor (S-SMx-M005) manual*. Available at: <http://www.onsetcomp.com/products/sensors/s-smc-m005> (Accessed: 16 June 2020).

ONSET (2019) *HOBO RX3000 Remote monitoring station data logger manual*. Available at: <https://www.onsetcomp.com/products/data-loggers/rx3000/> (Accessed: 16 June 2020).

Osinski, P., Toll, D., and Koda, E. (2016) 'Comparison of soil water retention curves for sandy clay, obtained using different laboratory testing methods', *E3S Web of Conferences*, 9(September). doi: 10.1051/e3sconf/20160911008.

Oven, K. J. (2009) *Landscape, livelihoods and risk: Community vulnerability to landslides in Nepal*, Durham theses. Durham University. Available at: [http://etheses.dur.ac.uk/183/1/Katie\\_Oven\\_PhD\\_thesis\\_copy\\_for\\_submission.pdf?DDD14+](http://etheses.dur.ac.uk/183/1/Katie_Oven_PhD_thesis_copy_for_submission.pdf?DDD14+)

Pan, H., Qing, Y., and Pei-Yong, L. (2010) 'Direct and indirect measurement of soil suction in the laboratory', *Electronic Journal of Geotechnical Engineering*, 15 A, pp. 1–14.

Peck, R. B., Hanson, W. E., and Thornburn, T. H. (1974) *Foundation engineering*. Wiley New York.

Penman, H. L. (1963) 'Vegetation and Hydrology Tech. Comm. No 53', *Commonwealth Bureau of Soils, Harpenden, England*, 125p.

Petley, D. (2010) 'Landslide hazards', in Alcantara-Ayala, I. and Goudie, A. S. (eds) *Geomorphological Hazards and Disaster Prevention*. Cambridge: Cambridge University Press, pp. 63–74. doi: DOI: 10.1017/CBO9780511807527.006.

Petley, D. (2012) 'Fatal landslides in Nepal in 2012'. AGU Blogosphere. Available at:

<https://blogs.agu.org/landslideblog/2012/11/03/fatal-landslides-in-nepal-in-2012/>

(Accessed: 2 May 2018).

Petley, D. N., Hearn, G. J., Hart, A., Rosser, N. J., Dunning, S. A., Oven, K., and Mitchell, W. A. (2007) 'Trends in landslide occurrence in Nepal', *Natural Hazards*, 43(1), pp. 23–44. doi: 10.1007/s11069-006-9100-3.

Pokharel, R., Acharya, S. R., and Investment, T. (2015) 'Sustainable transport development in Nepal: Challenges, opportunities and strategies', *Journal of the Eastern Asia Society for Transportation Studies*, 11(December 2015), pp. 209–226. doi: 10.11175/easts.11.209.

Potts, D. M., and Zdravkovid, L. (1999) *Finite element analysis in geotechnical engineering theory*. London, UK: Thomas Telford Publishing.

Pradhan, S., Toll, D. G., Rosser, N. J., and Brain, M. J. (2020) 'Field monitoring of soil-moisture to understand the hydrological response of a road-cut slope', *E3S Web of Conferences*. Edited by R. Cardoso, C. Jommi, and E. Romero, 195, p. 01029. doi: 10.1051/e3sconf/202019501029.

Premchitt, J., T.S.K., L., Shen, J. M., and Lam, H. F. (1995) *Rainstorm runoff on slopes, Geo Report No. 12*. Hong Kong.

Qi, S., and Vanapalli, S. K. (2015) 'Hydro-mechanical coupling effect on surficial layer stability of unsaturated expansive soil slopes', *Computers and Geotechnics*. Elsevier Ltd, 70, pp. 68–82. doi: 10.1016/j.compgeo.2015.07.006.

Queiroz, I. M. (2016) 'Comparison between deterministic and probabilistic stability analysis, Featuring a consequent Risk Analysis', in *ISRM VII Brazilian Symposium on Rock Mechanics, SBMR 2016*, pp. 636–643. doi: 10.20906/CPS/SBMR-03-0004.

Rahardjo, H., Lim, T. T., Chang, M. F., and Fredlund, D. G. (1995) 'Shear-strength characteristics of a residual soil', *Canadian Geotechnical Journal*, 32(1), pp. 60–77. doi: 10.1139/t95-005.

Rahardjo, H., Lee, T. T., Leong, E. C., and Rezaur, R. B. (2005) 'Response of a residual soil slope to rainfall', *Canadian Geotechnical Journal*. NRC Research Press, 42(2), pp. 340–351. doi: 10.1139/t04-101.

Rahardjo, H., Ong, T. H., Rezaur, R. B., and Leong, E. C. (2007) 'Factors Controlling Instability of Homogeneous Soil Slopes under Rainfall', *Geotechnical and Geoenvironmental*

*Engineering*, 133. doi: 10.1061/(ASCE) 1090-0241(2007)133:12(1532).

Rahardjo, H., Nio, A. S., Leong, E. C., and Song, N. Y. (2010) 'Effects of groundwater table position and soil properties on stability of slope during rainfall', *Journal of Geotechnical and Geoenvironmental Engineering*, 136(11), pp. 1555–1564. doi: 10.1061/(ASCE)GT.1943-5606.0000385.

Rahardjo, H., Leong, E. C., Ortigao, J. A. R., and Rezaur, R. B. (2012) 'Slopes', in Huat, B. B. K., Toll, D. G., and Prasad, A. (eds) *Handbook of Tropical Residual Soils Engineering*. CRC Press, pp. 213–282. doi: 10.1201/b12302-7.

Rahardjo, H., and Fredlund, D. G. (1991) 'Calculation procedures for slope stability analyses involving negative pore-water pressures', in *Slope stability engineering developments and applications*. Thomas Telford Publishing, pp. 43–49. doi: 10.1680/ssedaa.16606.0008.

Rahardjo, H., Kim, Y., and Satyanaga, A. (2019) 'Role of unsaturated soil mechanics in geotechnical engineering', *International Journal of Geo-Engineering*. Springer Singapore, 10(1), pp. 1–23. doi: 10.1186/s40703-019-0104-8.

Rahardjo, H., Leong, E. C., and Rezaur, R. B. (2002) 'Studies of rainfall-induced slope failures', in *Proceedings of the National Seminar, Slope 2002*. Bandung, pp. 15–29.

Rahimi, A., Rahardjo, H., and Leong, E. C. (2010) 'Effect of hydraulic properties of soil on rainfall-induced slope failure', *Engineering Geology*. Elsevier B.V., 114(3–4), pp. 135–143. doi: 10.1016/j.enggeo.2010.04.010.

Richards, Lorenzo Adolph (1931) 'Capillary conduction of liquids through porous mediums', *Physics*. American Institute of Physics, 1(5), pp. 318–333.

Richards, L. A. (1931) 'Capillary conduction of liquids through porous mediums', *Physics*, 1(5), pp. 318–333. doi: 10.1063/1.1745010.

Roback, K., Clark, M. K., West, A. J., Zekkos, D., Li, G., Gallen, S. F., Chamlagain, D., and Godt, J. W. (2018) 'The size, distribution, and mobility of landslides caused by the 2015 Mw7.8 Gorkha earthquake, Nepal', *Geomorphology*, 301, pp. 121–138. doi: <https://doi.org/10.1016/j.geomorph.2017.01.030>.

Robinson, D. A., Campbell, C. S., Hopmans, J. W., Hornbuckle, B. K., Jones, S. B., Knight, R., Ogden, F., Selker, J., and Wendroth, O. (2008) 'Soil moisture measurement for ecological and hydrological watershed-scale observatories: a review', *Vadose Zone Journal*, 7(1), pp.

358–389. doi: 10.2136/vzj2007.0143.

Robson, E., Utili, S., Milledge, D., and Upadhaya, N. (2021) 'Road slope stabilisation in Nepal: stakeholder perspectives', in Cabrera, M. A., Prada-Sarmiento, L. F., and Monter, J. (eds) *13th International Symposium on Landslides*. Cartagena, Colombia.

Rocscience Inc. (2020) <https://www.roscience.com/software>.

Sandström, M. (2016) *Numerical Modelling and Sensitivity Analysis of Tunnel Deformations in London Clay*. KTH Royal Institute of Technology. Available at: <http://kth.diva-portal.org/smash/get/diva2:955792/FULLTEXT01.pdf>.

Schaap, M. G., and Leij, F. J. (2000) 'Improved prediction of unsaturated hydraulic conductivity with the Mualem-Van Genuchten model', *Soil Sci. Soc. Am. J.*, 64(1985), pp. 843–851.

Schofield, A., and Wroth, P. (1968) *Critical state soil mechanics*. Cambridge, UK: McGraw-Hill, Inc.

Schuster, R. L., and Krizek, R. (1978) *Landslides analysis and control. Special Report 176*. Edited by R. L. Schuster and R. Krizek. Washington D.C.: National Academy of Sciences.

Seki, K. (2007) 'SWRC fit - a nonlinear fitting program with a water retention curve for soils having unimodal and bimodal pore structure', *Hydrology and Earth System Sciences Discussions*, 4(1), pp. 407–437. doi: 10.5194/hessd-4-407-2007.

Sharma, S., and Maskay, M. L. (1999) *Community participation and environmental protection in the construction of mountain roads: promotion of the "Green Road" approach in Nepal*, *Transport and Communications Bulletin for Asia and the Pacific*. United Nations.

Shrestha, M. L. (2000) 'Interannual variation of summer monsoon rainfall over Nepal and its relation to Southern Oscillation Index', *Meteorology and Atmospheric Physics*, 75(1–2), pp. 21–28. doi: 10.1007/s007030070012.

Side, R. C. (1992) 'A theoretical model of the effects of timber harvesting on slope stability', *Water Resources Research*, 28(7), pp. 1897–1910. doi: 10.1029/92WR00804.

Side, R. C., Ziegler, A. D., Negishi, J. N., Nik, A. R., Siew, R., and Turkelboom, F. (2006) 'Erosion processes in steep terrain - Truths, myths, and uncertainties related to forest management in Southeast Asia', *Forest Ecology and Management*, 224(1–2), pp. 199–225. doi: 10.1016/j.foreco.2005.12.019.

Sidle, R. C., Ghestem, M., and Stokes, A. (2014) 'Epic landslide erosion from mountain roads in Yunnan, China-challenges for sustainable development', *Natural Hazards and Earth System Sciences*, 14(11), pp. 3093–3104. doi: 10.5194/nhess-14-3093-2014.

Sidle, R. C., and Ochiai, H. (2006) *Landslides: Processes, prediction, and land use*. Washington DC: American Geophysical Union (Water Resources Monograph). doi: 10.1029/WM018.

Sidle, R. C., and Ziegler, A. D. (2012) 'The dilemma of mountain roads', *Nature Geoscience*, 5(7), pp. 437–438. doi: 10.1038/ngeo1512.

Šimůnek, J., Huang, K., Šejna, M., and van Genuchten, M. T. (1998) 'The Hydrus-1D software package for simulating the one-dimensional movement of water, heat, and multiple solutes in variably-saturated media. Version 1.0, IGWMC - TPS - 70', *International Ground Water Modeling Center, Colorado School of Mines, Golden, Colorado*.

Sivrikaya, O., and Toğrol, E. (2006) 'Determination of undrained strength of fine-grained soils by means of SPT and its application in Turkey', *Engineering Geology*, 86(1), pp. 52–69. doi: 10.1016/j.enggeo.2006.05.002.

Skempton, A. W. (1986) 'Standard penetration test procedures and the effects in sands of overburden pressure, relative density, particle size, ageing and overconsolidation', *Geotechnique*. Thomas Telford Ltd, 36(3), pp. 425–447.

Smith, B. J. B., Godt, J. W., Baum, R. L., Coe, J. A., Burns, W. J., Lu, N., Morse, M. M., and Jewell, S. (2013) 'Hydrologic monitoring of a landslide-prone hillslope in the Elliott state forest, Southern coast range, Oregon, 2009 – 2012', *U.S. Geological Survey Open-file Report 2013-1283*, pp. 1–66.

SoilVision (2020) <https://www.bentley.com/en/products/product-line/geotechnical-engineering-software/svflux>.

Song, X., and Borja, R. I. (2014) 'Mathematical framework for unsaturated flow in the finite deformation range', *International Journal for Numerical Methods in Engineering*, 97(9), pp. 658–682. doi: 10.1002/nme.4605.

Song, Y. S., Chae, B. G., and Lee, J. (2016) 'A method for evaluating the stability of an unsaturated slope in natural terrain during rainfall', *Engineering Geology*. Elsevier B.V., 210, pp. 84–92. doi: 10.1016/j.enggeo.2016.06.007.

Springman, S. M., Jommi, C., and Teyssere, P. (2003) 'Instabilities on moraine slopes

induced by loss of suction: A case history', *Geotechnique*, 53(1), pp. 3–10. doi: 10.1680/geot.2003.53.1.3.

Di Stefano, C., Ferro, V., and Mirabile, S. (2010) 'Comparison between grain-size analyses using laser diffraction and sedimentation methods', *Biosystems Engineering*. IAgRE, 106(2), pp. 205–215. doi: 10.1016/j.biosystemseng.2010.03.013.

Sudmeier-rieux, K., Mcadoo, B. G., Devkota, S., Chandra, P., Rajbhandari, L., and Howell, J. (2019) 'Invited perspectives : Mountain roads in Nepal at a new crossroads', pp. 655–660.

Sudmeier-Rieux, K., McAdoo, B. G., Devkota, S., and Lal Chandra Rajbhandari, P. (2018) 'Brief Communication: Vehicles for development or disaster? The new Silk Route, landslides and geopolitics in Nepal', *Natural Hazards and Earth System Sciences Discussions*, 2018, pp. 1–7. doi: 10.5194/nhess-2017-462.

Sun, H. W., Wong, H. N., and Ho, K. K. S. (1998) 'Analysis of infiltration in unsaturated ground', in *Proceedings of the annual seminar on slope engineering in Hong Kong*, pp. 101–109.

Switała, B. M., and Wu, W. (2018) 'Numerical modelling of rainfall-induced instability of vegetated slopes', *Geotechnique*, 68(6), pp. 481–491. doi: 10.1680/jgeot.16.P.176.

Tami, D., Rahardjo, H., and Leong, E. C. (2004) 'Effect of hysteresis on steady-state infiltration in unsaturated slopes', *Journal of Geotechnical and Geoenvironmental Engineering*, 130(9), pp. 956–967. doi: 10.1061/(asce)1090-0241(2004)130:9(956).

Tang, A. M., Hughes, P. N., Dijkstra, T. A., Askarinejad, A., Brenčič, M., Cui, Y. J., Diez, J. J., Firgi, T., Gajewska, B., Gentile, F., Grossi, G., Jommi, C., Kehagia, F., Koda, E., ter Maat, H. W., Lenart, S., Lourenco, S., Oliveira, M., Osinski, P. *et al.* (2018) 'Atmosphere–vegetation–soil interactions in a climate change context; impact of changing conditions on engineered transport infrastructure slopes in Europe', *Quarterly Journal of Engineering Geology and Hydrogeology*, 51(2), pp. 156–168. doi: 10.1144/qjegh2017-103.

Tanoli, J. I., Ningsheng, C., Regmi, A. D., and Jun, L. (2017) 'Spatial distribution analysis and susceptibility mapping of landslides triggered before and after Mw7.8 Gorkha earthquake along Upper Bhote Koshi, Nepal', *Arabian Journal of Geosciences*, 10(13), p. 277. doi: 10.1007/s12517-017-3026-9.

Taylor, D. W. (1948) 'Fundamentals of soil mechanics'.

Terzaghi, K., Peck, R. B., and Mesri, G. (1996) *Soil mechanics in engineering practice*. 3rd

edn. USA: John Wiley & Sons, Inc.

Terzaghi, K. von (1936) 'The shearing resistance of saturated soils and the angle between the planes of shear', in Casgrande, A., Rutledge, P. C., and Watson, J. D. (eds) *International Conference on Soil Mechanics and Foundation Engineering*. Harvard University Press, pp. 54–56. Available at: [https://www.issmge.org/uploads/publications/1/44/1936\\_01\\_0017.pdf](https://www.issmge.org/uploads/publications/1/44/1936_01_0017.pdf).

Thapa, P. B. (2015) 'Occurrence of landslides in Nepal and their mitigation options', *Nepal Geological Society*, 49, pp. 17–28.

Tian, Y., Owen, L. A., Xu, C., Ma, S., Li, K., Xu, X., Figueiredo, P. M., Kang, W., Guo, P., Wang, S., Liang, X., and Maharjan, S. B. (2020) 'Landslide development within 3 years after the 2015 Mw 7.8 Gorkha earthquake, Nepal', *Landslides*. *Landslides*, 17(5), pp. 1251–1267. doi: 10.1007/s10346-020-01366-x.

Tohari, A. (2018) 'Study of rainfall-induced landslide : a review', in *IOP Conference Series: Earth and Environmental Science*. IOP Conference Series: Earth and Environmental Science, p. 118.

Toll, D. (2001) 'Rainfall-induced landslides in Singapore', *Ground Engineering*, 39(4), pp. 35–36.

Toll, D. (2006) 'Landslides in Singapore', *Ground Engineering*, 39(4), pp. 35–36.

Toll, D., Asquith, J., Fraser, A., Hassan, A., Liu, G., Lourenço, S., Mendes, J., Noguchi, T., Osinski, P., and Stirling, R. (2015) 'Tensiometer techniques for determining soil water retention curves', in *Unsaturated Soil Mechanics - from Theory to Practice*. CRC Press, pp. 15–22. doi: 10.1201/b19248-4.

Toll, D. G., Lourenço, S. D. N., Mendes, J., Gallipoli, D., Evans, F. D., Augarde, C. E., Cui, Y. J., Tang, A. M., Rojas, J. C., Pagano, L., Mancuso, C., Zingariello, C., and Tarantino, A. (2011) 'Soil suction monitoring for landslides and slopes', *Quarterly Journal of Engineering Geology and Hydrogeology*, 44(1), pp. 23–33. doi: 10.1144/1470-9236/09-010.

Toll, D. G. (2012) 'The behaviour of unsaturated soil', in Huat, B. B. K., Toll, David G., and Prasad, A. (eds) *Handbook of Tropical Residual Soils Engineering*. 1st edn. CRC Press, pp. 117–143.

Toll, D. G., Rahim, M. S., Karthikeyan, M., and Tsaparas, I. (2014) 'Soil atmosphere interactions for analysing slopes in tropical soils', *The 14th International conference of the*



*International Association of Computer Methods and Advances in Geomechanics*, (May), pp. 1333–1338.

Toll, D. G., Md. Rahim, M. S., Karthikeyan, M., and Tsaparas, I. (2019) 'Soil-atmosphere interactions for analysing slopes in tropical soils in Singapore', *Environmental Geotechnics*, 6(6), pp. 361–372. doi: 10.1680/jenge.15.00071.

Toll, D. G. (2020) 'Stress components in unsaturated soils', *Geotechnical Engineering*, 51(3), pp. 19–24.

Toll, D. G., Lourenço, S. D. N., and Mendes, J. (2013) 'Advances in suction measurements using high suction tensiometers', *Engineering Geology*. Elsevier B.V., 165, pp. 29–37. doi: 10.1016/j.enggeo.2012.04.013.

Topp, G. C. (2003) 'State of the art of measuring soil water content', *Hydrological Processes*, 17(14), pp. 2993–2996. doi: 10.1002/hyp.5148.

TRL (1997) *Overseas road note 16: Principles of low cost road engineering in mountainous regions*. Berkshire, UK.

Tsaparas, I., Rahardjo, H., Toll, D. ., and Leong, E. . (2002) 'Controlling parameters for rainfall-induced landslides', *Computers and Geotechnics*, 29(1), pp. 1–27. doi: 10.1016/S0266-352X(01)00019-2.

Tsaparas, I. (2002) *Field measurements and numerical modelling of infiltration and matric suctions within slopes*, PhD Thesis. Durham University. Available at: <http://etheses.dur.ac.uk/1715/>.

Tsaparas, I., Rahardjo, H., Toll, D. G., and Leong, E. C. (2003) 'Infiltration characteristics of two instrumented residual soil slopes', *Canadian Geotechnical Journal*, 40(5), pp. 1012–1032. doi: 10.1139/t03-049.

Tu, X. B., Kwong, A. K. L., Dai, F. C., Tham, L. G., and Min, H. (2009) 'Field monitoring of rainfall infiltration in a loess slope and analysis of failure mechanism of rainfall-induced landslides', *Engineering Geology*. Elsevier B.V., 105(1–2), pp. 134–150. doi: 10.1016/j.enggeo.2008.11.011.

Tuller, M., and Or, D. (2004) 'Water Retention and Characteristic Curve', *Encyclopedia of Soils in the Environment*, 4(April), pp. 278–289. doi: 10.1016/B0-12-348530-4/00376-3.

Turner, A. K., and Schuster, R. L. (1996) *Landslides - Investigation and mitigation. Special Report 247*. Edited by A. K. Turner and R. L. Schuster.

UNDP (2011) *Economic analysis of local government investment in rural roads in Nepal 2011*. Lalitpur, Nepal: Ministry of Local Development; Local Governance and Community Development Programme (LGCDP); United Nations Development Programme (UNDP). Available at: <https://un.info.np/Net/NeoDocs/View/6385> (Accessed: 16 May 2018).

Upreti, B. N. (2001) 'The physiography and geology of Nepal and their bearing on the landslide problem', *Landslide Hazard Mitigation in the Hindu Kush-Himalayas*, pp. 31–50.

Upreti, B. N., and Dhital, M. R. (1996) *Landslide studies and management in Nepal*. Kathmandu, Nepal: International Centre for Integrated Mountain Development (ICIMOD).

Uzielli, M., Lacasse, S., Nadim, F., and Phoon, K. (2006) 'Soil variability analysis for geotechnical practice', *Characterisation and Engineering Properties of Natural Soils*, (December). doi: 10.1201/noe0415426916.ch3.

Vanapalli, S. K., Fredlund, D. G., Pufahl, D. E., and Clifton, A. W. (1996) 'Model for the prediction of shear strength with respect to soil suction', *Canadian Geotechnical Journal*, 33(3), pp. 379–392. doi: 10.1139/t96-060.

Vanapalli, S. K., Salinas, L. M., Avila, D., and Karube, D. (2002) 'Suction and storage characteristics of unsaturated soils', in *3rd International Conference of Unsaturated Soils*, pp. 1045–1070.

Vanapalli, S. K., Fredlund, D. G., and Pufahl, D. E. (1999) 'The influence of soil structure and stress history on the soil-water characteristics of a compacted till', *Geotechnique*, 49(2), pp. 143–159. doi: 10.1680/geot.1999.49.2.143.

Varnes, D. J. (1958) 'Landslide types and processes', in Eckel, E. B. (ed.) *Landslides and Engineering Practice*. Washington, D.C.: National Research Council, pp. 20–47.

Varnes, D. J. (1978) 'Slope movement types and processes', in Schuster, R. L. and Krizek, R. J. (eds) *Landslides Analysis and Control, Special Report 176*. Washington, D.C.: National Academy of Sciences, p. 234.

Vaz, C. M. ., Jones, S. B., Meding, S., and Tuller, M. (2013) 'Evaluation of Standard Calibration Functions for Eight Electromagnetic Soil Moisture Sensors', *Vadose Zone*. doi: <https://doi.org/10.2136/vzj2012.0160>.

Vuillez, C., Tonini, M., Sudmeier-Rieux, K., Devkota, S., Derron, M. H., and Jaboyedoff, M. (2018) 'Land use changes, landslides and roads in the Phewa Watershed, Western Nepal from 1979 to 2016', *Applied Geography*, 94(March 2017), pp. 30–40. doi:

10.1016/j.apgeog.2018.03.003.

Walker, L. R., and Shiels, A. B. (2013) 'Living with landslides for Landslide Ecology', in *Landslide Ecology*. New York: Cambridge University Press, pp. 181–226. Available at: [https://digitalcommons.unl.edu/icwdm\\_usdanwrc/1637/?utm\\_source=digitalcommons.unl.edu%2Ficwdm\\_usdanwrc%2F1637&utm\\_medium=PDF&utm\\_campaign=PDFCoverPages](https://digitalcommons.unl.edu/icwdm_usdanwrc/1637/?utm_source=digitalcommons.unl.edu%2Ficwdm_usdanwrc%2F1637&utm_medium=PDF&utm_campaign=PDFCoverPages).

Wilkinson, P. L., Anderson, M. G., Lloyd, D. M., and Renaud, J. P. (2002) 'Landslide hazard and bioengineering: Towards providing improved decision support through integrated numerical model development', *Environmental Modelling and Software*, 17(4), pp. 333–344. doi: 10.1016/S1364-8152(01)00078-0.

World Bank (2012) *Nepal road sector assessment study: Annexes*. Available at: [http://rapnepal.com/sites/default/files/report-publication/road\\_sector\\_assessment\\_study\\_-\\_annexes\\_final\\_31\\_may\\_13.pdf](http://rapnepal.com/sites/default/files/report-publication/road_sector_assessment_study_-_annexes_final_31_may_13.pdf).

World Bank (2016) *Strengthening connectivity in Nepal*. World Bank. Available at: <http://www.worldbank.org/en/news/feature/2016/02/17/strengthening-rural-connectivity-in-nepal.print>.

Wu, T. H. (1984) 'Effect of vegetation on slope stability', *Transportation Research Record*, pp. 37–46. doi: 10.1016/0148-9062(85)92272-7.

Wu, W., Switala, B. M., Acharya, M. S., Tamagnini, R., Auer, M., Graf, F., te Kamp, L., and Xiang, W. (2015) 'Effect of vegetation on stability of soil slopes: Numerical aspect', in *Geomechanics and Geoengineering*, pp. 163–177. doi: 10.1007/978-3-319-11053-0\_15.

Xue, K., Ajmera, B., Tiwari, B., and Hu, Y. (2016) 'Effect of long duration rainstorm on stability of Red-clay slopes', *Geoenvironmental Disasters*. Geoenvironmental Disasters, (February 1986). doi: 10.1186/s40677-016-0046-9.

Yang, C., Sheng, D., and Carter, J. P. (2012) 'Effect of hydraulic hysteresis on seepage analysis for unsaturated soils', *Computers and Geotechnics*. Elsevier Ltd, 41, pp. 36–56. doi: 10.1016/j.compgeo.2011.11.006.

Yang, K.-H., Uzuoka, R., Thuo, J. N., Lin, G.-L., and Nakai, Y. (2017) 'Coupled hydro-mechanical analysis of two unstable unsaturated slopes subject to rainfall infiltration', *Engineering Geology*. Elsevier B.V., 216, pp. 13–30. doi: 10.1016/j.enggeo.2016.11.006.

Yang, K. H., Thuo, J. N., Chen, J. W., and Liu, C. N. (2019) 'Failure investigation of a

geosynthetic-reinforced soil slope subjected to rainfall', *Geosynthetics International*, 26(1), pp. 42–65. doi: 10.1680/jgein.18.00035.

Yang, K. H., Nguyen, T. S., Rahardjo, H., and Lin, D. G. (2020) 'Deformation characteristics of unstable shallow slopes triggered by rainfall infiltration', *Bulletin of Engineering Geology and the Environment*. *Bulletin of Engineering Geology and the Environment*. doi: 10.1007/s10064-020-01942-4.

Yoo, C., and Jung, H.-Y. (2006) 'Case history of geosynthetic reinforced segmental retaining wall failure', *Journal of Geotechnical and Geoenvironmental Engineering*, 132(12), pp. 1538–1548. doi: 10.1061/(ASCE)1090-0241(2006)132:12(1538).

Yubonchit, S., Chinkulkijniwat, A., Horpibulsuk, S., Jothityangkoon, C., Arulrajah, A., and Suddeepong, A. (2017) 'Influence factors involving rainfall-induced shallow slope failure: Numerical study', *International Journal of Geomechanics*, 17(7), p. 04016158. doi: 10.1061/(ASCE)GM.1943-5622.0000865.

Zhang, L., Li, J., Li, X., Zhang, J., and Zhu, H. (2018) *Rainfall-induced soil slope failure, Rainfall-Induced Soil Slope Failure*. CRC Press Taylor & Francis Group. doi: 10.1201/b20116.

Zhang, L. L., Zhang, J., Zhang, L. M., and Tang, W. H. (2011) 'Stability analysis of rainfall-induced slope failure: a review', *Proceedings of the Institution of Civil Engineers - Geotechnical Engineering*, 164(5), pp. 299–316. doi: 10.1680/geng.2011.164.5.299.

Zhang, L. L., Zhang, L. M., and Tang, W. H. (2005) 'Rainfall-induced slope failure considering variability of soil properties', *Geotechnique*, 55(2), pp. 183–188.

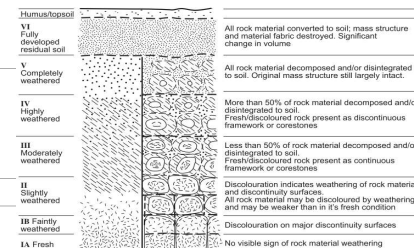
Zhang, Y., Zhou, A., Nazem, M., and Carter, J. (2019) 'Finite element implementation of a fully coupled hydro-mechanical model and unsaturated soil analysis under hydraulic and mechanical loads', *Computers and Geotechnics*. Elsevier, 110(February), pp. 222–241. doi: 10.1016/j.compgeo.2019.02.005.

# Appendix A-1

---

Landslide information sheet

## LANDSLIDE INFORMATION SHEET

Landslide ID:	GPS Waypoint No.:	Date of Recording:												
<b>LOCATION</b>														
	<b>Latitude</b>	<b>Longitude</b>												
<b>Start</b>	N	S												
<b>Mid</b>	N	S												
<b>End</b>	N	S												
<b>Aspect</b>														
<b>LANDSLIDE DETAILS</b>														
<b>Type of movement</b>	<input type="checkbox"/> Fall <input type="checkbox"/> Flow <input type="checkbox"/> Slide <input type="checkbox"/> Spread <input type="checkbox"/> Topple <input type="checkbox"/> Gully <input type="checkbox"/> Complex													
<b>Sub-type of Slides</b>	<input type="checkbox"/> Rotational <input type="checkbox"/> Translational <input type="checkbox"/> Complex <input type="checkbox"/> Unknown													
<b>Geometry of landslide</b>	Length (perpendicular to the road): Width (parallel to the road):													
<b>Depth</b>	<input type="checkbox"/> Surficial (<1.5m) <input type="checkbox"/> Shallow (1.5-5m) <input type="checkbox"/> Deep (5-20m) <input type="checkbox"/> Very deep (>20m)													
<b>Hillslope Angle (°)</b>	*will be obtained from topographical map													
<b>Road Induced Landslide?</b>	<input type="checkbox"/> Yes <input type="checkbox"/> No <input type="checkbox"/> Not sure													
<b>Triggering Factor</b>	<input type="checkbox"/> Rain <input type="checkbox"/> Earthquake <input type="checkbox"/> Human-induced, Specify:													
<b>New Failure?</b>	<input type="checkbox"/> Yes <input type="checkbox"/> No													
<b>Re-activated?</b>	<input type="checkbox"/> Yes <input type="checkbox"/> No													
<b>Age</b>	<input type="checkbox"/> This year <input type="checkbox"/> <2 years <input type="checkbox"/> 2 to 5 years <input type="checkbox"/> >5 years <input type="checkbox"/> Unknown													
<b>Signs of Movement</b>	<input type="checkbox"/> Tension cracks <input type="checkbox"/> Upheaval/Depression <input type="checkbox"/> Dislocation of slope protection/drainage <input type="checkbox"/> Disturbed vegetation <input type="checkbox"/> None <input type="checkbox"/> Others, Specify													
<b>Activity State</b>	<input type="checkbox"/> Stable <input type="checkbox"/> Dormant <input type="checkbox"/> Active													
<b>GEOLOGY</b>														
<b>Material Involved</b>	<input type="checkbox"/> Rock <input type="checkbox"/> Insitu weathered soil <input type="checkbox"/> Colluvium <input type="checkbox"/> Talus <input type="checkbox"/> Taluvium <input type="checkbox"/> Others													
<b>Material Condition</b>	<input type="checkbox"/> Dry <input type="checkbox"/> Wet													
<b>Principal Soil Type</b>	<table style="width: 100%; border: none;"> <tr> <td style="text-align: center; width: 20%;">Coarse</td> <td style="width: 20%;"><input type="checkbox"/> Boulder (&gt;200mm)</td> <td style="width: 20%;"><input type="checkbox"/> Cobble (200-63mm)</td> </tr> <tr> <td></td> <td><input type="checkbox"/> Gravel (63-2mm)</td> <td><input type="checkbox"/> Sand (2 to 0.063mm)</td> </tr> <tr> <td style="text-align: center;">Fine</td> <td><input type="checkbox"/> Silt (0.063-0.002mm)</td> <td><input type="checkbox"/> Clay (&lt;0.002mm)</td> </tr> <tr> <td></td> <td><input type="checkbox"/> Peat</td> <td></td> </tr> </table>		Coarse	<input type="checkbox"/> Boulder (>200mm)	<input type="checkbox"/> Cobble (200-63mm)		<input type="checkbox"/> Gravel (63-2mm)	<input type="checkbox"/> Sand (2 to 0.063mm)	Fine	<input type="checkbox"/> Silt (0.063-0.002mm)	<input type="checkbox"/> Clay (<0.002mm)		<input type="checkbox"/> Peat	
Coarse	<input type="checkbox"/> Boulder (>200mm)	<input type="checkbox"/> Cobble (200-63mm)												
	<input type="checkbox"/> Gravel (63-2mm)	<input type="checkbox"/> Sand (2 to 0.063mm)												
Fine	<input type="checkbox"/> Silt (0.063-0.002mm)	<input type="checkbox"/> Clay (<0.002mm)												
	<input type="checkbox"/> Peat													
<b>Principal Rock Type</b>	<input type="checkbox"/> Siltstone <input type="checkbox"/> Sandstone <input type="checkbox"/> Clay stone <input type="checkbox"/> Limestone <input type="checkbox"/> Slate <input type="checkbox"/> Phyllite <input type="checkbox"/> Schist <input type="checkbox"/> Gneiss <input type="checkbox"/> Quartzite <input type="checkbox"/> Dolomite <input type="checkbox"/> Granite <input type="checkbox"/> Others													
<b>Nature of Exposed Rock</b>	<input type="checkbox"/> Intact <input type="checkbox"/> Fractured <input type="checkbox"/> Weathered													
<b>Weathering Grade</b>	<input type="checkbox"/> VI <input type="checkbox"/> V <input type="checkbox"/> IV <input type="checkbox"/> III <input type="checkbox"/> II <input type="checkbox"/> I													
														
<b>IMPACT ON THE ROAD</b>														
<b>Road construction date:</b>	<b>Date of Widening:</b>													
<b>Road type</b>	<input type="checkbox"/> Full cut <input type="checkbox"/> Full fill <input type="checkbox"/> Cut-and-fill													
<b>Road construction method</b>	<input type="checkbox"/> EB <input type="checkbox"/> LB <input type="checkbox"/> Mixed													
<b>Road alignment location</b>	<input type="checkbox"/> Close to ridge crest <input type="checkbox"/> Middle slope <input type="checkbox"/> Foot of slope													
<b>Road Surface Type</b>	<input type="checkbox"/> Earthen <input type="checkbox"/> Gravel <input type="checkbox"/> Black-top													
<b>Roadcut height (m)</b>														
<b>Upslope/cutslope angle (°)</b>														
<b>Downslope angle (°)</b>														
<b>Roadside affected</b>	<input type="checkbox"/> Cutslope <input type="checkbox"/> Fillslope													
<b>Road condition</b>	<input type="checkbox"/> Drivable <input type="checkbox"/> Non-drivable													
<b>Impact on the road</b>	<input type="checkbox"/> Road partially blocked <input type="checkbox"/> Road totally blocked <input type="checkbox"/> Road in danger of blockage <input type="checkbox"/> Road in danger of failure <input type="checkbox"/> Road partly failed <input type="checkbox"/> Road completely failed <b>Reason:</b> <input type="checkbox"/> Landslide <input type="checkbox"/> Bad road surfacing													



## Appendix A-2

---

Rainfall events between 27 March 2019 and 28 March 2020



Event No.	Date (dd/mm/yy) Time (hh:mm)		Total rainfall (mm)	Average rainfall intensity (mm/hr)	Rainfall duration (hr)	Peak hourly rainfall intensity (mm/hr)	Minimum hourly rainfall intensity (mm/hr)
	Start	End					
1	31/03/19 18:00	31/03/19 20:00	11.2	3.7	3	6.6	0.4
2	06/04/19 07:00	06/04/19 10:00	6.4	1.6	4	3.6	0.2
3	07/04/19 00:00	07/04/19 06:00	11.6	1.7	7	5.4	0.2
4	09/04/19 00:00	09/04/19 03:00	12	3.0	4	6.4	0.2
5	13/04/19 05:00	13/04/19 06:00	4	2.0	2	3.8	0.2
6	14/04/19 17:00	14/04/19 20:00	3.8	1.0	4	3	0.2
7	16/04/19 15:00	16/04/19 17:00	11.6	3.9	3	7.8	0.2
8	16/04/19 19:00	16/04/19 23:00	16.2	3.2	5	5.2	0.6
9	17/04/19 15:00	17/04/19 17:00	15.8	5.3	3	8.2	2.4
10	19/04/19 14:00	19/04/19 18:00	9.4	1.9	5	4.2	0.4
11	25/04/19 14:00	25/04/19 17:00	15.8	4.0	4	12	0.6
12	29/04/19 13:00	29/04/19 15:00	4.6	1.5	3	2.6	0.4
13	03/05/19 13:00	03/05/19 15:00	3.6	1.2	3	3.2	0.2
14	11/05/19 20:00	11/05/19 21:00	2	1.0	2	1.4	0.6
15	12/05/19 16:00	12/05/19 17:00	4.4	2.2	2	3	1.4
16	14/05/19 15:00	14/05/19 15:00	5.2	5.2	1	5.2	5.2
17	15/05/19 13:00	15/05/19 15:00	22.6	7.5	3	16.8	2.8
18	19/05/19 19:00	19/05/19 23:00	16.6	3.3	5	7.4	0.6
19	20/05/19 13:00	20/05/19 15:00	13.6	4.5	3	10.8	0.6
20	21/05/19 12:00	21/05/19 14:00	24.8	8.3	3	15.2	1.6
21	21/05/19 20:00	21/05/19 20:00	4.2	4.2	1	4.2	4.2
22	24/05/19 19:00	24/05/19 20:00	3.2	1.6	2	3	0.2
23	25/05/19 21:00	25/05/19 21:00	6.4	6.4	1	6.4	6.4
24	28/05/19 13:00	28/05/19 15:00	13.4	4.5	3	9	0.8
25	29/05/19 16:00	29/05/19 18:00	2.2	0.7	3	1.4	0.2
26	30/05/19 17:00	30/05/19 18:00	3	1.5	2	2.8	0.2
27	01/06/19 16:00	01/06/19 17:00	10.4	5.2	2	9.4	1

Event No.	Date (dd/mm/yy) Time (hh:mm)		Total rainfall (mm)	Average rainfall intensity (mm/hr)	Rainfall duration (hr)	Peak hourly rainfall intensity (mm/hr)	Minimum hourly rainfall intensity (mm/hr)
	Start	End					
28	03/06/19 15:00	03/06/19 16:00	5.4	2.7	2	4.6	0.8
29	05/06/19 17:00	05/06/19 21:00	12	2.4	5	8.8	0.2
30	05/06/19 23:00	06/06/19 01:00	2.6	0.9	3	1.8	0.2
31	06/06/19 05:00	06/06/19 07:00	2.2	0.7	3	1.6	0.2
32	07/06/19 00:00	07/06/19 01:00	4.4	2.2	2	3.8	0.6
33	07/06/19 03:00	07/06/19 04:00	4.4	2.2	2	3.4	1
34	07/06/19 06:00	07/06/19 07:00	6.8	3.4	2	5.6	1.2
35	09/06/19 17:00	09/06/19 18:00	13.8	6.9	2	13.2	0.6
36	10/06/19 15:00	10/06/19 16:00	7	3.5	2	6.4	0.6
37	12/06/19 02:00	12/06/19 03:00	3.8	1.9	2	3.6	0.2
38	16/06/19 01:00	16/06/19 02:00	13	6.5	2	9.6	3.4
39	17/06/19 14:00	17/06/19 19:00	29.6	4.9	6	13.2	0.2
40	18/06/19 00:00	18/06/19 02:00	5.4	1.8	3	4.2	0.2
41	19/06/19 14:00	19/06/19 15:00	3.8	1.9	2	2.6	1.2
42	21/06/19 18:00	22/06/19 00:00	50.8	7.3	7	16.4	0.4
43	22/06/19 14:00	22/06/19 21:00	6.8	0.9	8	2.4	0.2
44	24/06/19 22:00	25/06/19 01:00	30.2	7.6	4	14.4	1.6
45	26/06/19 02:00	26/06/19 03:00	26.6	13.3	2	16.2	10.4
46	26/06/19 13:00	26/06/19 14:00	23.6	11.8	2	23.4	0.2
47	28/06/19 02:00	28/06/19 06:00	42.8	8.6	5	20.2	0.2
48	29/06/19 01:00	29/06/19 02:00	4	2.0	2	2	2
49	29/06/19 23:00	30/06/19 03:00	4	0.8	5	1.4	0.2
50	02/07/19 20:00	03/07/19 01:00	8	1.3	6	3.8	0.2
51	03/07/19 21:00	04/07/19 01:00	7.2	1.4	5	3.4	0.6
52	04/07/19 16:00	04/07/19 18:00	17.6	5.9	3	7.6	4.2
53	05/07/19 21:00	06/07/19 02:00	31.2	5.2	6	8.2	1.4
54	06/07/19 19:00	07/07/19 00:00	20.6	3.4	6	6	0.4

Event No.	Date (dd/mm/yy) Time (hh:mm)		Total rainfall (mm)	Average rainfall intensity (mm/hr)	Rainfall duration (hr)	Peak hourly rainfall intensity (mm/hr)	Minimum hourly rainfall intensity (mm/hr)
	Start	End					
55	08/07/19 12:00	08/07/19 14:00	4.2	1.4	3	2.2	0.2
56	08/07/19 16:00	08/07/19 20:00	40.8	8.2	5	28	0.4
57	08/07/19 23:00	09/07/19 03:00	2.2	0.4	5	0.6	0.2
58	09/07/19 16:00	09/07/19 18:00	6.2	2.1	3	3	1.4
59	09/07/19 22:00	10/07/19 02:00	6.8	1.4	5	3	0.4
60	10/07/19 10:00	10/07/19 14:00	18	3.6	5	11.8	0.6
61	11/07/19 12:00	11/07/19 12:00	3.2	3.2	1	3.2	3.2
62	11/07/19 21:00	11/07/19 23:00	2.4	0.8	3	1.4	0.4
63	12/07/19 04:00	12/07/19 22:00	52.8	2.8	19	10.2	0.2
64	13/07/19 00:00	13/07/19 05:00	5	0.8	6	1.8	0.2
65	13/07/19 23:00	14/07/19 03:00	5.8	1.2	5	1.6	0.8
66	14/07/19 17:00	14/07/19 18:00	4.4	2.2	2	2.8	1.6
67	14/07/19 20:00	14/07/19 22:00	4	1.3	3	3.4	0.2
68	15/07/19 03:00	15/07/19 09:00	19.6	2.8	7	5.8	0.4
69	16/07/19 06:00	16/07/19 08:00	7	2.3	3	5.2	0.6
70	17/07/19 21:00	18/07/19 00:00	5	1.3	4	3.2	0.4
71	18/07/19 03:00	18/07/19 07:00	3	0.6	5	1	0.2
72	19/07/19 01:00	19/07/19 03:00	9.4	3.1	3	3.6	2.6
73	19/07/19 05:00	19/07/19 08:00	4	1.0	4	3	0.2
74	19/07/19 15:00	19/07/19 16:00	14.6	7.3	2	13.6	1
75	20/07/19 02:00	20/07/19 06:00	12.8	2.6	5	4.4	0.2
76	20/07/19 08:00	20/07/19 10:00	4	1.3	3	3	0.2
77	20/07/19 19:00	21/07/19 00:00	18	3.0	6	8.4	0.4
78	22/07/19 09:00	22/07/19 11:00	2.2	0.7	3	1.4	0.2
79	23/07/19 14:00	23/07/19 15:00	2.2	1.1	2	1.6	0.6
80	23/07/19 20:00	23/07/19 23:00	3.4	0.9	4	1.8	0.2
81	24/07/19 11:00	24/07/19 17:00	15.4	2.2	7	5.4	0.2

Event No.	Date (dd/mm/yy) Time (hh:mm)		Total rainfall (mm)	Average rainfall intensity (mm/hr)	Rainfall duration (hr)	Peak hourly rainfall intensity (mm/hr)	Minimum hourly rainfall intensity (mm/hr)
	Start	End					
82	25/07/19 15:00	25/07/19 16:00	3.6	1.8	2	3	0.6
83	26/07/19 10:00	26/07/19 15:00	7.4	1.2	6	3	0.2
84	26/07/19 17:00	26/07/19 19:00	8.8	2.9	3	8	0.2
85	27/07/19 00:00	27/07/19 01:00	20.6	10.3	2	16.2	4.4
86	27/07/19 17:00	28/07/19 01:00	27.6	3.1	9	6.6	0.2
87	28/07/19 19:00	29/07/19 01:00	63.4	9.1	7	26.2	0.2
88	29/07/19 17:00	29/07/19 20:00	19	4.8	4	10.2	1.2
89	29/07/19 22:00	30/07/19 07:00	42.2	4.2	10	14.8	0.2
90	31/07/19 21:00	01/08/19 03:00	61.6	8.8	7	18.6	0.4
91	01/08/19 20:00	02/08/19 02:00	25.2	3.6	7	5.4	1
92	03/08/19 00:00	03/08/19 02:00	2.6	0.9	3	1.2	0.6
93	03/08/19 16:00	04/08/19 04:00	36.8	2.8	13	11.2	0.2
94	04/08/19 23:00	05/08/19 05:00	48.4	6.9	7	19.4	0.2
95	05/08/19 19:00	06/08/19 03:00	36.2	4.0	9	14.8	0.4
96	06/08/19 22:00	07/08/19 01:00	29.4	7.4	4	22.4	1.2
97	07/08/19 22:00	08/08/19 00:00	4.6	1.5	3	2.2	1
98	08/08/19 15:00	08/08/19 22:00	10.6	1.3	8	3.2	0.4
99	09/08/19 00:00	09/08/19 05:00	26	4.3	6	11.6	0.2
100	09/08/19 12:00	09/08/19 16:00	11.8	2.4	5	4.4	0.2
101	09/08/19 23:00	10/08/19 03:00	21.2	4.2	5	11.4	0.2
102	10/08/19 14:00	10/08/19 16:00	4	1.3	3	2.4	0.8
103	11/08/19 00:00	11/08/19 06:00	16.4	2.3	7	8.8	0.2
104	12/08/19 19:00	13/08/19 01:00	19.4	2.8	7	6.4	0.4
105	13/08/19 19:00	13/08/19 21:00	2.6	0.9	3	1.6	0.2
106	14/08/19 15:00	14/08/19 23:00	24.8	2.8	9	5.8	0.2
107	15/08/19 04:00	15/08/19 06:00	2.8	0.9	3	2	0.4
108	15/08/19 11:00	15/08/19 16:00	5	0.8	6	2.4	0.2

Event No.	Date (dd/mm/yy) Time (hh:mm)		Total rainfall (mm)	Average rainfall intensity (mm/hr)	Rainfall duration (hr)	Peak hourly rainfall intensity (mm/hr)	Minimum hourly rainfall intensity (mm/hr)
	Start	End					
109	16/08/19 17:00	16/08/19 22:00	19.2	3.2	6	5.8	0.4
110	18/08/19 13:00	18/08/19 20:00	6.6	0.8	8	3.4	0.2
111	19/08/19 21:00	19/08/19 23:00	22	7.3	3	20.8	0.2
112	21/08/19 20:00	22/08/19 01:00	67	11.2	6	21.8	0.2
113	23/08/19 17:00	24/08/19 02:00	25.2	2.5	10	5.6	0.8
114	24/08/19 18:00	25/08/19 03:00	54	5.4	10	13.2	0.2
115	25/08/19 15:00	25/08/19 15:00	3	3.0	1	3	3
116	26/08/19 00:00	26/08/19 01:00	14	7.0	2	12.2	1.8
117	28/08/19 21:00	29/08/19 01:00	10.4	2.1	5	4.6	0.2
118	30/08/19 23:00	31/08/19 06:00	33.8	4.2	8	11.4	0.4
119	31/08/19 23:00	01/09/19 08:00	60.4	6.0	10	20.6	0.2
120	02/09/19 20:00	03/09/19 02:00	27.2	3.9	7	9.8	0.2
121	03/09/19 20:00	04/09/19 03:00	40	5.0	8	16.4	0.2
122	05/09/19 02:00	05/09/19 04:00	2.4	0.8	3	1.4	0.2
123	05/09/19 21:00	06/09/19 05:00	90.8	10.1	8	35.2	0.2
124	06/09/19 18:00	07/09/19 01:00	24.4	3.1	8	11.4	0.4
125	07/09/19 15:00	07/09/19 16:00	4.8	2.4	2	3.2	1.6
126	09/09/19 22:00	10/09/19 02:00	16.8	3.4	5	12.2	0.2
127	10/09/19 04:00	10/09/19 07:00	22.2	5.6	4	12.4	0.8
128	10/09/19 15:00	10/09/19 16:00	3.2	1.6	2	1.8	1.4
129	10/09/19 18:00	10/09/19 21:00	9.6	2.4	4	4.8	0.6
130	11/09/19 02:00	11/09/19 07:00	16.6	2.8	6	7.2	1
131	11/09/19 15:00	11/09/19 22:00	22	2.8	8	8.2	0.2
132	12/09/19 14:00	12/09/19 15:00	2.8	1.4	2	1.8	1
133	12/09/19 20:00	12/09/19 22:00	7.4	2.5	3	4	0.6
134	13/09/19 05:00	13/09/19 09:00	6.6	1.3	5	2.2	0.2
135	13/09/19 13:00	13/09/19 22:00	18.4	1.8	10	3	0.2

Event No.	Date (dd/mm/yy) Time (hh:mm)		Total rainfall (mm)	Average rainfall intensity (mm/hr)	Rainfall duration (hr)	Peak hourly rainfall intensity (mm/hr)	Minimum hourly rainfall intensity (mm/hr)
	Start	End					
136	14/09/19 13:00	14/09/19 14:00	2.4	1.2	2	2	0.4
137	14/09/19 16:00	14/09/19 19:00	6.6	1.7	4	5.6	0.2
138	15/09/19 14:00	15/09/19 19:00	2.2	0.4	6	0.8	0.2
139	15/09/19 22:00	16/09/19 01:00	12.6	3.2	4	10.8	0.4
140	16/09/19 13:00	16/09/19 16:00	6.8	1.7	4	4.4	0.2
141	16/09/19 18:00	16/09/19 20:00	2.6	0.9	3	1	0.8
142	16/09/19 23:00	17/09/19 03:00	17	3.4	5	8.4	0.6
143	17/09/19 09:00	17/09/19 20:00	15.2	1.3	12	6.8	0.2
144	17/09/19 23:00	18/09/19 16:00	22.4	1.2	18	2.6	0.2
145	21/09/19 17:00	21/09/19 20:00	26.8	6.7	4	19.8	0.4
146	23/09/19 00:00	23/09/19 03:00	3.2	0.8	4	2.2	0.2
147	23/09/19 21:00	24/09/19 04:00	33	4.1	8	11.4	0.2
148	24/09/19 23:00	25/09/19 02:00	2.2	0.6	4	0.8	0.2
149	25/09/19 16:00	26/09/19 00:00	10.8	1.2	9	4.8	0.2
150	26/09/19 16:00	26/09/19 18:00	2.8	0.9	3	1.4	0.2
151	26/09/19 21:00	27/09/19 00:00	15.8	4.0	4	6.4	2.6
152	27/09/19 12:00	27/09/19 22:00	16.8	1.5	11	4.4	0.2
153	28/09/19 11:00	28/09/19 16:00	2.8	0.5	6	0.8	0.2
154	30/09/19 19:00	30/09/19 23:00	29	5.8	5	14.6	1
155	01/10/19 18:00	01/10/19 20:00	2.4	0.8	3	1.6	0.4
156	02/10/19 22:00	03/10/19 02:00	8.8	1.8	5	5	0.4
157	07/10/19 22:00	08/10/19 00:00	3.4	1.1	3	2.6	0.2
158	08/10/19 14:00	08/10/19 14:00	2	2.0	1	2	2
159	08/10/19 19:00	08/10/19 23:00	15	3.0	5	4	1
160	13/12/19 09:00	13/12/19 17:00	15.2	1.7	9	3.6	0.2
161	13/12/19 23:00	14/12/19 04:00	18.6	3.1	6	6.2	0.6
162	03/01/20 13:00	03/01/20 18:00	4.4	0.7	6	2	0.2

Event No.	Date (dd/mm/yy) Time (hh:mm)		Total rainfall (mm)	Average rainfall intensity (mm/hr)	Rainfall duration (hr)	Peak hourly rainfall intensity (mm/hr)	Minimum hourly rainfall intensity (mm/hr)
	Start	End					
163	04/01/20 16:00	04/01/20 17:00	6.2	3.1	2	5.2	1
164	08/01/20 15:00	08/01/20 19:00	2	0.4	5	0.6	0.2
165	16/01/20 20:00	16/01/20 22:00	3	1.0	3	1.2	0.6
166	17/01/20 01:00	17/01/20 21:00	38.8	1.8	21	3.8	0.2
167	19/01/20 16:00	19/01/20 18:00	2.2	0.7	3	1.2	0.2
168	11/02/20 15:00	11/02/20 15:00	6	6.0	1	6	6
169	21/02/20 19:00	21/02/20 23:00	4	0.8	5	2.6	0.2
170	25/02/20 14:00	25/02/20 15:00	2.2	1.1	2	1.6	0.6
171	25/02/20 20:00	26/02/20 09:00	17.4	1.2	14	3.6	0.2
172	01/03/20 14:00	01/03/20 15:00	5.6	2.8	2	3.6	2
173	06/03/20 03:00	06/03/20 04:00	5.2	2.6	2	3	2.2
174	07/03/20 08:00	07/03/20 09:00	2	1.0	2	1.8	0.2
175	13/03/20 21:00	13/03/20 23:00	2.4	0.8	3	1.8	0.2
176	15/03/20 17:00	15/03/20 17:00	2.2	2.2	1	2.2	2.2
177	17/03/20 17:00	17/03/20 20:00	2.2	0.6	4	0.6	0.4
178	19/03/20 16:00	19/03/20 19:00	11.2	2.8	4	5.8	0.2
179	20/03/20 10:00	20/03/20 11:00	8.8	4.4	2	7.8	1
180	21/03/20 15:00	21/03/20 16:00	3.2	1.6	2	1.8	1.4
181	22/03/20 17:00	23/03/20 01:00	14.8	1.6	9	3.6	0.2
182	27/03/20 21:00	28/03/20 00:00	2	0.5	4	0.8	0.2

## Appendix A-3

---

Conference paper: Field monitoring of soil-moisture to understand the hydrological response of a road-cut slope



# Field monitoring of soil-moisture to understand the hydrological response of a road-cut slope

Samprada Pradhan<sup>1\*</sup>, David G. Toll<sup>1</sup>, Nick J. Rosser<sup>1</sup>, and Matthew J. Brain<sup>1</sup>

<sup>1</sup> Institute of Hazard, Risk and Resilience, Durham University, UK.

**Abstract.** Rainfall and slope-cutting for road construction are two key landslide causative factors in Nepal, but how they interact to cause failures is poorly understood. To improve understanding of the effects of cut slopes during rainfall, geotechnical investigations and field monitoring were conducted in a mountainous district, Sindhupalchowk, located in central Nepal. This paper presents the results of the field-investigations and the measurements of volumetric water content obtained from the sensors installed in the study-site. Field-based evidence suggests that the slope that was cut for road construction during the dry period remained stable due to the presence of soil suction, which imparted additional strength to the soil. At the start of the monsoon, infiltration of rainwater caused saturation of the soil at shallow depth, consequently causing loss of suction and reduction of the soil strength. The presence of the road-cut in the hillslope resulting in steeper slopes then promoted the failure. These observations suggest that the presence of road-cuts in the hillslopes can cause landslides even during non-exceptional rainfall events.

## 1 Background

Landslides in Nepal are commonly associated with high amounts of rainfall during the monsoon season between June and September, which constitutes more than 80% of the total annual rainfall [1]. In addition, the construction of local roads (low-volume district and village roads) in the mountainous terrain has increased the susceptibility to landslides during rainfall [1-3]. However, how the two key factors, rainfall and roads, interact to cause landsliding is poorly understood. As the local road network is continuing to expand in Nepal as road-building is one of the main developmental priorities of the government [4], it is important to improve the understanding of the behaviour of road-related landslides during rainfall from a geotechnical perspective to prevent and mitigate such hazards in the future

This study aims to understand the role of rainfall as well as the effect of slope-cutting for road construction in causing landslides within the study area. Field investigations were conducted along a local road, where 97 slope failures occurred during 2018 monsoon. A reconnaissance field survey was carried out so as to examine the nature of the failures. A geotechnical investigation was conducted into one of the shallow slope failures along this road in order to assess the plausible causes and mechanism of the failure. With the understanding that the slope failure may have been caused by infiltration of rainwater into the unsaturated

zone, Volumetric Water Content (VWC) measurement sensors and rain-gauge were installed in the field. By observing the changing relationship between rainfall and VWC, the conditions in the field that may have led to the slope failure in July 2018 were examined. In this paper, the findings from the field investigations and the measurements from the field-instruments will be presented.

## 2 Study area

The study area is a 13.7 km long local road from Daklang to Listi located in the Sindhupalchok district, which is approximately 105 km north-east from the capital city, Kathmandu (Fig. 1). This road connects the surrounding villages to the strategically important highway connecting Kathmandu to the Chinese border at Kodari. The Daklang-Listi road is located in the Upper Bhote Koshi region, which is a narrow valley with steep slopes. This area lies in the Lesser Himalayan region, which is dominated by sedimentary and metasedimentary rocks including Shale, Sandstone, Limestone, Slate, Phyllite, Schist, Dolomite, Quartzite and carbonate rocks [5-7]. The alignment of Daklang-Listi road runs across the hillslopes composed in some places of bare bedrock and in other places of transported soil deposits such as talus, colluvium and taluvium.

\* Corresponding author: [samprada.pradhan@durham.ac.uk](mailto:samprada.pradhan@durham.ac.uk)

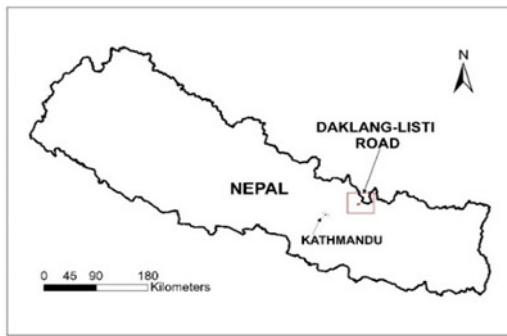


**Fig. 1** Map of Nepal showing location of Daklang-Listi road (left), Daklang-Listi road alignment showing the location of Kanglang landslide (right).

### 3 Reconnaissance field survey

The reconnaissance field survey was conducted in August 2018 to characterise the types of failure along Daklang-Listi road due to monsoonal rainfall. Prior to this, two field-visits were conducted in October 2017 and December 2017, when this road was being widened by cutting the hillslopes. In December 2017 (dry period), widening of the road was nearly completed, and within 7 months of completion, 97 new landslides had occurred along this road in August 2018, disrupting the road’s serviceability for almost 6 months. Based on the field observation of the failure characteristics, the landslides were classified into three major categories as shown in Fig. 2. The “failures in cut slope” were relatively small and localised in nature, while the “failures in valley slope” were mainly caused by debris-carrying surface runoff. The “failure in cut-slope extending to hillslope” was the most frequent type of failure found along the Daklang-Listi road. An example of this type of failure is the landslide located in Kanglang village, which will be referred to as Kanglang landslide hereafter (Fig. 1 and 3). The Kanglang landslide ( $27^{\circ}53'32.0''N$ ,  $85^{\circ}54'28.5''E$ ) occurred in July 2018 (Fig. 4) after the road widening was completed. The features of this landslide were obtained from direct field-measurements and have been summarised in Table 1. Based on the precipitation data from 1955 to 2018, obtained from the nearest rainfall station at Gumthang ( $27^{\circ}51'19.1''N$ ,  $85^{\circ}51'34.7''E$ ), it was noted that the rainfall in July 2018 was about 40% less than the 63-year average July rainfall from 1955 to 2017 (Fig. 4). Moreover, the daily rainfall during July 2018 did not exceed 30 mm [8], which is significantly lower than the 24-hour rainfall threshold for landslides as identified empirically by [9-10] for the Himalayan slopes in Nepal. This observation suggests that Kanglang landslide was triggered by a non-exceptional rainfall event, which leads us to the understanding that other external factors like slope-cutting for road construction may have contributed to the failure process.

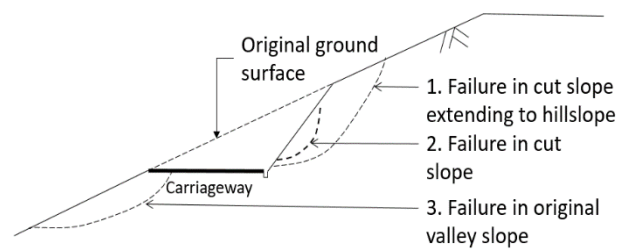


**Fig. 2** Major failure types along Daklang-Listi Road (modified after [11])

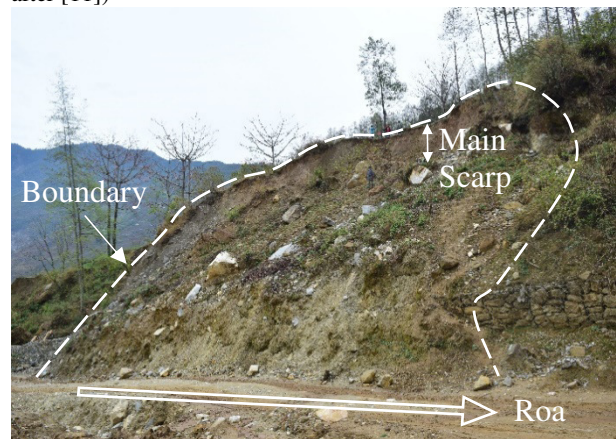


**Fig. 3** Photograph of the Kanglang landslide

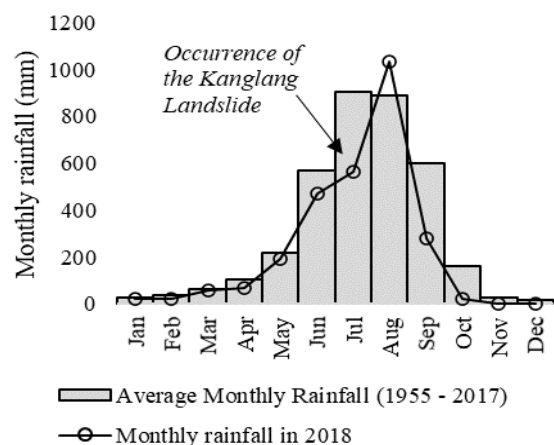


**Fig. 4.** Monthly rainfall in 2018 in comparison to the 63-year average measured at Gumthang rainfall station Source: [8]

**Table 1** Summary of the characteristics of Kanglang Landslide

<b>Length</b>	25 m
<b>Width</b>	45 m
<b>Depth of sliding surface</b>	~1.5 m
<b>Failure type</b>	Translational slide [12]
<b>Aspect</b>	North-east
<b>Elevation</b>	1442 m to 1463m
<b>Cut slope angle</b>	~70°
<b>Hillslope angle</b>	~23°

## 4 Geotechnical investigation

Geotechnical investigation was carried out into the Kanglang landslide in March 2019 for the characterisation of the in-situ soils. A trial pit (1.5 m × 1 m) was excavated manually down to 1.5 m depth near the landslide crown (27°53'28.79"N, 85°54'31.69"E). The ground-water table was not encountered to this depth. Disturbed and undisturbed samples were obtained from three depths: 0.3 m, 0.8 m, and 1.2 m. Undisturbed core samples were obtained by pushing open-ended tubes (38 mm internal diameter) into the pit bottom, which were then sealed with paraffin wax to limit moisture loss. The samples were imported to Durham University, UK to conduct laboratory testing. The physical parameters of the soil samples obtained from the laboratory tests are summarised in Table 2 and 3.

Atterberg limit tests were carried out as per BS EN ISO 17892-12:2018 and particle size analyses were conducted using a commercial laser diffraction particle size analyser (LS13320 analyser). The samples predominantly consisted of fine-grained soils showing border-line clay-silt behaviour and were hence, classified as silty clay of intermediate plasticity. As shown in Table 3, the in-situ water contents were lower than the plastic limits of the soils down to 1.5 m, which indicated that the soils were in an unsaturated state [13]. Furthermore, the soils near the ground were relatively loose and porous, with lower density and higher void ratio and porosity. When compared to the soils at greater depths from the surface, the soil near the ground was less saturated (degree of saturation of 47%), which would be expected due to atmospheric drying processes.

**Table 2** Summary of physical properties of the undisturbed samples

	Depth (m)			
	0.0 to 0.30	0.30 to 0.50	0.50 to 0.75	0.75 to 1.50
<b>Clay (%)</b>	6.6	9.0	12.3	7.5
<b>Silt (%)</b>	46.2	56.9	61.8	56.0
<b>Sand (%)</b>	47.3	34.1	26.0	36.5
<b>PL (%)</b>	22.5	24.2	24.7	23.4
<b>LL (%)</b>	39.1	38.3	39.9	37.1
<b>PI (%)</b>	16.6	14.1	15.2	13.8

PL: Plastic Limit, LL: Liquid Limit, PI: Plasticity Index

**Table 3** Summary of particle size distribution and Atterberg limits for disturbed samples

Properties	Depth (m)		
	0.5	1.0	1.5
<b>Bulk density (Mg/m<sup>3</sup>)</b>	1.57	1.85	1.98
<b>Specific gravity</b>	2.72	2.78	2.75
<b>Water content (%)</b>	18.0	17.7	13.3
<b>Void ratio</b>	1.04	0.77	0.57
<b>Porosity (%)</b>	51.0	43.4	36.4
<b>Degree of saturation (%)</b>	47.1	64.0	64.1
<b>Dry density (Mg/m<sup>3</sup>)</b>	1.33	1.57	1.75

## 5 Installation of field-monitoring station

The two important soil parameters directly affecting the stability of the slopes during rainfall are matric suction and soil water content within the slopes. Several studies have used field monitoring of soil suction to understand the hydrological response of the slopes under infiltration conditions [14-18]. As an alternative, direct measurement of the soil moisture in terms of Volumetric Water Content (VWC) using moisture sensors is increasingly being used when suctions cannot be measured [19-21]. In this study, real-time monitoring of VWC was carried out considering the advantages of this method such as quicker response to infiltration [21] and the elimination of the need for regular maintenance. The monitoring station was installed near the crown of Kanglang landslide in March 2019. It consists of three Decagon 10HS soil moisture smart sensors (resolution: 0.0008 m<sup>3</sup>/m<sup>3</sup>), tipping bucket-type rain-gauge (resolution: 0.2 mm), and HOBO RX3000 data logger (Fig. 5). The data logger continuously records the VWC and rainfall at 1-minute interval, which can be accessed remotely.

The 10HS soil moisture sensors use a capacitance-based technique to measure the VWC. The concept is to use the sensor probes as the capacitor electrodes and the soil surrounding these electrodes as the dielectric medium to measure the total dielectric permittivity of the medium i.e. soil, which is then converted into the VWC using standard calibration equations (with ±3% accuracy) [22]. In the field, the 10HS sensors were installed horizontally at 0.3 m, 0.8 m, and 1.2 m depths from the ground surface on the undisturbed vertical sides of the trial pit (Section 4). In this way, a natural flow of water was assured and the possibility of preferential flow paths was avoided. A dummy metallic sensor of the same thickness and length was pushed into the pit wall prior to installing the sensors so as to prevent any damage to the sensor prongs. After installation of the sensors, the trial pit was carefully backfilled with the excavated materials in small layers, so as achieve the approximate density of the surrounding soils. The cables above the trench were placed inside a PVC pipe to prevent any damage due to the external factors. The rain-gauge and the data-logger were mounted on a wooden frame next to the trial pit as shown in Fig. 5.



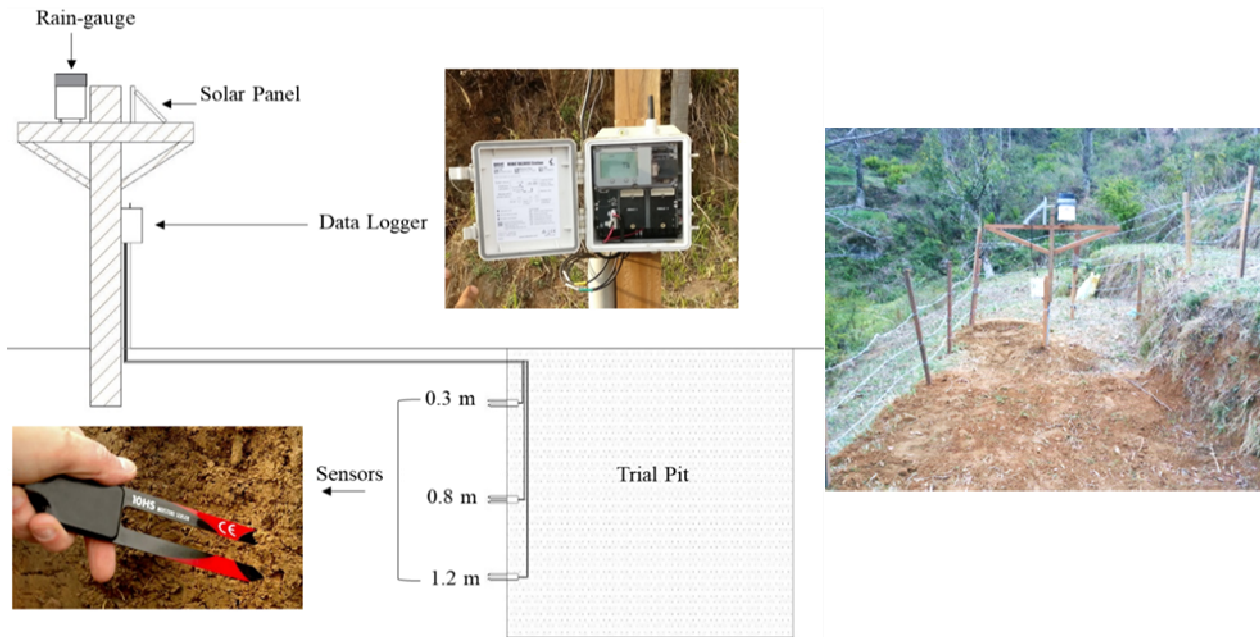


**Fig. 5** (a) HOBO RX3000 data logger, (b) 10HS soil moisture smart sensor, (c) Field–monitoring set-up

## 6 Field-monitoring results

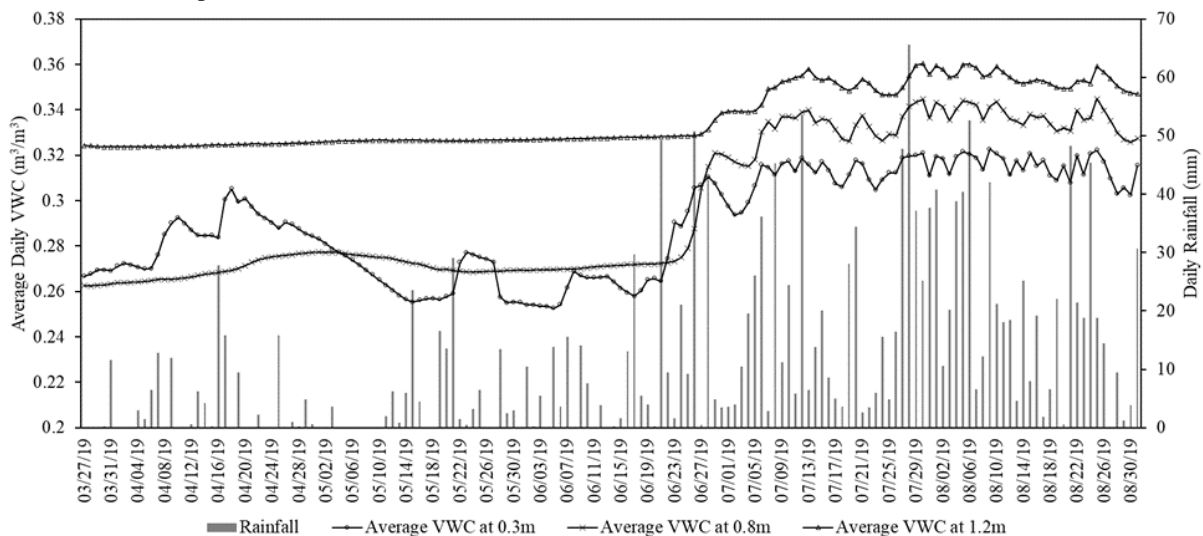
### 6.1 Pre-monsoon 2019

Fig. 6 presents the rainfall and average daily VWC measurements from 28 March to 31 August 2019. There exist notable differences in the response of the sensors located at different depths below the ground surface during this period.

The fluctuations in the VWC at 0.3 m was found to be directly connected to the amount of rainfall. The VWC at this layer responded quickly during and after the rainfall event, which can be attributed to the presence of surficial cracks that dominate the hydraulic conductivity of the soil near the surface. In contrast, the VWC at 1.2 m depth remained almost constant (<1%

change) until 31 May 2019, which indicated that the rainwater may have infiltrated beyond 0.8 m, but did not reach to 1.2 m.

It should be noted that the VWC at 0.3 m did not increase on 15 May 2019 after the rainfall event, which was comparable to the rainfall on 16 April 2019 that caused a significant increase in the VWC. This could be the effect of the prolonged dry period that existed before 15 May 2019, which caused a significant lowering of the VWC and approximately 8% decrease in the degree of saturation (Fig. 7(a)). Such a decrease may be due to evapotranspiration and vegetation roots that take up water during drying. The effect of atmospheric drying decreased with increasing depths from the surface as shown in Fig. 7(a). As a result, the soil at 1.2 m was wetter than the upper layers, which explains the consistently high VWC at this depth until 31 May 2019.



**Fig. 6** Average daily VWC ( $\text{m}^3/\text{m}^3$ ) and daily rainfall (mm) between 27 March 2019 and 31 August 2019.

### 6.2 Monsoon 2019

The variations in the daily rainfall and average daily VWC from June until the end of August 2019 are shown in Fig. 6. From the beginning of monitoring until 31 August 2019, 1840 mm rainfall was recorded, 85% of which occurred after 1 June 2019. Due to the heavy rainfall and consecutive wet days, changes in the VWC down to 1.2 m were recorded.

Similar to the pre-monsoon period, the VWC at 0.3 m changed quickly during and after a rainfall event. At 1.2 m, the VWC started rising after 28 June 2019, and interestingly, not during the high-intensity, intermittent rainfall with a maximum hourly intensity of 23 mm/hour on 26 June 2019. Moreover, the maximum hourly VWC at 0.3 m, 0.8 m, and 1.2 m were recorded successively

between 28 and 30 July 2019 (Fig. 8). The highest VWC at 0.3 m and 0.8 m occurred during a prolonged, heavy rainfall (64 mm in 12 hours) on 28 July 2019. Similarly, the rainfall on 30 July 2019 that increased the VWC at 1.2 m to maximum was a low-intensity, long-duration rainfall (42 mm in 10 hours). This behaviour shows that the heavy rainfall events, lasting for a relatively longer duration are capable of increasing the VWC at greater depths from the surface. During the continuous wet period between 25 and 30 July 2019, the degree of saturation increased by ~3% or more at all measured depths (Fig. 7(b)). In contrast to the observations during the dry period (Fig. 7(a)), rainfall infiltration caused a notable rise in the degree of saturation down to 1.2 m. Such progressive wetting by rainfall infiltration can cause reduction of matric suction and consequent loss of shear strength.

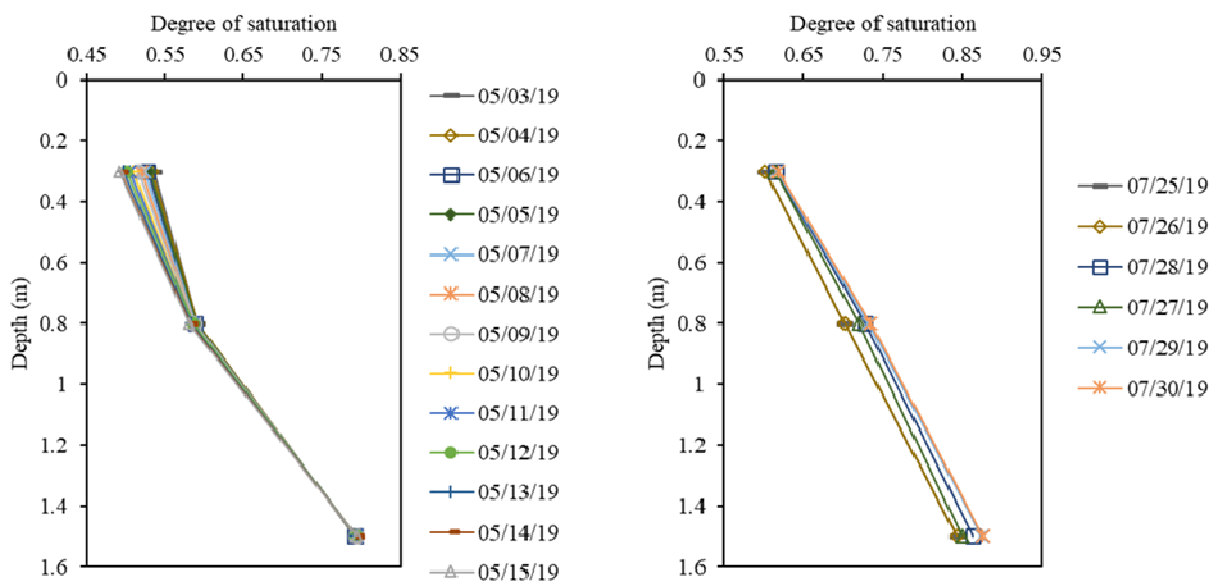


**Fig. 7** (a) Variations in the degree of saturation from 3 May 2019 to 15 May 2019 (13 days), (b) Variations in the degree of saturation from 25 July 2019 to 30 July 2019 (6 days)

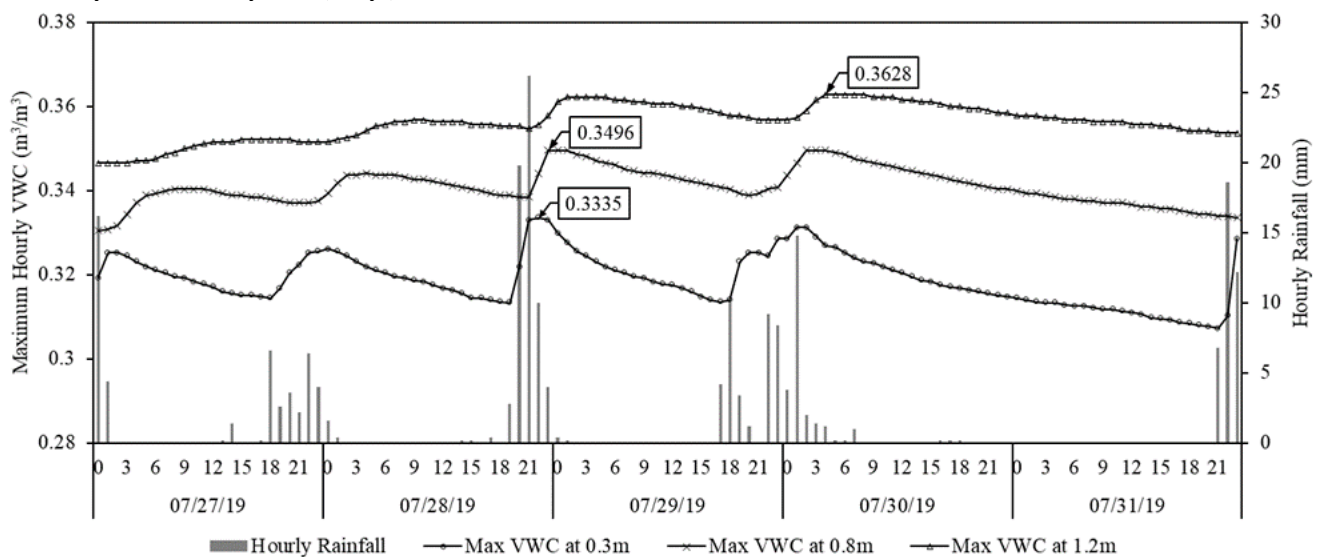


**Fig. 8.** Maximum hourly VWC ( $\text{m}^3/\text{m}^3$ ) and hourly rainfall (mm) between 27 July 2019 and 31 July 2019

Moreover, Fig. 8 highlights the pattern of the increasing response-time of VWC with depth. In general, decrease in the VWC at the upper layer is followed by increase in the VWC at the underlying layer. Such temporal variations of the VWC increments represent the infiltration pattern in the soil. If such conditions prevail throughout the depth of the soil, the decrease in the VWC at 1.2 m on 30 July 2019 after reaching the maximum value shall be followed by a rise in the VWC in the underlying layers. This means that the soil layer below 1.2 m can have a VWC greater than 0.363 m<sup>3</sup>/m<sup>3</sup>. Since the porosity of the soil at 1.5 m is 36.40%, the soil at this layer may have reached complete saturation on 30 July 2019.

In the case of Kanglang landslide in July 2018, slope-cutting for road was carried out during the dry season. Due to the additional shear strength imparted by soil suction during this period, the slope may have remained stable. As observed during the 2019 monsoon (Fig. 6), rainfall infiltration in July 2018 caused increase in the VWC and hence a loss of suction can be expected in the soil layers below 1.2 m. This loss of suction, and hence loss of shear strength, consequently could lead to failure.

## 7 Conclusions

The Kanglang Landslide occurred along Daklang-Listi road in July 2018, when the rainfall was not exceptionally high. This observation led to the understanding that steepening of the slopes due to slope-cutting for road construction can promote landsliding even during non-exceptional rainfall events. Geotechnical investigation was carried out at Kanglang landslide in March 2019, which showed that the soil near the surface existed in an unsaturated state during dry periods. Monitoring of the VWC and rainfall during March-August 2019 revealed that progressive infiltration during longer-duration rainfall and consecutive wet days can cause saturation of the soils and loss of matric suction at shallow depths. Since the slope cuttings along Daklang-Listi road were carried out during the dry season (October-December), the additional shear strength imparted by matric suction in the unsaturated soils may have allowed the cut-slope at Kanglang landslide to remain stable after cutting. On the onset of 2018 monsoon, rainfall infiltration may have caused loss of suction, leading to the failure. Hence, slope-cutting for road construction, relying on the unsaturated strength of the surficial soil can be the major cause of frequent shallow landslides occurring along the hillslopes of Nepal.

This is on-going research and long-term monitoring of the VWC and rainfall is being carried out. The temporal variations of the VWC with depth reflect the drying and infiltration pattern occurring in the soils. This dataset will further be used to evaluate the influence of the slope-cuttings on the hydrological response and stability of the slopes using coupled hydro-mechanical modelling.

## Acknowledgements

Special thanks to the Institute of Hazard Risk and Resilience (IHRR), Durham University, UK for funding.

## References

1. D.N. Petley, G.J. Hearn, A. Hart, N.J. Rosser, S.A. Dunning, K. Oven, W.A. Mitchell, *Nat. Hazards* **43**, 23 (2007).
2. M. Jaboyedoff, C. Michoud, M. Derron, J. Voumard, G. Leibundgut, K. Sudmeier-Rieux, C. Michoud, F. Nadim, E. Leroi, *Landslides and Engineered Slopes. Experience, Theory and Practice* (CRC Press, 2018).
3. G.J. Hearn, N.M. Shakya, Q. J. Eng. Geol. Hydrogeol. 2017 (2017).
4. R. Pokharel, S.R. Acharya, T. Investment, J. East. Asia Soc. Transp. Stud. **11**, 209 (2015).
5. J. Stöcklin, *J. Geol. Soc. London*. **137**, 1 (1980).
6. R. Dahal, *Geology for Technical Students* (2006).
7. B.N. Upreti, *Landslide Hazard Mitig. Hindu Kush-Himalayas* **31** (2001).
8. DHM Department of Hydrology and Meteorology (DHM), (2018).
9. N. Caine, P.K. Mool, *Mt. Res. Dev.* **2**, 157 (1982).
10. R.K. Dahal, S. Hasegawa, A. Nonomura, M. Yamanaka, S. Dhakal, P. Paudyal, *Geomorphology* **102**, 496 (2008).
11. G.J. Hearn, *Slope Engineering for Mountain Roads* (Geological Society of London, London, 2011).
12. D.J. Varnes, in *Landslides Eng. Pract.*, edited by E.B. Eckel (National Research Council, Washington, D.C., 1958).
13. H. Rahardjo, E.C. Leong, R.B. Rezaur, in *Proc. Natl. Semin. Slope 2002* (Bandung, 2002), pp. 15–29.
14. D.G. Toll, S.D.N. Lourenço, J. Mendes, D. Gallipoli, F.D. Evans, C.E. Augarde, Y.J. Cui, A.M. Tang, J.C. Rojas, L. Pagano, C. Mancuso, C. Zingariello, A. Tarantino, *Q. J. Eng. Geol. Hydrogeol.* **44**, 23 (2011).
15. O. Augusto Filho, M.A. Fernandes, *Bull. Eng. Geol. Environ.* (2018).
16. H. Rahardjo, V.A. Santoso, E.C. Leong, Y.S. Ng, C.J. Hua, *Soils Found.* **51**, 471 (2011).
17. S. Jeong, K. Lee, J. Kim, Y. Kim, *Sustainability* **9**, 1280 (2017).
18. I. Tsaparas, H. Rahardjo, D.G. Toll, E.C. Leong, *Can. Geotech. J.* **40**, 1012 (2003).
19. Y.K. Kim, D. Ph, S.R. Lee, M. Asce, *J. Geotech. Geoenvironmental Eng.* **136**, 248 (2010).
20. S.J. Harris, R.P. Orense, K. Itoh, *Landslides* **9**, 349 (2012).
21. B.-G. Chae, M.-I. Kim, *Environ. Earth Sci.* **66**, 1973 (2012).
22. G. Kargas, K.X. Soulis, *J. Irrig. Drain. Eng.* **138**, 632 (2012).